REPORT DOCUMENTATION PAGE

OMB No. 0704-0188

1. AGENCY USE ONLY *(Leave blank)*	2. REPORT DATE February 9, 1996	3. REPORT TYPE AND DATES COVERED Technical 1/1/94 – 12/31/95

4. TITLE AND SUBTITLE Experimental Evaluation of Pressure-Strain Models in Complex 3-D Turbulent Flow Near a Wing/Body Junction	5. FUNDING NUMBERS N00014-94-1-0092 N00014-90-J-1909

6. AUTHOR(S)

M. Semih Ölçmen and R.L. Simpson

7. PERFORMING ORGANIZATION NAME(S) AND ADDRESS(ES) Dept. of Aerospace and Ocean Engineering Virginia Polytechnic Institute & State University Blacksburg, VA 24061-0203	8. PERFORMING ORGANIZATION REPORT NUMBER VPI – AOE – 228

9. SPONSORING / MONITORING AGENCY NAME(S) AND ADDRESS(ES) Advanced Research Projects Agency, 3701 N. Fairfax Drive, Suite 100, Arlington, VA 22203-7714; Office of Naval Research, 800 N. Quincy St., ARLINGTON, VA 22217	10. SPONSORING / MONITORING AGENCY REPORT NUMBER

11. SUPPLEMENTARY NOTES

12a. DISTRIBUTION / AVAILABILITY STATEMENT

Unlimited

12b. DISTRIBUTION CODE

19960422 133

13. ABSTRACT *(Maximum 200 words)*

Comparisons of experimentally-extracted pressure/rate-of-strain values were made to theoretical pressure-strain models for several locations of a wing-body junction flow. The experimental pressure/rate-of-strain results were calculated from data obtained with a LDV technique. The data consist of profiles of mean velocity and higher order moments including quadruple products in a two-dimensional turbulent boundary layer (2DTBL), a strongly skewed three-dimensional turbulent boundary layer (3DTBL), in the vicinity of a 3-D separation line, and around the center of the horse-shoe vortex that forms around the wing. Terms in the transport equations for the Reynolds' stresses and the turbulent kinetic energy are also presented here. Several linear and non-linear pressure/rate-of-strain models are tested using the measured quantities as input to the models. The tested models are the Launder-Reece-Rodi (1975), Gibson-Launder (1978), Oberlack-Peters (1993), Fu-Launder-Tselepidakis (1987) (2 models), Shih-Lumley/Choi-Lumley (1985, 1984), and Speziale-Sarkar-Gatski (1991). The measurements were carried out in the Virginia Tech Boundary Layer Tunnel, at nominal air speed of 27.5 m/s around a NACA 0020 tailed and 3:2 elliptical nosed wing shape.

Near-wall correction effects on the theoretical pressure/rate-of-strain models; effect of approximation for the pressure diffusion, the anisotropic dissipation approximation as well as isotropic dissipation approximation on the experimental pressure-strain data are examined. The results are compared to previous Direct Numerical Simulation data qualitatively. Data show that the pressure-diffusion approximation by Lumley (1978) is an important term in the $\overline{v^2}$, $\overline{uv}$, and $\overline{vw}$ stress budgets. Qualitative comparison of experimental budgets of transport of stresses to DNS solutions show a better agreement between the two with the anisotropic dissipation of Hallbäck, Groth, and Johansson (1990). Pressure-strain model estimates deteriorate with increased complexity of the flow. The models agree with the data better relatively away from the wall. Superiority of the models depends on the approximations used.

14. SUBJECT TERMS Three-dimensional flow pressure-strain models Second-moment closures Turbulence Modeling	15. NUMBER OF PAGES 157
	16. PRICE CODE

17. SECURITY CLASSIFICATION OF REPORT unclassified	18. SECURITY CLASSIFICATION OF THIS PAGE unclassified	19. SECURITY CLASSIFICATION OF ABSTRACT unclassified	20. LIMITATION OF ABSTRACT unlimited

DISCLAIMER NOTICE

UNCLASSIFIED

Technical Report
distributed by

**DEFENSE
TECHNICAL
INFORMATION
CENTER**

DTIC Acquiring Information-
Imparting Knowledge

Cameron Station
Alexandria, Virginia 22304-6145

UNCLASSIFIED

THIS DOCUMENT IS BEST
QUALITY AVAILABLE. THE
COPY FURNISHED TO DTIC
CONTAINED A SIGNIFICANT
NUMBER OF PAGES WHICH DO
NOT REPRODUCE LEGIBLY.

ABSTRACT

Comparisons of experimentally-extracted pressure/rate-of-strain values were made to theoretical pressure-strain models for several locations of a wing-body junction flow. The experimental pressure/rate-of-strain results were calculated from data obtained with a LDV technique. The data consist of profiles of mean velocity and higher order moments including quadruple products in a two-dimensional turbulent boundary layer (2DTBL), a strongly skewed three-dimensional turbulent boundary layer (3DTBL), in the vicinity of a 3-D separation line, and around the center of the horse-shoe vortex that forms around the wing. Terms in the transport equations for the Reynolds' stresses and the turbulent kinetic energy are also presented here. Several linear and non-linear pressure/rate-of-strain models are tested using the measured quantities as input to the models. The tested models are the Launder-Reece-Rodi (1975), Gibson-Launder (1978), Oberlack-Peters (1993), Fu-Launder-Tselepidakis (1987) (2 models), Shih-Lumley/Choi-Lumley (1985, 1984), and Speziale-Sarkar-Gatski (1991). The measurements were carried out in the Virginia Tech Boundary Layer Tunnel, at nominal air speed of 27.5 m/s around a NACA 0020 tailed and 3:2 elliptical nosed wing shape.

Near-wall correction effects on the theoretical pressure/rate-of-strain models; effect of approximation for the pressure diffusion, the anisotropic dissipation approximation as well as isotropic dissipation approximation on the experimental pressure-strain data are examined. The results are compared to previous Direct Numerical Simulation data qualitatively. Data show that the pressure-diffusion approximation by Lumley (1978) is an important term in the $\overline{v^2}$, $\overline{uv}$, and $\overline{vw}$ stress budgets. Qualitative comparison of experimental budgets of transport of stresses to DNS solutions show a better agreement between the two with the anisotropic dissipation of Hallbäck, Groth, and Johansson (1990). Pressure-strain model estimates deteriorate with increased complexity of the flow. The models agree with the data better relatively away from the wall. Superiority of the models depends on the approximations used.

NOMENCLATURE

$A_1 = \dfrac{\sqrt{(\overline{uv})^2 + (\overline{vw})^2}}{(\overline{u^2} + \overline{v^2} + \overline{w^2})}$ Townsend's structural parameter

b_{ij} anisotropy tensor

C_p static pressure coefficient

$(\partial C_p / \partial x)_{FS}$ static pressure coefficient gradient

C_{ij} convection tensor

$FA = \arctan(W/U)$ flow angle

$FGA = \arctan\left(\dfrac{\partial W/\partial y}{\partial U/\partial y}\right)$ flow gradient angle

$N_{TC} = \dfrac{-\overline{vw}/(\partial W/\partial y)}{-\overline{uv}/(\partial U/\partial y)}$ anisotropy constant in tunnel coordinates

p   fluctuating pressure component

PR_{ij} production tensor

PD_{ij} pressure diffusion tensor

Re_θ Reynolds number based on momentum thickness

S_{ij} rate-of-strain tensor

$SSA = \arctan\left(\dfrac{\overline{vw}}{\overline{uv}}\right)$ shear stress angle

TD_{ij} turbulent-diffusion tensor

$TKE = k = (\overline{u^2} + \overline{v^2} + \overline{w^2})/2 = (\overline{u_i u_i})/2$ turbulent kinetic energy

U_e velocity magnitude at the boundary layer edge

U_i mean velocity components

$\overline{u_i u_j}$ Reynolds stress tensor. i=1, 2, 3; j=1, 2, 3.

$\overline{u_i u_j u_k}$ triple velocity correlation tensor

$U^+ = \dfrac{U}{u_\tau}$ nondimensional mean velocity

$u_\tau = \sqrt{\tau_w / \rho}$ skin friction velocity

VD_{ij} viscous diffusion tensor

x_{TC}, y_{TC}, z_{TC} tunnel coordinates

$y^+ = y u_\tau / \nu$ wall-law variable

β_{FS} flow angle at the boundary layer edge

β_{WC} wall-stress direction

δ_{ij} Dirac delta function. $\delta_{ij} = 1$ if i=j, $\delta_{ij} = 0$ if i≠j.

δ boundary layer thickness

ε_{ij} viscous dissipation tensor

$\varepsilon = \varepsilon_{ii}/2$ dissipation of turbulent kinetic energy

$$\theta = \int_0^\infty \left(1 - \frac{U}{U_e}\right)\frac{U}{U_e}\,dy$$ momentum thickness

ν kinematic viscosity

ρ density

σ standard deviation

$$\tau = \sqrt{\left(-\rho\,\overline{uv}\right)^2 + \left(-\rho\,\overline{vw}\right)^2}$$ shear stress magnitude in the flow

τ_w wall shear stress

Φ_{ij} pressure-strain tensor

Ω_{ij} vorticity tensor

Table of Contents

List of Figures

List of Tables

CHAPTER I - INTRODUCTION AND EXPERIMENTAL DATA

The data presented here are part of a set of measurements made in the horse-shoe vortex that forms around a wing-body junction vortex. The wing used is a 3:2 elliptical nosed, NACA 0020 tailed wing profile with maximum thickness of 2.824 inches, chord length of 12 inches, and a height of 9 inches. The wing was mounted perpendicular on the flat bottom surface of the Boundary Layer Tunnel with a 3 feet x 10 inches rectangular cross section and 8 m long tunnel test section at Virginia Tech. The nominal speed of air was 27.5 m/sec and Re_θ (Reynolds number based on momentum thickness) of the flow at 0.75 chord upstream of the wing was 5936.

Previous measurements using the same tunnel and wing configuration were reported by several researchers. The approach flow in front of the wing at the symmetry plane were reported by Devenport and Simpson (1990), and Shinpaugh and Simpson (1995). Three-dimensional turbulent boundary layer (3DTBL) measurements on the tunnel floor due to the presence of the wing away from the horse-shoe vortex were reported by Ölçmen and Simpson (1995a). Measurements of 3DTBL at the side and at the wake of the wing were reported by Fleming et al. (1993). Ha and Simpson (1993) analyzed the flow structure using several hot-wire probes and surface hot-film probes at the same locations of Ölçmen and Simpson (1995a). Ölçmen and Simpson (1992) studied the surface pressure-fluctuations on a stagnation line on the symmetry plane of the wing. Lewis et al. (1994) studied the heat flux fluctuations at the same locations. Using the similar shape but a water tunnel many researchers studied the flow using flow visualization methods (Fleming et al. (1995), Kim et al. (1991))

The flow is well documented. The mean surface-pressure distribution was measured and reported by Ölçmen (1990). Oil flow visualization methods were used to document the surface skin friction lines. In this Chapter several profiles measured by the LDV technique using the three-component portion of the five-component-LDV probe (Ölçmen and Simpson, 1995b) developed at Virginia Tech to study the structure of the 3DTBLs are presented.

Figure 1 shows the schematic of the wing-body junction. The measurement locations on the line passing through Station 5 and perpendicular to the wing (23° line) and the coordinate system definitions are also shown. $()_{FS}$ stands for the free-stream coordinates and the $()_{TC}$ stands for the tunnel coordinates. y axis is perpendicular to the floor. Positive x_{TC} is along the tunnel axis looking downstream with its origin at the wing-floor intersection. Positive x_{FS} is in the direction of the mean velocity direction at the edge of the boundary layer. The z axes complete right-handed coordinate systems. Figure 2 shows the oil flow visualization picture obtained on the wall. Figure shows that incoming flow separates at the nose region and rolls around the wing to form the horse-shoe vortex region. At downstream of the separation line, line-of-low-shear forms. Line-of-low-shear and the separation line merge together downstream of the nose. Fish-tailed structure of the horse-shoe vortex is also shown. The profiles presented are 4 out of 38 profiles measured. These profiles presented were obtained in a 2-D boundary layer without the wing presence, and in the horse-shoe vortex forms around the wing. 30 profiles measured inside the horse-shoe vortex were closely spaced in order to calculate the x and z derivatives of the flow quantities. Measurements were made on a line passing through Station 5 (Ölçmen and Simpson, 1995a) and perpendicular to the wing making ≈23° to

the z axis and on a line 0.125 inches downstream of this line and parallel to it. 5 profiles were also taken at Station 5 location. Measurements include the mean velocities, and fluctuating velocity products including 4th order products. The measurements were used to calculate the terms in transport of Reynolds stresses and the extracted data were used to compare pressure-strain models to the pressure-strain data. Figure 3 shows the mean velocity magnitude and the secondary flow streamlines in the plane perpendicular to the floor passing through the 23° line. Abscissa shows the distance from the wing, where the wing is located at $\Delta S=0$. The ordinate is logarithmically spaced. Figure 3 shows that a large vortex is located at the outer region and entrains the high speed free-stream flow closer to the wall especially closer to the wing. At $\Delta S \approx -4.2$cm the flow experiences a three-dimensional separation where all the secondary streamlines merge towards a point. At distances closer to the wing ($\Delta S \approx >-0.4$cm) the flow direction is reversed (figure 3).

Measurements presented in this report are mean velocity, and fluctuating velocity products including the 3rd order at selected locations. Presentation of the other profiles will be in an accompanying report. The locations selected are the 2-D station, Station 5, Separation, and Vortex-core stations. Plots of the measured profiles in a plane perpendicular to the tunnel floor encompassing the measurement station locations show that the Separation and Vortex-core stations correspond to the location where the 3DTBL goes through a 3-D separation and to the location where the center of the outer region vortex is located, respectively. Presentation of the data and the following discussions are presented in tunnel coordinates throughout the report.

I-A) Mean velocities

The U/u_τ mean velocity profile at the 2-D station was used to calculate the skin-friction coefficient at the wall using Coles' law-of-the-wall fit, therefore the profile follows the Coles' law of the wall ($U^+ = \dfrac{1}{0.41} \ln(y^+) + 5$) (Fig. 4). In tunnel coordinates, at Station 5 the U/u_τ profile is lower above $y^+ \approx 50$. At the separation station velocity gradients are higher near the wall. The profile is also higher than both the 2D and Station 5 profiles. At the Vortex-core station in the region $y^+ \approx 50$ to 200 the U/u_τ velocity gradient is approximately zero.

The V/u_τ velocities are not affected by the coordinate system rotation (Fig. 5). At the 2-D station velocities increase towards the layer edge. At Station 5 a peak at $y^+ \approx 500$ forms. At separation station a negative peak at $y^+ \approx 60$ is accompanied by a positive peak at $y^+ \approx 500$. At the Vortex-core station velocities increase till $y^+ \approx 400$ and a sharp decrease towards the layer edge is observed. V/u_τ changes sign and the magnitude is increased towards the Vortex-core station.

The W/u_τ at 2-D station is very close to zero (Fig. 6). The velocity magnitude peak is increased and shifted further away from the wall progressing towards the Vortex-core station. At the Vortex-core station the W/u_τ decreases quickly above the peak location.

I-B) Normal stresses

At Station 5 the $\overline{u^2}/u_\tau^2$ profile values are 1/4 lower than the values at 2-D station

throughout the layer (Fig. 7). However at the Separation station the values are increased to follow the 2-D variation very closely except in the $y^+ \approx 15$ to 150 region. At the Vortex-core station the values are increased by 1.5 times compared to 2-D and about 2 times compared to the Station 5 values. Above $y^+ \approx 400$ a quick decrease in the $\overline{u^2}/u_\tau^2$ results in values less than the 2-D values above $y^+ \approx 800$.

The $\overline{v^2}/u_\tau^2$ increases to very large values at the Vortex-core station (Fig. 8). $\overline{v^2}/u_\tau^2$ at Station 5 compared to 2-D flow near wall values between $y^+ \approx 20$ to 150 region have differences. Between $y^+ \approx 50$ to 1000 region $\overline{v^2}/u_\tau^2$ values at Separation station are ≈ 1.5 times larger than the 2-D values. At the Vortex-core station $\overline{v^2}/u_\tau^2$ is ≈ 7 times larger than 2-D value peak.

At the Vortex-core station the $\overline{w^2}/u_\tau^2$ values are also different from the 2-D distribution (Fig. 9). The peak value at the Vortex-core station is 8 to 9 times larger than the 2-D values. At Station 5 $\overline{w^2}/u_\tau^2$ near the wall is slightly higher than the 2-D values. At the Separation station values are 2 to 3 times to that of 2-D values.

The $\overline{v^2}/u_\tau^2$ profile very near the wall and above $y^+ \approx 1000$ vary similarly at all stations. The $\overline{w^2}/u_\tau^2$ show similar variations above $y^+ \approx 1000$ at every station.

I-C) Shear stresses

The $\overline{uv}/u_\tau^2$ shear stress profiles in the 3-D flow also show larger variations than the 2-D flow (Fig. 10). At Station 5 and at the Separation station, near wall values below $y^+ \approx 300$ and below $y^+ \approx 100$ are lower than the 2-D values, respectively. At the Separation station above $y^+ \approx 100$ the values are higher than the 2-D. Vortex core station values peak at $y^+ \approx 400$ with a value ≈ 3 times higher than the 2-D values.

The $\overline{uw}$ and $\overline{vw}$ shear stresses in a 2-D TBL are nominally zero. The location in the 3-D flow profiles where $\overline{uw}/u_\tau^2$ is zero shifts towards the wall progressing towards the Vortex-core station (Fig. 11). The positive peak value at the Vortex-core station is an order of magnitude larger than the Station 5 peak value. Above $y^+ \approx 500$ the stress values are very close to zero, showing that the $\overline{uw}/u_\tau^2$ stress in this region is not effected by the near wall structure.

Similarly, $\overline{vw}$ stresses are also very close to zero above $y^+ \approx 700$ (Fig. 12). The positive and the negative peak values are increased and the location where $\overline{vw} \approx 0$ in the profile is closer to the wall towards the Vortex-core station.

I-D) Triple products

Triple products very broadly describe the flux of a normal stress in some certain direction. For example $\overline{u^2 v}$ is the flux of $\overline{u^2}$ normal stress in the v fluctuating velocity direction. Also the triple products give information about the simultaneous occurrences of different velocity fluctuations in the average sense. For example $\overline{u^2 v} > 0$ shows that the

u fluctuating velocities in the average are associated with large positive v fluctuating velocities. Also this example shows that at the locations where $\overline{u^2v}>0$ the motion is associated with positive v fluctuations, therefore moving away from the wall. The "sweep" and "ejection" motions are the motions when (u>0, v<0), and (u<0, v>0) fluctuation velocities occur simultaneously, respectively. Therefore the locations where $\overline{u^2v}<0$ and $\overline{uv^2}>0$ denote "sweep" motion dominated regions. Quadrants defined with the signs of the u and the v fluctuating velocities can be generalized to include the sign of w fluctuations therefore octants can be defined.

In general the triple products at the Vortex-core station are larger compared to the other stations (Fig. 13). The variation of $\overline{u^2v}$ profiles show the local maxima and two local minima at all stations. The minimum near the wall is located at $y^+\approx10$ showing that the flux of $\overline{u^2}$ is towards the wall. Second local minimum is located around $y^+\approx100$ to 250 region shows a very high negative value at the Vortex-core station. At the Vortex-core station large gradients of the quantity are observed. Direction of the $\overline{u^2}$ flux changes 3 times at this station, similar to that at Station 5 with larger magnitudes.

The $\overline{u^2w}$ is nominally zero for the 2-D flow (Fig. 14). Large negative values at $y^+\approx8$ to 10 are followed by large positive values at $y^+\approx235$ to 300 at all stations. Large differences between the Separation and the Vortex-core station are observed for $\overline{u^2w}/u_\tau^3$. While the quantity peaks at $y^+\approx200$ at the Vortex-core station with positive values, Station 5 peak values are negative at $y^+\approx300$. This shows that the lateral flux of the $\overline{u^2}$ normal stress is opposite to each other at these two stations.

The $\overline{v^2w}$ is also nominally zero at 2-D station (Fig. 15). However the values at Separation and Vortex-core stations are overwhelmingly large compared to Station 5. $\overline{v^2w}/u_\tau^3$ shows a negative peak at $y^+\approx250$ at Separation station where it shows a positive peak at $y^+\approx45$ and a negative peak at $y^+\approx400$ at the Vortex-core station. The flux of $\overline{u^2}$ with the lateral fluctuations change sign in the layer at $y^+\approx150$ at the Vortex-core station.

The $\overline{v^2u}/u_\tau^3$ is also overwhelmingly large with negative values at the Vortex-core station compared to the other stations (Fig. 16). The value shows a negative peak at $y^+\approx400$. The negative peak value at Separation station is located at $y^+\approx225$. The sign of the quantity stays the same through out the Separation and Vortex-core stations.Showing that the flux of $\overline{v^2}$ is associated with the negative u fluctuations. Together the $\overline{u^2v}$ and $\overline{uv^2}$ at the Vortex-core station show that near the wall and in the outer region ejection motions are highly dominant and between $y^+\approx150$ to 300 negative v fluctuations are associated with negative u fluctuations.

The $\overline{uw^2}/u_\tau^3$ values show different characteristics at different stations (Fig. 17). The location where the quantity changes sign from positive top negative near the wall is closest to the wall proceeding towards the Separation station. Values above $y^+\approx100$ at 2-D and Separation stations are much smaller than the values at Separation and Vortex-core stations. At the Separation station and at the Vortex-core station profiles show two negative peaks. At the Vortex-core station also a positive peak is observed at $y^+\approx175$.

Magnitudes of the $\overline{vw^2}/u_\tau^3$ values are very small compared to the values at

separation and Vortex-core stations (Fig. 18). Near wall values at 3-D stations are negative below $y^+ \approx 25$. At Separation and Vortex-core stations the profiles show two peaks. Negative $\overline{vw^2}$ shows that $\overline{w^2}$ normal stress flux is towards the wall. Combined with the observations for $\overline{v^2w}$ figures show that below $y^+ \approx 25$ there is a region where v<0 and w> 0 fluctuations are dominant. Between $y^+ \approx 25$ till $y^+ \approx 150$, w>0 is accompanied by v>0 and between $y^+ \approx 150$ till $y^+ \approx 550$ w<0 is accompanied with v<0 fluctuations.

The $\overline{uvw}/u_\tau^3$ is nominally zero at the 2-D station (Fig. 19). At all stations near wall values below $y^+ \approx 17$ are positive. At Separation station and at Station 5 the values change sign to positive between $y^+ \approx 100$ to 200. However the variation of the quantity at the Vortex-core station changes sign many times in the layer.

The $\overline{u^3}/u_\tau^3$ profiles show positive peaks between $y^+ \approx 7$ to 15 at different stations (Fig. 20). The sign of the variation becomes negative at different y^+ locations between $y^+ \approx 15$ to 30. At 2-D station and at Station 5 the quantity becomes positive between $y^+ \approx 60$ to 300. However values at the Separation station and the Vortex-core station do not change sign, stay negative and show two local minima.

The $\overline{v^3}/u_\tau^3$ values at the Vortex-core station are overwhelmingly larger than the 2-D and Station 5 values (Fig. 21). The maximum value obtained at Vortex-core station is ≈ 14 times larger than the maximum value ≈ 1 obtained at Separation station.

The $\overline{w^3}/u_\tau^3$ values reach to very high negative values ($\approx$-50) around $y^+ \approx 30$ at Vortex-core station (Fig. 22). This value is approximately an order of magnitude larger than the ones obtained at Separation station and two orders of magnitude of the values at Station 5. Vortex-core station profiles show two smaller peaks above $y^+ \approx 100$.

1-E) Estimates of uncertainty

The uncertainty in each term of the mean velocity, Reynolds stress, and triple products were calculated using the two different data sets acquired at the Separation station and using Chauvent's criterion to calculate the standard deviation. The equation used is

$$\frac{d_{max}}{\sigma} = 1.15$$

where d_{max} is the average of the half of the differences between two calculated values for that term. 20 to 1 odds uncertainties calculated as $\pm 2\sigma$ are tabulated in table 1.

I-F) Derived quantities

I-F-1) Flow angle (FA)

The flow angle is calculated using,

$$FA = \arctan(\frac{W}{U})$$

The 2-D flow angles are nominally zero (Fig. 23). Flow angle magnitudes increase proceeding towards the Vortex-core station. The minimum location in the profile shift up into the layers. Around $y^+ \approx 800$ flow angles at every station are close to one another. Flow

angle at Vortex-core station increases more steeply at y^+ above the minimum location.

I-F-2) Flow Gradient angle (FGA)

The FGA is calculated using,

$$FGA = \arctan\left(\frac{\partial W/\partial y}{\partial U/\partial y}\right)$$

The FGA variation near the wall below $y^+ \approx 10$ is similar at Station 5 and at Separation station (Fig. 24). The values at the Vortex-core station near the wall are lower than the other two stations. The FGA changes sign at higher y^+ locations in the profiles. FGA at the Vortex-core station passes through zero value vary abruptly. The magnitude of the values are larger proceeding towards the Vortex-core station.

I-F-3) Shear stress angle (SSA)

The shear stress angle is calculated using,

$$SSA = \arctan\left(\frac{-\overline{vw}}{-\overline{uv}}\right)$$

The magnitude of the SSA in the profiles increases and the locations in the profiles where SSA changes sign are closer to the wall proceeding towards the Vortex-core station (Fig. 25). The FGA and SSA profile values do not follow each other. While at Station 5, FGA and SSA change sign at a location closer to each other at the Separation station and at Vortex-core station SSA changes sign closer to the wall. Near wall values of SSA are much different than the FGA values.

I-F-4) A_1, Townsend's structural parameter

This structural parameter is defined as:

$$A_1 = \frac{\sqrt{(\overline{uv})^2 + (\overline{vw})^2}}{\overline{u^2} + \overline{v^2} + \overline{w^2}}$$

The variations of the parameter below $y^+ \approx 10$ are close to each other at the 2-D, Station 5 and Separation stations (Fig. 26). At the Vortex-core station this variation is not followed. Between $y^+ \approx 100$ to 1000 the value is close to a constant at the 2-D flow station. At Station 5 the values reach to a maximum of 0.17 at $y^+ \approx 1000$. At the Separation station the values are reduced throughout the layer compared to Station 5. At the Vortex-core station very large double peaks are observed. This shows that u, v, and v, w fluctuating velocities are better correlated for this station.

I-F-5) Turbulent Kinetic Energy (TKE)

The TKE/u_τ^2 is calculated using

$$\frac{TKE}{u_\tau^2} = \frac{\overline{u^2} + \overline{v^2} + \overline{w^2}}{2u_\tau^2}$$

The TKE of the flow at Station 5 is reduced compared to 2-D station (Fig. 27). The values

rapidly increase towards the Vortex-core station. At the Vortex-core station values are ≈2.5 times that of the 2-D station. Near the wall and above $y^+ \approx 1000$, variations are similar to each other at every station.

I-F-6) Anisotropy constant (N_{TC})

The anisotropy constant N_{TC} is calculated using,

$$N_{TC} = \frac{-\overline{vw}/(\partial W/\partial y)}{-\overline{uv}/(\partial U/\partial y)}$$

The N_{TC} is the ratio of the eddy viscosities in the z and the x directions (Fig. 28). Many algebraic-eddy viscosity turbulence models assume that the ratio is ≈1. The figure shows that the ratio is increasingly away from 1 towards the Vortex-core station near the wall. Towards the layer outer edge the values become close to zero.

CHAPTER II - TRANSPORT BALANCE OF THE STRESSES

The Reynolds-stress transport equation with summation-subscript notation can be written as:

$$C_{ij} = PR_{ij} + \Phi_{ij} + TD_{ij} + PD_{ij} + VD_{ij} - \varepsilon_{ij}$$

where

$$C_{ij} = \frac{\partial \overline{u_i u_j}}{\partial t} + U_l \frac{\partial \overline{u_i u_j}}{\partial x_l} \qquad \text{convection}$$

$$PR_{ij} = -(\overline{u_i u_l} \frac{\partial U_j}{\partial x_l} + \overline{u_j u_l} \frac{\partial U_i}{\partial x_l}) \qquad \text{production}$$

$$\Phi_{ij} = \frac{\overline{p}}{\rho}(\frac{\partial u_i}{\partial x_j} + \frac{\partial u_j}{\partial x_i}) \qquad \text{pressure-strain}$$

$$TD_{ij} = -\frac{\partial \overline{(u_i u_j u_l)}}{\partial x_l} \qquad \text{turbulent diffusion}$$

$$PD_{ij} = -\frac{1}{\rho}(\frac{\partial (\overline{p u_j})}{\partial x_i} + \frac{\partial (\overline{p u_i})}{\partial x_j}) \qquad \text{pressure-diffusion}$$

$$VD_{ij} = +\nu \frac{\partial^2 \overline{u_i u_j}}{\partial x_l^2} \qquad \text{viscous-diffusion}$$

$$\varepsilon_{ij} = +2\nu \frac{\overline{\partial u_i}}{\partial x_l} \frac{\partial u_j}{\partial x_l} \qquad \text{viscous-dissipation}$$

The subscripts denote the axes. Repeated dummy indices in a multiplication denote summation. Here $\overline{u_i u_j}$ denote the Reynolds stress tensor, U_i stands for the three components of the mean velocity vector, p is the fluctuating pressure, ν is the kinematic viscosity, ρ is the density, and t is the time. Note the minus sign in front of the ε_{ij}.

All the terms are point dependent except the Φ_{ij} and PD_{ij} which are functions of space because of the pressure fluctuation. The terms with the fluctuating pressure contain the history effects due to the mathematical nature of the pressure fluctuations. Pressure fluctuations at a point can be expressed as the integral of correlations of velocity fluctuations in the whole domain using the Green's theorem on solving the Poisson equation (Rotta, 1962). Measurement techniques measurement of pressure fluctuations within a flow is not possible at high Reynolds numbers. Measurement of viscous dissipation with reasonable accuracy very near a boundary proves to be very difficult. Therefore in the individual stress transport equations Φ_{ij}, PD_{ij}, ε_{ij} terms can not be directly measured or calculated from the measured data. While approximate approaches are to be used for two of the terms, the third one can be extracted from the balance of the transport equation. The turbulent kinetic energy (TKE$=\frac{1}{2}\overline{u_i u_i}$) transport equation is equal to the sum of the transport equations for the normal stresses divided by 2

(Convection of TKE=$\frac{1}{2}(C_{11}+C_{22}+C_{33})$). Due to the continuity equation for incompressible

flows ($\frac{\partial u_i}{\partial x_i}=0$), the pressure-strain term in the TKE transport equals zero. Therefore TKE transport equation involves two unknown terms; pressure-diffusion and viscous dissipation. This allows one to use an approximate model for one of the terms and extract the other term from the balance of the TKE transport. Generally the pressure-diffusion term is accepted to be very small throughout the layer and an error is therefore introduced to the dissipation term (Schwarz and Bradshaw, 1994).

The pressure-diffusion term for a homogenous flow was modelled by Lumley (1978) using a Gaussian model. In this model he made use of the moment generating function to generate an equivalent scalar, velocity joint density. Using this equation and using Fourier transforms for homogeneous stochastic fields (Lumley, 1970), he obtained the equation

$$\frac{1}{\rho}\overline{pu_k}=-\frac{1}{5}(\overline{u_k(u^2+v^2+w^2)})$$

However, the large-eddy simulations of Shao et al. (1990), of a shearless turbulence mixing layer flow shows that the constant (1/5) is an overestimated figure, and neglecting pressure diffusion gives a better prediction. The constant multiplier was also discussed in Shih et al. (1987), but a new number was not proposed. The pressure-diffusion term was assumed to be small by Schwarz and Bradshaw (1993, 1994) mainly because their work compared the experimentally extracted pressure-strain data to the theoretical ones above $y^+\approx150$. Indeed the pressure-diffusion terms prove to be small away from the wall above $y^+\approx100$. However the pressure-diffusion term is not necessarily small below this y^+ location using Lumley's approximation. In fact the study of Launder and Tselepidakis (1990) of second moment closure within the sublayer show that the pressure diffusion has substantial importance in shaping the sublayer turbulence structure. They used 0.15 for the constant coefficient but the constant was not derived through a rigorous analysis. Latest DNS studies (Sumitani, and Kasagi, 1995) show that the pressure-diffusion term in the normal and shear stresses are large and as large as the pressure-strain term below $y^+\approx10$ near the wall and the pressure- diffusion term for the TKE balance is practically zero. This is also approximately true for the pressure-diffusion terms estimated for the TKE equation using Lumley's approximation. This ensures that the dissipation term in the

TKE transport equation $\varepsilon=\nu\overline{\dfrac{\partial u_i}{\partial x_l}\dfrac{\partial u_i}{\partial x_l}}$ calculated whether using Lumley's approach or not

will not be very much in error. Since the pressure-strain models which will be discussed later mainly use the ε and the anisotropy of the shear stress tensor, they are also not affected by this approximation to the pressure-diffusion term. However, the individual pressure-strain terms extracted from the data will have large errors especially near the wall if the pressure-diffusion terms are neglected. Therefore, the error introduced by using this approximation is believed to be smaller than neglecting it. If the term is neglected, the Φ_{ij} calculated will include the effect of the pressure-diffusion term in it.

The TKE dissipation was extracted from the TKE transport equation budget balance. In order to calculate the pressure diffusion both in TKE transport equation as well as in the stress transport equations, Lumley's approximation with its original coefficient was used. To judge the effect of neglecting or keeping the pressure-diffusion

term in the balance of the TKE budget, the very near wall variation of the dissipation term could not be extracted from the measured normal and shear stress data. The near wall limiting value of the dissipation and variation very near the wall can be written using the continuity relations and the variations of the fluctuating velocities very near the wall. The analysis showed that in the calculations of the near wall variation of the dissipation, at least second order approximations perpendicular to the wall need to be made in order for the variation to be physically possible. This second order approximation could not be calculated from the measured normal and shear stress data since the coefficients extracted from near wall variations of normal and shear stresses used in the dissipation variation become coupled. The analysis of ε_{ij} near the wall shows that (Reynolds, 1983, Lai, and So, 1990, Mansour, et al., 1988) the dissipation of the $\overline{u^2}$ and $\overline{w^2}$ vary linearly with y near the wall with a constant value at the wall and that the dissipation for the $\overline{v^2}$ is zero at the wall and varies as y^2 near the wall. This necessitates use of an anisotropic dissipation tensor for asymptotically correct modelling. However the correction factor for the present study was calculated as practically zero using the anisotropic dissipation tensor of Lai and So, (1990). In this study the effect of anisotropic dissipation approximation on the stress transport budget and on the predictions of the pressure-strain models is also tested and reported using the anisotropic dissipation rate algebraic model of Hallbäck, Groth, and Johansson (1990).

Viscous dissipation terms in shear stress transport equations are found to be small by direct numerical studies of 3-D TBLs at low Reynolds numbers (Spalart, 1989). However, the viscous dissipation terms in the normal stress transport equations are not small.

Once an isotropic dissipation is assumed, the original pressure-diffusion terms included in the dissipation terms for the individual stresses are replaced with equal distribution for each of the stresses. Use of an anisotropic dissipation tensor is still a research topic. At high Reynolds numbers the dissipation is usually assumed isotropic. However within the limits of the proposed algebraic dissipation rate tensors (Hallback, 1994), an anisotropic dissipation approximation is much different than the isotropic dissipation. Under the restrictions of present discussions it is believed that the pressure-diffusion term should be kept at least as proposed by Lumley.

The dissipation in this study was estimated both using the isotropic and anisotropic dissipation approximations. The models which account for the anisotropy of the dissipation, show effects only very near the wall below $y^+ \approx 5$ due to very small correction factor $f_{w,1}$ as proposed by Lai and So as discussed in Chapter V, or to very large differences in the dissipation rates throughout the layers as proposed by Hallback et al.. The effect of anisotropic dissipation rate and near wall corrections are discussed later in Chapter IV.

From an experimental point of view derivatives of any quantity can not be measured directly, therefore approximations are made using either a Taylor series expansion or fitting a function to the data and calculating the derivatives of this function at that point of interest. The gradients of the mean velocities and stresses in the y direction were calculated using a parabola fit at 5 consecutive points to the original data and taking the derivative of this curve fit at the third point location. As mentioned earlier, several profiles at closely spaced x and z separations around the four main measurement locations were made. Derivatives in the y direction were calculated at each measurement location separately. The original data values were next replaced with the parabola fit

values after the derivatives of the 19 quantities (mean velocities, stresses, and the triple products) were calculated in the y direction. The procedure was used in order to smooth the data and therefore to reduce the uncertainties. Next, y locations of one of the profiles were chosen as the base. Other profile data values were replaced with linear interpolation results at the same y locations of the base profile. The x and z derivatives were calculated either with a second or a first order accurate in space finite difference approximation using the interpolated data.

Calculations of the "Convection", "Production", "Turbulent diffusion", and the "Viscous diffusion" terms are straightforward. The Viscous-diffusion term was calculated best by a 5 point parabola fit to the first order y derivative of the variables and calculating the derivative of this parabola fit, rather than a 5 point parabola fit to the data values and taking the second derivative of this function. Another scheme tested was a 5 point forward-finite-differencing scheme which resulted in high fluctuations of the second order derivatives. In the calculation of the viscous diffusion term only the y derivatives were used to reduce the effect of the uncertainties involved in calculating the second order derivatives in x and z directions. The first order derivatives used are the derivatives interpolated to the same y locations of the base stations.

The ε term in the TKE equation was extracted using Lumley's approach for the pressure-diffusion term. The "Dissipation" terms in the normal stress transport equations were approximated both with isotropic dissipation and the anisotropic dissipation model of Hallbäck, Groth and Johansson (1991). In the isotropic dissipation assumption for individual normal stresses 2/3 of the TKE Dissipation was used. The "Pressure-Strain" terms in the both normal and shear stress equations were extracted from the balance of the equations. The $\partial V/\partial y$ term was extracted from the continuity equation for the mean flow.

Figures 28 through 52 show the terms in the transport of individual stresses nondimensionalized with u_τ^4/ν vs. y^+ in the tunnel coordinates. For each flow type, the six plots presented belong to the terms in the transport equation for the Reynolds' stresses. In this section the dissipation is assumed isotropic, and therefore, equally distributed among the normal stresses. Dissipation terms in the shear stress equations are assumed zero. Individual terms with anisotropic dissipation approximation are presented and discussed in Chapter IV. Pressure-diffusion terms are estimated using Lumley's approach.

II-A) Estimates of uncertainty

The uncertainty in each term of the stress balance equations were calculated using the two values calculated for that individual term using the two different data sets acquired at the Separation station and using Chauvent's criterion to calculate the standard deviation. 20 to 1 odds uncertainties calculated as $\pm 2\sigma$ are tabulated in table 2.

II-B) Stress transport equation budget

II-B-1) Balance at the 2-D station

Transport equation budget for $\overline{u^2}$ stress shows that the production term is the largest term among all terms especially near the wall region (Fig. 29). The $\overline{u^2}$ production

peaks near the wall at $y^+\approx15$ to 20 with a value of 0.34. The turbulent diffusion changes sign at $y^+\approx40$ and magnitude at the peak location ($y^+\approx20$) is comparable to dissipation and convection peak magnitude terms. Above $y^+\approx100$ pressure-strain, production and the dissipation terms are larger than other terms. The pressure-diffusion term is practically zero throughout the layer for this stress. Except the convection term all profiles show peaks between $y^+\approx15$ to 20 range.

The $\overline{v^2}$ transport balance shows that the major contributors are the pressure-strain and the dissipation terms with the same sign (Fig. 30). The $\overline{v^2}$ production is practically zero for the 2-D station since the major contributors $-\overline{uv}\,\partial V/\partial y$ and $-\overline{v^2}\,\partial V/\partial y$ have opposite signs to each other throughout the layer and $\overline{v^2}/|\tau/\rho|\approx1$ for 2-D boundary layers. Turbulent diffusion changes sign around $y^+\approx10$, 20, and 100. Convection value peaks around $y^+\approx15$ and both are important only near the wall below $y^+\approx100$. Above $y^+\approx100$ dissipation and pressure-strain terms follow each other closely. In the near-wall region below $y^+\approx50$ pressure-diffusion term is a large contributor with a peak around $y^+\approx20$ with a value $\approx2/5$th of the dissipation term. Viscous diffusion is important only below $y^+\approx20$.

Production of $\overline{w^2}$ is practically zero in a 2-D flow since $\overline{uw}, \overline{vw}$, and $\partial W/\partial y$ are zero (Fig. 31). The pressure-strain term is the highest term in the transport of $\overline{w^2}$. This also shows that the $\overline{w^2}$ normal stress is due to redistribution of the TKE by the pressure-strain term between the v and w fluctuations. Convection, viscous diffusion, and turbulent diffusion terms are important near the wall below $y^+\approx40$. Dissipation values and pressure-strain values follow each other closely above $y^+\approx50$.

For the normal stresses in general the dissipation and the pressure-strain terms are at the same order of magnitude. Pressure-strain term redistributes the $\overline{u^2}$ production to the other fluctuating components.

In this section of the discussion the dissipation in $\overline{uv}$ transport equation is approximated by zero, based on the DNS simulations. The production, pressure-strain and the pressure-diffusion terms are the dominating terms throughout the layer. An order of magnitude smaller convection, turbulent-diffusion, viscous-diffusion terms are away from zero below $y^+\approx50$ to 60 (Fig. 32). Pressure-diffusion term peaks at the same location of the production term at $y^+\approx15$ with a value half of that of the production term. Other stresses in a 2-D flow are zero (Figures 33, and 34).

Turbulent kinetic energy budget shows that the dissipation and the production terms follow each other closely above $y^+\approx35$, and all other terms are close to zero above this location (Fig. 35). Production profile peaks at $y^+\approx15$ to 20 and values are larger than the dissipation term values at this location. Pressure-diffusion and viscous-diffusion have similar profiles with opposite signs to each other. Compared to the production and dissipation terms the pressure-diffusion is much smaller through out the layer, which shows that the dissipation term calculated from the TKE budget balance using Lumley's approach for the pressure-diffusion term does not have a substantial effect on this value. The convection term at $y^+\approx10$ is close to the dissipation term values. Turbulent diffusion values are twice that of the viscous diffusion at $y^+\approx20$.

II-B-2) Balance at Station 5

At Station 5 $\overline{u^2}$ transport budget shows that production term is higher than the other terms (Fig. 36). All the term values are close to zero above $y^+\approx125$. Below this location turbulent-diffusion, dissipation, convection, and the pressure-strain are all large and important. Viscous-diffusion term is important below $y^+\approx30$ are on the same order of magnitude. Compared to the 2-D flow all the terms are reduced in magnitude. The decrease in magnitude for pressure-strain and production terms are more pronounced than the other terms.

In the transport of $\overline{v^2}$, pressure-strain, dissipation and pressure-diffusion terms are the largest contributors (Fig. 37). Compared to 2-D flow the convection and turbulent diffusion terms are much smaller. Pressure-diffusion term shows a peak at $y^+\approx20$ and is negligibly small above $y^+\approx100$. Above $y^+\approx100$ the dissipation and pressure-strain term values are close in magnitude.

On contrary to 2-D flow, at Station 5 production of $\overline{w^2}$ is the largest term in the transport budget of this stress (Fig. 38). Dissipation values are at the same order of magnitude of the production but are smaller throughout the layer. Convection, pressure-strain, turbulent-diffusion and viscous-diffusion terms are ≈4 times smaller than the production throughout the layer. Pressure-strain and turbulent-diffusion term profiles vary as mirror images to one another.

The pressure-diffusion, pressure-strain, and production terms are the major terms in the budget balance of the $\overline{uv}$ stress, and the turbulent diffusion, convection and the viscous-diffusion are negligibly small (Fig. 39). Pressure-strain term variation follows the pressure-diffusion term variation with an opposite sign.

The $\overline{uw}$ production is larger than the $\overline{uv}$ production (Fig. 40). Pressure-strain and production terms are the major terms and they have opposite signs throughout the layer. The turbulent-diffusion, viscous-diffusion and convection terms are larger in magnitude then the equivalent $\overline{uv}$ terms.

The convection and turbulent diffusion terms are also small for the $\overline{vw}$ transport equation (Fig. 41). The dominant terms are the pressure-strain, production, and the pressure-diffusion terms. The distribution of pressure-diffusion term largely shapes the variation of the pressure-strain term.

The dissipation and the production terms are the major terms in the balance of the TKE (Fig. 42). Production and dissipation profiles peak at $y^+\approx15$. Effects of convection, turbulent, viscous, and pressure-diffusion terms are small but not negligible below $y^+\approx40$. The diffusion terms change sign very near the wall in the $y^+\approx8$ to 12 range and also at $y^+\approx40$. The pressure-diffusion and viscous diffusion profile peak values are close to each other with opposite signs.

II-B-3) Balance at Separation station

The production term for the $\overline{u^2}$ balance at the Separation station is higher than the 2-D and the Station 5 values near the wall (Fig. 43). The dissipation and turbulent diffusion are increased more than twice. The convection term does not change sign within the layer as observed in 2-D station and is positive. However all the terms reduce close to zero values much earlier than the 2-D and the Station 5 values at $y^+\approx50$. Pressure diffusion is negligibly small and viscous diffusion is increased especially very near the

wall. Large pressure-strain contribution is confined into a narrow region near the wall to $y^+\approx20$ range with values slightly higher than that of Station 5.

In the transport equation of $\overline{v^2}$ the dissipation and the pressure-strain terms are increased significantly by twice compared to both 2-D station and Station 5 values (Fig. 44). The production is also increased slightly in the outer region around $y^+\approx200$. The convection, and turbulent-diffusion values are close to zero at this station and are slightly larger than zero at $y^+\approx300$. The pressure-diffusion term is $\approx1/3$ of the dissipation term at $y^+\approx20$ with larger values than at both 2-D and Station 5 profiles.

Except the pressure-strain the terms all the terms in the $\overline{w^2}$ budget are increased by 2.5 times that of Station 5 (Fig. 45). Pressure-strain term is increased by 5 times throughout the layer. The dissipation and the production terms peak at $y^+\approx15$ to 20. The convection term is negative in the $y^+\approx7$ to 300 range. Pressure-strain term is also negative throughout the layer. While at the 2-D station the pressure-strain and dissipation are the main terms in the development of $\overline{w^2}$ at 3-D stations the production plays an important role diminishing the effect of the pressure-strain.

Compared to the 2-D flow the pressure-strain term of $\overline{uv}$ budget is doubled and the pressure-diffusion term is tripled (Fig. 46). Production, pressure-strain and pressure-diffusion terms all show extremum at $y^+\approx15$. The location where the pressure-diffusion term changes sign very near the wall is shifted towards the wall. With increased 3-D effects the large variations near the wall are confined to a smaller near wall region. Convection, turbulent-diffusion, and viscous-diffusion terms are relatively much small throughout the layers.

The production and the pressure-strain terms in the $\overline{uw}$ transport equation are increased more than twice compared to the Station 5 values at $y^+\approx15$ where they peak (Fig. 47). The turbulent diffusion is also increased, especially below $y^+\approx10$. This term is large with values as high as 1/5 of the production peak value below $y^+\approx40$. Viscous diffusion increases when the wall is approached below $y^+\approx30$.

Similar observation are made in the transport equation for the $\overline{vw}$ as in the transport equation of $\overline{uv}$ (Fig. 48). The magnitudes of the pressure-strain, pressure-diffusion and the production terms are increased by more than twice below $y^+\approx100$ and about 5 times above this y^+ location compared to the Station 5 values. Pressure-diffusion term below $y^+\approx30$ is a major contributor shaping the variation of the pressure-strain profile. The production and the pressure-strain terms change sign at $y^+\approx100$.

TKE budget balance shows that except the convection term all the term values are elevated more than twice compared to those at Station 5 (Fig. 49). Effects of the diffusion terms are important below $y^+\approx40$. Turbulent and pressure-diffusion terms change sign at $y^+\approx10$ and away from the wall at $y^+\approx40$. The profile shapes at this Separation station are not highly different than profiles at Station 5.

II-B-4) Balance at Vortex-core station

The peak value of the production term of $\overline{u^2}$ shows a decrease at the Vortex-core station compared both to the 2-D and the other 3-D cases (Fig. 50). The peak value is comparable to the Separation station value. The term changes sign and becomes negative at $y^+\approx60$. The turbulent diffusion term magnitude is as high as the value at

Separation station. The term changes sign to positive at $y^+\approx10$ similar to the other station profiles. The pressure-strain term is positive near the wall till $y^+\approx125$ on contrary to the variations at other stations. The dissipation and the convection terms are larger in magnitude compared to that of the Separation station. Convection profile forms a negative peak at $y^+\approx30$. The magnitudes of all the terms are not small in the outer region contrary to the observations made at other stations. Viscous-diffusion term is on the same order of magnitude of the Separation station. Pressure diffusion is different than zero at this station.

The profiles of the terms in the transport of $\overline{v^2}$ are highly different than the other station profiles (Fig. 51). The dissipation term shows peaks around $y^+\approx30$ and around $y^+\approx300$. The pressure-strain term is approximately flat till $y^+\approx150$. The convection term oscillates around zero. The turbulent diffusion term peak around $y^+\approx150$ and magnitude of the peak value is larger then that of the production. The production term is negative near the wall and changes sign around $y^+\approx300$ and shows a positive peak around $y^+\approx400$. Pressure-diffusion term peak value at $y^+\approx25$ is increased ≈2 times that of Separation station.

The $\overline{w^2}$ transport terms except the dissipation term show a further increase in magnitude in the whole layer compared to the Separation station (Fig. 52). The dissipation term values are close to that of the Separation station. The elevated levels of the terms persist further up in to the layer. Both the production and pressure-strain values are increased more than twice compared to the Separation station. The turbulent diffusion term attains values larger than the pressure-strain term in magnitude at $y^+\approx35$ to 100 region. The convection term shows a peak minimum at $y^+\approx45$ and the values in the layer are approximately an order of magnitude larger than the Station 5 and 2-D station values. Pressure-diffusion is positive and large between $y^+\approx20$ to 300. Viscous diffusion increases below $y^+\approx10$.

The terms in the transport equation of $\overline{uv}$ are similar in shape of other stations with elevated values till $y^+\approx50$ (Fig. 53). The large vortex in the outer region effects the variations at this region. Pressure-strain, pressure-diffusion and production terms change sign 3 times with in the layer. Production and pressure-strain terms show local peaks with opposite signs at $y^+\approx20$ and at $y^+\approx400$. Pressure-diffusion peak magnitude value at $y^+\approx20$ is more than twice of the production peak value at the same location.

Near wall variations of the $\overline{uw}$ transport terms below $y^+\approx70$ is similar to other 3-D stations (Fig. 54). The turbulent diffusion term is suppressed. Near the vortex core at $y^+\approx300$ the production and the pressure-strain values show large local peaks with opposite signs.

One of the largest effects of the vortex located in the outer region is observed in $\overline{vw}$ transport (Fig. 55). The production term distribution term is similar to Station 5 values with larger negative values in the outer region. Between $y^+\approx6$ to 150 pressure-diffusion and pressure-strain terms vary similarly with opposite signs to each other. A similar variation between pressure-strain and production is observed between $y^+\approx150$ to 800. Pressure-strain and pressure-diffusion peak locations for Separation station at $y^+\approx15$ to 20 are shifted away from the wall to $y^+\approx60$. Near the wall new peaks at $y^+\approx10$ are developed. Pressure-strain profile shows a wave-like variation throughout the layer.

The profiles of the terms in the TKE balance at this location differ highly than the other three cases studied (Fig. 56). Even though the production and dissipation values

are close to the values at Separation station the convection, turbulent diffusion, pressure-diffusion terms are highly increased. All the terms except the viscous diffusion are important in the whole layers, and the effect of the terms are not confined to $y^+ < 100$ region. Turbulent diffusion terms above $y^+ \approx 100$ are comparable to the production and dissipation terms. Viscous diffusion changes sign at $y^+ \approx 10$ and increases towards the wall. It is important below $y^+ \approx 60$. High negative convection values are obtained away from the wall with a peak at $y^+ \approx 40$.

II-C) Differences in the stress transport due to flow conditions at different stations

$\overline{u^2}$

In general three dimensionality of the flow reduces the production of the $\overline{u^2}$ stress for highly skewed 3DTBLs. At Separation station however the production is higher than the 2-D flows. Turbulent diffusion decreases at Station 5 compared to 2-D flow station but at Separation and Vortex-core stations it is larger. Turbulent diffusion progressively increases towards the Vortex-core from Station 5. Dissipation terms are unchanged at Station 5 compared to 2-D values. However at Separation and Vortex-core stations dissipation is progressively increased compared to Station 5. Pressure-strain values decrease in magnitude progressively at Station 5 and at Separation station compared to 2-D values. At the Vortex-core station the sign is changed to positive and the magnitude is as high as in 2-D flow. Large positive peak value of convection is shifted away from the wall progressively at 2-D, Station 5, and Separation stations. The Vortex-core value is large very near the wall but shows a larger negative value away from the wall at $y^+ \approx 30$. Pressure diffusion is practically zero for this stress only with slightly elevated values at the Vortex-core station. Viscous diffusion term stays on the same order of magnitude for all stations. The existence of a large vortex in the outer region alters the variation of the near wall flow entirely at the Vortex-core station. Pressure-strain term becomes positive. Convection term is negative and turbulent diffusion term is as high as the convection term. Production is reduced and becomes negative around $y^+ \approx 60$. Dissipation term variation is close to the Separation station value.

$\overline{v^2}$

The effect of three-dimensionality on the $\overline{v^2}$ transport is more pronounced then the $\overline{u^2}$ transport. Compared to 2-D station, at the 3-D stations both the convection and turbulent diffusion terms are reduced near the wall. At the Vortex-core station both the convection and turbulent-diffusion profiles show large negative peaks away from the wall around $y^+ \approx 200$. Dissipation peak value is increased with increased three-dimensionality. The pressure-strain peak values near the wall are increased, and the effect of the term extends further in to the layer with increased three-dimensionality and shows two maxima. The pressure-diffusion peak value located at $y^+ \approx 20$ for all the cases increase with increased 3-D effects. For the Vortex-core station the convection, production, and turbulent diffusion terms become important away from the wall.

$\overline{w^2}$

For a 2-D TBL the production of $\overline{w^2}$ transport rate is zero which results in the pressure-strain and the dissipation to be the major terms in the transport. However for the 3-D flows the production term is one of the major terms. The dissipation values gradually increase with increased three-dimensionality. Convection is reduced towards the Vortex-core station. The term at the Separation station is practically zero and at the Vortex-core station the convection becomes negative with a minimum around $y^+\approx45$. Turbulent diffusion negative minima above $y^+\approx10$ decrease with increased three-dimensionality. Pressure-strain terms at with positive values at some regions decrease and become negative through out the layer towards the Vortex-core station. The magnitude of the pressure-strain term is highly increased more than two times by the Vortex-core station compared to the Separation station.

$\overline{uv}$

Three-dimensionality of the flow results in less in production magnitude and larger in magnitude pressure-diffusion term at Station 5 compared to 2-D flow. Towards the Vortex-core station the production, the pressure-diffusion, and the pressure-strain term magnitudes increase. Even though the variations are confined to a narrower region near the wall, the variations of the profiles are similar to each other in the near wall region including the Separation station. At the Vortex-core station the effect of the outer region vortex results in large negative production and large positive pressure-strain terms in the outer region. The y^+ location where pressure-strain and pressure-diffusion terms are equal very near the wall shifts slightly away from the wall at the vortex core station.

$\overline{uw}$

Both at the Separation and Vortex-core stations the negative production and the positive pressure-strain values are more than twice of the Station 5. At the Vortex-core station this is accompanied by the positive production and the negative pressure-strain values away from the wall. Convection becomes important only at the Vortex-core station away from the wall at $y^+\approx40$ to 400 region.

$\overline{vw}$

Pressure-strain term shows double peaked variation at the Separation station and the triple-peaked variation at the Vortex-core station. At the Separation and Vortex-core stations production profiles show two peaks with opposite signs to each other. Pressure-diffusion term for the Vortex-core station shows two peaks one at $y^+\approx10$ and the other at $y^+\approx70$, which corresponds in magnitude to the one observed at $y^+\approx15$ to 20 for the Station 5 and Separation stations.

CHAPTER III - THEORETICAL PRESSURE-STRAIN MODELS

In this Chapter seven theoretical pressure-strain models reported in the literature are briefly described. The models belong to Gibson-Launder (1978), Launder-Reece-Rodi (1975), Oberlack-Peters (1993), Fu-Launder-Tselepidakis (2 models), Shih/Lumley-Choi/Lumley, Speziale-Sarkar-Gatski (1991).

Pressure fluctuations at a point in the flow can be expressed by taking the divergence of the Navier-Stokes equations. Following Chou (1945) the equation for the pressure fluctuations is written as:

$$-\frac{1}{\rho}p_{,jj}=2\,U_{i,j}\,u_{j,i}+u_{i,j}\,u_{j,i}+\overline{u_{i,j}\,u_{j,i}}$$

The customary means of splitting this equation is 1) "Rapid" pressure term, which is the first term on the right-hand side of the equation, and 2) "Slow" term (1978, Lumley), or the return pressure (Mansour et al., 1988) which are the last two terms. The pressure-strain term obtained using the pressure-fluctuation equation is also split into two parts and these parts are named similarly as the "rapid" term which involves the mean velocity gradients and the "slow" term. The "slow" term is also called the "return-to-isotropy" term since it drives the turbulence into isotropic state (Shih et al., 1993).

In the pressure-strain model equations the following abbreviations are used.

$$b_{ij}=\frac{\overline{u_i u_j}}{\overline{q^2}}-\frac{1}{3}\delta_{ij}\ ,\ S_{ij}=\frac{1}{2}(U_{i,j}+U_{j,i})\ ,\ \Omega_{ij}=\frac{1}{2}(U_{i,j}-U_{j,i})$$

$\delta_{ij}=1$ when $i=j$
$\quad=0$ when $i\neq j$

$$\overline{q^2}=\overline{u_k u_k}\ ,\ \varepsilon=\frac{\varepsilon_{kk}}{2}\ ,\ k=\frac{1}{2}\overline{u_k u_k}$$

where ε_{ij} is the dissipation tensor, S_{ij} is the rate of strain tensor, Ω_{ij} is the vorticity tensor, and ε is the dissipation of the turbulent kinetic energy "TKE=k". (,i) denotes partial derivative of the quantity along the "i" th axis.

In each model the first line is the model for the "return-to-isotropy" part, other lines are for the "rapid" part of the pressure-strain (redistribution) term.

III-A) Gibson-Launder model (1978)

The Gibson and Launder (1978) model was used to calculate the gravitational effects on the atmospheric boundary layer and on a nearly homogenous free-shear flow. The model is linear in Reynolds stresses and similar to Launder-Reece-Rodi model. This model was used by Schwarz and Bradshaw (1994) as Launder-Reece-Rodi model.

$$\Phi_{ij}=-c_1\varepsilon\,b_{ij}$$
$$+c_2[(\overline{u_i u_l}U_{j,l}+\overline{u_j u_l}U_{i,l})-\frac{2}{3}\overline{u_l u_m}U_{l,m}\delta_{ij}]$$

where, $c_1=3.6$, $c_2=0.6$.

Gibson-Launder model has a near wall correction, additional terms both for the return to isotropy and rapid terms. The correction for the return-to-isotropy was adopted from Shir (1973), and the correction for the rapid term was developed following this model (Gibson, Launder, 1978).

$$\Phi_{ij,1w} = c_1' \left(\frac{\varepsilon}{k}\right) \left(\overline{u_k u_m} n_k n_m \delta_{ij} - \frac{3}{2} \overline{u_k u_i} n_k n_j - \frac{3}{2} \overline{u_k u_j} n_k n_i\right) f\left(\frac{l}{n_i r_i}\right)$$

and

$$\Phi_{ij,2w} = c_2' \left(\Phi_{km,2} n_k n_m \delta_{ij} - \frac{3}{2} \Phi_{ik,2} n_k n_j - \frac{3}{2} \Phi_{jk,2} n_k n_i\right) f\left(\frac{l}{n_i r_i}\right)$$

where

$c_1' = 0.5$, $c_2' = 0.3$, $n_k = (0,1,0)$, $f = \dfrac{l}{\kappa y}$, $l \equiv \dfrac{(-\overline{uv})^{3/2}}{\varepsilon}$, $\kappa = 0.41$ and r is the position vector.

For consistency only one near-wall correction method was applied to all the models. The model used is the Launder-Reece-Rodi (1975) near wall correction model given below.

III-B) Launder-Reece-Rodi model (1975)

One of the earlier models presented for the pressure-strain model is of Launder, Reece, and Rodi, (1975). The model was tested against free shear flows, plane channel flow, and distorted homogenous flows data with reasonable success. They concluded that the discrepancies between computations and the data were due more to the modelling of dissipation and diffusion processes or to the uncertainties in the measured quantities rather than the pressure-strain modelling. Return to isotropy term was adopted from Rotta, (1951). Rapid term away from a boundary was developed using another Rotta (1951) approximation that $\Phi_{ij,rapid} = (\partial U_l / \partial x_m) a_{ij}^{mi}$, where a_{ij}^{mi} is the most general form of a fourth order tensor which satisfies a series of kinematic constraints.

$$\Phi_{ij} = -c_1 \varepsilon b_{ij}$$
$$+ 2\overline{q^2}\left[0.2 S_{ij} + \frac{9c_2 + 6}{22}\left(b_{ik} S_{jk} + b_{jk} S_{ik} - \frac{2}{3}\delta_{ij} b_{kl} S_{kl}\right) + \frac{10 - 7c_2}{22}\left(b_{ik}\Omega_{jk} + b_{jk}\Omega_{ik}\right)\right]$$

where, $c_1 = 3.0$, $c_2 = 0.4$.
The model also contains an additive near wall correction to the pressure-strain correlation.

$$\Phi_{ij,w} = \frac{k^{3/2}}{\varepsilon y}\left[0.125 \frac{\varepsilon}{k}\left(\overline{u_i u_j} - \frac{2}{3} k\delta_{ij}\right) + 0.015 (P_{ij} - D_{ij})\right]$$

where y is the distance perpendicular to the wall. This model was used by Shih and Lumley (1993) as Launder-Reece-Rodi model.

III-C) Oberlack-Peters model (1993).

Oberlack and Peters developed their pressure-strain model based on the two-point correlation function transport. This correlation function was asymptotically expanded and the leading order terms were kept. This resulted in a mathematically simplified presentation of the correlation function. This function was used to calculate the rapid part

of the pressure-strain correlation. The model is used here together with Rotta's (1951) return-to-isotropy formulation. The model originally does not include a near wall correction.

$$\Phi_{ij} = -c_1 \varepsilon b_{ij}$$

$$+2\overline{q^2}[\,0.2\,S_{ij} + 0.6\,(b_{ik}S_{jk} + b_{jk}S_{ik} - \frac{2}{3}\delta_{ij}b_{kl}S_{kl}) + 0.2\,(b_{ik}\Omega_{jk} + b_{jk}\Omega_{ik})\,]$$

where $c_1 = 3.0$. This model is similar to Launder-Reece-Rodi model in form however the constants are different.

III-D) Speziale-Sarkar-Gatski model (1991)

SSG model originally does not include a near wall correction for the pressure-strain modelling and uses the homogenous turbulent flow approximations throughout the mathematical simplifications. With homogenous flow assumption for turbulent flows at high Reynolds numbers the turbulent diffusion and pressure-diffusion terms drop out and the dissipation can be assumed isotropic. The model was developed to satisfy many physical and asymptotical consistency constraints. Model results were compared to LRR model results for different types of flows with different numerical simulations. Large-eddy simulation and direct numerical simulation results show better performance by the SSG model. The model was calibrated using data from isotropic decay, return to isotropy, and homogenous shear flow experiments along with Rapid Distortion Theory results.

$$\Phi_{ij} = -\varepsilon[c_1 b_{ij} - 3(c_1 - 2)(b^2_{ij} - \frac{1}{3}b^2_{kk}\delta_{ij})]$$

$$+2\overline{q^2}[\,\frac{0.8 - c_{32}}{4}S_{ij} - \frac{c_{11}P}{2\overline{q^2}}b_{ij} + \frac{c_4}{4}(b_{ik}S_{jk} + b_{jk}S_{ik} - \frac{2}{3}\delta_{ij}b_{kl}S_{kl}) + \frac{c_5}{4}(b_{ik}\Omega_{jk} + b_{jk}\Omega_{ik})\,]$$

where $c_{32} = c_{31}(b_{ij}b_{ij})^{1/2}$, $P = -\overline{u_i u_j}U_{i,j}$, $c_{11} = 1.8$, $c_{31} = 1.3$, $c_4 = 1.25$, $c_5 = 0.4$

III-E) Shih-Lumley (1985), Choi-Lumley (1984) model

$$\Phi_{ij} = -\varepsilon[\beta b_{ij} + \gamma(b^2_{ij} + 2\,II\,\frac{\delta_{ij}}{3})]$$

$$+2\overline{q^2}[\,0.2\,S_{ij} + 3\alpha_5(b_{ik}S_{jk} + b_{jk}S_{ik} - \frac{2}{3}\delta_{ij}b_{kl}S_{kl})$$

$$+\frac{1}{3}(2 - 7\alpha_5)(b_{ik}\Omega_{jk} + b_{jk}\Omega_{ik}) + 0.2(b^2_{il}S_{jl} + b^2_{jl}S_{il} - 2b_{kj}b_{li}S_{kl} - 3b_{ij}b_{kl}S_{kl})$$

$$+0.2(b^2_{il}\Omega_{jl} + b^2_{jl}\Omega_{il})\,]$$

If $III \geq 0$ then

$$\beta = 2 + \frac{\rho^* \, F^{1/2}}{1 + G\chi^2}$$

$$\gamma = \frac{\rho^* \, F^{1/2}}{1 + G\chi^2} \frac{G}{\xi}$$

$$\xi = (\frac{III}{2})^{1/3}, \quad \eta = (-\frac{II}{3})^{1/2}$$

$$\chi = \frac{\xi}{\eta}, \quad G = -\chi^4 + 0.8\chi^6$$

$$\rho^* = \exp[-\frac{9.29}{Re^{1/2}}] \, [(\frac{7.69}{Re^{1/2}} + \frac{73.7}{Re}) - (296 - 16.2 \, (\chi + 1)^4) \, II]$$

$$Re = \frac{\overline{q^2}^2}{9\varepsilon\nu}, \quad II = -\frac{b_{ij}b_{ij}}{2}, \quad III = \frac{b_{ij}b_{jk}b_{ki}}{3}$$

If III < 0 then

$$\beta = 2 + \frac{F}{9}\exp[-\frac{7.77}{Re^{1/2}}] \, [\frac{72}{Re^{1/2}} + 80.1 \, \ln(1 + 62.4 \, (-II + 2.3 \, III))]$$

$$\gamma = 0$$

$$Re = \frac{\overline{q^2}^2}{9\varepsilon\nu}$$

Following parameters are not dependent on the sign of III.

$$\alpha_5 = \frac{1}{10}(1 + 0.8 \, F^{1/2}), \quad F = 1 + 9 \, b_{ij}b_{jk}b_{ki} - \frac{9}{2} b_{ij}b_{ij}$$

III-F) Fu-Launder-Tselepidakis model I (1987)

The rapid part of the Fu, Launder, Tselepidakis (FLT) model was developed following Shih and Lumley's (1985) approach. Shih and Lumley kept the quadratic products of the stress anisotropies. FLT kept including the cubic products. A similar approach for the return-to-isotropy term was also developed, (Launder, 1988). Shih and Lumley, (1993) point out that this model does not satisfy the Schwarz's inequality between the velocity and scalar fields.

$$\Phi_{ij} = 8A^{1/2} \, II\varepsilon[b_{ij} + 1.2 \, (b_{im}b_{mj} + \frac{2}{3}\delta_{ij} \, II)] - b_{ij}\varepsilon$$

$$-0.6 \, (P_{ij} - \frac{1}{3}\delta_{ij}P_{kk}) + 0.3\varepsilon \, b_{ij}(\frac{P_{kk}}{\varepsilon})$$

$$-(\frac{1}{5k})[\overline{u_k u_j} \, \overline{u_l u_i} \, (U_{k,l} + U_{l,k}) - \overline{u_l u_k}(\overline{u_j u_k} \, U_{j,l} + \overline{u_j u_k} \, U_{i,l})]$$

$$-r[-2 \, II \, (P_{ij} - D_{ij}) + 3b_{mi}b_{nj} \, (P_{mn} - D_{mn})]$$

where

CHAPTER III

$$k = \frac{1}{2}\overline{u_i u_i}$$

$$P_{ij} = -(\overline{u_i u_k}\, U_{j,k} + \overline{u_j u_k}\, U_{i,k})$$

$$D_{ij} = -(\overline{u_i u_k}\, U_{k,j} + \overline{u_j u_k}\, U_{k,i})$$

$$r = 0.65, \quad A = 1 - \frac{9}{8}(-2\,II - 3\,III)$$

This model was used as Fu-Launder-Tselepidakis model by Schwarz and Bradshaw (1994).

III-G) Fu-Launder-Tselepidakis model II (1987)

$$\Phi_{ij} = 8A^{1/2}\,II\,\varepsilon\,[b_{ij} + 1.2\,(b_{im} b_{mj} + \frac{2}{3}\delta_{ij}\,II)] - b_{ij}\varepsilon$$

$$+2\overline{q^2}\,[\,0.2 S_{ij} + 0.3\,(b_{ik} S_{jk} + b_{jk} S_{ik} - \frac{2}{3}\delta_{ij} b_{kl} S_{kl})$$

$$+\frac{1.3}{3}(b_{ik}\Omega_{jk} + b_{jk}\Omega_{ik})$$

$$+0.2\,(b^2_{il}\,S_{jl} + b^2_{jl}\,S_{il} - 2 b_{kj} b_{li} S_{kl} - 3 b_{ij} b_{kl} S_{kl})$$

$$+0.2\,(b^2_{il}\,\Omega_{jl} + b^2_{jl}\,\Omega_{il})$$

$$+r[4 b^2_{nn}\,(b_{ik}\Omega_{jk} + b_{jk}\Omega_{ik}) + 12 b_{mi} b_{nj}(b_{mk}\Omega_{nk} + b_{nk}\Omega_{mk})]\,]\,]$$

where

$$r = 0.7, \quad A = 1 - \frac{9}{8}(-2\,II - 3\,III)$$

This model was used as Fu-Launder-Tselepidakis model by Shih and Lumley (1993).

III-H) Lai-So model (1990)

Lai and So chose to model the velocity-pressure-gradient term, which includes both the pressure-strain and pressure-diffusion terms together. They assumed that the existing pressure-strain models work satisfactorily away from the wall since they agree well with the data in that region. The modelling effort was directed to formulate an additional term which will not only correct the pressure-strain model for the near wall effects but also will model the pressure-diffusion term. The model consists of an anisotropic dissipation model similar to that of Launder and Tselepidakis (1990) model and a new near wall correction similar to that of Gibson-Launder (1978) and Launder-Reece-Rodi (1975) models. The model adopts the Launder-Reece-Rodi model as the pressure-strain model that needs to be modified near the wall.

The additional term to the LRR model for the right hand side of the Φ_{ij} equation is given by:

$$\Phi_{ij,w}\,f_{w,1} = C_1\,\frac{\varepsilon}{k}\,(\overline{u_i u_j} - \frac{2}{3}\delta_{ij} k) - \frac{\varepsilon}{k}(\overline{u_i u_k}\,n_k n_j + \overline{u_j u_k}\,n_k n_i) + \alpha^*(P_{ij} - \frac{2}{3}\delta_{ij} P)$$

where $P_{ij} = -(\overline{u_i u_k}\frac{\partial U_j}{\partial x_k} + \overline{u_j u_k}\frac{\partial U_i}{\partial x_k})$, $P = \frac{1}{2}P_{ii}$, $\alpha^* = 0.45$, $n_k = (0,1,0)$, $C_1 = 1.5$

to be used together with

$$\varepsilon_{ij} = \frac{2}{3}\varepsilon(1-f_{w,1})\delta_{ij} + \frac{f_{w,1}(\frac{\varepsilon}{k})[\overline{u_iu_j}+\overline{u_iu_k}n_kn_j+\overline{u_ju_k}n_kn_i+n_in_j\overline{u_ku_l}n_kn_l]}{1+\frac{3}{2k}\overline{u_ku_l}n_ln_k}$$

where $f_{w,1}=\exp[-(\frac{R_T}{150})^2]$, $R_T=\frac{k^2}{\nu\varepsilon}$. The model did not have any observable effect on the near wall numbers of the 2-D flow, even with different forms for $f_{w,1}$. Other different forms that were examined included $f_{w,1}=\exp(-R_T/20)$ and $f_{w,1}=\exp(-R_T/60)$, which were also tested by Launder and Tselepidakis (1990). The $f_{w,1}$ varies between 0.1 to 0.001 for different forms and additional term effects make barely any observable changes below $y^+\approx10$. The model performs very similar to the LRR model. Therefore this model is excluded from the comparisons.

CHAPTER IV - COMPARISON OF THE THEORETICAL AND EXPERIMENTAL PRESSURE-STRAIN TERMS

IV-A) No near wall correction and isotropic dissipation approximation

IV-A-1) 2-D flow station

Except the FLT models all the models and the data follow each other closely above $y^+ \approx 40$ for the $\overline{u^2}$ transport pressure-strain values (Fig. 57). For the $\overline{v^2}$ only GL, LRR, SLCL, and SSG model predictions agree with the data above $y^+ \approx 40$ (Fig. 58). Near wall variation of $\overline{w^2}$ pressure-strain term up to $y^+ \approx 25$ is well predicted by the FLT1 model, above $y^+ \approx 35$ however LRR, GL, SLCL, SSG models do a superior job (Fig. 59). $\overline{uv}$ pressure-strain term estimated by the SLCL model above $y^+ \approx 20$ is closest to the data values (Fig. 60). For all the pressure-strain terms the data values and the predictions above $y^+ \approx 100$ are close to zero and close to each other. Very near wall values for $\overline{u^2}$, $\overline{v^2}$, and $\overline{uv}$ are not very well predicted by the models. $\overline{uw}$ and $\overline{vw}$ pressure-strain values and predictions are given in figures 61 and 62.

IV-A-2) Station 5

The $\overline{u^2}$ pressure-strain term above $y^+ \approx 50$ is well predicted by all the models accept the FLT models (Fig. 63). All the models underpredict the value very near the wall. $\overline{v^2}$ pressure-strain term is very well predicted by the OP, SLCL, and FLT1 models till $y^+ \approx 8$ (Fig. 64). Between $y^+ \approx 8$ to 60 none of the models follow the trend of the data values. Above $y^+ \approx 60$ GL, LRR, SLCL, and SSG values follow the data values closely. The variation of $\overline{w^2}$ is not well predicted throughout the layer except in $y^+ \approx 30$ to 60 region by FLT2 model (Fig. 65). Although the trend of the predictions and the trend of the data are same, both values are close to zero. $\overline{uv}$ pressure-strain values above $y^+ \approx 30$ are equally well predicted by the LRR, GL, and SSG models (Fig. 66). Above $y^+ \approx 60$ all the model estimates are close to the data and close to the zero value. Near the wall between $y^+ \approx 15$ to 30 SLCL model values are very close to data values. Trend of the data nearest the wall is not followed by any of the models. $\overline{uw}$ pressure-strain term was well predicted above $y^+ \approx 15$ by the FLT1 model (Fig. 67). Near wall prediction of the model is also not far away from the data. OP, SSG, LRR, GL models do a better job below $y^+ \approx 7$. Between $y^+ \approx 15$ to 30 only SLCL model predicts the $\overline{vw}$ pressure-strain variation (Fig. 68). Above $y^+ \approx 40$ all model estimates and the data values are both close to each other and to the zero value.

IV-A-3) Separation station

$\overline{u^2}$ pressure-strain value is not well estimated by any model at this station except when the data values and estimates are very close to zero (Fig. 69). $\overline{v^2}$ pressure-strain variation is well approximated only above $y^+\approx40$ (Fig. 70). Even though the estimates and the $\overline{w^2}$ data values overlap at certain regions none of the models were able to predict the data values until $y^+\approx500$ (Fig. 71). $\overline{uv}$ value is predicted well by the SLCL model above $y^+\approx20$ (Fig. 72). The trend of SLCL and FLT1 models are closer to the trend of the $\overline{uw}$ data throughout the layer, with superior agreement of FLT1 model (Fig. 73). Above $y^+\approx30$ all model values and data values are close to each other. $\overline{vw}$ pressure-strain values are equally well predicted by the FLT1 and SLCL models above $y^+\approx15$ (Fig. 74).

IV-A-4) Vortex-core station

The variations of $\overline{u^2}$, $\overline{v^2}$. $\overline{w^2}$ are not well predicted by any model (Figures 75, 76, and 77). Values predicted by FLT models above $y^+\approx300$ are closer to the pressure-strain data values. Shear stress pressure-strain estimates at this station are also much different than the data values through out the layer especially near the wall. Estimated values follow the same trend of the data above $y^+\approx100$, $y^+\approx400$, and $y^+\approx200$ for the $\overline{uv}$, $\overline{uw}$, and $\overline{vw}$ stresses respectively (Figures 78, 79, and 80).

IV-B) Algebraic anisotropic dissipation rate models

The fact that the limiting value of the dissipation at the wall is not isotropic is realized by many researchers and different algebraic models are proposed in the literature. Nagano and Tagawa (1991) argued that simple algebraic models could not capture the physics and developed a new closure scheme which is not algebraic. In this report several algebraic dissipation rate models are summarized. For consistency only one model (Hallbäck, et al., 1990) was used and tested in comparison of measured and predicted pressure-strain models.

IV-B-1) Launder and Reynolds (1983) model

Launder and Reynolds (1983), using the near wall variations of the fluctuating velocity components, show that the common assumption of $\varepsilon_{ij}=(\dfrac{\overline{u_iu_j}}{k})\varepsilon$ underestimates the dissipation in the $\overline{v^2}$ transport equation by a factor of 4. They propose a model which satisfy the near wall variation:

$$\varepsilon_{ij}=(\frac{\varepsilon}{k})\,[\,\overline{u_iu_j}+\alpha(\overline{u_iu_k}n_kn_j+\overline{u_ju_k}n_kn_i)+\beta\,\delta_{ij}\overline{u_ku_l}n_kn_l\,]$$

where $n_j=(0,1,0)$, $\alpha=1$, and $\beta=1$ with the provisions that for ε_{11} or ε_{33}, $\overline{v^2}$ is negligible compared to $\overline{u^2}$ or $\overline{w^2}$.(Therefore, $\beta=0$ when i=1,j=1 and i=3,j=3). This equation shows that the dissipation of each shear stresses is different than zero.

IV-B-2) Hallbäck, Groth, and Johansson model (1990)

Hallbäck, Groth, and Johansson developed an explicit model relating the anisotropies of the dissipation rate tensor to the anisotropies of the Reynolds stress tensor using Lumley's invariant theory (1978). The general expression for the dissipation rate anisotropies given by the invariant theory was expanded in power series of the Reynolds stress anisotropies. A series of mathematical and physical constraints were employed on this expansion to obtain the dissipation rate anisotropy tensor e_{ij}.

$$e_{ij} = (\frac{\varepsilon_{ij}}{\varepsilon}) - \frac{2}{3}\delta_{ij} \text{ and}$$

$$e_{ij} = [1 + \alpha(\frac{1}{2}II - \frac{2}{3})]a_{ij} - \alpha(a_{ik}a_{kj} - \frac{1}{3}II\delta_{ij})$$

where, $a_{ij} \equiv (\frac{\overline{u_i u_j}}{k}) - \frac{2}{3}\delta_{ij}$, $k = \frac{1}{2}\overline{u_i u_i}$, $II = a_{ik}a_{ki}$, $\alpha = \frac{3}{4}$

The model was tested against numerical simulations of homogeneous turbulence with success.

IV-B-3) Lai, and So model (1990)

Lai and So developed an anisotropic dissipation rate tensor model similar to the Launder and Reynolds (1983) model. The model does not need any provisions for ε_{11}, and ε_{33}.

$$\varepsilon_{ij} = \frac{2}{3}\varepsilon(1 - f_{w,1})\delta_{ij} + \frac{f_{w,1}(\varepsilon/k)[\overline{u_i u_j} + \overline{u_i u_k}n_k n_j + \overline{u_j u_k}n_k n_i + n_i n_j \overline{u_k u_l}n_k n_l]}{1 + 3\overline{u_k u_l}n_i u_k/(2k)}$$

where

$$f_{w,1} = \exp[-(R_T/150)^2] , R_T = \frac{k^2}{\nu\varepsilon}$$

IV-B-4) Launder, and Tselepidakis model (1990)

$$\varepsilon_{ij} = f_\varepsilon \varepsilon_{ij}^* + (1 - f_\varepsilon)\frac{2}{3}\delta_{ij}\varepsilon$$

where

$$\varepsilon_{ij}^* = \frac{\varepsilon}{k} \frac{[\overline{u_i u_j} + \overline{u_i u_k}n_k n_j + \overline{u_j u_k}n_k n_i + \delta_{ij}\overline{u_k u_l}n_k n_l]}{[1 + \frac{5}{2}\frac{\overline{u_p u_q}n_p n_q}{k}]}$$

and $f_\varepsilon = \exp[-R_t/20]$, $R_t = \frac{k^2}{\nu\varepsilon}$, $k = \frac{1}{2}\overline{u_i u_i}$

IV-C) Anisotropic dissipation rate effects on the experimental stress transport rate budget

IV-C-1) Anisotropic dissipation rate distribution

Anisotropy of the dissipation rate tensor affects the pressure-strain rate term extracted from the Reynolds' stress transport equations. Calculation of convection, production, and viscous diffusion are not affected by the anisotropy of the dissipation rate tensor. Since the pressure-strain term is extracted from the balance of the budget of transport equations, it is the only term affected. Anisotropy of the dissipation term also does not affect the TKE transport budget. Figures 81 to 84 show the distribution of the dissipation rates for different stresses. The figures also include the isotropic dissipation rate for comparison. For the 2-D case, figure (81) shows that while the $\overline{w^2}$ dissipation rate is very similar to the isotropic dissipation rate, the $\overline{u^2}$ dissipation rate is much larger than both isotropic and $\overline{v^2}$ dissipation rates (Fig. 81). While the peak value of the $\overline{u^2}$ dissipation is close to 2 times of the isotropic dissipation rate, the dissipation in the $\overline{v^2}$ transport is halved. The dissipation in the $\overline{uw}$ and $\overline{vw}$ transport are practically zero and the dissipation in the transport of $\overline{uv}$ is negative with a peak value of approximately 1/3 of the $\overline{v^2}$ dissipation.

At Station 5 the anisotropy of the $\overline{w^2}$ dissipation rate is noticeable. Compared to the 2-D case the $\overline{v^2}$ dissipation rate is reduced (Fig. 82). The $\overline{uw}$ dissipation rate is higher in magnitude than the $\overline{v^2}$ dissipation rate. The $\overline{uv}$ and $\overline{vw}$ dissipation rate absolute values reach to half of the $\overline{v^2}$ dissipation rate, however they are an order of magnitude smaller than the $\overline{u^2}$ and $\overline{w^2}$ dissipation rate values. Dissipation rate is close to isotropic distribution above $y^+\approx100$.

The magnitude of the dissipation rate values in general are increased more than twice by the Separation station compared to the 2-D station values (Fig. 83). The $\overline{u^2}$ dissipation rate is the highest near the wall. Above $y^+\approx25$, $\overline{u^2}$ and $\overline{w^2}$ dissipation rate values follow each other closely. The $\overline{v^2}$ dissipation rate is relatively smaller than $\overline{u^2}$ dissipation rate values compared to Station 5. Shear stress dissipation rate terms are also increased.

At the Vortex-core station above $y^+\approx20$, $\overline{w^2}$ dissipation rate is larger is larger than $\overline{u^2}$ dissipation rate (Fig. 84). The magnitudes of the dissipation rate values are higher than compared to other stations and difference between the isotropic distribution and $\overline{u^2}$ and $\overline{w^2}$ dissipation rate values are further increased. The $\overline{uw}$ dissipation rate changes sign around $y^+\approx20$ and shows a positive peak around $y^+\approx40$. Normal stress dissipation rate terms follow each other closely above $y^+\approx125$ and show a relative maxima at $y^+\approx300$. Stress dissipation rate values above $y^+\approx100$ are close to zero.

IV-C-2) Effects of anisotropic dissipation rate on the experimentally extracted pressure-strain terms

Following the Hallbäck et al. model, the dissipation process near a wall is highly anisotropic with most of the dissipation occurring in the $\overline{u^2}$ and the $\overline{w^2}$ transport. However above $y^+\approx100$ the dissipation rate is isotropic for the 3-D flows. In the 2-D flow, the dissipation rate becomes isotropic at a higher y^+ ($y^+\approx350$) location. The dissipation

rate values for the $\overline{u^2}$ and $\overline{w^2}$ transport are increased by the three-dimensionality of the flow and the shear stress transport dissipation rate values are away from zero with values an order of magnitude smaller than the $\overline{u^2}$ values.

The anisotropy of the dissipation rate effects only the pressure-strain value extracted from the balance of the budget of a stress. The increase in the dissipation rate value of a stress above the isotropic distribution value at a point in the profile also results to an increase by the same amount to the pressure-strain value at the same point in the profile extracted using isotropic dissipation rate distribution. This results in reduced values in magnitude of the pressure-strain values for the $\overline{u^2}$ in the 2-D flow (Fig. 85). $\overline{v^2}$ transport pressure-strain term becomes negative very near the wall below $y^+\approx 20$ (Fig. 86). The magnitude of the dissipation rate for the $\overline{uv}$ stress is too small to have any observable changes in the pressure-strain term of this stress (Fig. 87). $\overline{w^2}$ pressure-strain distribution is very similar to the one calculated with isotropic dissipation rate approximation (Fig. 88).

At Station 5 location the effect of anisotropic dissipation rate in the $\overline{u^2}$ transport is to reduce the magnitude of $\overline{u^2}$ pressure-strain rate (Fig. 89). The values near the wall below $y^+\approx 15$ become close to zero. Negative peak value at $y^+\approx 20$ is halved. The pressure-strain profile of $\overline{v^2}$ transport shows two distinct positive peaks, one at $y^+\approx 8$ and one at $y^+\approx 50$, and a negative peak at $y^+\approx 20$ (Fig. 90). The peak dissipation rate value is 2/3 of the positive peak value of the pressure-diffusion term. Effect on $\overline{w^2}$ pressure-strain term is felt at $y^+\approx 25$, the positive peak value is increased by 0.01 from a value of 0.015 (Fig. 91). The $\overline{uv}$ and $\overline{vw}$ pressure-strain distributions (Figures 92, and 93) are not effected since the dissipation rate predicted for these stresses are small in magnitude. However the peak value of the pressure-strain term for the $\overline{uw}$ transport is decreased by ≈ 0.035 from a value of ≈ 0.125 (Fig. 94).

At the Separation station the effect of the anisotropy results in positive pressure-strain values near the wall below $y^+\approx 20$ for the $\overline{u^2}$ transport equation (Fig. 95). The profile shows a positive peak at $y^+\approx 20$ rather than a negative peak at $y^+\approx 10$ that was observed with isotropic dissipation rate approximation. The profile for the pressure-strain term of the $\overline{v^2}$ transport is also drastically affected (Fig. 96). This profile shows a negative peak at $y^+\approx 18$ rather than a positive peak around $y^+\approx 10$ with reduced values throughout the layer. The variation becomes a mirror image of the pressure-diffusion around a value of 0.01. The values of the pressure-strain in the transport equation of $\overline{w^2}$ (Fig. 97) are about constant between $y^+\approx 10$ to 80. Both the $\overline{uv}$ and $\overline{vw}$ pressure-strain term profiles are very similar to the profiles obtained with isotropic dissipation rate (Figures 98, and 99). $\overline{uw}$ pressure-strain profile is also similar with slightly reduced peak value (Fig. 100).

At the Vortex-core station the pressure-strain values of the $\overline{u^2}$ transport are elevated below $y^+\approx 100$, resulting in larger values than the production values in $y^+\approx 15$ to 30 range (Fig.101). The variation of the $\overline{v^2}$ pressure-strain rate is also highly affected by the anisotropy of dissipation rate as in the other stations (Fig.102). While the distribution is positive till $y^+\approx 400$ where the dissipation rate is isotropic, the profile shows a negative

peak at $y^+ \approx 25$ with anisotropic dissipation rate approximation. The pressure-diffusion term becomes one of the most important terms below $y^+ \approx 50$ in describing the transport of $\overline{v^2}$. The $\overline{w^2}$ pressure-strain term is increased by an amount of 0.1 below $y^+ \approx 50$ (Fig.103). The variation is similar to results when the isotropic dissipation rate is used. Pressure-strain terms in the shear stress transport equations are not affected by the anisotropy of the dissipation rate since the anisotropic dissipation rate values for this station are close to zero (Figures 104, 105, and 106).

IV-D) Anisotropic dissipation rate effects on theoretical and experimental pressure-strain comparison

Anisotropic dissipation rate approximation of Hallbäck et al (1990) does not affect the pressure-strain distribution estimated by the models. However, it affects the experimental values extracted from the stress transport budget balances. Anisotropic distribution results in better agreement of the predictions and the data of different models at different regions. In the next paragraphs, anisotropic dissipation rate effects in predictions of the models will be discussed.

IV-D-1) 2-D station

The $\overline{u^2}$ pressure-strain term is well predicted by the FLT2 model near the wall below $y^+ \approx 25$ (Fig.107). None of the models predicts the data in this range with the isotropic assumption. Between $y^+ \approx 25$ to 50, none of the models predicts the variation; above $y^+ \approx 50$ all the model estimates follow each other and the data values closely except the FLT models. The $\overline{v^2}$ pressure-strain is also well predicted by the FLT2 model near the wall below $y^+ \approx 25$ (Fig.108). Above $y^+ \approx 40$, data values are closer to FLT1 and OP model predictions rather than the GL, LRR, SLCL, or SSG models. Both the $\overline{w^2}$ and the $\overline{uv}$ pressure-strain values are similar to the isotropic dissipation rate approximation variation since the dissipation rate distributions for $\overline{w^2}$ and $\overline{uv}$ are very similar to that of isotropic dissipation rate (Figures 109, and 110).

IV-D-2) Station 5

Pressure-strain data near the wall for the $\overline{u^2}$ transport equation is close to zero till $y^+ \approx 15$. At $y^+ \approx 15$ the estimated profiles show negative peaks (Fig.111). Above $y^+ \approx 50$ all the model values are not far away from the data. Below $y^+ \approx 40$, data and the predictions are further apart from each other then the isotropic dissipation rate approximation. The $\overline{v^2}$ data are closely predicted by the FLT2 model throughout the layer (Fig.112). This model behaved as the worst model with the isotropic dissipation rate approximation. Between $y^+ \approx 25$ to $y^+ \approx 60$, the $\overline{w^2}$ data variation is closely followed by the OP model estimates (Fig.113) rather than the FLT2 model with the isotropic dissipation rate approximation. Above this location data values and all the predictions are close to each other and to the zero value. The variations of the pressure-strain data for $\overline{uv}$ and $\overline{vw}$ are not different than the isotropic dissipation rate distribution case (Figures 114, 115). Predictions by the

models for the $\overline{uw}$ stress are less in agreement with the data in the $y^+ \approx 10$ to 30 range (Fig.116). Variations near the wall are well approximated by the SLCL, FLT1 models. Also above $y^+ \approx 50$ all the model estimates follow the data closely.

IV-D-3) Separation station

The anisotropic dissipation rate results in much different pressure-strain distribution in the $\overline{u^2}$ transport equation than the isotropic dissipation rate approximation (Fig.117). The model variations are also very much different than data. While the data show a positive peak at $y^+ \approx 20$, the models predict much larger negative peak at $y^+ \approx 15$. The trend of the data is opposite to the trend of the predictions. The $\overline{v^2}$ prediction by FLT2 is very good throughout the layer (Fig.118), while the other models show a positive peak value at the location where the data show a negative peak value. The FLT2 model with the isotropic dissipation rate approximation was the only model which predicted values with an opposite trend to the data. The $\overline{w^2}$ pressure-strain data are not predicted well by the models (Fig.119). Although the estimates are in the vicinity of the data, the variations are much different. The $\overline{uv}$ data values are closely predicted by the SLCL and FLT1 models above $y^+ \approx 15$ (Fig.120) similar to with isotropic dissipation rate. The $\overline{uw}$ pressure-strain data agreement with the FLT1 model with an isotropic dissipation rate approximation is poorer (Fig.121). However the model distributions are close to that of the data above $y^+ \approx 25$. The $\overline{vw}$ pressure-strain distribution is not different than isotropic dissipation rate distribution and is well predicted by the SLCL and FLT1 models above $y^+ \approx 15$ (Fig.122).

IV-D-4) Vortex-core station

As previously observed for all the normal and shear stresses the pressure-strain data are very poorly predicted by all the models. The differences between the data and the predictions increase (Figures 123 through 128).

IV-E) Effect of the near-wall correction on the theoretical pressure-strain models

Near wall corrections were calculated using the Launder-Reece-Rodi (1975) model. For consistency the model corrections were applied to the other models. The near wall corrections are large below $y^+ \approx 100$ for the 2-D, Station 5 and Separation stations (Figures 129, 130, and 131). The corrections span up to $y^+ \approx 300$ at the Vortex-core station (Fig.132). The near wall corrections affect only the mathematical pressure-strain models. The corrections are additive to the model estimates. At all 3-D stations the largest corrections are estimated for the $\overline{uv}$ and $\overline{vw}$ stresses. At 2-D station the $\overline{uv}$ correction is the largest. The $\overline{u^2}$ corrections at all stations are close to one another. The $\overline{v^2}$ corrections are on the same order of $\overline{u^2}$ corrections and become large at the Vortex-core station. The $\overline{w^2}$ correction is small for the 2-D, Station 5 and Separation stations and is on the same order of magnitude of the $\overline{u^2}$ correction for the Vortex-core station. The $\overline{uw}$

correction is on the same order of the $\overline{v^2}$ correction for the Station 5 and Separation stations. However, at the Vortex-core station the correction is larger.

IV-F) Evaluation of near-wall correction effects on theoretical and experimental pressure-strain with isotropic dissipation rate approximation

IV-F-1) 2-D Station

At the 2-D station near-wall corrections to the normal stress pressure-strain models improve the prediction of the data values. However differences between the data and the predictions appear above $y^+ \approx 40$. Below $y^+ \approx 40$, the OP model estimates are closer to the data for $\overline{u^2}$ (Fig.133). For $\overline{v^2}$ and $\overline{w^2}$ LRR and GL models are relatively closer to the data, respectively (Figures 134, and 135). For the $\overline{uv}$ stress the corrections near the wall below $y^+ \approx 20$ result in highly overpredicted values (Fig.136).

IV-F-2) Station 5

Near-wall corrections affect the estimated values by the models to be closer to the data values for the pressure-strain term of $\overline{u^2}$ (Fig.137). However the estimates are still very much different than the data. The FLT1 model trend is closest to the data variation. Double-peaked pressure-strain term variation for the $\overline{v^2}$ is not followed by any of the models (Fig.138). Near wall correction results in reduced agreement throughout the profile, especially near the wall. Model predictions for the pressure-strain variation of $\overline{w^2}$ are closer to the data values (Fig.139), but the change in the predicted values compared to the no-near-wall-corrected estimates is very small. Near wall corrections for the $\overline{uv}$ shear stress pressure-strain term are opposite to the trend of the data near the wall especially below $y^+ \approx 15$ (Fig.140). The pressure-strain term is well predicted both by the GL and LRR models above this y^+ location. The agreement between the data and all the models' estimates except the FLT models is better above $y^+ \approx 30$ for the $\overline{uw}$ (Fig.141). The $\overline{vw}$ pressure-strain term is well predicted by the FLT1, LRR, and GL models above $y^+ \approx 20$ (Fig.142).

IV-F-3) Separation station

Near-wall corrections affect the model estimates in a similar way as at Station 5. The correction causes the trend of the predictions for the $\overline{u^2}$ and $\overline{v^2}$ normal stresses to be closer to the data variations, but the amount of correction does not result in collapse of the data and predicted profiles (Figures 143, and 144). The near-wall corrected estimates for the $\overline{w^2}$ results in reduced agreement (Fig.145). The shear stress pressure-strain data and predictions differ highly below $y^+ \approx 15$ to 20. The $\overline{uv}$ data profile is closely followed by the GL, LRR, SSG, and SLCL models above $y^+ \approx 15$ (Fig.146). The $\overline{uw}$ data

are well predicted by all the models, except the FLT models above $y^+\approx20$ (Fig.147). The $\overline{vw}$ pressure-strain estimates by the SSG, LRR, and GL models are in good agreement with the data above $y^+\approx15$ (Fig.148).

IV-F-4) Vortex-core station

The near-wall corrections results in good agreement of OP, FLT2, and FLT1 models with the pressure-strain term of $\overline{u^2}$ normal stress below $y^+\approx15$ (Fig.149). Data and predictions of GL, SSG, and FLT1 are in agreement in the $y^+\approx70$ to 150 range. Also in the $y^+\approx300$ to 700 range FLT models predict the data well. The data values for the pressure-strain of $\overline{v^2}$ do not change in the profile up to $y^+\approx200$ where the predictions in the same range highly vary (Fig.150). In similar fashion as to the values predicted without the wall corrections, the predicted values with the near wall corrections are far away from the data values, except in the $y^+\approx250$ to 450 limited range. In this range, the FLT models' estimates are close to the data values. Closer agreement of the $\overline{w^2}$ data and the predictions in the region above $y^+\approx70$ without the near-wall corrections is delayed till $y^+\approx150$ (Fig.151). Above $y^+\approx150$, data and predictions of FLT models are in good agreement. Near wall corrections bring the $\overline{uv}$ data estimates of the GL model above $y^+\approx20$ and SLCL model above $y^+\approx30$ closer to the data (Fig.152). The $\overline{uw}$ pressure-strain term is poorly estimated throughout the layer (Fig.153). The $\overline{vw}$ data estimates of the models are opposite to the near wall data (Fig.154). Above $y^+\approx100$ the data and the predictions follow each other.

IV-G) Combined effect of the near-wall correction and the anisotropic dissipation rate on the theoretical pressure-strain model predictions

It was previously discussed that the anisotropic dissipation rate assumption results in different distributions of the experimental pressure-strain term extracted from the stress transport budget. A near-wall correction term is used to take into account the existence of the wall in the wall bounded flows and affects the pressure-strain term calculated by the model. In this section the combined effects of this correction and the anisotropic dissipation rate approximation on the agreement of the data and the calculations will be discussed.

IV-G-1) 2-D station

Even though the $\overline{u^2}$ pressure-strain term is well predicted near the wall below $y^+\approx20$ with only an anisotropic dissipation rate approximation and reasonable well estimated above $y^+\approx15$ with only the near-wall corrections applied models, both effects together do not result in better agreement (Fig.155). The data are well predicted by all the models except the FLT models above $y^+\approx40$. The $\overline{v^2}$ pressure-strain data were well predicted by the FLT2 using anisotropic dissipation rate approximation very near the wall (Fig.156). The combined effect reduces this agreement. The region above $y^+\approx40$ is well

estimated by different models with or without the correction or approximations made. The $\overline{w^2}$ pressure-strain variation is very well approximated by the models with or without the assumptions (Fig.157). The $\overline{uv}$ pressure-strain predictions are very similar to the near-wall corrected predictions. SSG, GL, SLCL model estimates agree with the data above $y^+\approx18$ (Fig.158).

IV-G-2) Station 5

Estimates to the $\overline{u^2}$ pressure-strain term variation are improved by the combined effect below $y^+\approx8$ (Fig.159). However the differences between the data and the predictions in the $y^+\approx10$ to 50 region are not reduced. The combined effect on the $\overline{v^2}$ pressure-strain term is similar to the near-wall correction effect. The data and the estimates differ highly below $y^+\approx50$ (Fig.160). The near wall variation of $\overline{w^2}$ data up to $y^+\approx25$ is not well predicted with or without the effects of dissipation rate anisotropy and near-wall correction (Fig.161). Above this y^+ location OP model values follow the data closely with the current assumptions. The $\overline{uv}$ pressure-strain variation is well estimated by the LRR, GL, and FLT1 models above $y^+\approx15$, similar to near-wall corrected model estimates (Fig.162). Agreement between the $\overline{uw}$ data and the predictions appears to be degraded with the near-wall correction or the anisotropic dissipation rate approximation, or the combined effects of these assumptions (Fig.163). Above $y^+\approx15$ the $\overline{vw}$ data and the estimates of LRR, GL, and FLT2 model agree closely (Fig.164). The near wall variation is not well estimated by any assumptions.

IV-G-3) Separation station

The variation of the model predictions for $\overline{u^2}$ pressure-strain and the data highly differ from each other with opposite signed peaks at different y^+ locations (Fig.165). The good agreement between the $\overline{v^2}$ pressure-strain data and the LRR model with the anisotropic dissipation rate approximation is canceled with the combined effect (Fig.166). The $\overline{w^2}$ data are well approximated by the OP model in the $y^+\approx18$ to 70 region when the effects are combined (Fig.167). Combined effects results in $\overline{uv}$ pressure-strain data to be followed by the LRR, and GL models starting at $y^+\approx15$ (Fig.168). Combined effects or each effect singly degrades the agreement between the models and the data for $\overline{uw}$ (Fig.169). For the $\overline{vw}$ pressure-strain term SLCL, LRR, and GL model predictions are in good agreement above $y^+\approx15$ (Fig.170). However, the differences between the variations of the estimates and the data are increased closer to the wall.

IV-G-4) Vortex-core station

The close agreement between the model estimates and the data for $\overline{u^2}$ at this station is reduced compared to only near-wall corrected model estimates (Fig.171). The differences between the models and the data for the other normal and shear stress

pressure-strain data are very large and adjustments due to the anisotropic dissipation rate approximation and near-wall correction separately or together are not large enough to compensate for them (Figures 172 through 176).

CHAPTER V - DIRECT NUMERICAL SIMULATION (DNS) COMPARISON

In this Chapter comparison of several existing DNS calculations to the present transport rate budgets are made. DNS simulations are usually calculated at low Reynolds numbers due to very costly computer time requirements. DNS studies are also directed to much simpler flow configurations than the present study configuration. Comparisons are therefore qualitative rather than quantitative. General trends of the transport budget terms are outlined and compared.

V-A) Study of Sumitani-Kasagi (1995)

Sumitani and Kasagi (1995) studied a fully turbulent channel flow with heat transfer and uniform wall injection at a low Reynolds number (Re=150=channel half width x u_τ / v). Their results showed that while the normal stresses and the shear stress increased on the injection side and decreased on the suction side, skin friction increased on the suction side and decreased on the injection side. Balance of the TKE, normal stress, shear stress, and dissipation rate transport equations were calculated and presented. ^The present 2-D case data of the terms in the budget of the transport equations show similar characteristics to the presented DNS calculations by Sumitani and Kasagi.

For $\overline{u^2}$ the similarities can be summarized. The production terms both for the DNS and the 2-D data peak at the similar y^+ locations on the suction side ($y^+{\approx}15$). Convection terms on the suction side show increased values below $y^+{\approx}10$. Pressure-diffusion is not presented by DNS. For the present data it is calculated as approximately zero. Pressure-strain terms on the suction side are close to the dissipation rate variation above $y^+{\approx}30$ and values are also not far away from the production values with an opposite sign. A similar variation is observed for the present data. Dissipation rate values were observed to be larger than the pressure-strain terms for the DNS study on the suction side below $y^+{\approx}35$ which is more closely approximated by the anisotropic dissipation rate approximation applied to the present data. On the suction side DNS results show that pressure-strain values are close to zero, which is not the case observed with the present data. DNS shows that the dissipation rate and the viscous diffusion terms are not zero at the wall for this stress.
Experimental data for Station 5 and Separation stations are qualitatively similar to the 2-D data, however the distributions for the Vortex-core station are very much different both from the 2-D data and the DNS solutions.

The $\overline{v^2}$ DNS results shows that all the $\overline{v^2}$ transport terms at the wall are zero. The pressure-diffusion term on the suction side was elevated as high as the dissipation rate from near the wall to about $y^+{\approx}60$. Pressure-strain, and pressure-diffusion terms on the injection side are equally high with opposite signs very near the wall below $y^+{\approx}5$, convection was practically zero, viscous diffusion was elevated near the wall below $y^+{\approx}15$, and turbulent diffusion changed sign around $y^+{\approx}18$. Pressure-strain and the dissipation rate terms are the dominant terms away from the wall. Similar trends are observed for the present 2-D, Station 5, and Separation stations.

DNS results for $\overline{w^2}$ showed that the viscous-diffusion and dissipation rate terms at the wall are not zero for this normal stress. The dominant terms very near the wall

below $y^+ \approx 5$ are the viscous diffusion and the dissipation rate terms both on the suction and injection sides. Away from the wall pressure-strain and the dissipation rate term values are approximately equal to each other with opposite signs to each other. Production and pressure-diffusion terms were not presented since they are practically zero. These observations are also valid for the present 2-D data. At 3-D flow stations the production term for this stress is the largest term and highly alters the budget.

Pressure-diffusion and pressure-strain terms are the only terms that are not zero at the wall for $\overline{uv}$, with values larger than the peak values observed within the layer. Both terms are reduced to near zero values at $y^+ \approx 5$ before they reach maxima values at the wall. They are approximately equal to each other with an opposite sign near the wall below $y^+ \approx 5$. Away from the wall pressure-strain and production terms are the dominant terms on the injection side. On the suction side the pressure-diffusion term is also as high as these two terms. Pressure-diffusion changes sign three times, at $y^+ \approx 5$, near $y^+ \approx 10$ and one around $y^+ \approx 35$. Pressure-strain is positive. Turbulent diffusion is also high for both cases. These trends are also very similar to the 2-D, Station 5, and Separation station data of the present study.

V-B) Study of Perot-Moin (1993)

Perot studied cases of $Re_T = \dfrac{k^2}{\varepsilon \nu} = 54$ and 134 in a temporally developing boundary layer obtained by instantaneously inserting a moving solid wall to an isotropic homogenous turbulence (1993). The development of the layer depends on time and distance away from the wall. The solutions were obtained in time spanning to 3 large eddy turnover time. ($T_0 = \dfrac{k}{\varepsilon} =$ large eddy turnover at initial conditions). The turbulence is decaying over time. The flow can be thought as a 2-D TBL with high free-stream turbulence.

DNS data for $\overline{u^2}$ show that the production and diffusion peak at closeby distances away from the wall for $Re_T = 54$ case ($u_0'/U_{wall} = 0.5$, $u_0' =$ initial rms of u fluctuations). Pressure-diffusion is close to zero. These observations are similar to the present 2-D data. However, the following observations show marked differences between data and DNS solutions: Dissipation rate is the highest term. Pressure-strain is as high as the production term. Turbulent-diffusion is positive near the wall and changes sign away from the wall.

For $\overline{v^2}$ the DNS shows that pressure-diffusion is observed as high as the pressure-strain near the wall, and dissipation rate is larger than both of the terms away from the wall. Viscous-diffusion increased near the wall and reduced to zero at the wall. Production is approximately zero. Similar observations were made for the 2-D flow $\overline{v^2}$ transport budget terms with the anisotropic dissipation rate approximation. DNS solutions show that the pressure-diffusion term is one of the most important terms shaping the structure of the near-wall flow. Turbulent transport was positive throughout the layer, which is not supported by the present data.

At the wall viscous-diffusion and dissipation rate terms are the only terms different than zero for $\overline{w^2}$. Convection and pressure-diffusion terms are practically zero. These are

the only observations from the 2-D flow data that agree with the DNS solutions. DNS shows that dissipation rate is higher than pressure-strain and that viscous diffusion is as high as the pressure-strain near the wall.

Pressure-strain and the production terms are the largest contributors to the transport rate of $\overline{uv}$ with opposite signs, which are similar observations from the present 2-D data. The following observations are not made in the present 2-D data. Dissipation rate and viscous-diffusion are approximately equal to each other with opposite sign. The pressure-diffusion term is zero. Turbulent diffusion is positive near the wall and changes sign to show a negative peak at the location where production profile peaks.

V-C) Study of Mansour-Kim-Moin (1988)

Mansour, Kim, and Moin studied Reynolds-stress and dissipation-rate budgets in a turbulent channel flow using DNS. The Reynolds number of the flow was $Re_\tau = u_\tau \delta/v = 180$ (δ=channel half width). Pressure-velocity gradient terms were not split into pressure-strain and pressure-diffusion, but together.

For $\overline{u^2}$, variations of the DNS data and the present 2-D data are in good agreement globally. For the low Re number channel flow the terms are closer to zero at $y^+ \approx 150$ where in the present data the values are different than zero till $y^+ \approx 1500$. Also the scales of the variations, even though nondimensionalized with the same parameter, are different from each other.

For $\overline{v^2}$, $\overline{w^2}$, $\overline{uv}$, agreement between the data and the DNS simulations are globally very good. The variations of the dissipation rate, turbulent diffusion and viscous-diffusion terms within the layer are in very good agreement with the 2-D data.

The TKE budget term variations of the DNS and the 2-D data are in good agreement. DNS data show that the pressure-diffusion term is very close to zero, except below $y^+ \approx 10$ with a zero value at the wall. Viscous-diffusion and dissipation rate are the only terms that are different than zero at the wall and their peak values occur at the wall. The differences observed are: the pressure-diffusion term of the present data is slightly higher than the DNS data relatively, the negative peak values obtained for the viscous-diffusion and the turbulent-diffusion are not at the same level for the 2-D data as observed in DNS. The dip of the dissipation rate profile below $y^+ \approx 15$ is not observed for the DNS data.

They analyzed the near wall asymptotic behavior of the Reynolds stress transport terms. For $\overline{u^2}$, the viscous-diffusion term becomes positive nearer to the wall than the turbulent-diffusion term. Viscous-diffusion at the wall is a positive constant. The pressure-gradient term asymptotically varies with y^+ near the wall and is zero at the wall. Dissipation rate is a positive constant at the wall.

For $\overline{v^2}$, all dissipation rate, viscous-diffusion, and pressure-gradient terms vary as y^{+2} towards the wall. Variations dictate that while the diffusion and dissipation rates near the wall should vary as positive, pressure-gradient term close to the wall should be negative. This is observed to be true for the present case only with the anisotropic dissipation rate approximation.

Viscous-diffusion and dissipation rate terms for $\overline{w^2}$ transport are positive constants at the wall. The pressure-gradient term should be positive near the wall, which is also

observed for the present data as the sum of the pressure-strain and pressure-diffusion terms. For $\overline{uv}$, analysis showed that while dissipation rate, viscous-diffusion, and pressure-gradient vary with y^+, production and turbulent diffusion vary with y^{+4}.

Their further analysis by splitting the pressure-gradient term as sum of pressure-strain and pressure-diffusion showed that the pressure-strain and the pressure-diffusion terms show peaks very close to the wall around $y^+\approx 5$ and are both zero at the wall. Similar variations are observed for the 2-D data with an anisotropic dissipation rate approximation further away from the wall in the $y^+\approx 10$ to 20 region. This also confirms the fact that the pressure-diffusion term affects the near wall distribution highly.

V-D) Study of Moin-Shih-Driver-Mansour (1990)

Moin, Shih, Driver, and Mansour computed a three-dimensional turbulent boundary layer (3DTBL) generated with a sudden pressure gradient ($\partial P/\partial z = 10\,\tau_w/\delta$) on a 2-d fully developed plane channel flow. The Reynolds number based on channel half width was 3300. The flow is a temporally evolving flow with zero streamwise velocity gradients rather than a spatially developing pressure-driven 3DTBL.

In a 3DTBL turbulent kinetic energy (TKE) was reduced. The $\overline{w^2}$ increased while $\overline{u^2}$ and $\overline{v^2}$ decreased. Townsend's A_1 structural parameter decreased with three-dimensionality. The shear-stress angle lagged behind the flow-gradient angle near the wall and led away from the wall. The pressure-strain was reduced in general for the 3-D case.

Increased three-dimensionality reduced the TKE. Turbulent transport and pressure-diffusion are reduced. Dissipation rate is increased. The production term was observed as the first term to respond to the three-dimensionality.

For $\overline{v^2}$, appreciable reduction in the velocity-pressure gradient term was observed. Production of $\overline{uv}$ decrease, which is believed to be due to the $\overline{v^2}$ reduction. Energy is transferred from $\overline{u^2}$ into $\overline{w^2}$ which is believed to be due to the flow turning.

A chain of events causing the decrease of TKE was described. Three-dimensionality reduces the pressure-strain in the $\overline{v^2}$ equation, which in turn reduces the $\overline{v^2}$ values. Reduction of $\overline{v^2}$ reduces the $\overline{uv}$, and reduction of $\overline{uv}$ reduces TKE production, which in turn reduces the TKE.

In comparison the present study shows that the nondimensional terms of the TKE transport at the 2-D station and at Station 5 are not much different from each other with slightly elevated magnitudes at Station 5, especially of the dissipation rate term. However the terms decay faster away from the wall at Station 5 as compared to the 2-D station.

For the present data there is a reduction in the pressure-strain term for the $\overline{v^2}$ transport and the reduction of the production term magnitude for the $\overline{uv}$ transport at Station 5 as compared to the 2-D station. The $\overline{v^2}$ and $\overline{uv}$ data also show the reduction of these quantities with three-dimensionality at Station 5 in nondimensional form.

V-E) Study of Spalart (1989)

Spalart studied a 3-D boundary layer on an infinite plate generated by the steadily rotating free-stream velocity for three different Reynolds numbers. The Reynolds numbers of the flow based on the laminar boundary layer thickness studied are $Re_l = U_0 \delta_l / v = 500, 620,$ and 767 ($\delta_l = \sqrt{2v/f}$, f=angular rate, U_0=free-stream velocity). Rotation had little effect on the turbulence. The viscous-diffusion plus dissipation rate and convection plus production terms along with the pressure-gradient term and a time-dependent term were presented. Turbulent-diffusion is not presented.

The TKE and Reynolds stress budgets are presented for $Re_l=767$ case. The TKE distribution shows that production is equal to dissipation rate with peaks located around $y^+\approx8$. Pressure-diffusion is an important contributor near the wall below $y^+\approx15$ and changes sign to positive away from the wall. In the present study both at Station 5 and the 2-D station, dissipation rate and production values peak at $y^+\approx15$ with different values of the peak and pressure-diffusion term is important up to $y^+\approx40$. As pointed out by Spalart due to the low Reynolds number of the study the flow simulated is weakly three-dimensional.

The $\overline{u^2}$ budget shows similar trends of the TKE distribution with highly elevated values of the combined pressure-strain and pressure-diffusion term and lower values of the convection plus production. However below $y^+\approx50$ viscous-diffusion plus dissipation rate and production plus convection terms are larger in magnitude than the pressure-strain plus pressure-diffusion term. In the present study for the 2-D flow production plus convection is 3 times larger than the dissipation rate and pressure-strain plus pressure-diffusion term. At Station 5 the dissipation rate term is closer to the production than the 2-D station. Present data show similar trends to each other with or without the anisotropic dissipation rate approximation.

From the DNS the $\overline{v^2}$ budget shows that the pressure term is positive and higher in magnitude than the dissipation rate plus viscous-diffusion. The convection plus production term changes sign from positive to negative around $y^+\approx20$. Dissipation rate plus viscous-diffusion term changes sign to positive around $y^+\approx5$. Similar observations are made for the present data with anisotropic dissipation rate approximation. For the 2-D station, data show that convection does not change sign but is close to zero at $y^+\approx100$; viscous terms change sign below $y^+\approx10$. At Station 5 convection plus production changes sign around $y^+\approx40$ and, viscous terms become positive around $y^+\approx5$. Pressure terms are close to but larger than the dissipation rate plus viscous-diffusion in magnitude.

The DNS budget for $\overline{w^2}$ shows that pressure terms are lower in magnitude than the viscosity involving terms. Production plus convection is negative near the wall below $y^+\approx15$. Pressure terms change sign from positive to negative away from the wall at $y/\delta\approx0.1$. At Station 5 with or without the anisotropic dissipation rate approximation, data show that pressure terms are low in magnitude than the viscous terms; however, the pressure term is negative below $y^+\approx15$ opposite to the trend in the DNS, it becomes positive between $y^+\approx15$ to 40 and negative above this y^+ value. The production plus convection term does not change sign as calculated by DNS.

The sum of the pressure terms in the $-\overline{uv}$ DNS budget are close in magnitude to the production plus convection terms. The dissipation rate term changes sign to negative at $y^+\approx5$. Away from the wall above $y/\delta>0.35$ production plus convection term and pressure terms change sign. The dissipation rate term is comparatively very small. For the presently reported data pressure terms and production plus convection terms follow each

other in magnitude closely similar to DNS results, however they do not change sign away from the wall.

The $-\overline{vw}$ budget shows that the pressure terms and the production plus convection terms follow each other closely in magnitude. Dissipation rate plus viscous-diffusion is relatively small compared to these terms above $y^+ \approx 10$. Similarly, pressure terms and the production term at Station 5 are close in magnitude to one another. Dissipation rate and convection terms are negligibly small throughout the layer. Pressure terms and production terms change sign above $y^+ \approx 100$ for the present data which is not observed for the DNS.

The $-\overline{uw}$ budget shows that viscous terms show a negative peak at $y^+ \approx 10$ and pressure terms around $y^+ \approx 25$. Positive peak of production+convection is at $y^+ \approx 15$. All the peak values are comparable to each other. Dissipation rate decay is faster than the other terms. Present data with anisotropic dissipation rate approximation show that all terms in comparison to DNS peak at the same y^+ location with higher peak magnitude value of production. The data show that pressure term and production term change sign away from the wall but at a lower y^+ location then the DNS results show.

CHAPTER VI - CONCLUSIONS

Some conclusions of the present study can be made about the effect of certain terms in the transport equations:

1) The pressure-diffusion term largely affects the transport rate budget of the $\overline{v^2}$ normal stress, and $\overline{uv}$ and $\overline{vw}$ shear stresses at all stations. The effect of the term is negligible for the transport rate budget of the TKE and other stresses.

2) At Station 5, Separation and Vortex-core stations the distributions of the transport budget terms decrease progressively more steeply to approximately zero values than the 2-D flow station at lower y^+ locations. This is more clearly visible for the $\overline{u^2}$, $\overline{w^2}$, and $\overline{uv}$ stresses. At the Vortex station these observations are accompanied with the effects of the outer region vortex. Vortex affects the terms to be away from zero. At the 2-D station $\overline{uw}$ and $\overline{vw}$ stresses are zero.

3) The effects of not using a near wall correction and an isotropic dissipation rate approximation were examined. Model predictions and the data agreement deteriorates with the increased complexity of the flow. Very near wall data values and predictions are different from each other for all stations below $y^+\approx35$. Overall different models predict different stress transport pressure-strain terms better. The FLT2 model behaves better in predicting the $\overline{u^2}$, and $\overline{v^2}$ stresses for complex Station 5 and Separation stations but not the other stations. The $\overline{u^2}$ and $\overline{v^2}$ estimates are very different than the data for the Vortex-core station. At the 2-D station for $\overline{u^2}$, above $y^+\approx40$ all the models except the FLT models, and in the same region for the $\overline{v^2}$ all the models except the FLT and OP models work best. At the 2-D station near wall variation of $\overline{w^2}$ is well approximated by FLT1 model. Above $y^+\approx35$, SSG, SLCL, GL, and LRR models work best. At Station 5, FLT2 model is better above $y^+\approx30$. The $\overline{w^2}$ pressure-strain term is not well predicted for Separation and Vortex-core stations by any model. None of the models predicts the pressure-strain variation of any shear stress transport for the Vortex-core station. The $\overline{uv}$ stress is better predicted by the SLCL model for 2-D and Separation stations. For Station 5 LRR and SSG models predict results closer to the data. The $\overline{uw}$ pressure-strain value is better predicted by the FLT1 model and $\overline{vw}$ is better predicted by the SLCL models.

4) Anisotropic dissipation rate effects were also examined. The isotropic dissipation rate assumption results in equally distributed dissipation rate for the normal stresses and no dissipation rate for the shear stresses. On the other hand the anisotropic dissipation rate model of Hallback et. al. shows that the dissipation rate is increasingly anisotropic with increased three-dimensionality effects. The dissipation rate in the $\overline{v^2}$ normal stress is relatively smaller then the $\overline{u^2}$ and $\overline{w^2}$ dissipation rate terms for the 3-D flow stations than the 2-D flow station. Dissipation rate in $\overline{uv}$ and $\overline{vw}$ stresses are on the order of half of the $\overline{v^2}$ terms. The $\overline{uw}$ dissipation rate near the wall is larger than the $\overline{v^2}$ dissipation rate with an opposite sign for the Station 5, and Separation stations. For 3-D flow stations

dissipation rate distributions are approximately isotropic above $y^+ \approx 100$. However for 2-D flow it becomes isotropic above $y^+ \approx 350$.

Anisotropy of the dissipation rate highly changes the experimental pressure-strain distributions extracted for the normal stresses; especially of the $\overline{v^2}$ normal stress. Near the wall between y^+ of 10-15 to 30-40, $\overline{v^2}$ pressure-strain distributions become negative and show negative peaks. The effect of an anisotropic distribution for the shear stress pressure-strain transport terms is non-negligible but small.

Anisotropic dissipation rate approximation increases the differences between the predictions and the data especially near the wall below $y^+ \approx 50$ for all the models except the FLT2 model. With the anisotropic dissipation rate approximation FLT2 model works well near the wall especially for the $\overline{v^2}$ for 2-D, Station 5, and Separation stations. The models which work best for the other stresses with isotropic dissipation rate approximation also work best with the anisotropic dissipation rate approximation.

Comparison of the present data to the DNS results shows that the present data are in better agreement with the DNS solutions with the anisotropic dissipation rate approximation.

5) The near-wall corrections with the isotropic dissipation rate approximation bring the data and the estimates close to each other for the normal stresses. Corrections for the $\overline{uv}$ stresses very near the wall are very large and corrections to the $\overline{uw}$ data do not make the agreement better. $\overline{vw}$ corrections very near the wall below $y^+ \approx 15$ is opposite to the trend of the data. Near wall corrections result in LRR, and GL models to be much closer to the data especially for the shear stress pressure-strain values, above $y^+ \approx 15$.

6) The combined effect of near-wall correction and the anisotropic dissipation rate approximation in general reduces the agreement between the data and the estimates for $\overline{u^2}$ and $\overline{v^2}$. The $\overline{w^2}$ agreement is not affected by the approximations. Agreement between the shear stress data and predictions with the combined effect is similar to the case with only the near wall correction.

V-A) Future work

The TKE and shear stress transport budget balance were extracted using the pressure-diffusion model of Lumley (1978). Experimental dissipation rate terms extracted for the TKE transport equation are not highly affected by this modelling. However, the pressure-strain terms extracted from the shear stress transport equations show that pressure-diffusion is one of the most prominent terms in the balance using Lumley's approach, especially for the $\overline{v^2}$, $\overline{uv}$, and $\overline{vw}$ stresses. The validity of this model or more improved models are needed. A recent study by Kim and Chung (1995) was directed towards this issue.

Other important needed research is the further validation of the anisotropic dissipation rate models. The dissipation rate term (ε), extracted from the TKE budget is distributed among the stresses. An isotropic dissipation rate approximation results in equally distributed dissipation rate terms among the normal stresses and no dissipation rate term in the shear stresses. Anisotropic dissipation rate models which are asymptotically correct near the wall did not seem to vary differently then the isotropic distributions for the high Re_θ cases studied in the present report away from the wall. The

Hallbäck, Groth, and Johansson anisotropic dissipation rate model not only satisfied near wall variations but also resulted in different variations throughout the layers for different stresses. Both isotropic dissipation rate and anisotropic dissipation rate approximations were studied in this report. Presented budget distributions with anisotropic dissipation rate approximations are closer to the DNS results, which is a further support for the anisotropic dissipation rate model chosen in the present study. However, the Reynolds numbers of the DNS are usually very low to make complete direct comparisons.

REFERENCES

Choi, K.S., and Lumley, J.L., "Turbulence and chaotic phenomena in fluids", 1984, *Proceedings of the IUTAM symposium* (Kyoto, Japan), edited by T. Tatsumi, North-Holland, Amsterdam, p.267.

Chou, P.Y., 1945 ,"On velocity correlations and the solutions of the equations of turbulent fluctuation", *Quarterly of Applied Math.*, vol. 3, pp. 38-54.

Devenport, W.J., and Simpson, R.L., 1990, "A time-dependent and time-averaged turbulence structure near the nose of a wing-body junction", *Journal of Fluid Mechanics*, vol. 210, pp. 23-55.

Fleming, J., Simpson, R.L., and Devenport, W.J., 1993, "An experimental study of a turbulent wing-body junction and wake flow", *Experiments in Fluids*, vol. 14, pp. 366-378.

Fleming, J., Simpson, R.L., and Shinpaugh, K.A., 1995, "Further investigation of the near wall flow structure of a low Reynolds number 3-D turbulent boundary layer", AIAA paper AIAA-95-0788, 33rd Aerospace sciences meeting and exhibit, Jan. 9-12, Reno, NV.

Fu, S., Launder, B.E., and Tselepidakis, D.P., "Accommodating the effects of high strain rates in modeling the pressure-strain correlation", 1987, UMIST Mechanical Engineering Dept. Rept. TFD/87/5.

Gatski, T.B., and Speziale, C.G., 1993, "On explicit algebraic stress models for complex turbulent flows", *Journal of Fluid Mechanics*, vol. 254, pp. 59-78.

Gibson, M.M., and Launder, B.E., 1978, "Ground effects on pressure fluctuations in the atmospheric boundary layer", *Journal of Fluid Mechanics*, vol. 86, part 3, pp. 491-511.

Ha, S.M., and Simpson, R.L., 1993, "*An experimental study of coherent structures in a three dimensional turbulent boundary layer*", Report# VPI-AOE-205, Virginia Tech, Aerospace and Ocean Engineering Department, Blacksburg, VA 24061.

Hallbäck, M., Groth, J., and Johansson, A.V., 1990, "An algebraic model for nonisotropic turbulent dissipation rate in Reynolds stress closure", October, *Physics of Fluids A*, 2 (10), pp. 1859-1866.

Johansson, A.V., and Hallbäck, M., 1994, "Modelling of rapid pressure-strain in Reynolds-stress closures", *Journal of Fluid Mechanics*, vol 269, pp. 143-168.

Kim, S., Walker, D.A., and Simpson, R.L., 1991, "*Observation and measurement of flow structures in the stagnation region of a wing-body junction*", Report# VPI-E-91-20, Virginia Tech, Engineering Science and Mechanics, Blacksburg, VA 24061.

Kim, Soong Kee, and Chung, Myung Kyoon, 1995, "Roles of pressure-transport and intermittency for computation of turbulent free shear flows", *International Journal of Heat and Fluid Flow*, Vol. 16, No. 3, pp.194-201.

Lai, Y.G., and So, R.M.C., "On near-wall turbulent flow modelling", 1990, *Journal of Fluid Mechanics*, vol 221, pp. 641-673.

Launder, B.E., and Tselepidakis, D.P., 1990, "Contribution to the second-moment modeling of sublayer turbulent transport", *Near-wall Turbulence*, pp. 818-833. 1988 Zoran Zaric Memorial Conference. Edited by S.J. Kline and N.H. Afgan. Hemisphere Publishing Corp., Newyork,

REFERENCES

Washington, London.

Launder,B.E., and Reynolds, W.C., 1983, "Asymptotic near-wall dissipation rates in a turbulent flow", May, *Physics of Fluids*, 26 (5), pp. 1157-1158.

Launder, B.E., Reece, G.J., and Rodi, W., 1975, "Progress in the development of a Reynolds-stress turbulence closure", *Journal of Fluid Mechanics*, vol. 68, part 3, pp. 537-566.

Launder, B.E., 1975, "On the effects of a gravitational field on the turbulent transport of heat and momentum", *Journal of Fluid Mechanics*, 67, pp. 569-581.

Launder, B.E., 1988, "Turbulence modelling of three-dimensional shear flows", AGARD-CP-438, Fluid Dynamics of Three-Dimensional Turbulent Shear Flows and Transition, pp. 26-1 26-20. AGARD, 7 Rue Ancelle, 92200, Neuilly sur Seine, France.

Launder, B.E., 1989, "Review:Second-moment closure:present.....and future?", *International Journal of Heat and Fluid Flow*, vol.10, no. 4, pp. 282-300, Dec.

Lewis, D.J., Simpson, R.L., and Diller, T., 1994, "Time resolved surface heat flux measurements in the wing/body junction vortex", *AIAA Journal, Thermophysics and Heat Transfer*, vol. 8, pp. 656-663.

Lumley, J.L., 1970, *Stochastic Tools in Turbulence*, Academic Press, New York.

Lumley, J.L., 1978, "Computation Modelling of Turbulent Flows", *Advances in Applied Mechanics*, vol 18., pp. 124-176.

Lumley, J.L., 1981, "Coherent structures in turbulence", *Transition and Turbulence*, pp. 215-241, Edited by Richard Meyer, Academic Press, New York, London, Toronto, Sydney.

Mansour, N.N., Kim, J., and Moin, P., 1988, "Reynolds-stress and dissipation-rate budgets in a turbulent channel flow", *Journal of Fluid Mechanics*, vol. 194, pp. 15-44.

Mansour, N.N., Kim. J., and Moin., P., 1989, "Near-wall k-epsilon turbulence modelling", *AIAA Journal*, vol. 27, no. 8, pp. 1068-1073.

Moin, P., Shih, T.H., Driver, D., and Mansour, N.N, 1990, "Direct numerical simulation of a three-dimensional turbulent boundary layer", *Physics of Fluids A*, vol. 2, no. 10, pp. 1846-1853.

Oberlack, M., and Peters, N., 1993, "Closure of the dissipation tensor equation and the pressure velocity correlation based on the two-point correlation equation", 9th Symposium on Turbulent Shear Flows, pp. 23-3-1 to 23-3-6, Kyoto, Japan,

Ölçmen, M.S., 1990, *An experimental study of a three-dimensional pressure-driven turbulent boundary layer*, Ph.D. Dissertation, Virginia Tech, AOE Dept., Blacksburg, VA, 24061.

Ölçmen, M.S., and Simpson, R.L., 1994, "Influences of wing shapes on the surface pressure fluctuations of a wing-body junction.", *AIAA Journal*, vol. 32, no. 1, pp. 6-15.

Ölçmen, M.S., and Simpson, R.L., 1995a, "An experimental study of a three-dimensional pressure-driven turbulent boundary layer", *Journal of Fluid Mechanics*, vol. 290, pp. 225-262.

Ölçmen, M.S., and Simpson, R.L., 1995b, "A five-velocity-component laser-Doppler velocimeter for measurements of a three-dimensional turbulent boundary layer", *Measurement Science and Technology*, vol 6., pp. 702-716.

Perot, B., and Moin, P., 1993, "Shear-free turbulent boundary layers: physics and modeling", Report No TF-60, Thermosciences Division, Dept. of ME, Stanford University, Stanford, California, 94305.

Rotta, J.C., 1951, "Statistische Theorie nichthomogener Turbulenz", Z. Phys., 129, 547.

Rotta, J.C., 1962, "Turbulent Boundary Layers in Incompressible Flow", *Progress in Aeronautical Sciences*, Volume 2, Boundary Layer Problems, Ferri, A., Küchemann, D., Sterne, L.H.G., editors, Pergamon Press.

Schwarz, W.R., and Bradshaw, P., 1994, "Term-by-term tests of stress-transport turbulence models in a three-dimensional boundary layer", February, *Physics of Fluids* 6 (2), pp. 986-999.

Schwarz, W.R., and Bradshaw, P., 1994, "Turbulence structural changes for a three-dimensional turbulent boundary layer in a 30° bend", *Journal of Fluid Mechanics*, vol.272, pp. 183-209.

Shao, L., Le Penven, L., and Bertoglio, J.P., 1990, "Study of the modelling of the transport terms in one-point closures using large eddy simulation of turbulence", *Engineering Turbulence Modelling and Experiments*, pp. 83-92. Rodi and Ganic, editors. Elsevier Science Publishing Co., Inc.

Shih, T.H., and Lumley, J.L., 1985, "Modelling of pressure correlation terms in Reynolds stress and scalar flux equations", Sibley School of Mechanical and Aeronautical Engineering, Cornell Univ., Rept. FDA-85-3, Ithaca, NY.

Shih, T.H., and Lumley, J.L., 1986, "Influence of timescale ratio on scalar flux relaxation: modelling Sirivat and Warhaft's homogenous passive scalar fluctuations", *Journal of Fluid Mechanics*, vol. 162, pp. 211-222.

Shih, T.H., Lumley, J.L., and Janicka, J., 1987, "Second-order modelling of a variable density mixing layer", *Journal of Fluid Mechanics*, vol. 180, pp. 93-116.

Shih, T.H., and Lumley, J.L., 1993, "Critical comparison of second-order closures with direct numerical simulations of homogenous turbulence", *AIAA Journal*, vol. 31, no. 4, pp. 663-670.

Shih, T.H., and Mansour, N.N., 1990, "Modeling of near-wall turbulence", *Engineering Turbulence Modelling and Experiments*, pp. 13-22. Rodi and Ganic, editors. Elsevier Science Publishing Co., Inc.

Shir, C.C., 1973, "A preliminary numerical study of atmospheric turbulent flows in the idealized planetary boundary layer", *Journal of Atmospheric Sciences*, 30, pp. 1327-1339.

Shinpaugh, K.A., and Simpson, R.L., 1995, "A rapidly scanning two-velocity-component laser Doppler velocimeter", *Measurement Science and Technology*, vol 6., pp. 690-701.

Spalart, P.R., 1989, "Theoretical and numerical study of a three-dimensional turbulent boundary layer", *Journal of Fluid Mechanics*, vol. 205, pp. 319-340.

Speziale, C.G., Sarkar, S., and Gatski, T.B., 1991, "Modelling the pressure-strain correlation of turbulence:an invariant dynamical systems approach", *Journal of Fluid Mechanics*, vol. 227, pp. 245-272.

Sumitani, Y., and Kasagi, N., 1995, July, "Direct numerical simulation of turbulent transport with uniform wall injection and suction", *AIAA Journal*, Volume 33, number 7, pp. 1220-1228.

Tagawa, M., Nagano, Y., and Tsuji, T., 1991, "Turbulence model for the dissipation components of Reynolds stresses", 8th symposium on turbulent shear flows, 9-11/1991, Munich, Germany

TABLE.1 LASER-DOPPLER VELOCIMETER LOCATIONS AND FLOW PARAMETERS.

Stations	X (inch.)	Z (inch.)	U_{ref} (m/sec)	U_e (m/sec)	β_{FS} (deg.)	β_w (deg.)	u_τ (m/sec)	ν (m²/sec) x1E05	$(\partial C_p/\partial x)_{FS}$ (1/m)	$(\partial C_p/\partial z)_{FS}$ (1/m)	daily pressure (millibar)	daily temperature (degrees Centigrade)
2-D	---	---	27.4	27.2	0	0	0.98	1.67	0	0	941.2	24
Station 5	0.26	-2.94	27.5	29.2	-7.71	-19.7	1.15	1.64	-6.25	-1.95	945.05	23
Separation	0.44	-2.50	27.6	30.2	-10.38	-23.6	1.048	1.68	-8.92	-4.92	935.3	24
Vortex-core	0.62	-2.07	27.5	32.3	-13.11	-29.47	1.33	1.67	-12.33	-7.93	941.3	24.8

Pressure coefficient gradients are calculated from the measured pressure distribution.
U_e=Velocity magnitude at the layer edge.

Stations	δ (mm)	δ_1 (mm)	δ_2 (mm)	δ_3 (mm)	δ_4 (mm)	δ_5 (mm)	δ_6 (mm)	δ_7 (mm)
TABLE.2 SOME LENGTH SCALES OBTAINED FROM LDV DATA IN TUNNEL COORDINATES.								
2-D station	39.1	6.28	6.27	4.55	-0.29	0.04	-0.26	-0.00
Station 5	40.0	6.26	5.38	4.64	7.47	-1.29	6.18	-1.39
Separation station	39.3	6.40	5.16	4.71	9.04	-1.54	7.49	-1.96
Vortex station	40.9	6.59	4.78	4.85	10.67	-1.92	8.75	-2.83

U_e=Velocity magnitude at the layer edge.

$\delta = y$ where $\sqrt{U^2 + W^2}/U_e = 0.995 =$ Boundary Layer Thickness

$\delta_1 = \int_0^\infty (1 - \dfrac{U}{U_e}) dy =$ Streamwise Displacement Thickness

$\delta_2 = \int_0^\infty (1 - \dfrac{\sqrt{U^2 + W^2}}{U_e}) dy =$ Magnitude Displacement Thickness

$\delta_3 = \int_0^\infty (1 - \dfrac{U}{U_e}) \dfrac{U}{U_e} dy =$ Streamwise Momentum Thickness

$\delta_4 = \int_0^\infty (-\dfrac{W}{U_e}) dy =$ Lateral Displacement Thickness

$\delta_5 = \int_0^\infty \dfrac{W}{U_e} (1 - \dfrac{U}{U_e}) dy =$ Lateral Momentum Thickness

$\delta_6 = \int_0^\infty -\dfrac{WU}{U_e^2} dy =$ Cross Product Momentum Thickness

$\delta_7 = \int_0^\infty -\dfrac{W^2}{U_e^2} dy =$ Crossflow Momentum Thickness

TABLE 3. 20:1 odds $+2\sigma$ uncertainties of means velocities, Reynolds' stresses and triple products.			
Term	Uncertainty	Term	Uncertainty
U/u_τ	0.148	$\overline{u^2v}/u_\tau^3$	0.082
V/u_τ	0.033	$\overline{u^2w}/u_\tau^3$	0.144
W/u_τ	0.097	$\overline{v^2w}/u_\tau^3$	0.051
$\overline{u^2}/u_\tau^2$	0.062	$\overline{uv^2}/u_\tau^3$	0.055
$\overline{v^2}/u_\tau^2$	0.04	$\overline{uw^2}/u_\tau^3$	0.165
$\overline{w^2}/u_\tau^2$	0.07	$\overline{vw^2}/u_\tau^3$	0.053
$\overline{uv}/u_\tau^2$	0.025	$\overline{uvw}/u_\tau^3$	0.05
$\overline{uw}/u_\tau^2$	0.037	$\overline{u^3}/u_\tau^3$	0.254
$\overline{vw}/u_\tau^2$	0.019	$\overline{v^3}/u_\tau^3$	0.043
		$\overline{w^3}/u_\tau^3$	0.424

TABLE 4. 20:1 odds $+2\sigma$ uncertainties of stress-transport terms for the six stresses. Uncertainties are non-dimensionalized by u_τ^4/ν. Numbers in the second row show the uncertainties below $y^+=100$.

Transport of	Term	Convection	Production	Turbulent-Diffusion	Pressure-diffusion	Pressure-Strain	Viscous-Diffusion	Dissipation rate
$\overline{u^2}$		0.0047	0.0086	0.0049	0.0009	0.011	0.00066	0.0073
		0.0068	0.015	0.0091	0.0014	0.019	0.00137	0.0108
$\overline{v^2}$		0.0021	0.0011	0.0011	0.0023	0.0076	0.00036	0.0073
		0.0011	0.0009	0.0009	0.0044	0.014	0.00074	0.0108
$\overline{w^2}$		0.0071	0.0029	0.0036	0.0008	0.0068	0.00022	0.0073
		0.0071	0.0049	0.0048	0.0008	0.0094	0.00045	0.0108
$\overline{uv}$		0.00132	0.0025	0.0016	0.0071	0.0089	0.00056	
		0.00144	0.0042	0.0022	0.0141	0.0162	0.00117	
$\overline{uw}$		0.0017	0.0047	0.0027	0.0005	0.0061	0.00067	
		0.0019	0.0077	0.0048	0.0005	0.0111	0.00014	
$\overline{vw}$		0.0014	0.0017	0.0011	0.0061	0.0077	0.00025	
		0.0010	0.0029	0.0010	0.0118	0.0140	0.00052	

Figure 1. Schematic view of the wing and the measurement locations, and description of the coordinate systems. $()_{FS}$, free-stream coordinates, $()_{TC}$, tunnel coordinates.
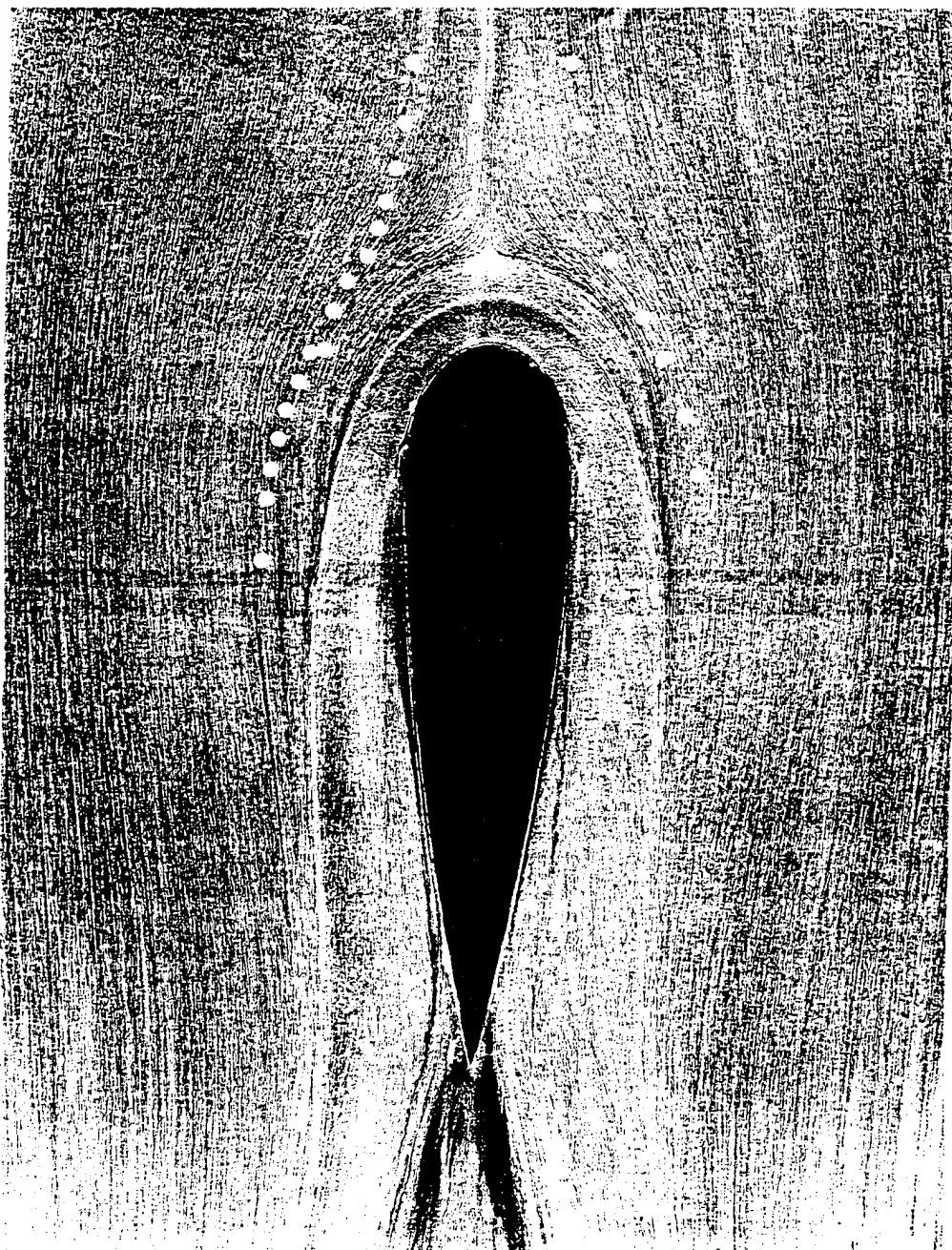
Figures

Figure 2. Oil-flow visualization picture obtained on the tunnel floor.

Velocity magnitude contours and secondary flow streamlines

m/sec

40.6
38.4
36.2
33.9
31.7
29.4
27.2
24.9
22.7
20.5
18.2
16.0
13.7
11.5
9.2
7.0
4.8
2.5
0.3
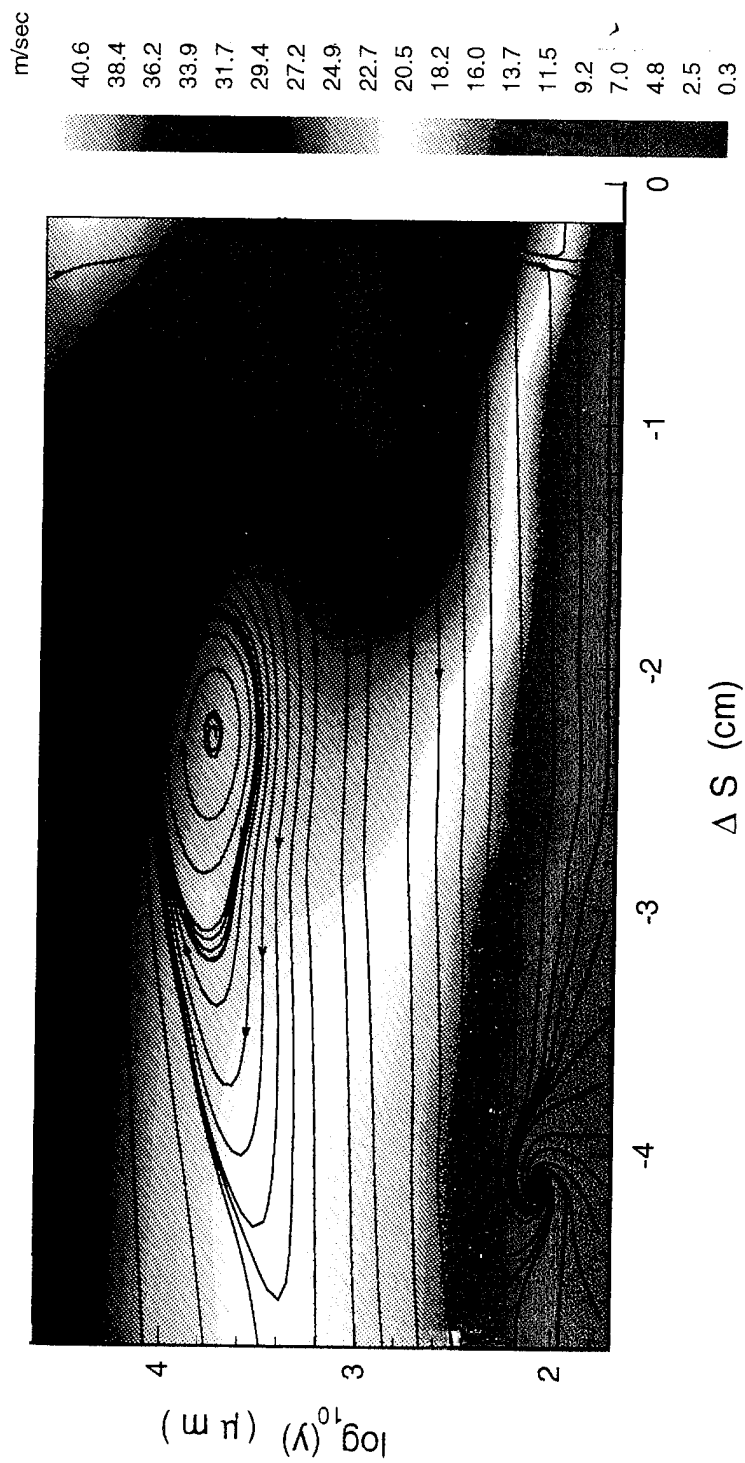
Figure 3. Velocity magnitude contours and secondary flow streamlines measured at stations along the 23° line.
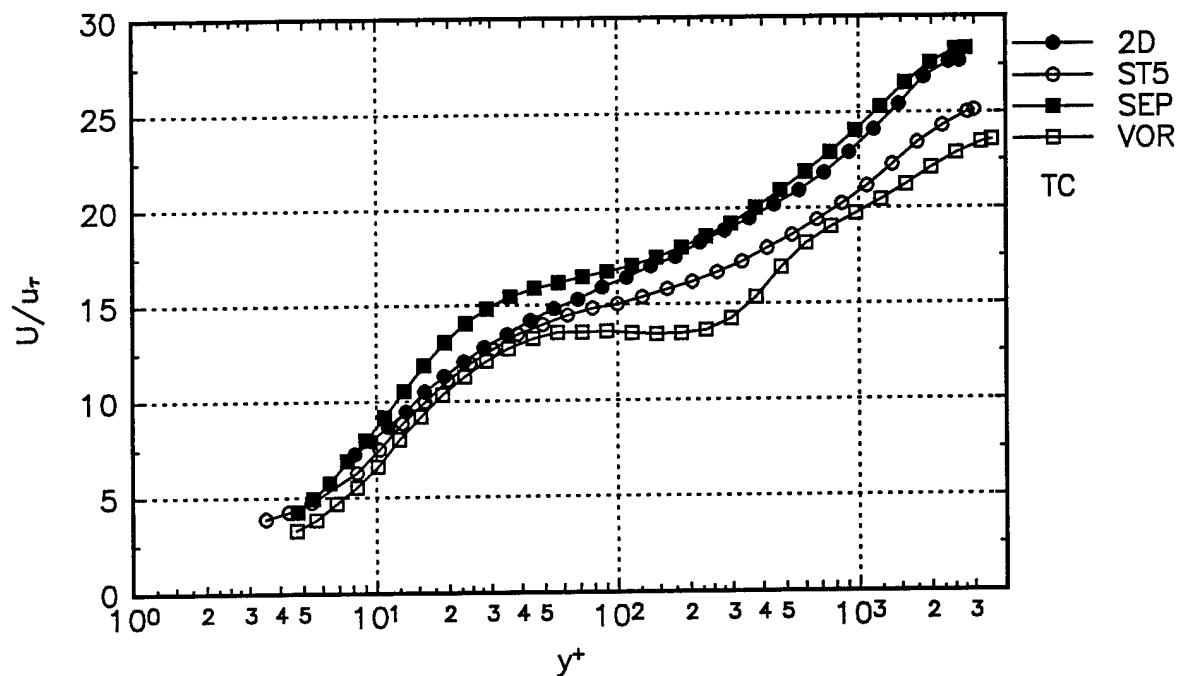
Figure 4. U/u_τ mean velocity at different stations in tunnel coordinates. ●, 2-D; O, Station 5, ■, Separation station; □, Vortex station.
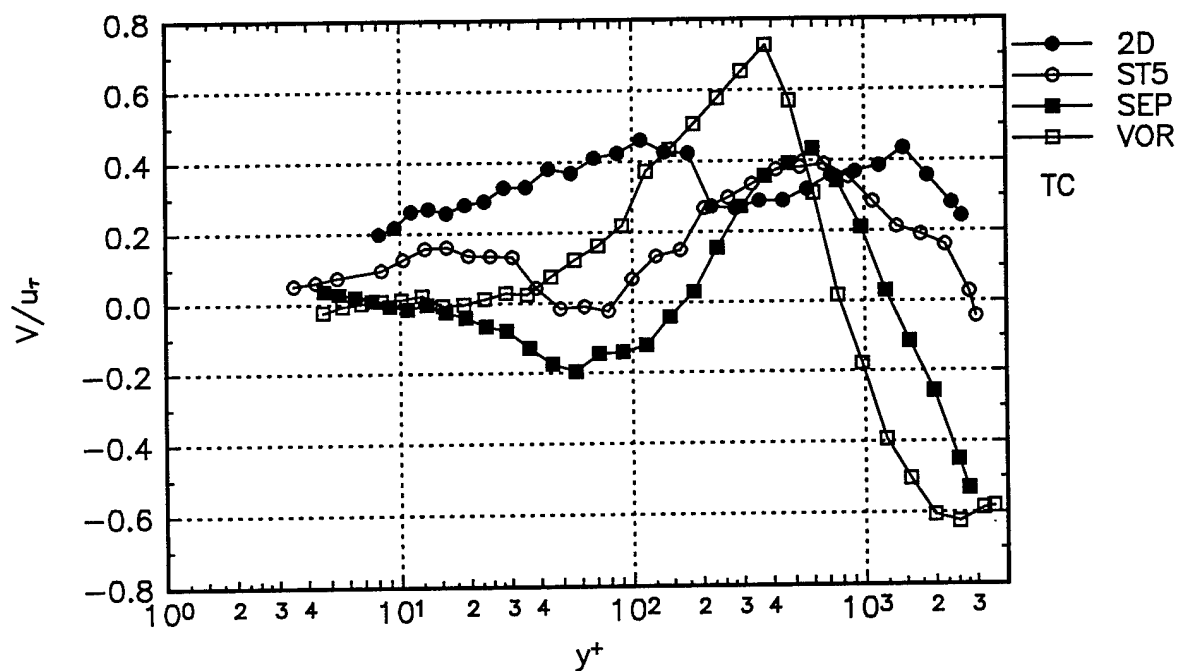
Figure 5. V/u_τ mean velocity at different stations in tunnel coordinates. ●, 2-D; O, Station 5, ■, Separation station; □, Vortex station.
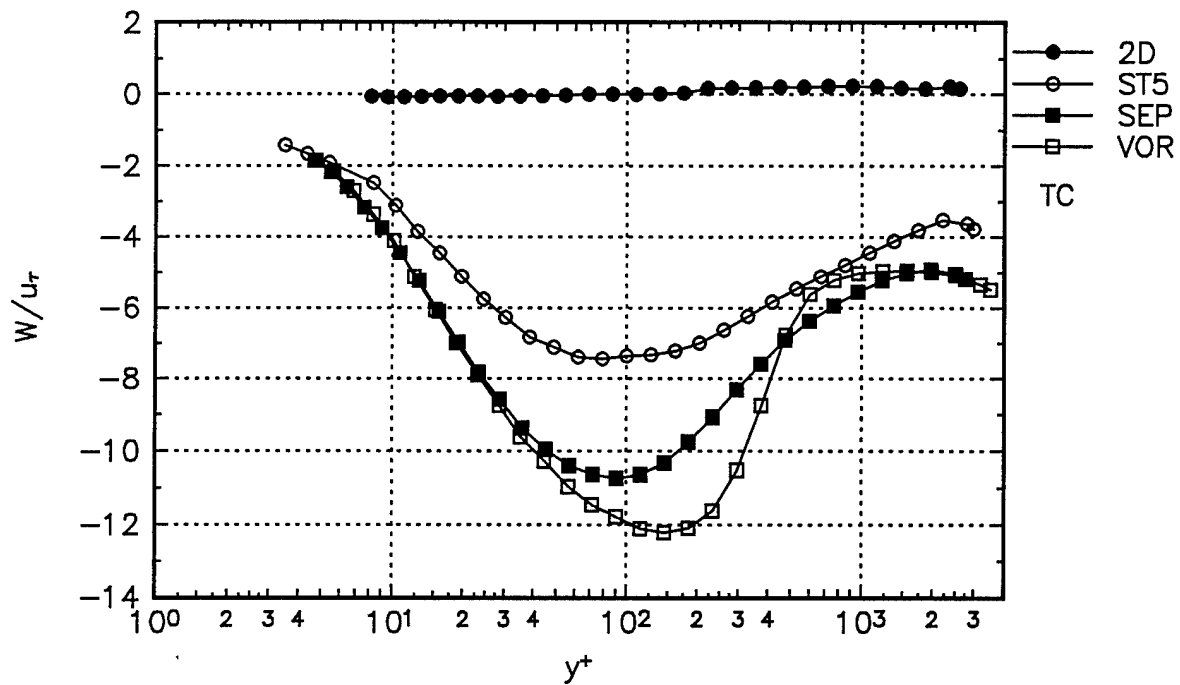
Figure 6. W/u_τ mean velocity at different stations in tunnel coordinates. ●, 2-D; ○, Station 5, ■, Separation station; □, Vortex station.
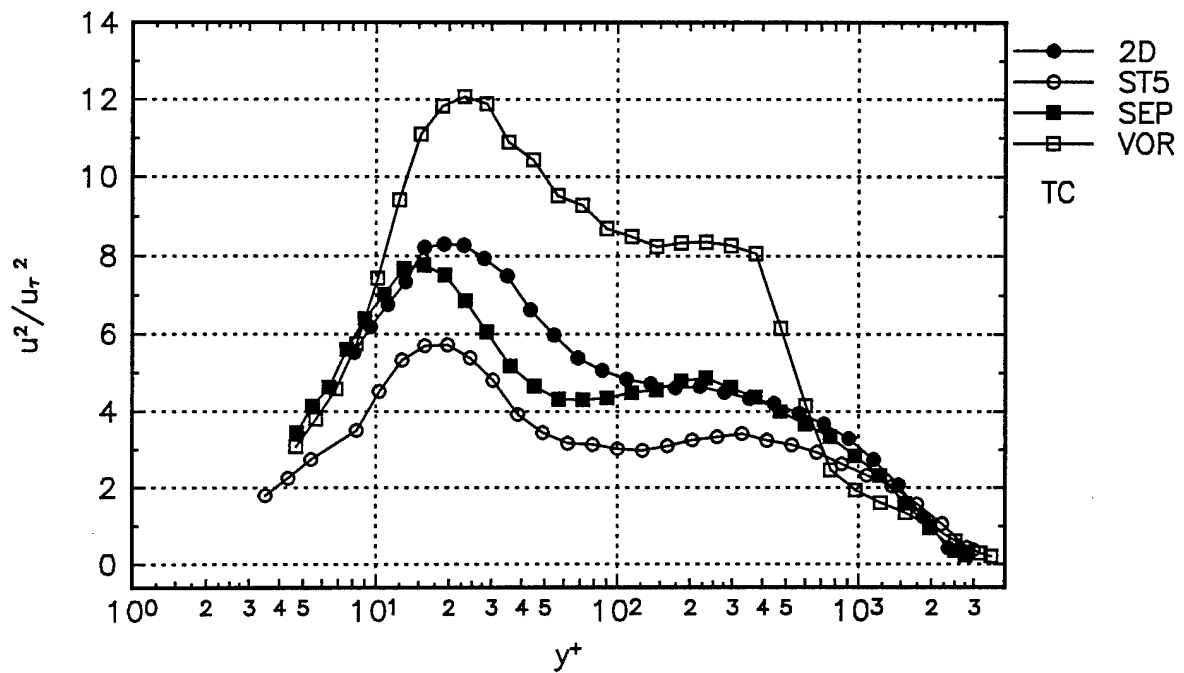
Figure 7. $\overline{u'^2}/u_\tau^2$ normal stress component at different stations in tunnel coordinates. ●, 2-D; ○, Station 5, ■, Separation station; □, Vortex station.
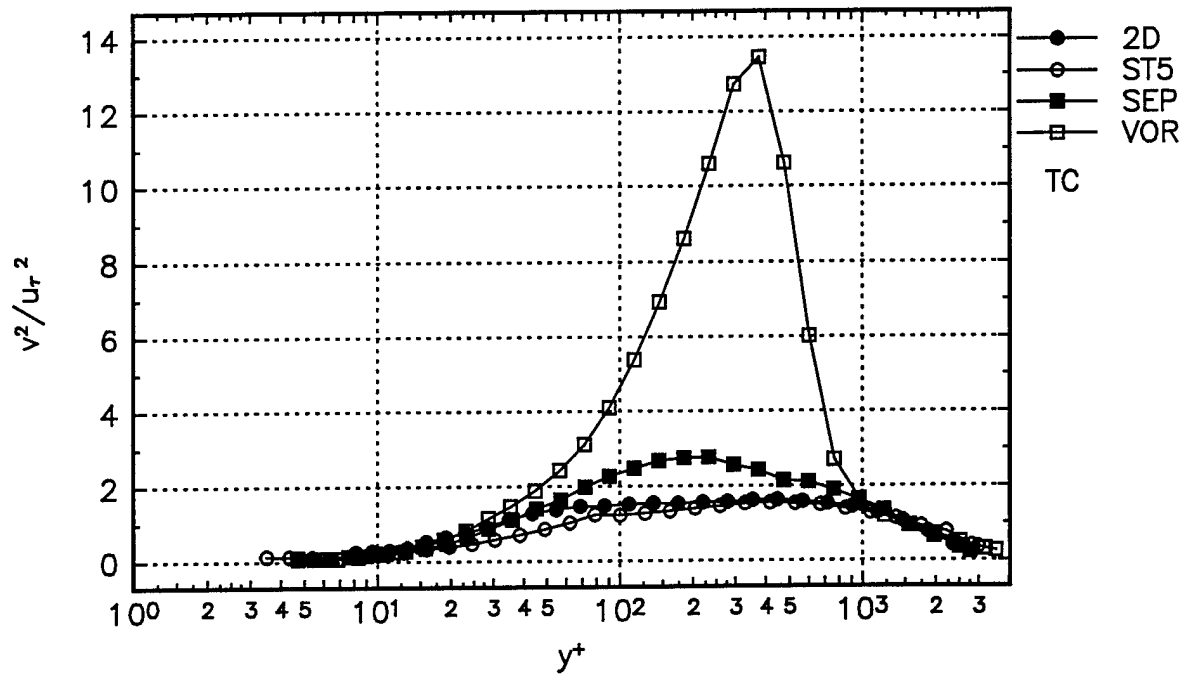
Figure 8. $\overline{v^2}/u_\tau^2$ normal stress component at different stations in tunnel coordinates. ●, 2-D; O, Station 5, ■, Separation station; □, Vortex station.
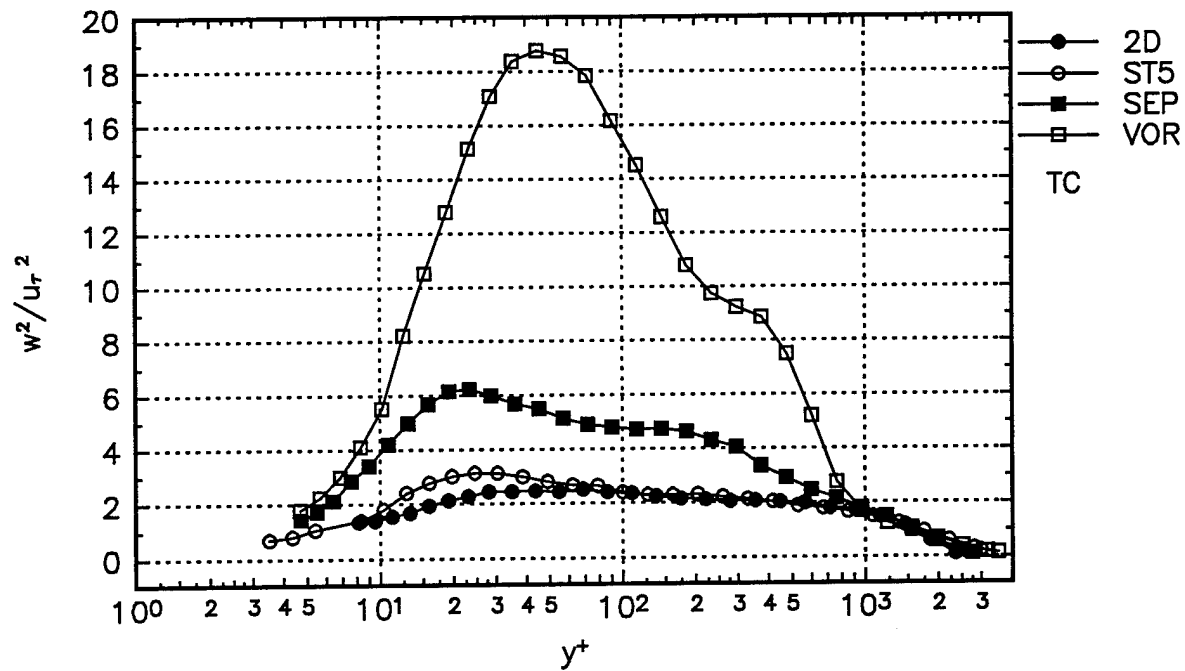
Figure 9. $\overline{w^2}/u_\tau^2$ normal stress component at different stations in tunnel coordinates. ●, 2-D; O, Station 5, ■, Separation station; □, Vortex station.
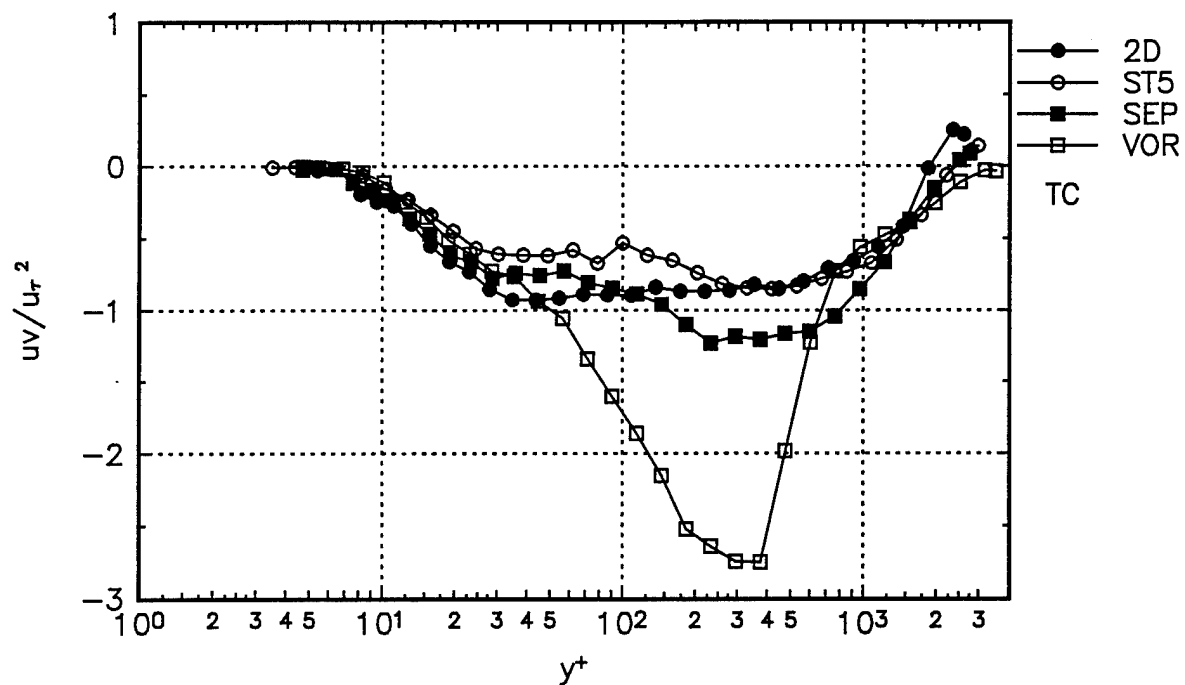
Figures

Figure 10. $\overline{uv}/u_\tau^2$ shear stress component at different stations in tunnel coordinates. ●, 2-D; O, Station 5, ■, Separation station; □, Vortex station.
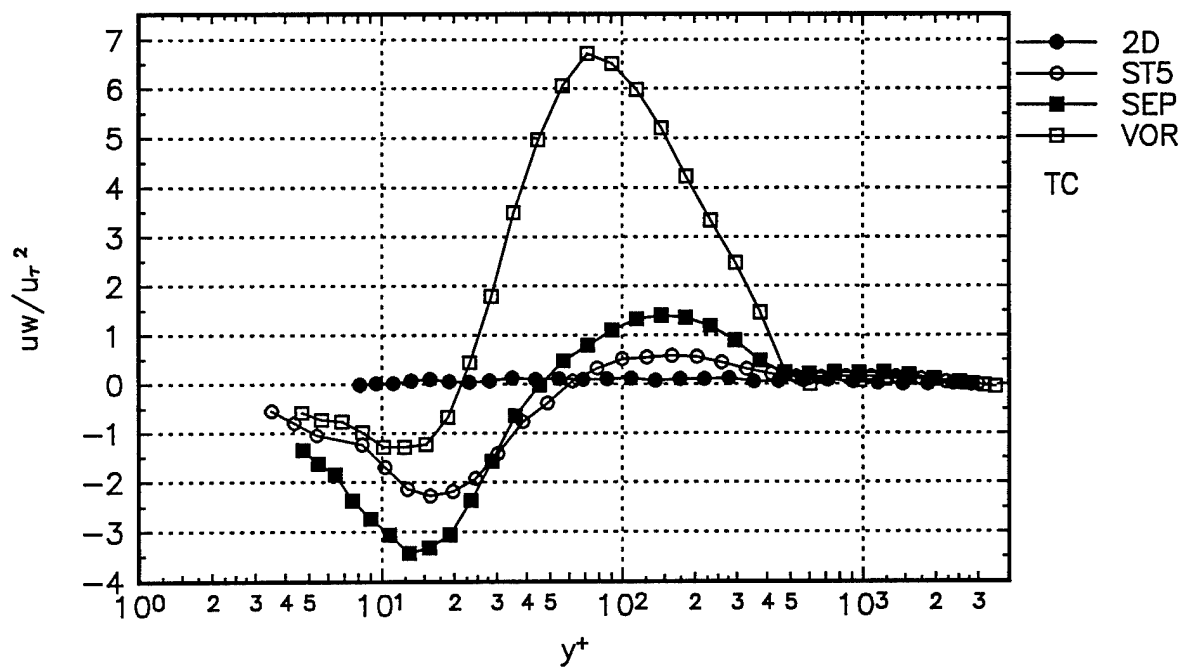
Figure 11. $\overline{uw}/u_\tau^2$ shear stress component at different stations in tunnel coordinates. ●, 2-D; O, Station 5, ■, Separation station; □, Vortex station.
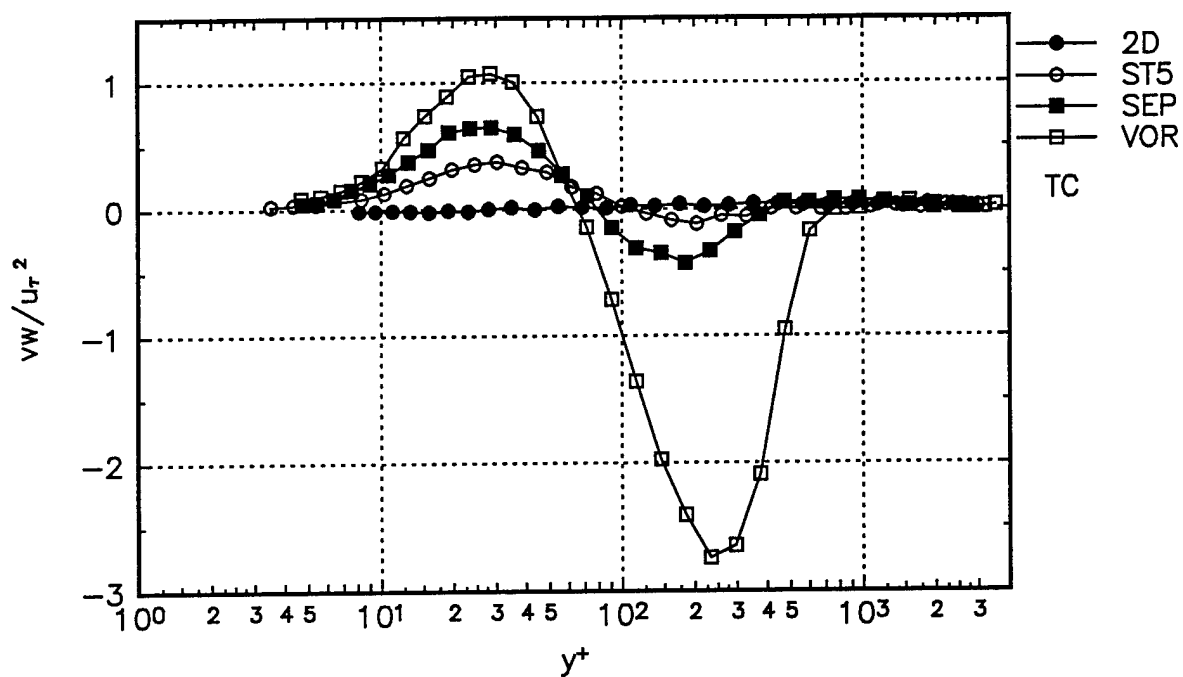
Figure 12. $\overline{vw}/u_\tau^2$ shear stress component at different stations in tunnel coordinates. ●, 2-D; O, Station 5, ■, Separation station; □, Vortex station.
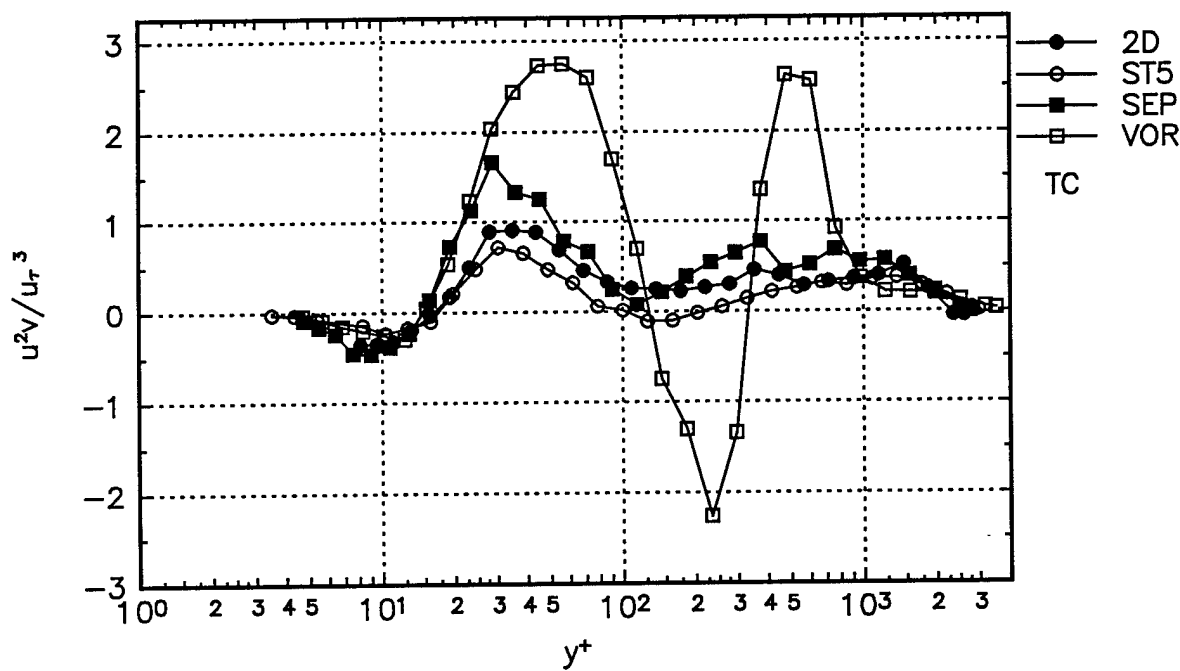
Figure 13. $\overline{u^2v}/u_\tau^3$ triple product at different stations in tunnel coordinates. ●, 2-D; O, Station 5, ■, Separation station; □, Vortex station.
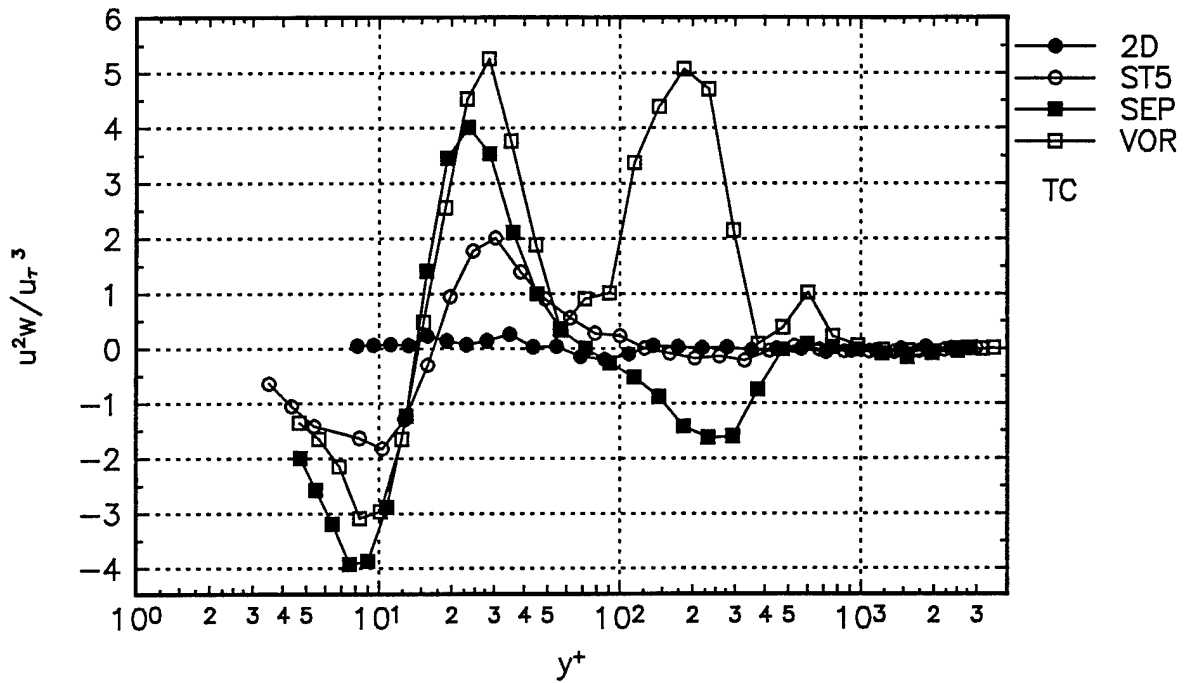
Figure 14. $\overline{u^2w}/u_\tau^3$ triple product at different stations in tunnel coordinates. ●, 2-D; ○, Station 5, ■, Separation station; □, Vortex station.
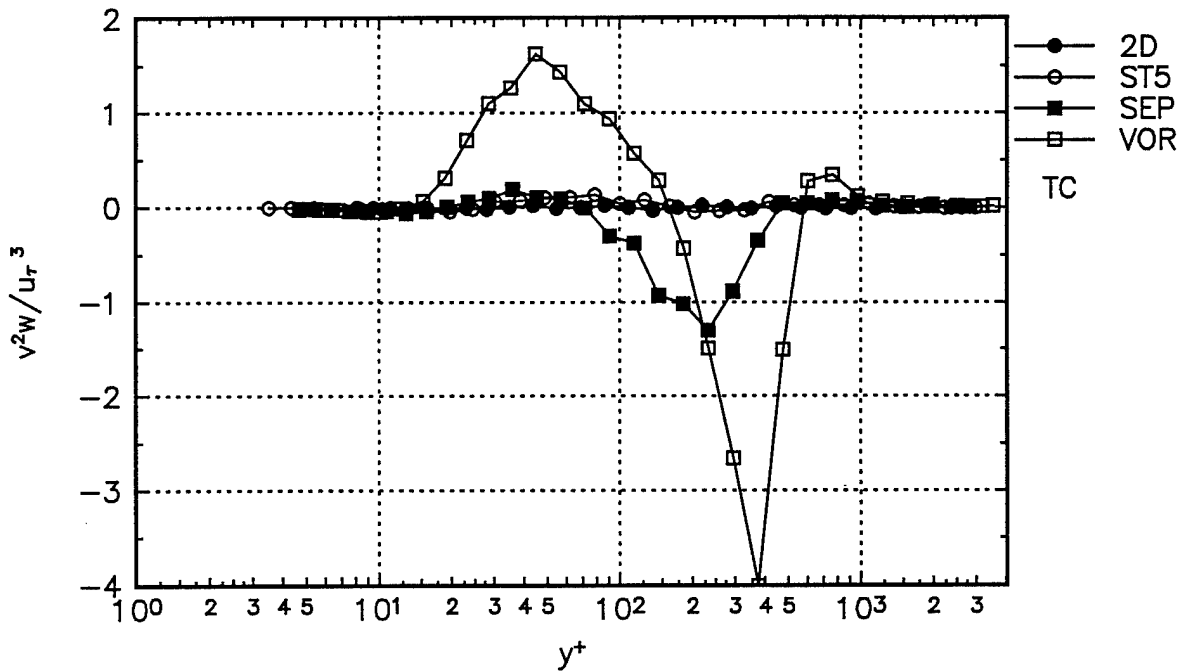
Figure 15. $\overline{v^2w}/u_\tau^3$ triple product at different stations in tunnel coordinates. ●, 2-D; ○, Station 5, ■, Separation station; □, Vortex station.
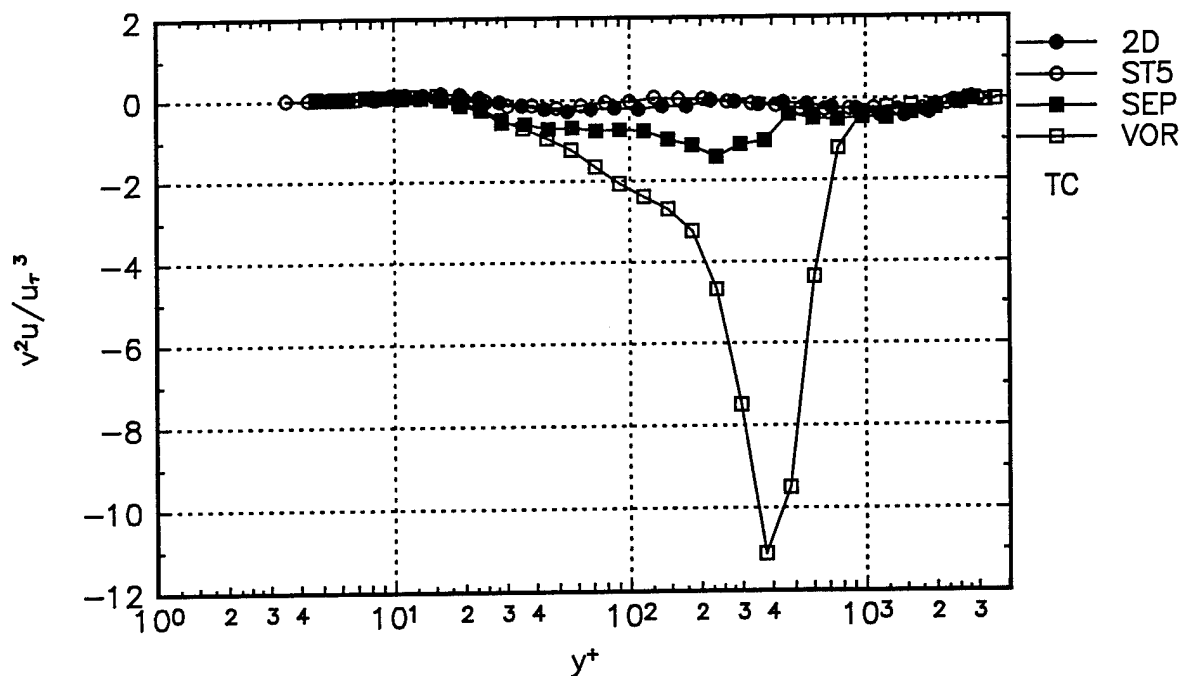
Figure 16. $\overline{v^2 u}/u_\tau^3$ triple product at different stations in tunnel coordinates. ●, 2-D; ○, Station 5, ■, Separation station; □, Vortex station.
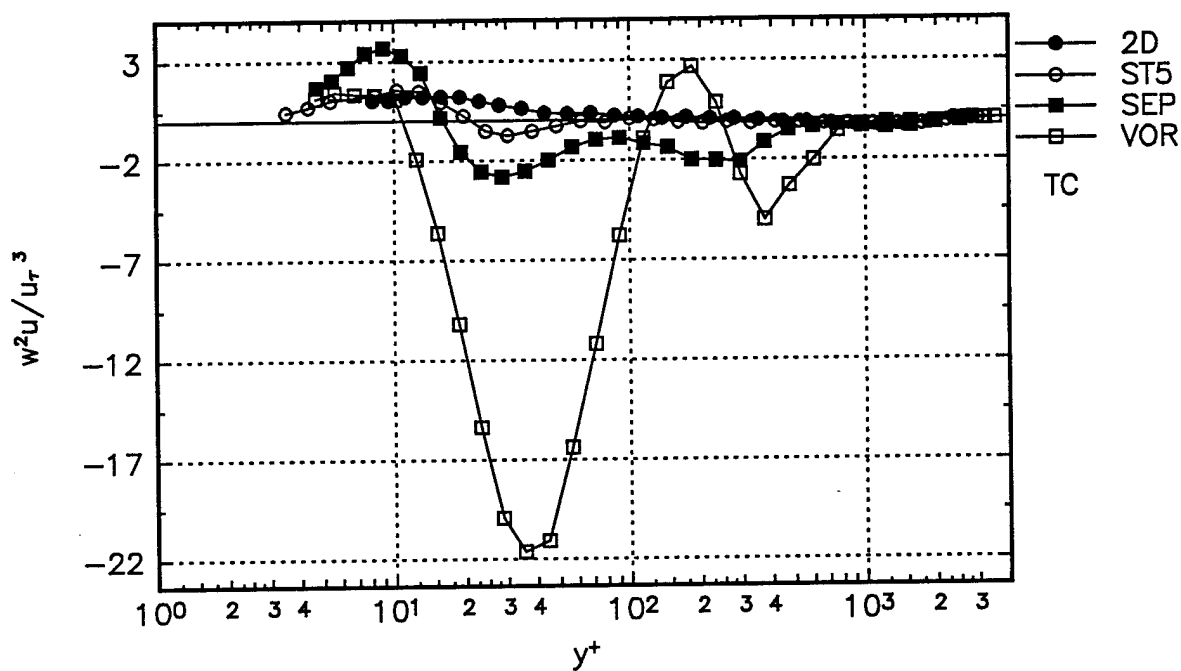
Figure 17. $\overline{w^2 u}/u_\tau^3$ triple product at different stations in tunnel coordinates. ●, 2-D; ○, Station 5, ■, Separation station; □, Vortex station.
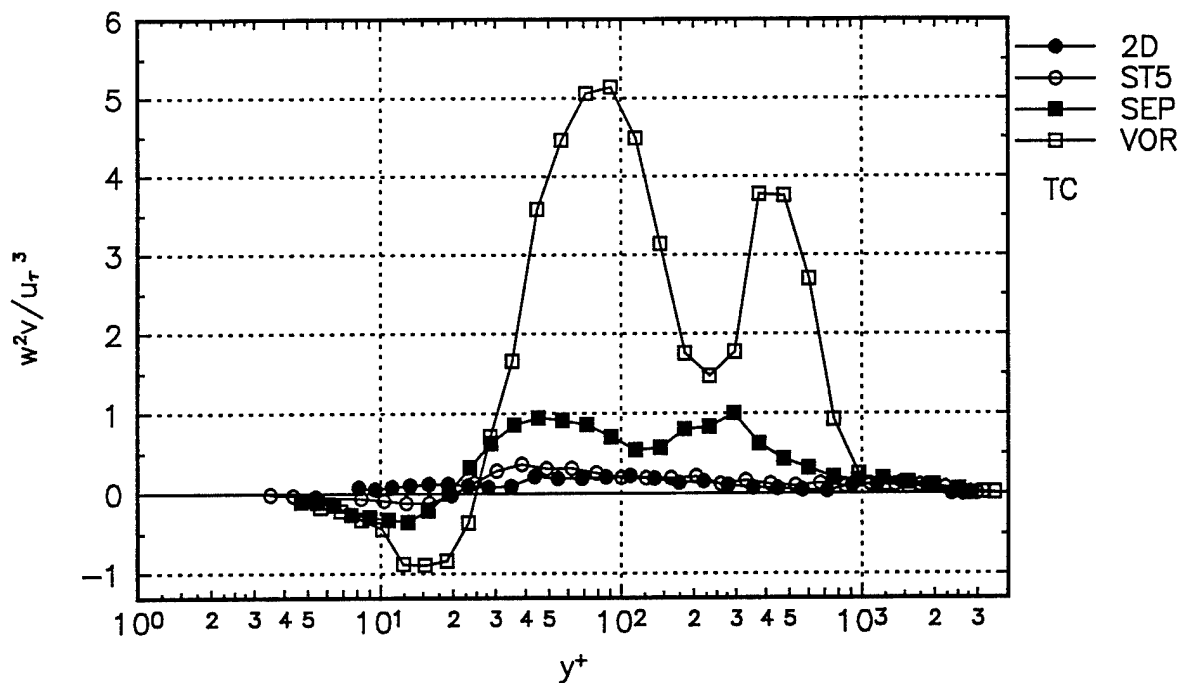
Figure 18. $\overline{w^2v}/u_\tau^3$ triple product at different stations in tunnel coordinates. ●, 2-D; ○, Station 5, ■, Separation station; □, Vortex station.
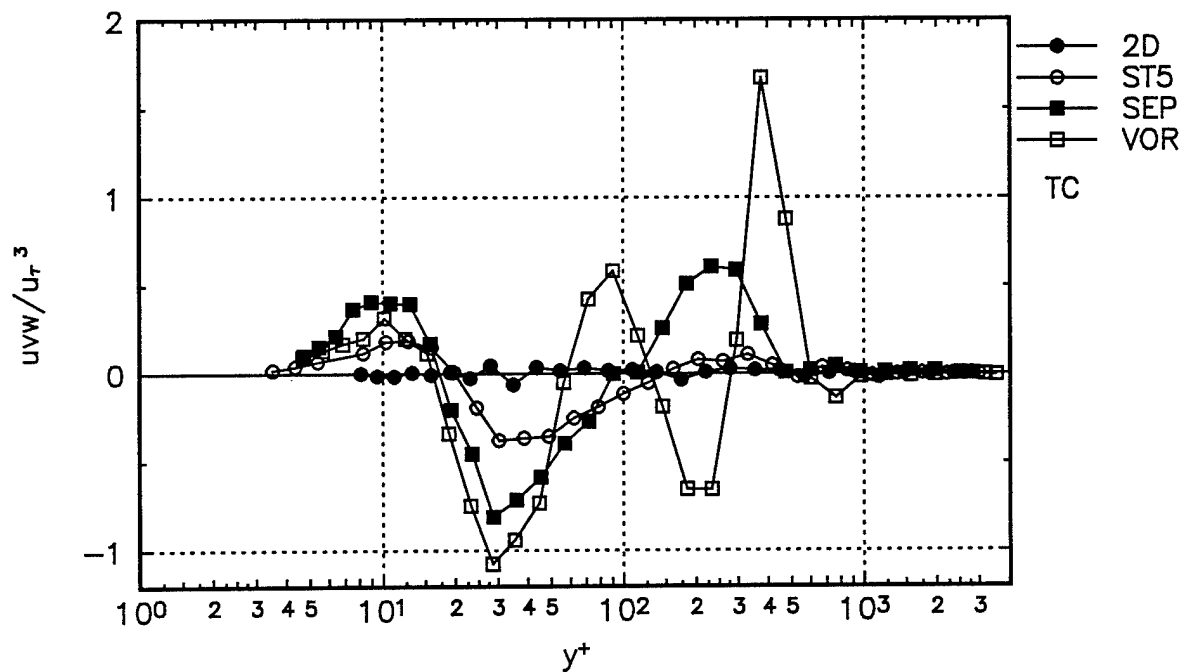
Figure 19. $\overline{uvw}/u_\tau^3$ triple product at different stations in tunnel coordinates. ●, 2-D; ○, Station 5, ■, Separation station; □, Vortex station.
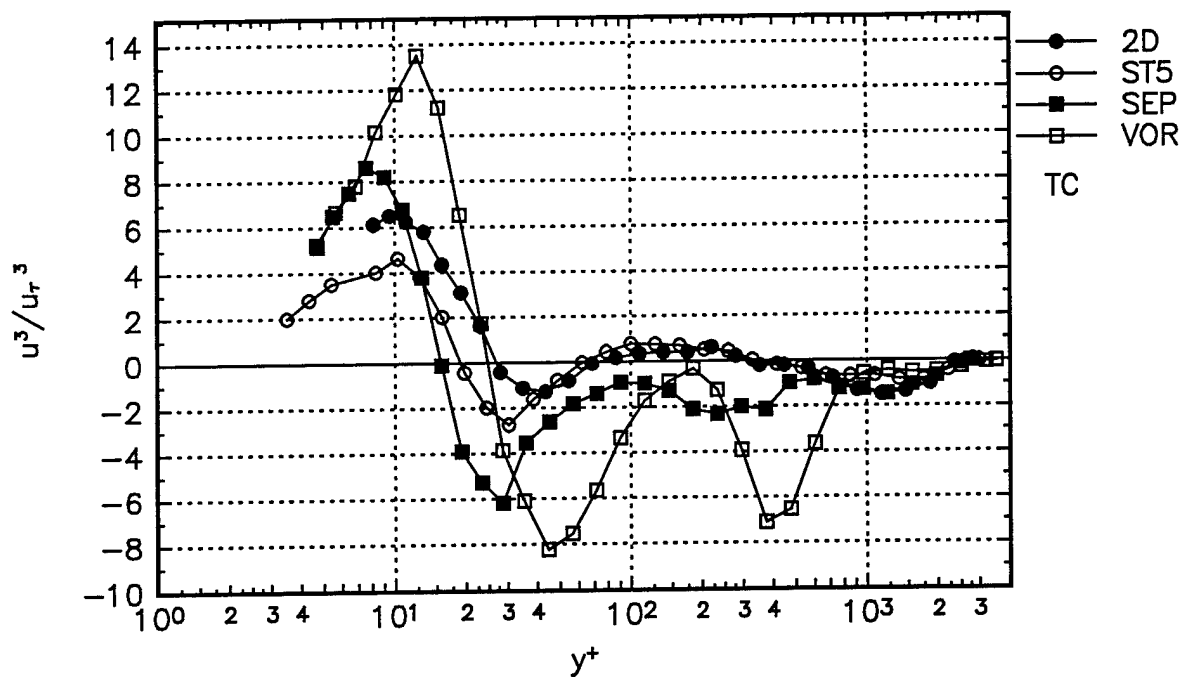
Figure 20. $\overline{u^3}/u_\tau^3$ triple product at different stations in tunnel coordinates. ●, 2-D; O, Station 5, ■, Separation station; □, Vortex station.
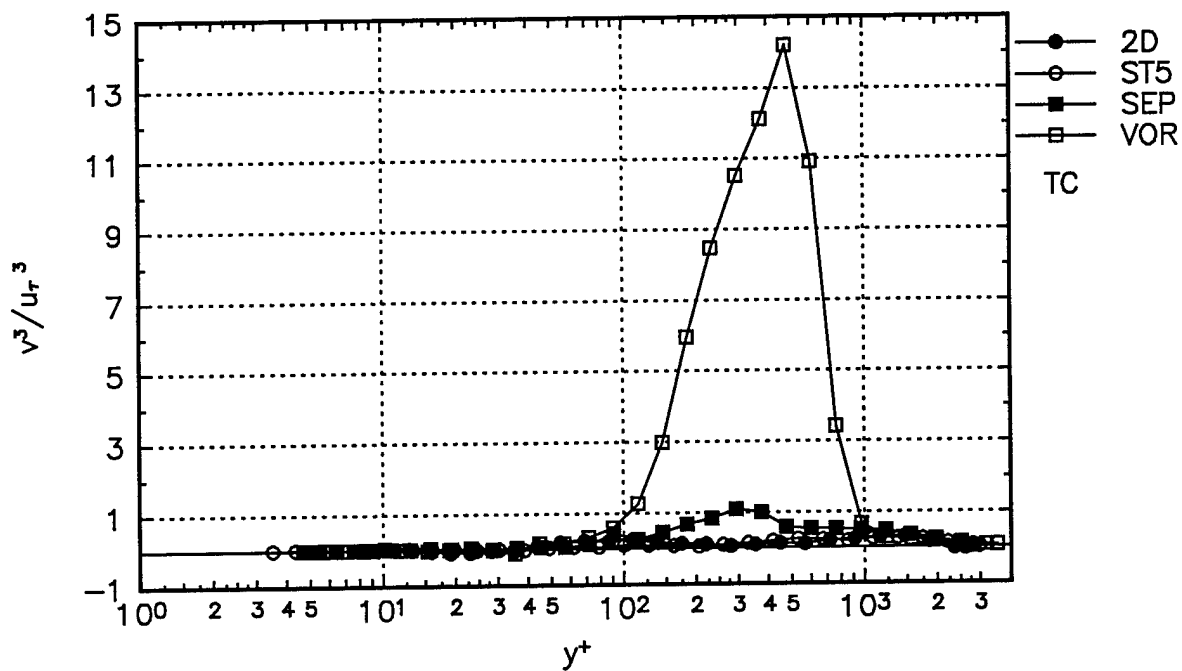
Figure 21. $\overline{v^3}/u_\tau^3$ triple product at different stations in tunnel coordinates. ●, 2-D; O, Station 5, ■, Separation station; □, Vortex station.
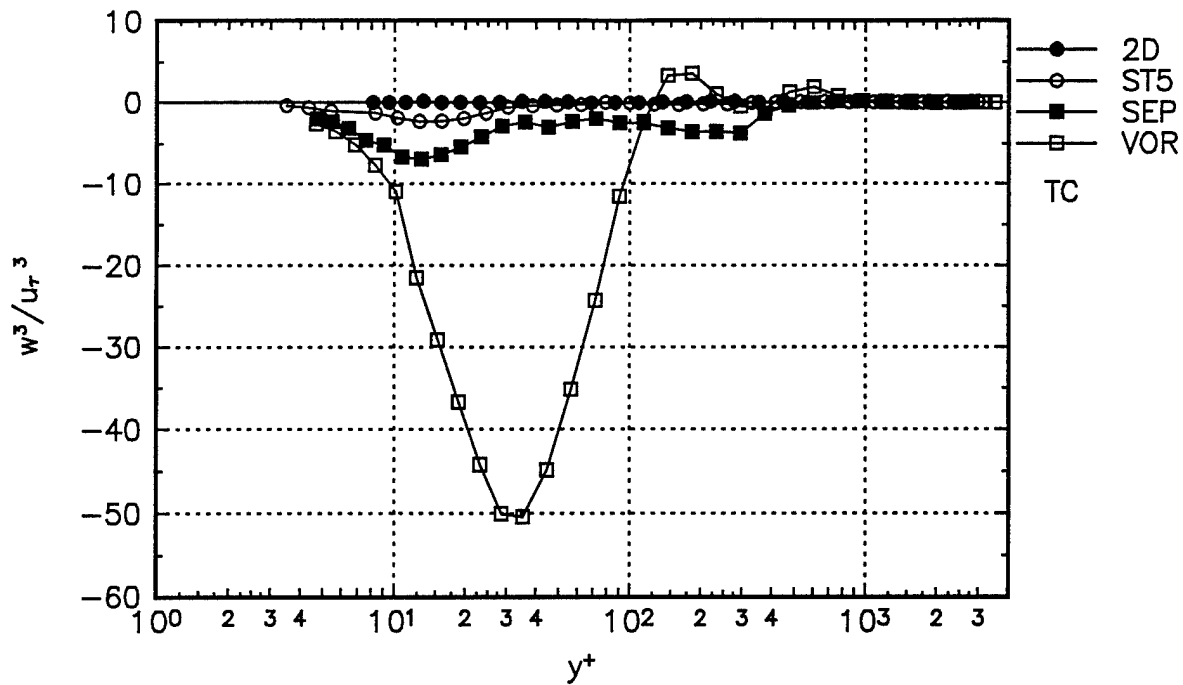
Figure 22. $\overline{w^3}/u_\tau^3$ triple product at different stations in tunnel coordinates. ●, 2-D; ○, Station 5, ■, Separation station; □, Vortex station.
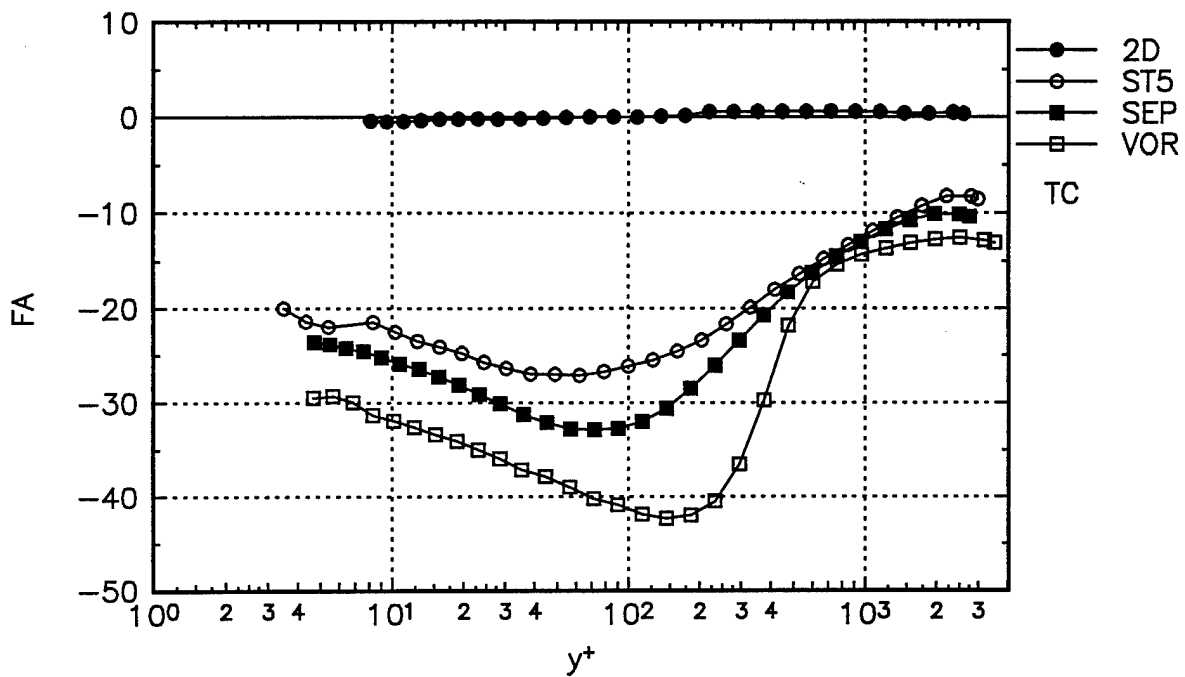
Figure 23. Flow angle (FA) calculated at different stations in tunnel coordinates. ●, 2-D; ○, Station 5, ■, Separation station; □, Vortex station.
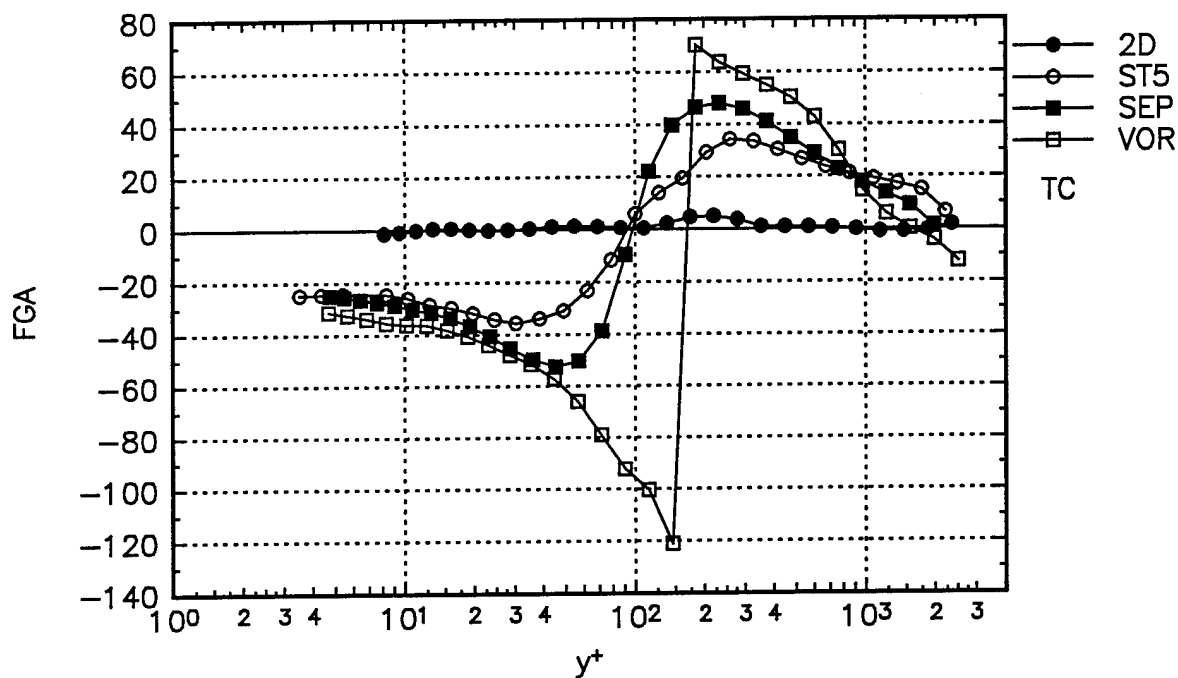
Figure 24. Flow gradient angle (FGA) calculated at different stations in tunnel coordinates. ●, 2-D; O, Station 5, ■, Separation station; □, Vortex station.
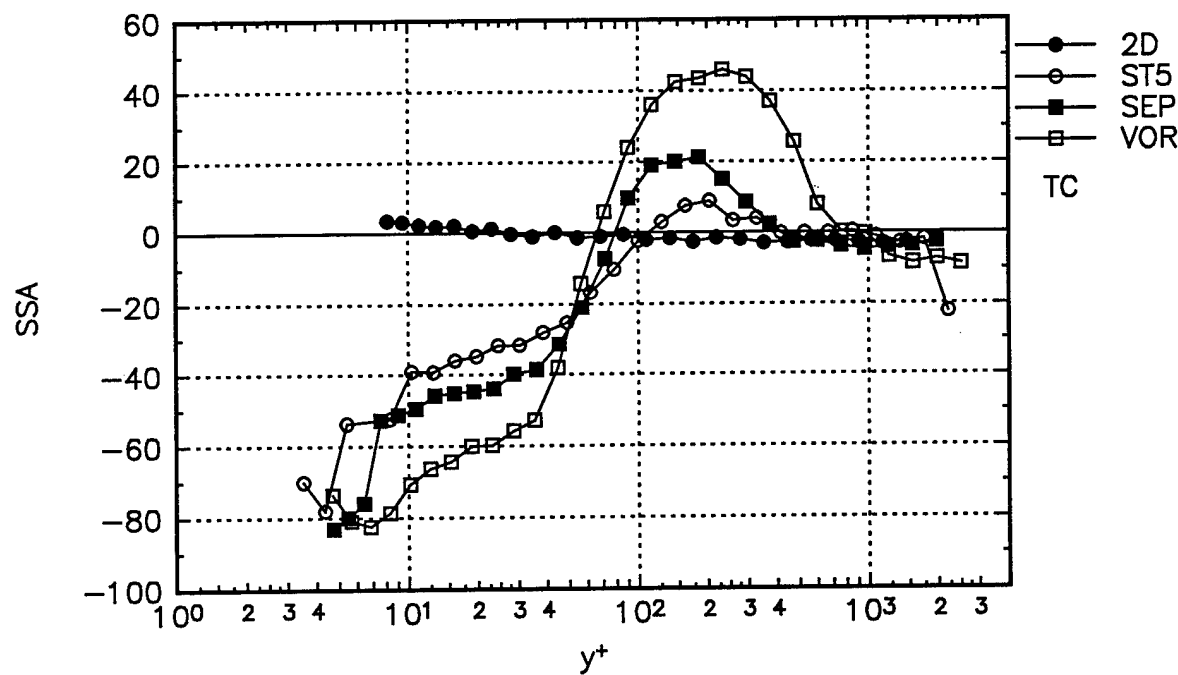
Figure 25. Shear stress angle (SSA) calculated at different stations in tunnel coordinates. ●, 2-D; O, Station 5, ■, Separation station; □, Vortex station.
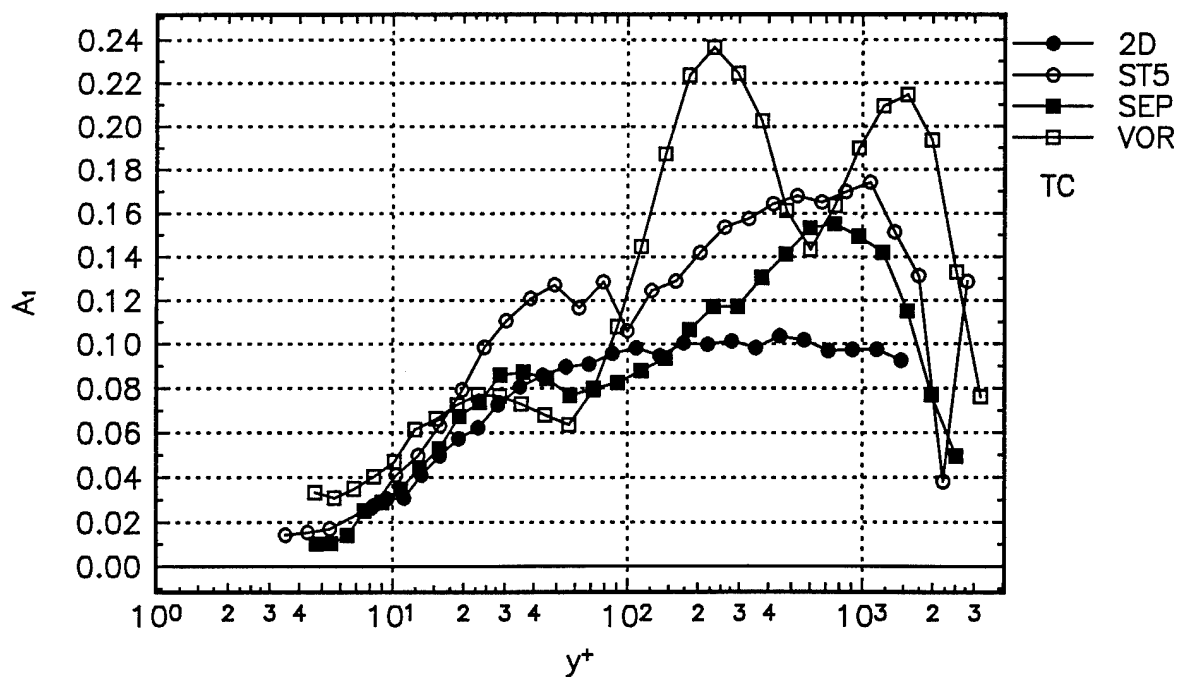
Figure 26. $A_1 = \dfrac{\sqrt{(\overline{uv})^2 + (\overline{vw})^2}}{\overline{u^2} + \overline{v^2} + \overline{w^2}}$, Townsend's structural parameter calculated at different stations. ●, 2-D; O, Station 5, ■, Separation station; □, Vortex station.
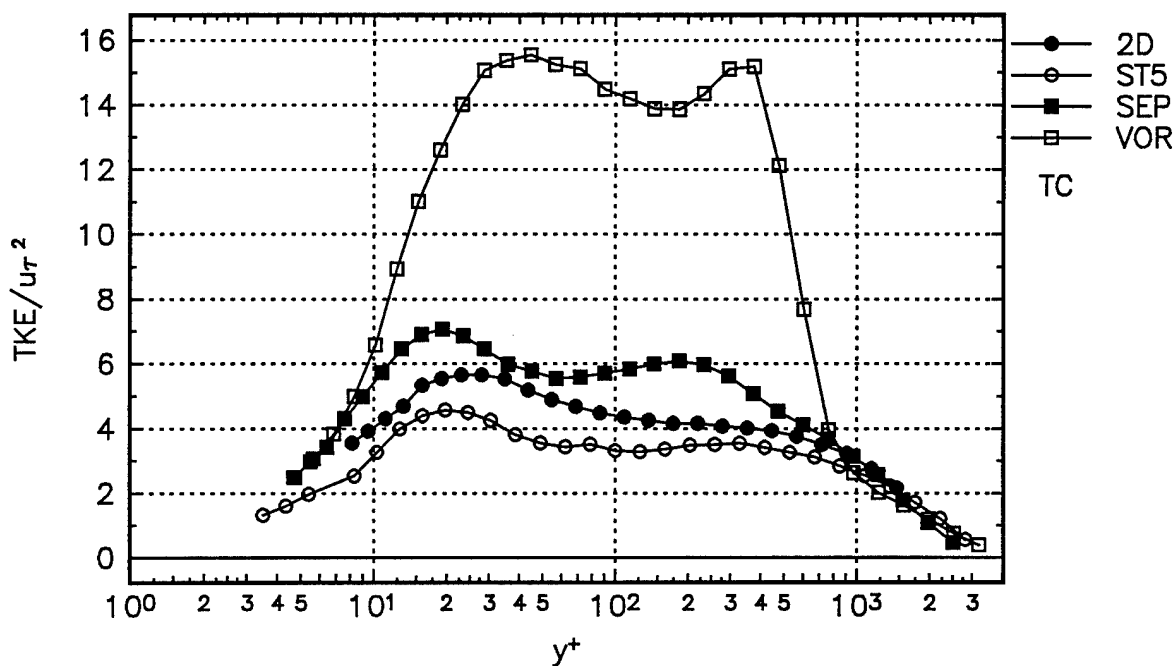
Figure 27. Turbulent kinetic energy profiles calculated at different stations. ●, 2-D; O, Station 5, ■, Separation station; □, Vortex station.
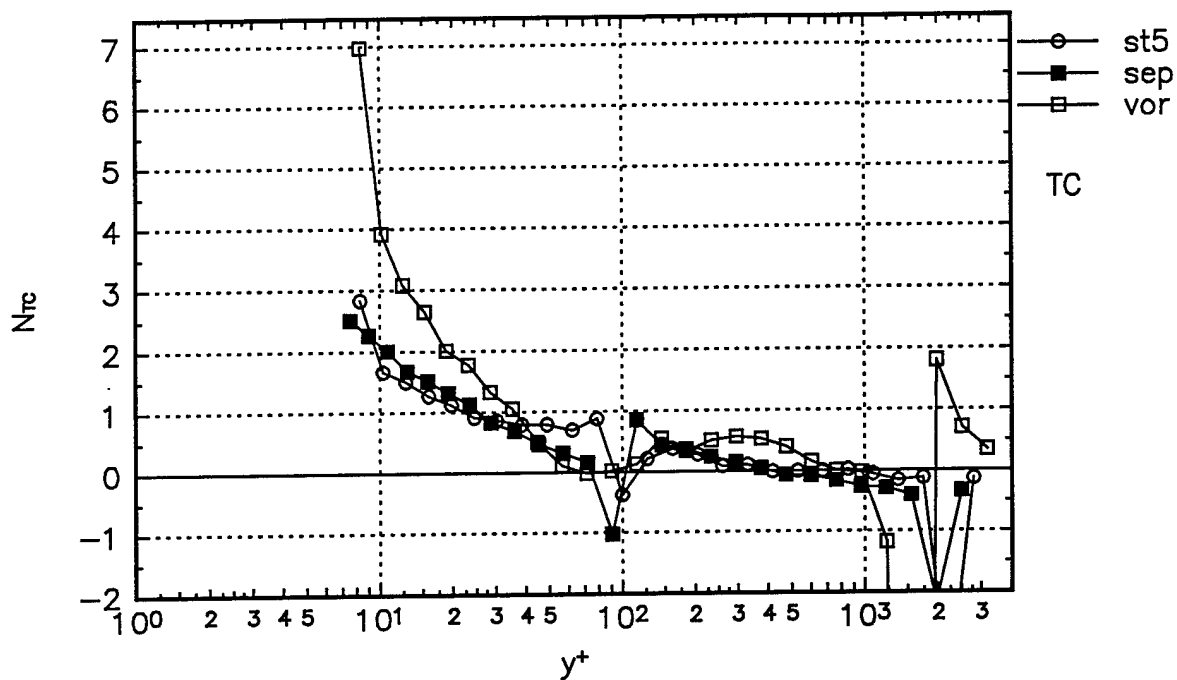
Figure 28. $N = \dfrac{(\overline{-vw})/(\partial w/\partial y)}{(\overline{-uv})/(\partial U/\partial y)}$, anisotropy parameter calculated at different stations in tunnel coordinates. ●, 2-D; O, Station 5, ■, Separation station; □, Vortex station.
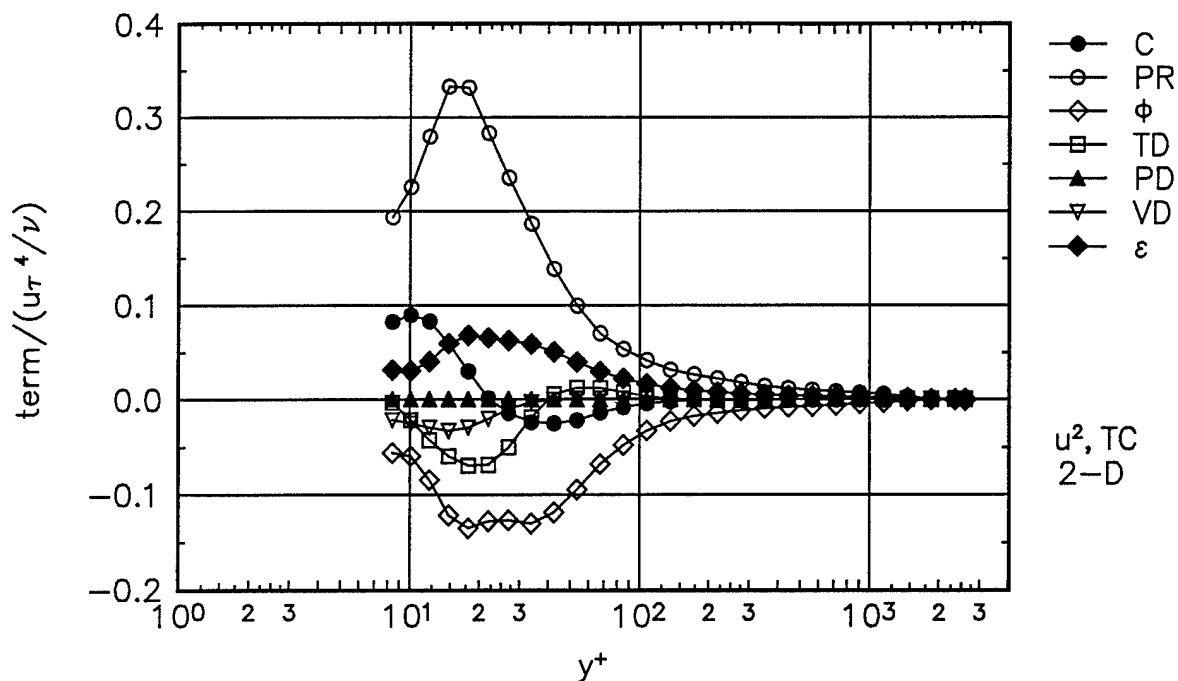
Figure 29. $\overline{u^2}$ normal stress transport budget with isotropic dissipation assumption at 2-D station in tunnel coordinates. ●, convection (C); O, production (PR); ◊, pressure-strain (φ); □, turbulent diffusion (TD); ▲, pressure diffusion (PD); ▽, viscous diffusion (VD); ♦, dissipation (ε).
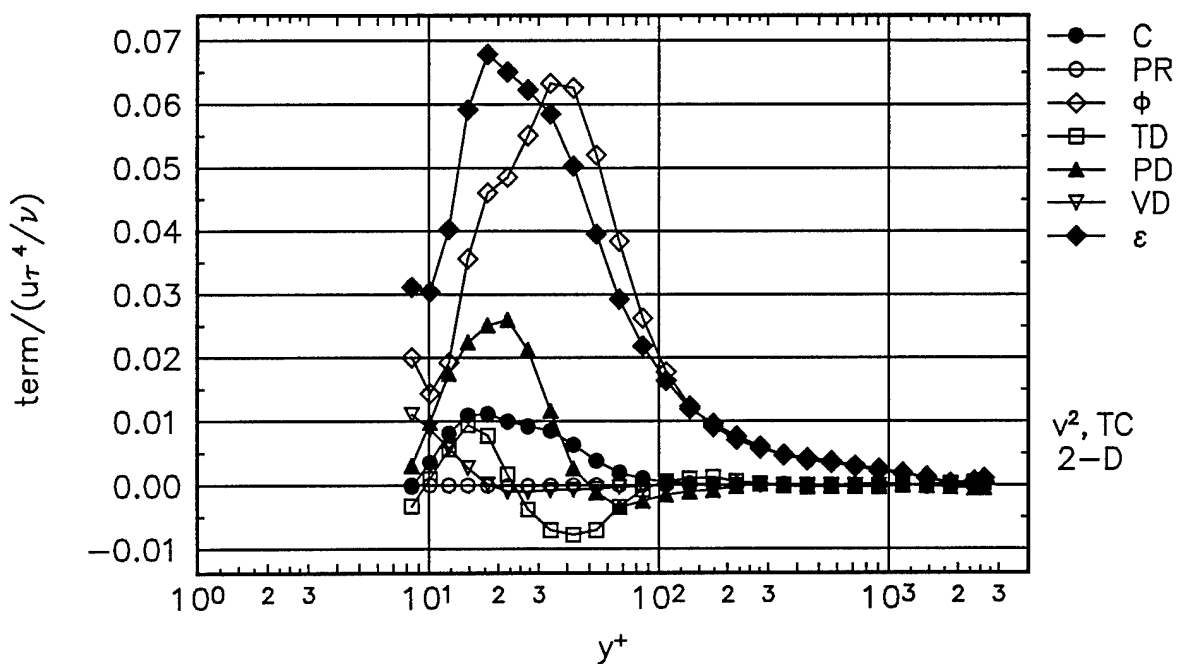
Figure 30. $\overline{v^2}$ normal stress transport budget with isotropic dissipation assumption at 2-D station in tunnel coordinates. ●, convection (C); O, production (PR); ◊, pressure-strain (φ); □, turbulent diffusion (TD); ▲, pressure diffusion (PD); ▽, viscous diffusion (VD); ♦, dissipation (ε).
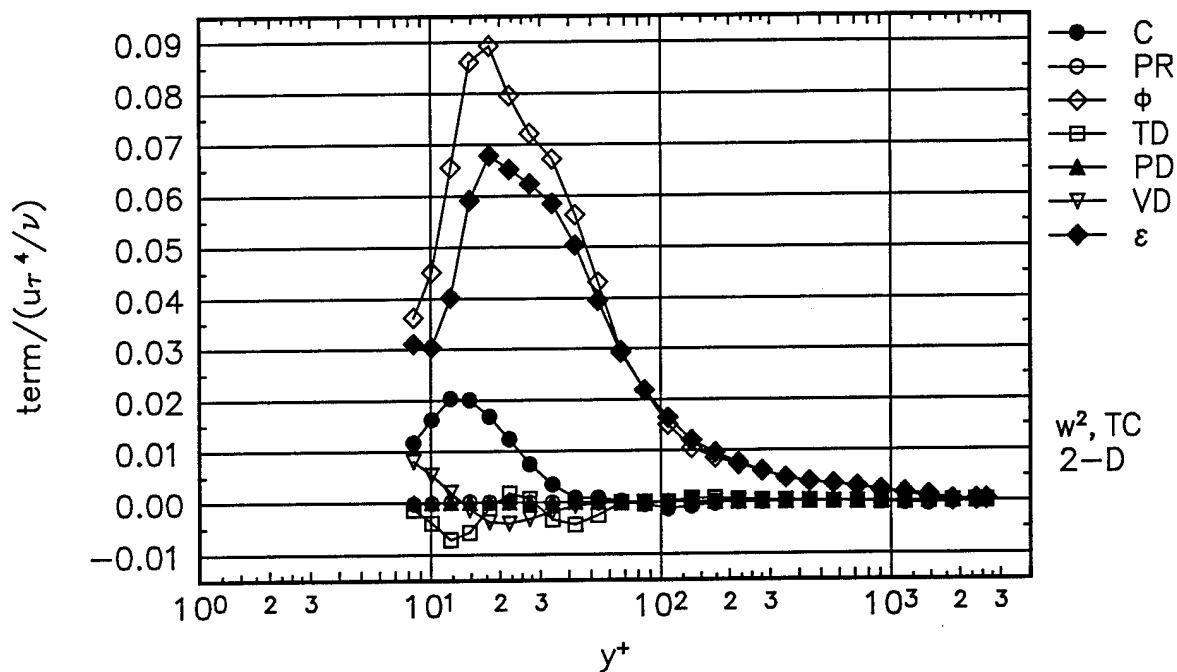
Figure 31. $\overline{w^2}$ normal stress transport budget with isotropic dissipation assumption at 2-D station in tunnel coordinates. ●, convection (C); O, production (PR); ◊, pressure-strain (φ); □, turbulent diffusion (TD); ▲, pressure diffusion (PD); ▽, viscous diffusion (VD); ◆, dissipation (ε).
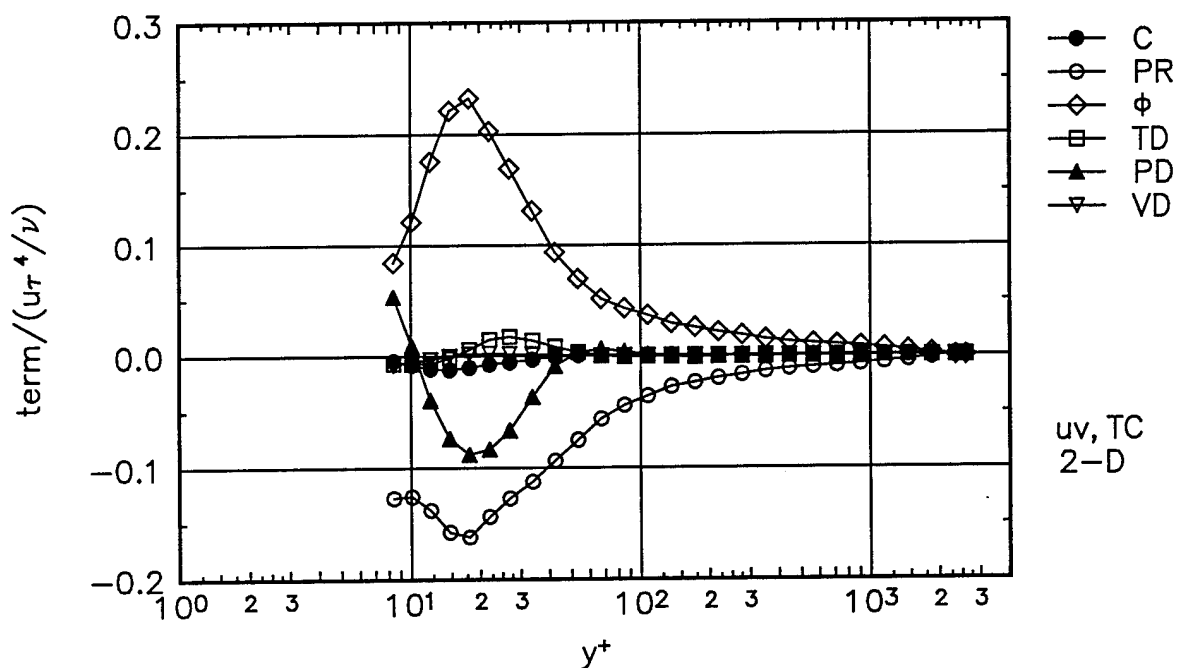
Figure 32. $\overline{uv}$ shear stress transport budget at 2-D station in tunnel coordinates. ●, convection (C); O, production (PR); ◊, pressure-strain (φ); □, turbulent diffusion (TD); ▲, pressure diffusion (PD); ▽, viscous diffusion (VD). Dissipation is assumed zero.
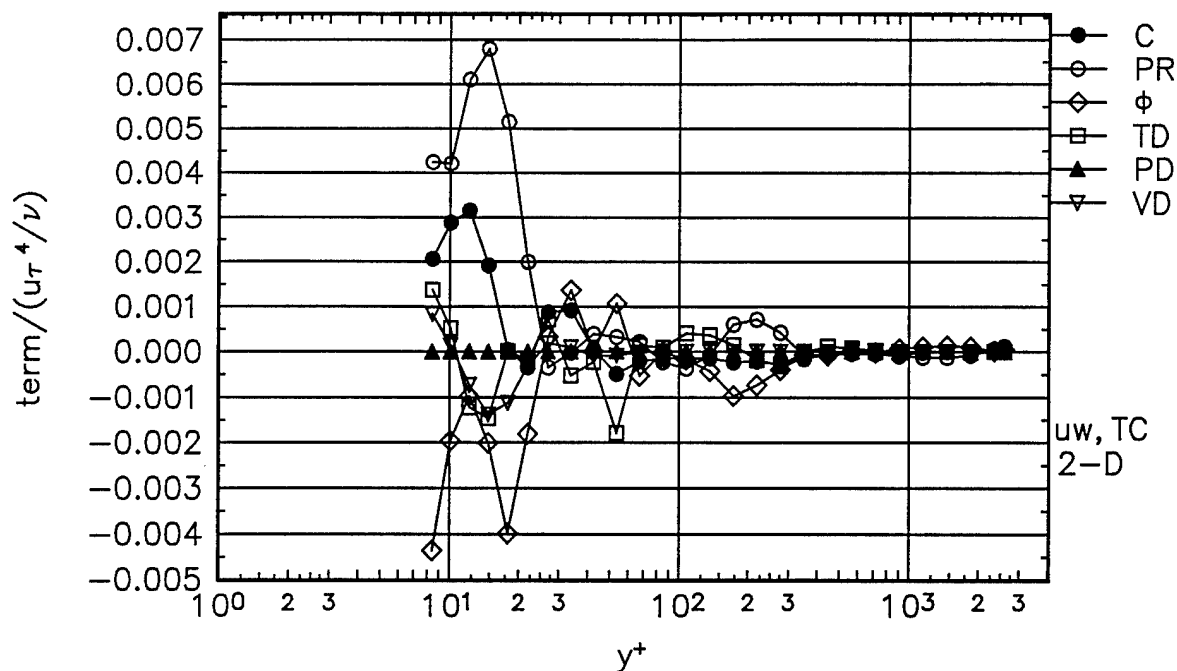
Figure 33. $\overline{uw}$ shear stress transport budget at 2-D station in tunnel coordinates. ●, convection (C); ○, production (PR); ◊, pressure-strain (φ); □, turbulent diffusion (TD); ▲, pressure diffusion (PD); ▽, viscous diffusion (VD). Dissipation is assumed zero.
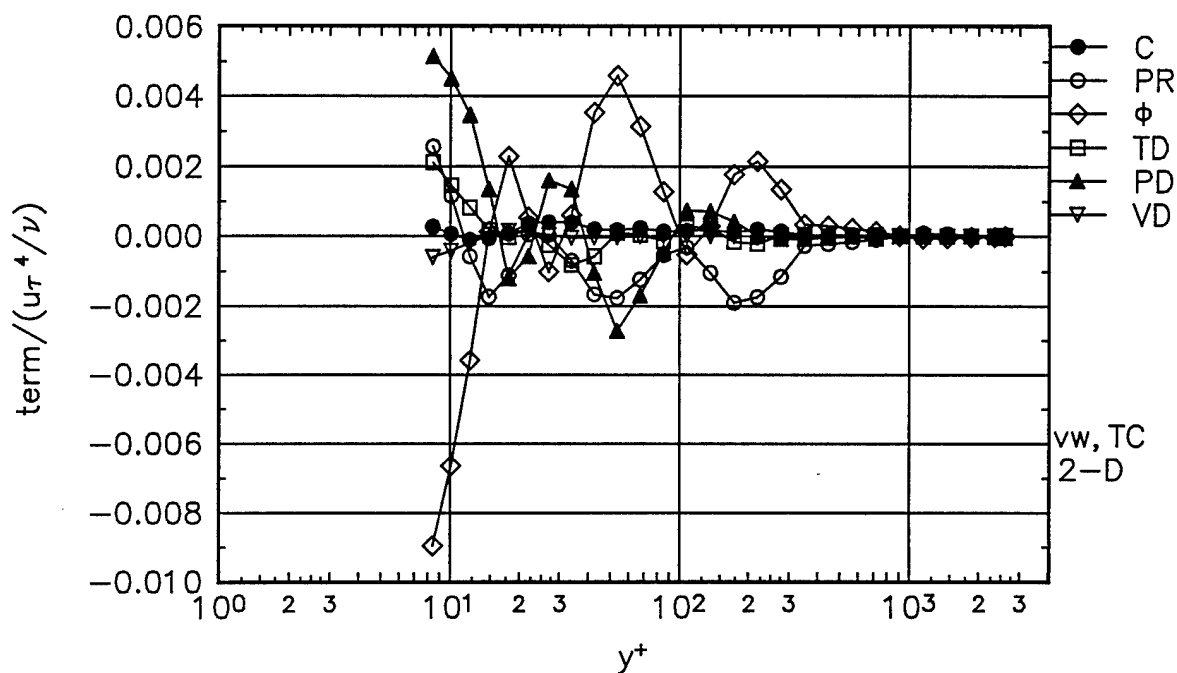
Figure 34. $\overline{vw}$ shear stress transport budget at 2-D station in tunnel coordinates. ●, convection (C); ○, production (PR); ◊, pressure-strain (φ); □, turbulent diffusion (TD); ▲, pressure diffusion (PD); ▽, viscous diffusion (VD). Dissipation is assumed zero.
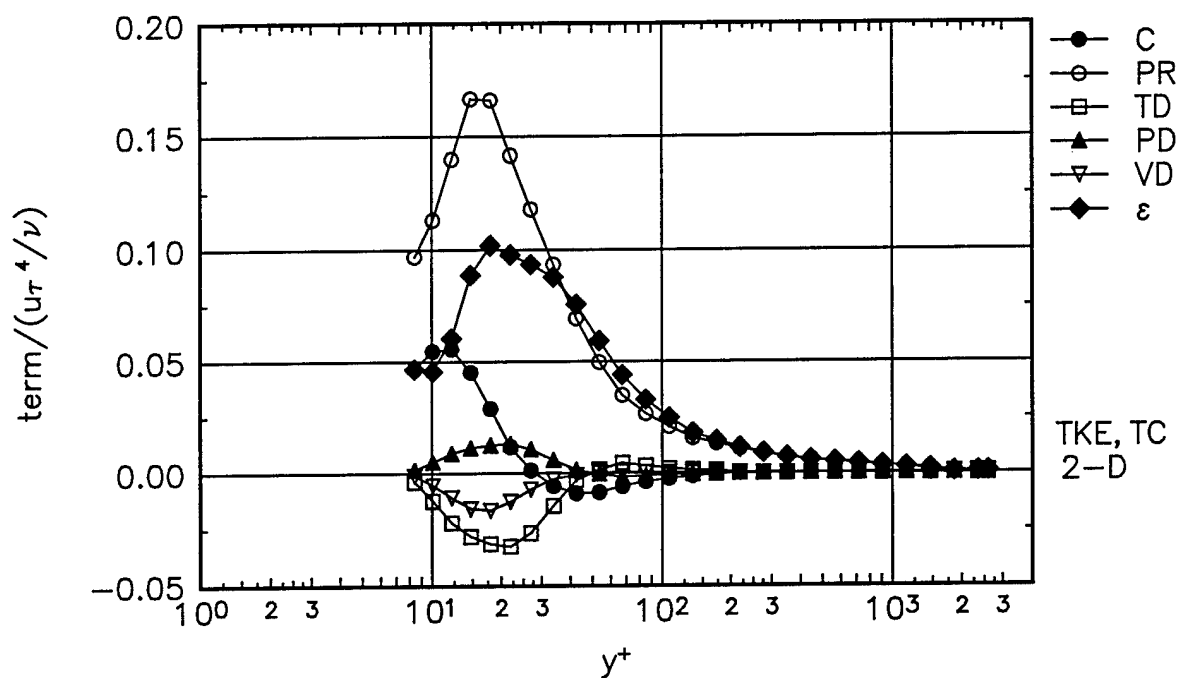
Figure 35. Turbulent kinetic energy transport budget at 2-D station in tunnel coordinates. ●, convection (C); O, production (PR); □, turbulent diffusion (TD); ▲, pressure diffusion (PD); ▽, viscous diffusion (VD); ◆, dissipation (ε). Pressure-strain term is zero by definition.
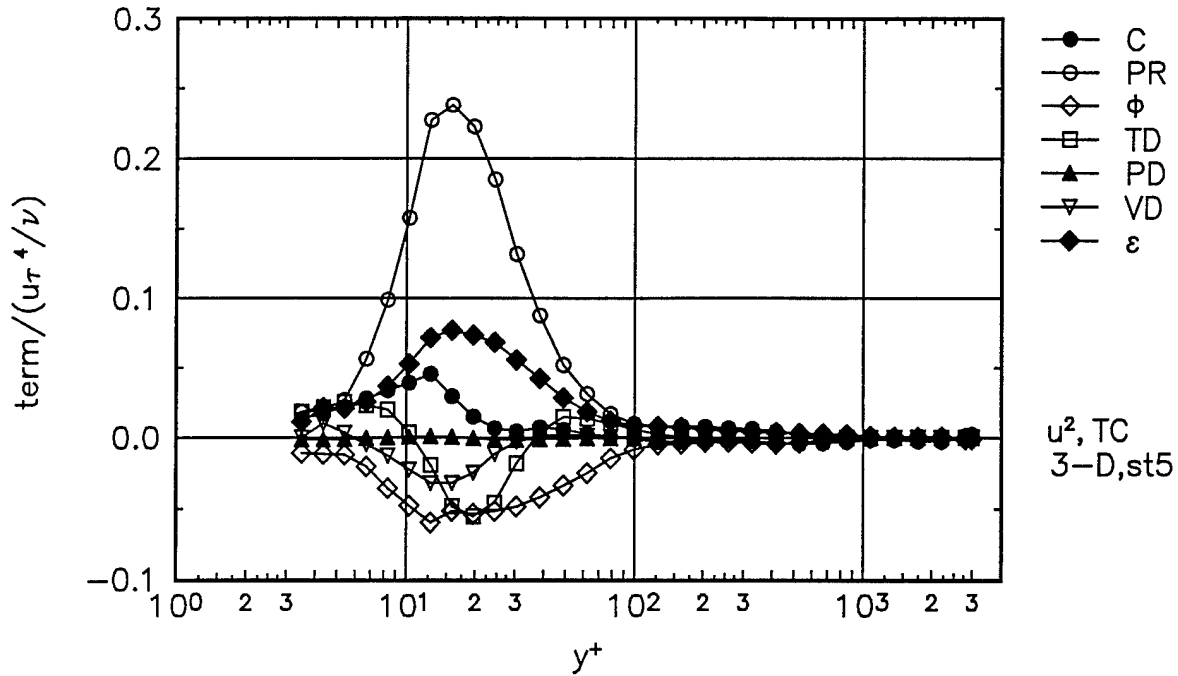
Figure 36. $\overline{u^2}$ normal stress transport budget with isotropic dissipation assumption at Station 5 in tunnel coordinates. ●, convection (C); O, production (PR); ◊, pressure-strain (φ); □, turbulent diffusion (TD); ▲, pressure diffusion (PD); ▽, viscous diffusion (VD); ♦, dissipation (ε).
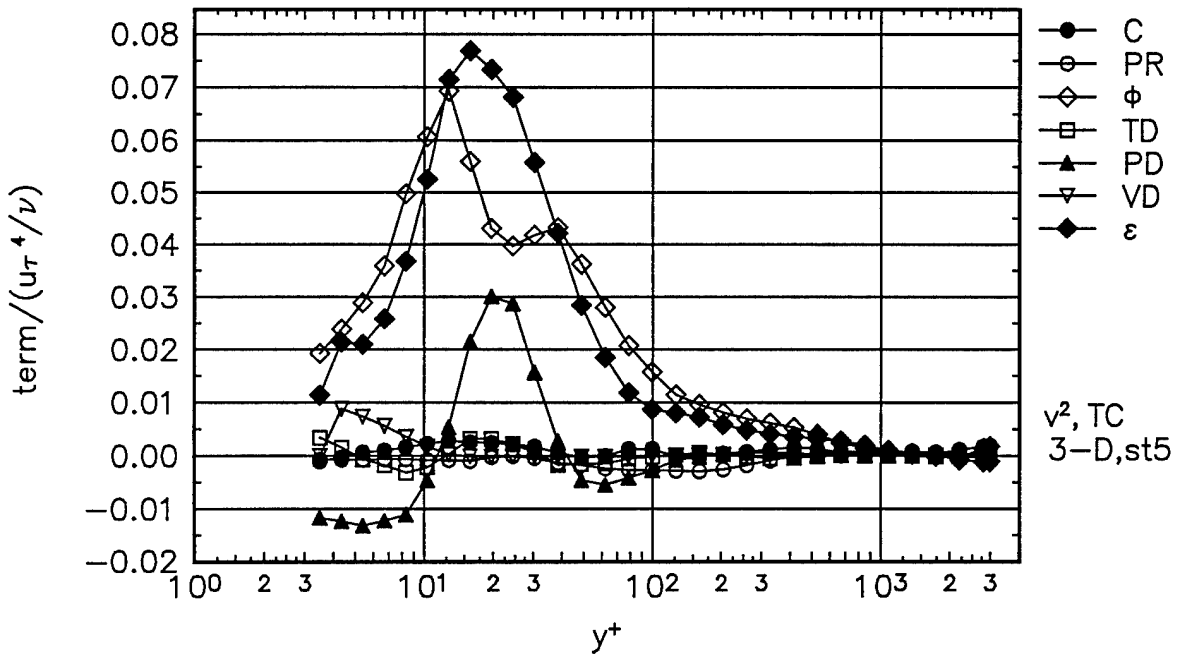
Figure 37. $\overline{v^2}$ normal stress transport budget with isotropic dissipation assumption at Station 5 in tunnel coordinates. ●, convection (C); O, production (PR); ◊, pressure-strain (φ); □, turbulent diffusion (TD); ▲, pressure diffusion (PD); ▽, viscous diffusion (VD); ♦, dissipation (ε).
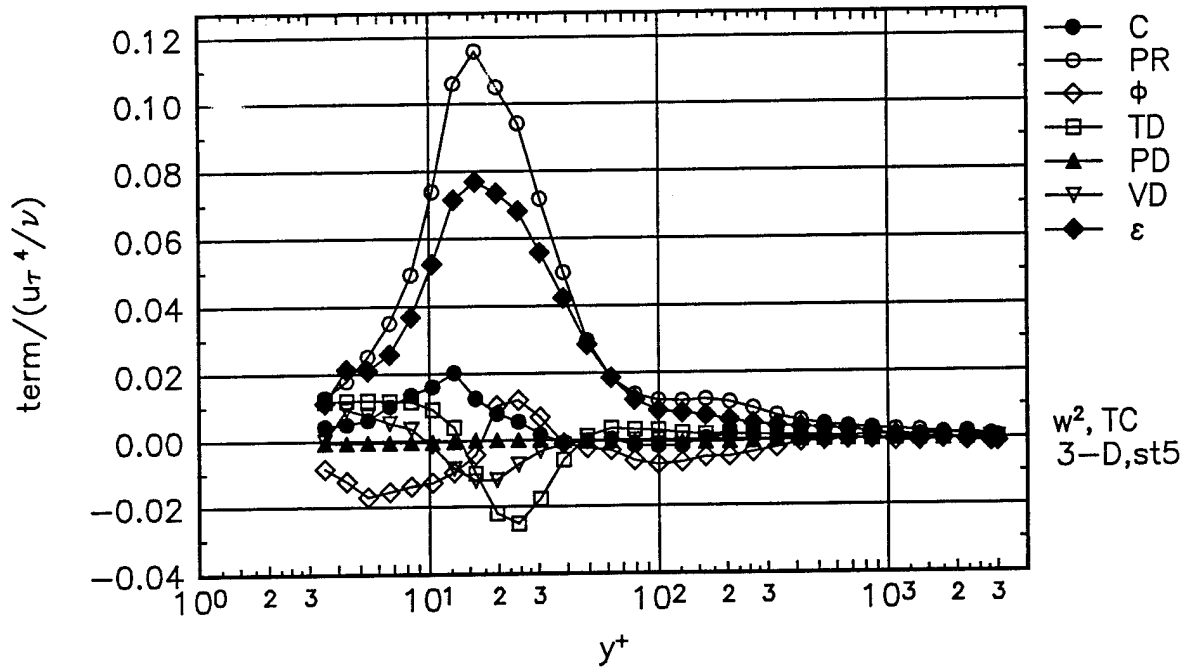
Figure 38. $\overline{w^2}$ normal stress transport budget with isotropic dissipation assumption at Station 5 in tunnel coordinates. ●, convection (C); O, production (PR); ◊, pressure-strain (φ); □, turbulent diffusion (TD); ▲, pressure diffusion (PD); ▽, viscous diffusion (VD); ♦, dissipation (ε).
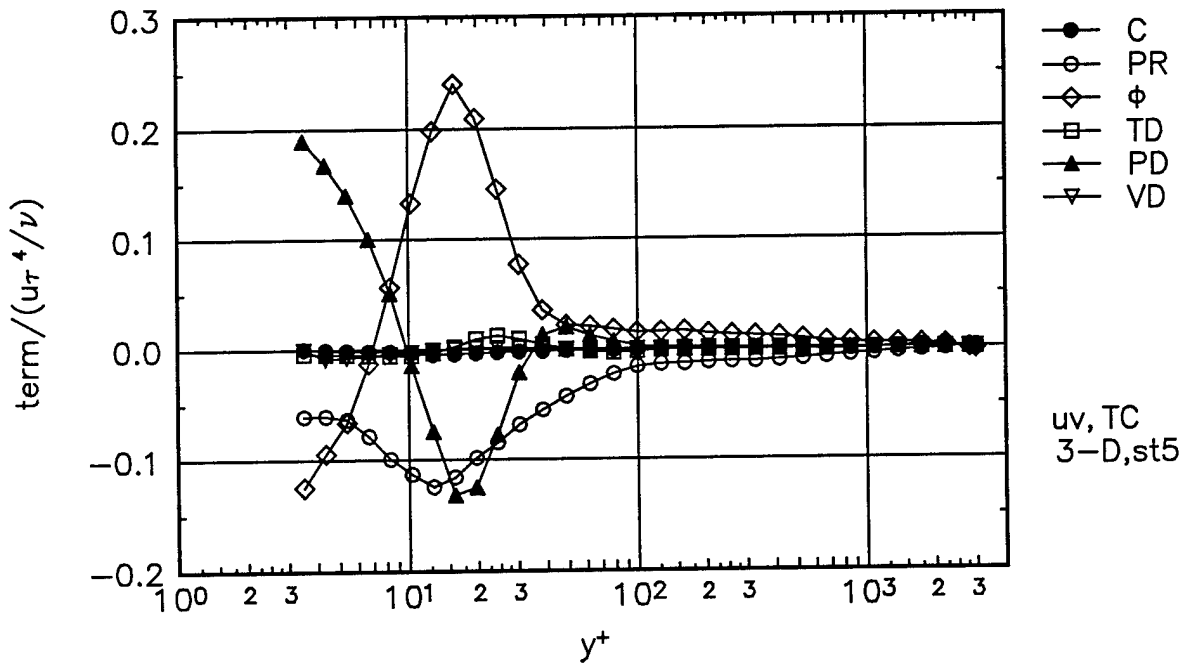
Figure 39. $\overline{uv}$ shear stress transport budget at Station 5 in tunnel coordinates. ●, convection (C); O, production (PR); ◊, pressure-strain (φ); □, turbulent diffusion (TD); ▲, pressure diffusion (PD); ▽, viscous diffusion (VD). Dissipation is assumed zero.
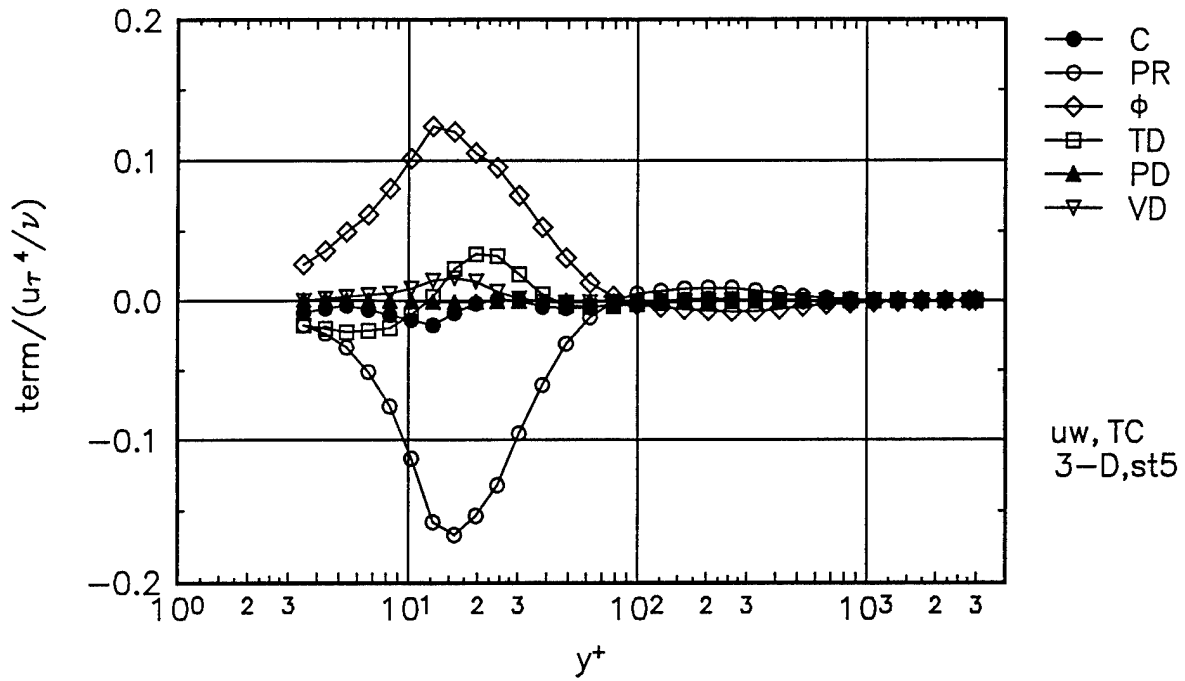
Figure 40. $\overline{uw}$ shear stress transport budget at Station 5 in tunnel coordinates. ●, convection (C); O, production (PR); ◊, pressure-strain (φ); □, turbulent diffusion (TD); ▲, pressure diffusion (PD); ▽, viscous diffusion (VD). Dissipation is assumed zero.
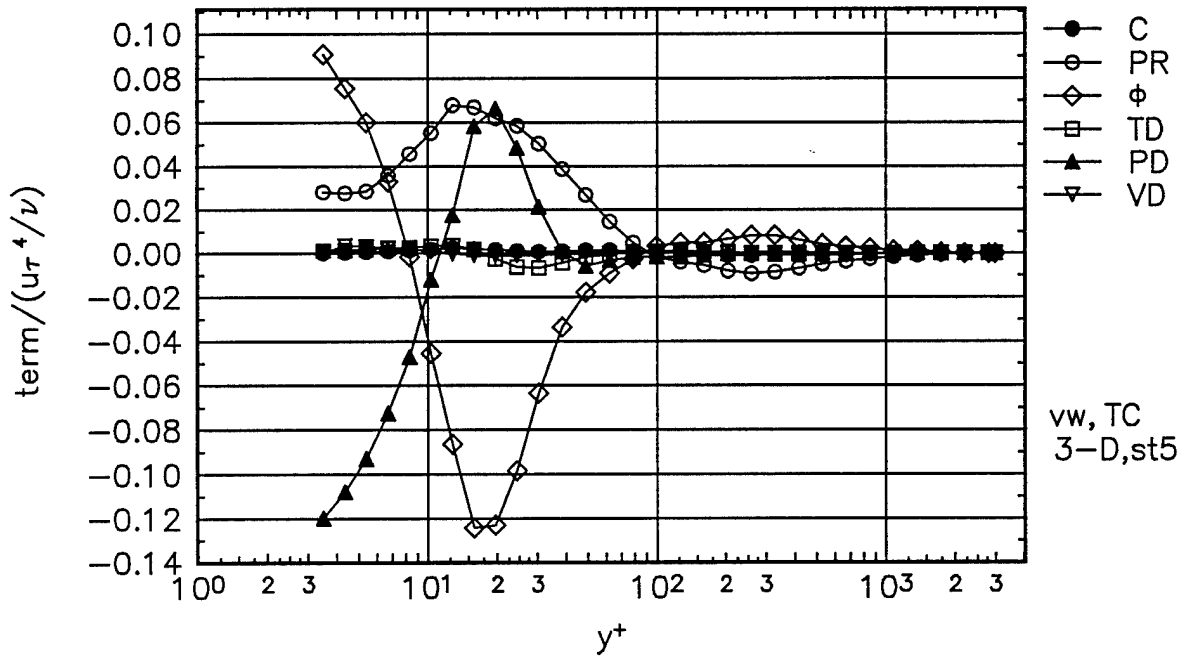
Figure 41. $\overline{vw}$ shear stress transport budget at Station 5 in tunnel coordinates. ●, convection (C); O, production (PR); ◊, pressure-strain (φ); □, turbulent diffusion (TD); ▲, pressure diffusion (PD); ▽, viscous diffusion (VD). Dissipation is assumed zero.
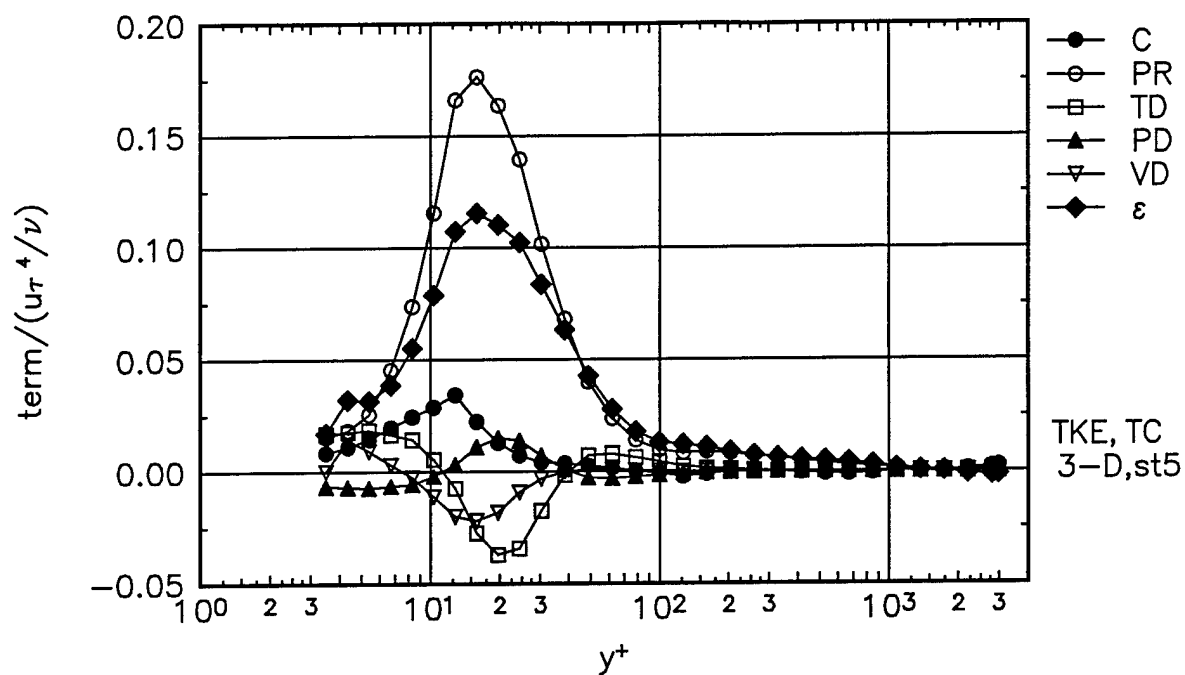
Figure 42. Turbulent kinetic energy transport budget at Station 5 in tunnel coordinates. ●, convection (C); O, production (PR); □, turbulent diffusion (TD); ▲, pressure diffusion (PD); ▽, viscous diffusion (VD); ◆, dissipation (ε). Pressure-strain term is zero by definition.
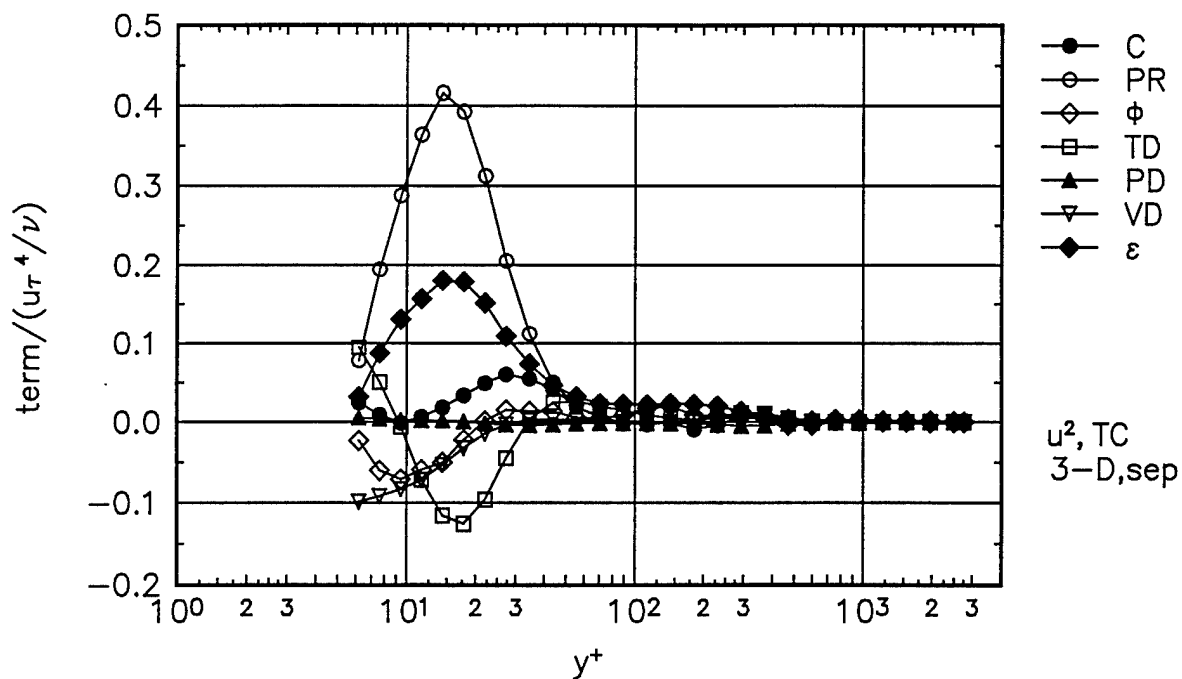
Figure 43. $\overline{u^2}$ normal stress transport budget with isotropic dissipation assumption at Separation station in tunnel coordinates. ●, convection (C); ○, production (PR); ◊, pressure-strain (φ); □, turbulent diffusion (TD); ▲, pressure diffusion (PD); ▽, viscous diffusion (VD); ◆, dissipation (ε).
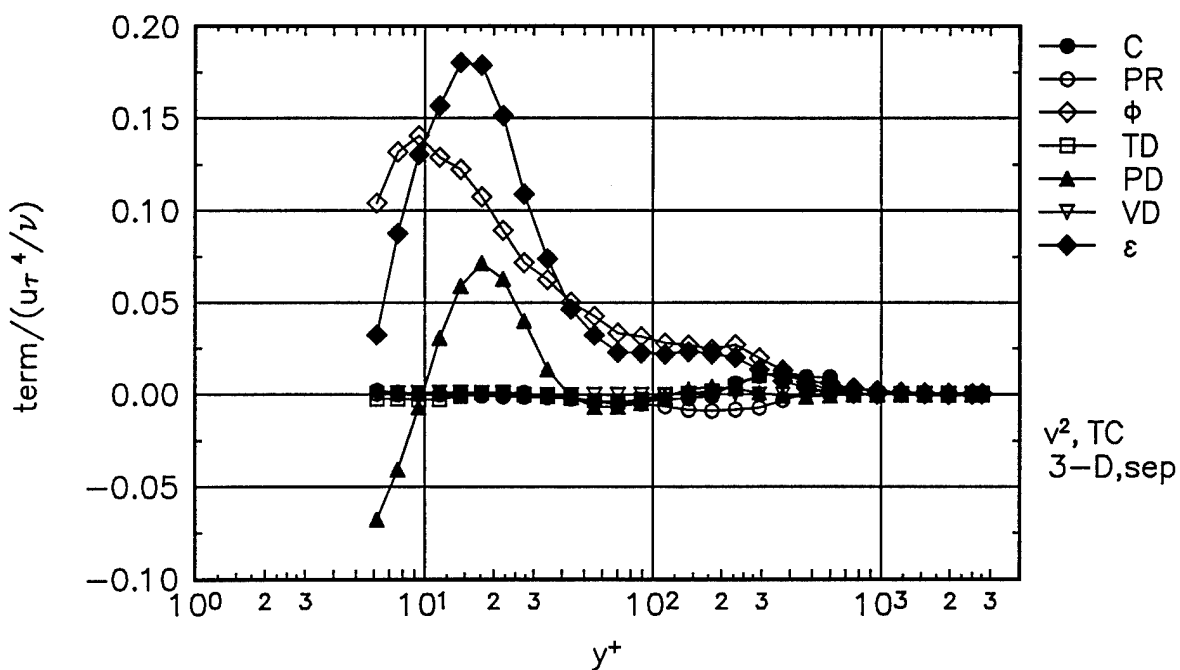
Figure 44. $\overline{v^2}$ normal stress transport budget with isotropic dissipation assumption at Separation station in tunnel coordinates. ●, convection (C); ○, production (PR); ◊, pressure-strain (φ); □, turbulent diffusion (TD); ▲, pressure diffusion (PD); ▽, viscous diffusion (VD); ◆, dissipation (ε).
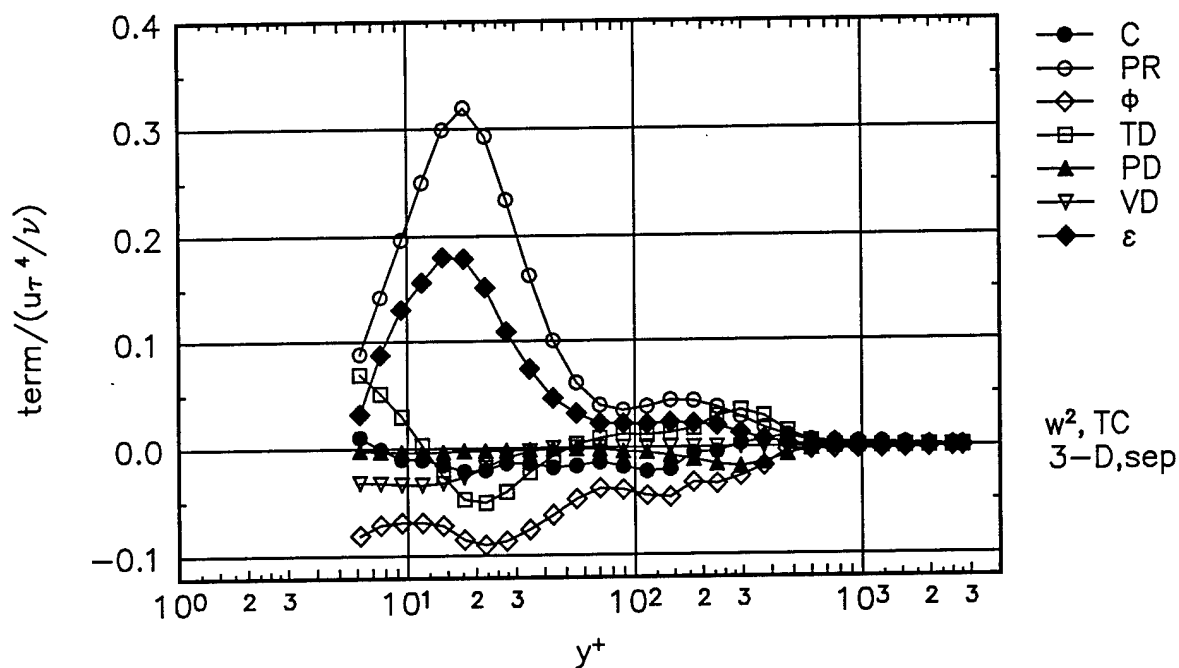
Figure 45. $\overline{w^2}$ normal stress transport budget with isotropic dissipation assumption at Separation station in tunnel coordinates. ●, convection (C); O, production (PR); ◊, pressure-strain (φ); □, turbulent diffusion (TD); ▲, pressure diffusion (PD); ▽, viscous diffusion (VD); ♦, dissipation (ε).
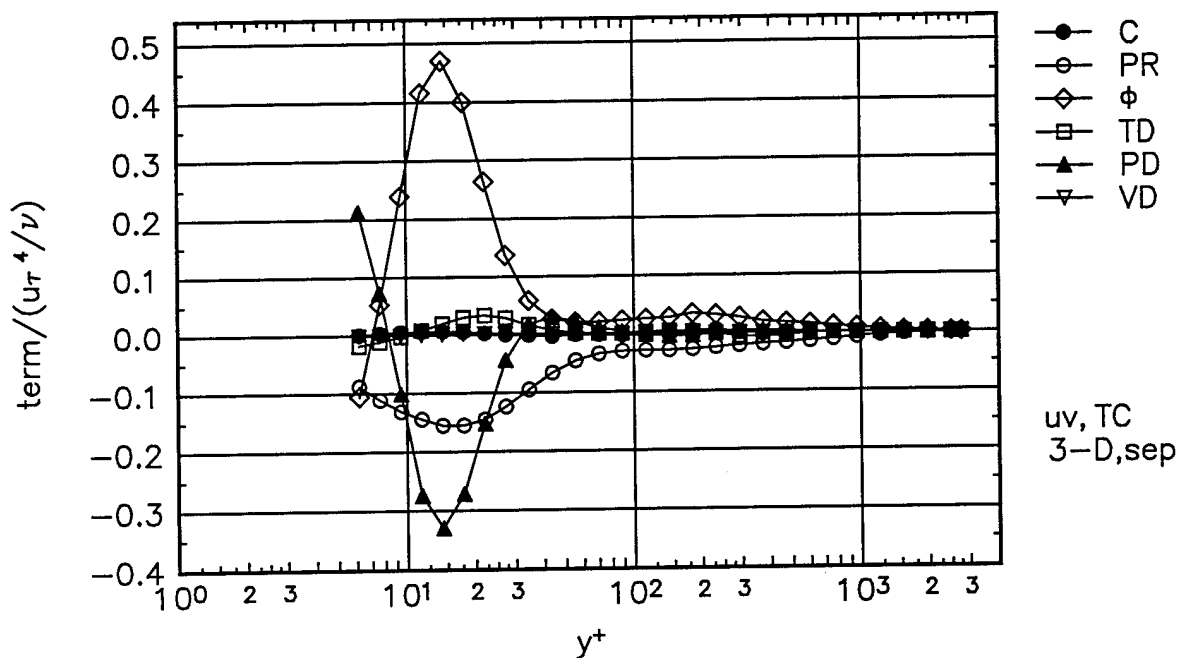
Figure 46. $\overline{uv}$ shear stress transport budget at Separation station in tunnel coordinates. ●, convection (C); O, production (PR); ◊, pressure-strain (φ); □, turbulent diffusion (TD); ▲, pressure diffusion (PD); ▽, viscous diffusion (VD). Dissipation is assumed zero.
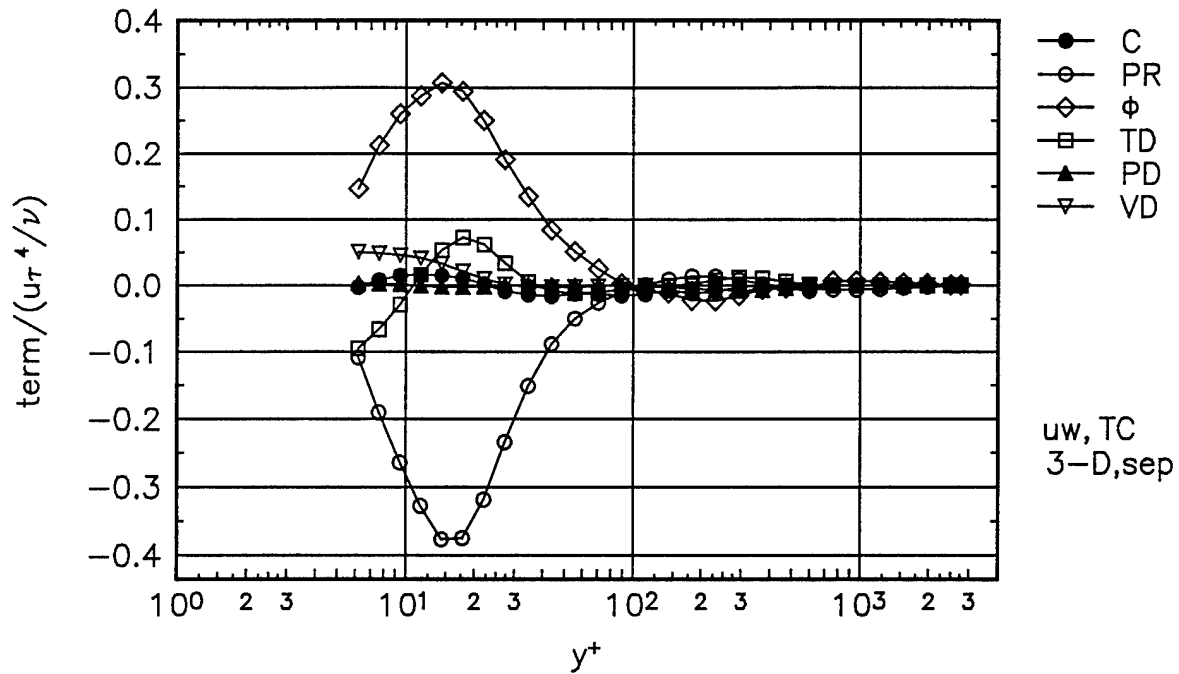
Figure 47. $\overline{uw}$ shear stress transport budget at Separation station in tunnel coordinates. ●, convection (C); ○, production (PR); ◊, pressure-strain (φ); □, turbulent diffusion (TD); ▲, pressure diffusion (PD); ▽, viscous diffusion (VD). Dissipation is assumed zero.
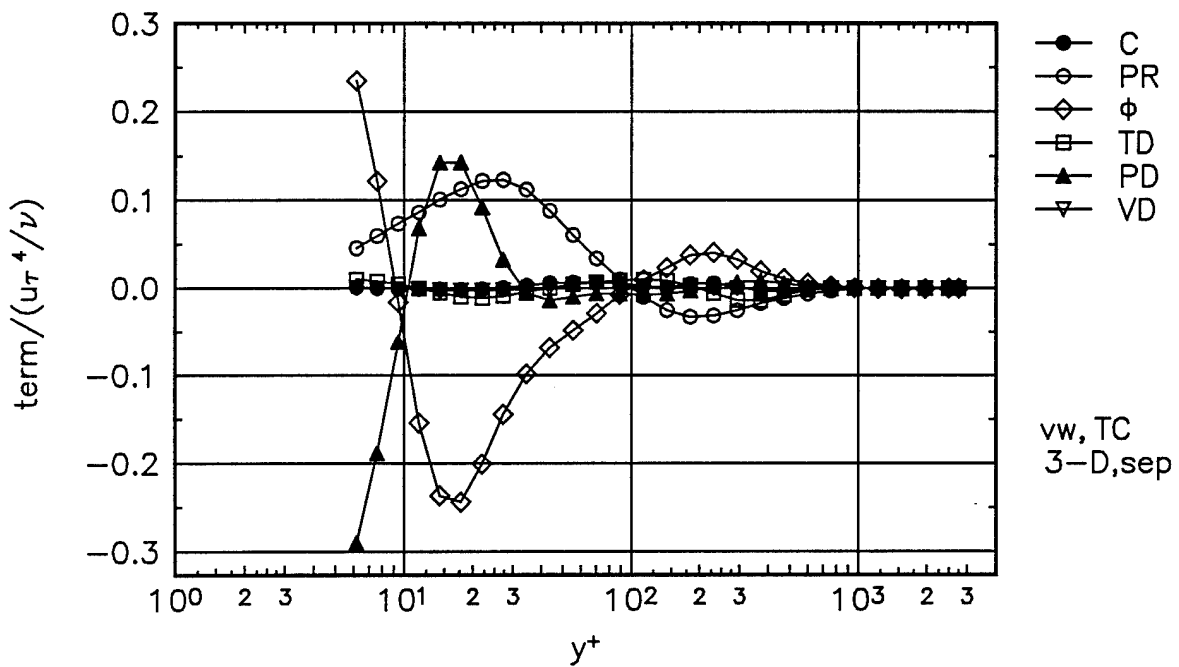
Figure 48. $\overline{vw}$ shear stress transport budget at Separation station in tunnel coordinates. ●, convection (C); ○, production (PR); ◊, pressure-strain (φ); □, turbulent diffusion (TD); ▲, pressure diffusion (PD); ▽, viscous diffusion (VD). Dissipation is assumed zero.
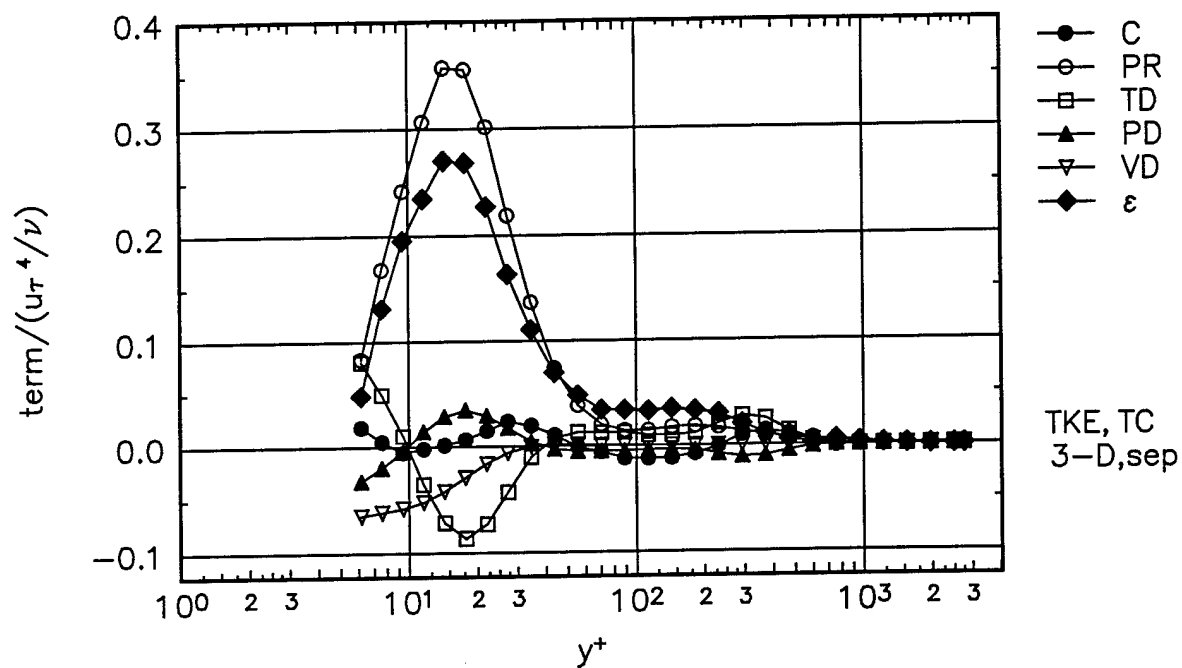
Figure 49. Turbulent kinetic energy transport budget at Separation station in tunnel coordinates. ●, convection (C); O, production (PR); □, turbulent diffusion (TD); ▲, pressure diffusion (PD); ▽, viscous diffusion (VD); ◆, dissipation (ε). Pressure-strain term is zero by definition.
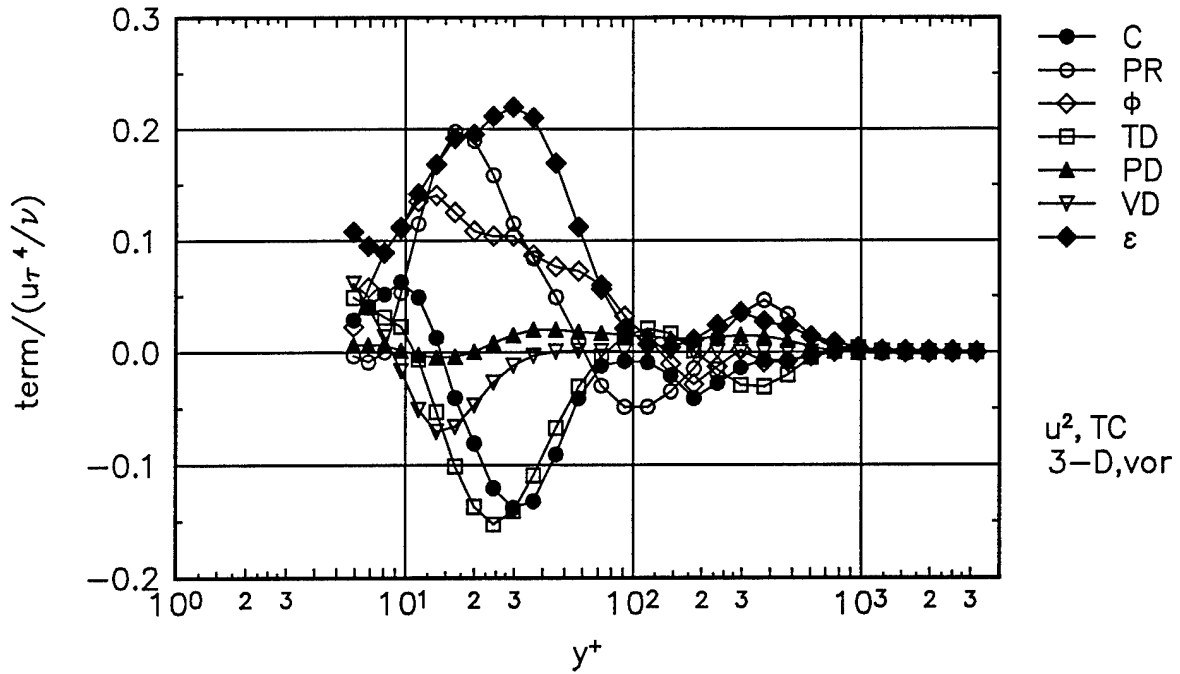
Figure 50. $\overline{u^2}$ normal stress transport budget with isotropic dissipation assumption at Vortex station in tunnel coordinates. ●, convection (C); O, production (PR); ◊, pressure-strain (φ); □, turbulent diffusion (TD); ▲, pressure diffusion (PD); ▽, viscous diffusion (VD); ◆, dissipation (ε).
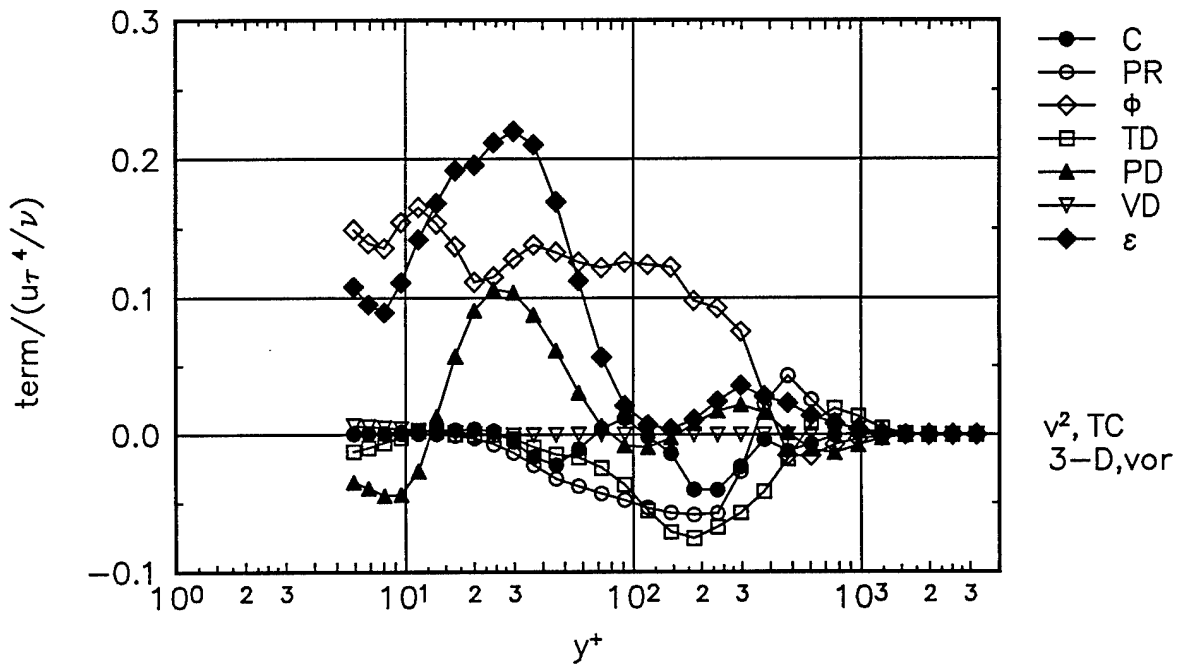
Figure 51. $\overline{v^2}$ normal stress transport budget with isotropic dissipation assumption at Vortex station in tunnel coordinates. ●, convection (C); O, production (PR); ◊, pressure-strain (φ); □, turbulent diffusion (TD); ▲, pressure diffusion (PD); ▽, viscous diffusion (VD); ◆, dissipation (ε).
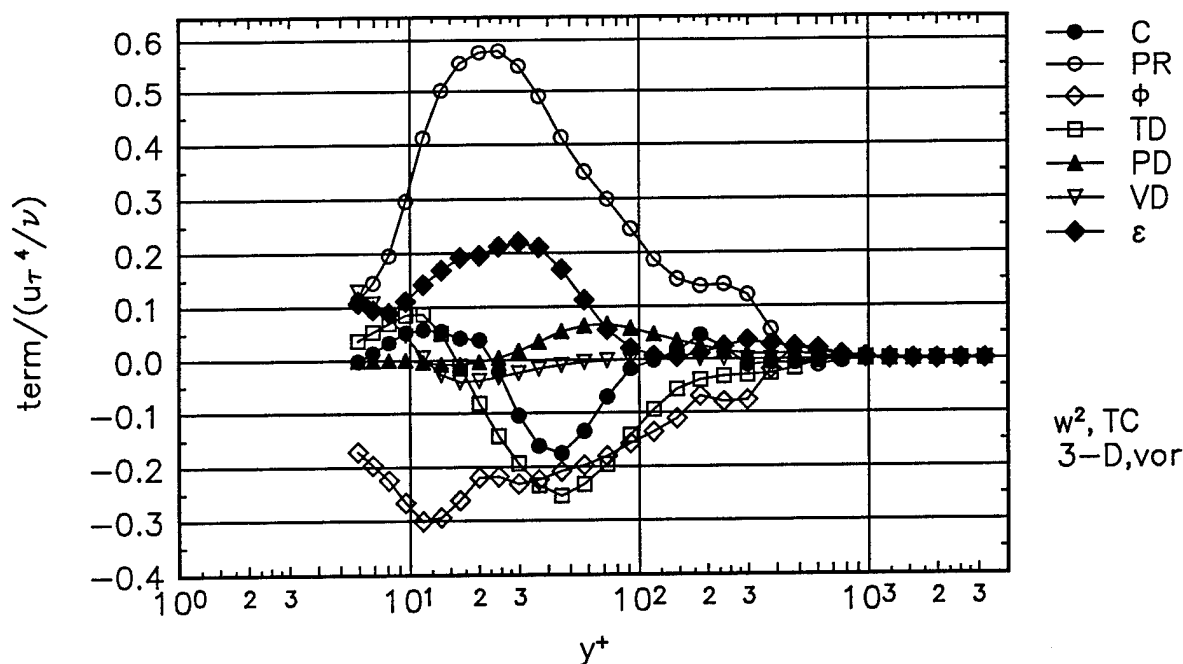
Figure 52. $\overline{w^2}$ normal stress transport budget with isotropic dissipation assumption at Vortex station in tunnel coordinates. ●, convection (C); O, production (PR); ◊, pressure-strain (φ); □, turbulent diffusion (TD); ▲, pressure diffusion (PD); ▽, viscous diffusion (VD); ♦, dissipation (ε).
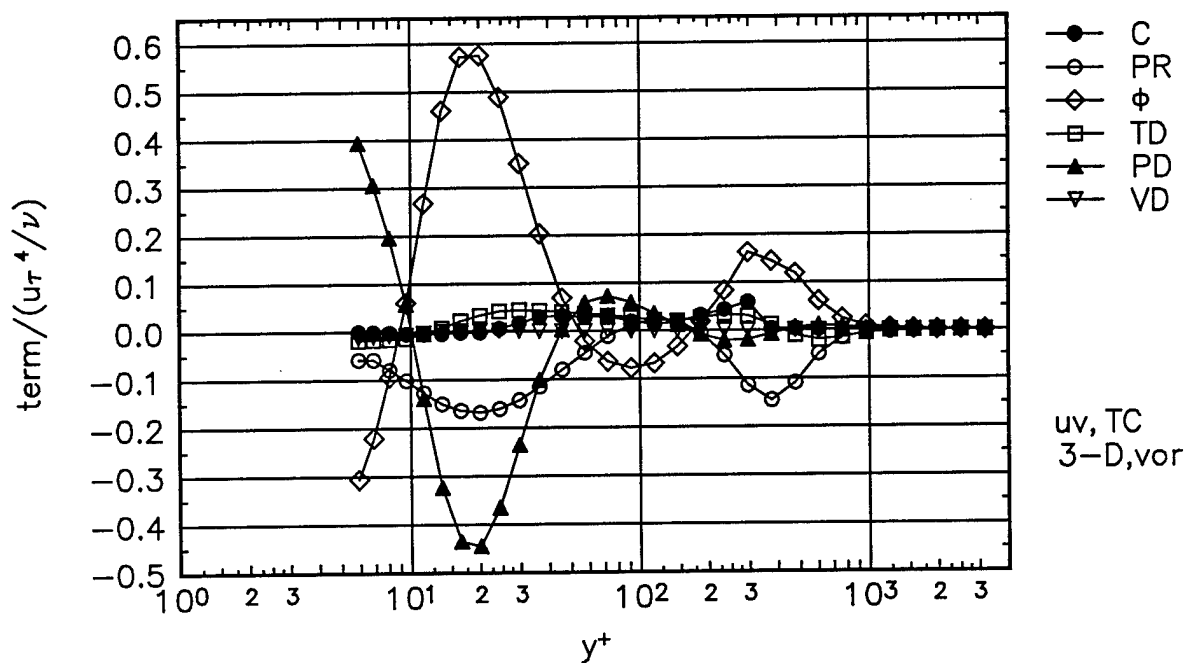
Figure 53. $\overline{uv}$ shear stress transport budget at Vortex station in tunnel coordinates. ●, convection (C); O, production (PR); ◊, pressure-strain (φ); □, turbulent diffusion (TD); ▲, pressure diffusion (PD); ▽, viscous diffusion (VD). Dissipation is assumed zero.
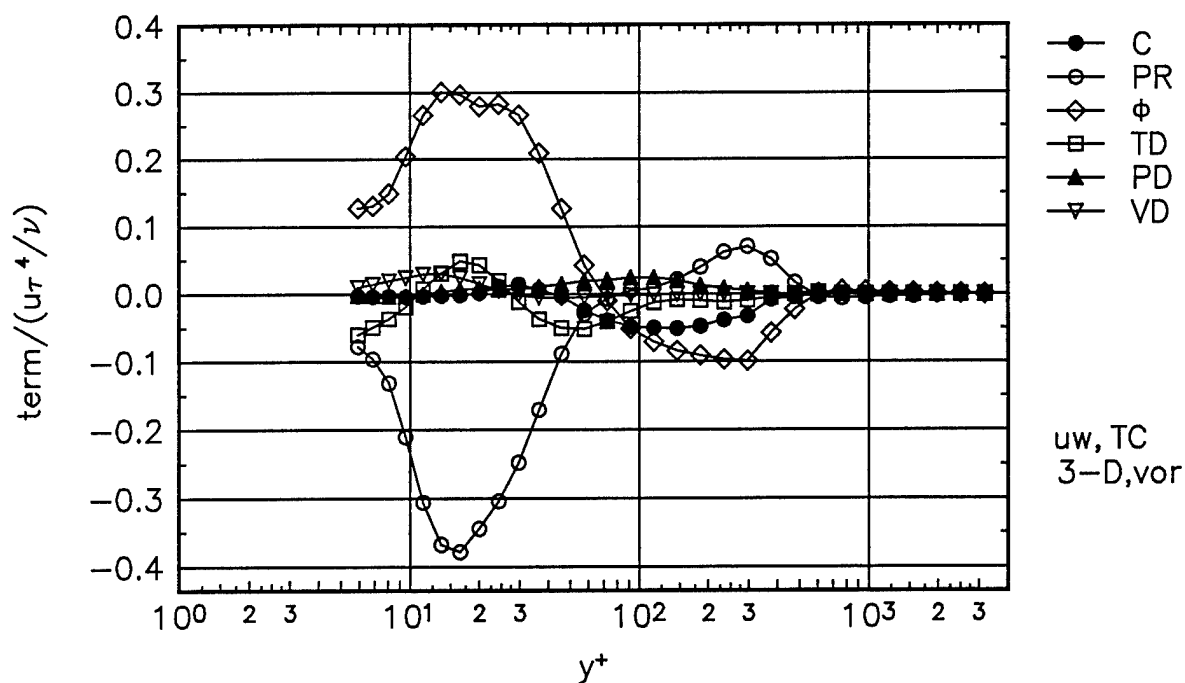
Figure 54. $\overline{uw}$ shear stress transport budget at Vortex station in tunnel coordinates. ●, convection (C); O, production (PR); ◊, pressure-strain (φ); □, turbulent diffusion (TD); ▲, pressure diffusion (PD); ▽, viscous diffusion (VD). Dissipation is assumed zero.
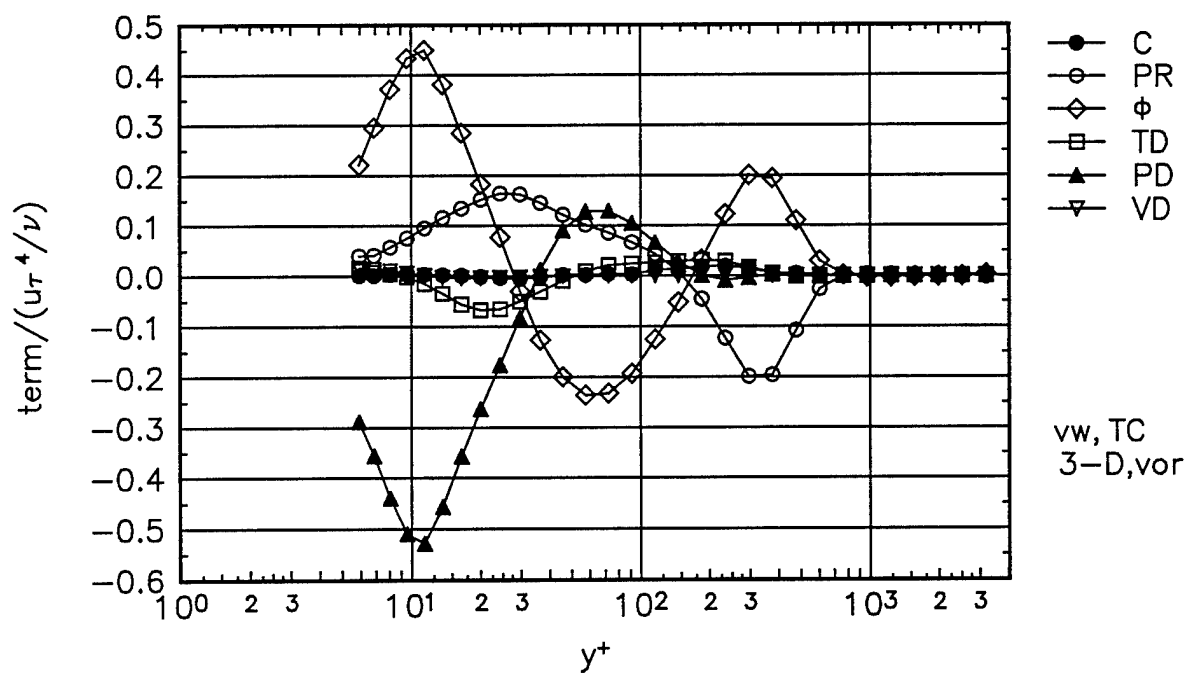
Figure 55. $\overline{vw}$ shear stress transport budget at Vortex station in tunnel coordinates. ●, convection (C); O, production (PR); ◊, pressure-strain (φ); □, turbulent diffusion (TD); ▲, pressure diffusion (PD); ▽, viscous diffusion (VD). Dissipation is assumed zero.
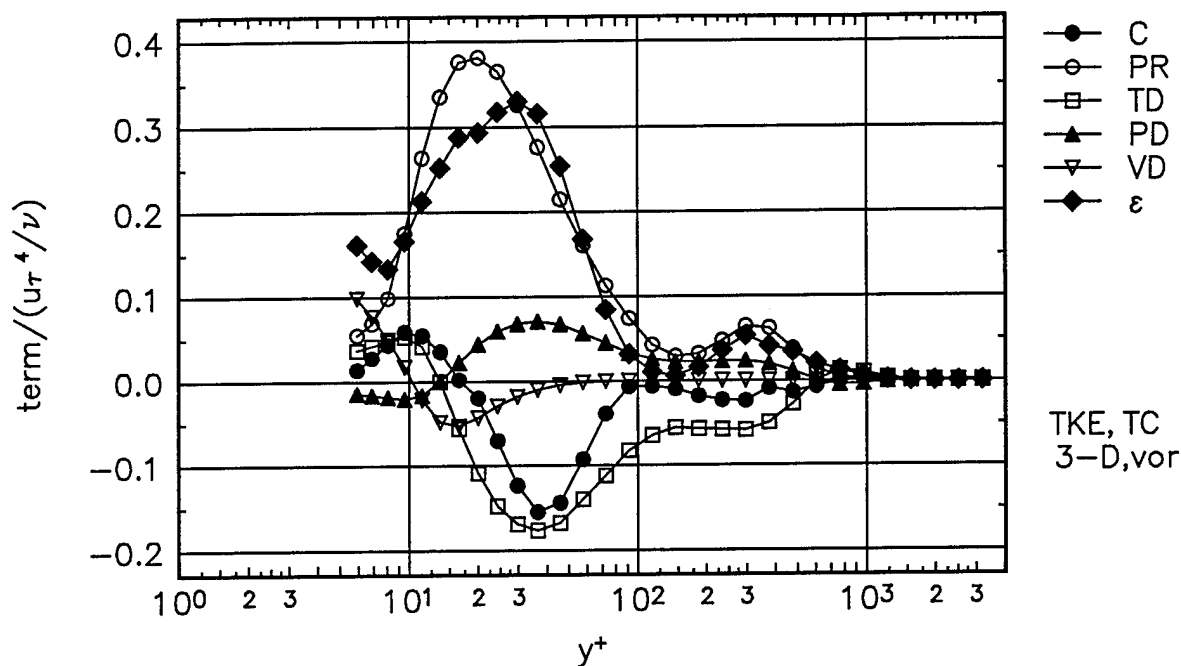
Figure 56. Turbulent kinetic energy transport budget at Vortex station in tunnel coordinates. ●, convection (C); O, production (PR); □, turbulent diffusion (TD); ▲, pressure diffusion (PD); ▽, viscous diffusion (VD); ◆, dissipation (ε). Pressure-strain term is zero by definition.
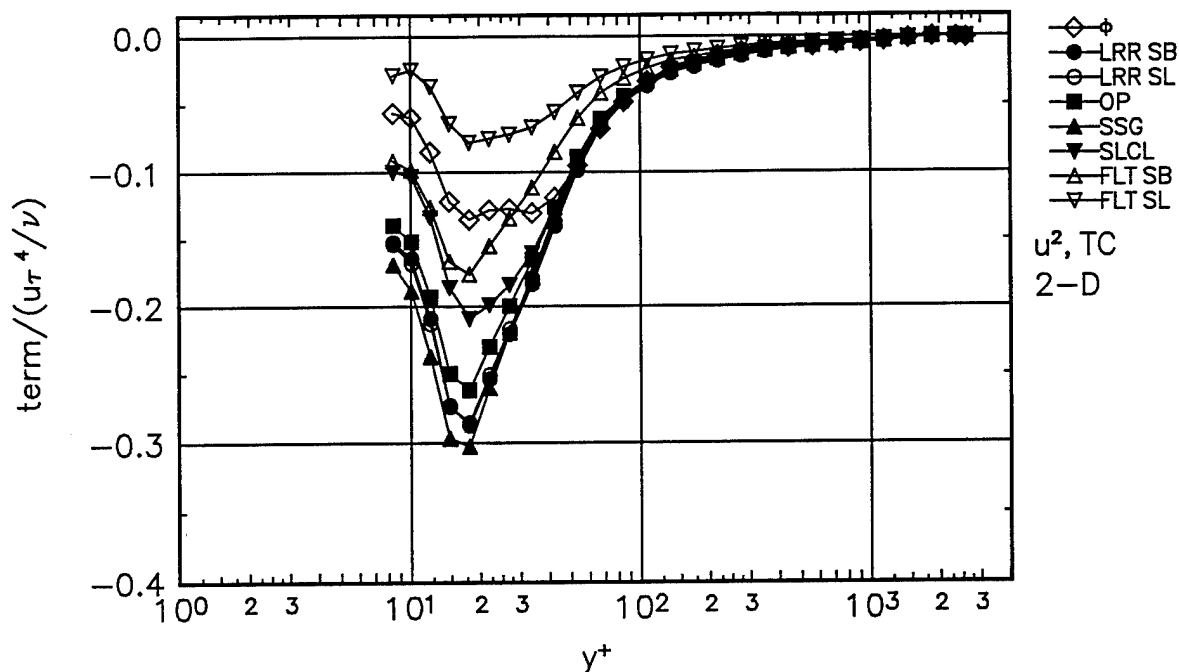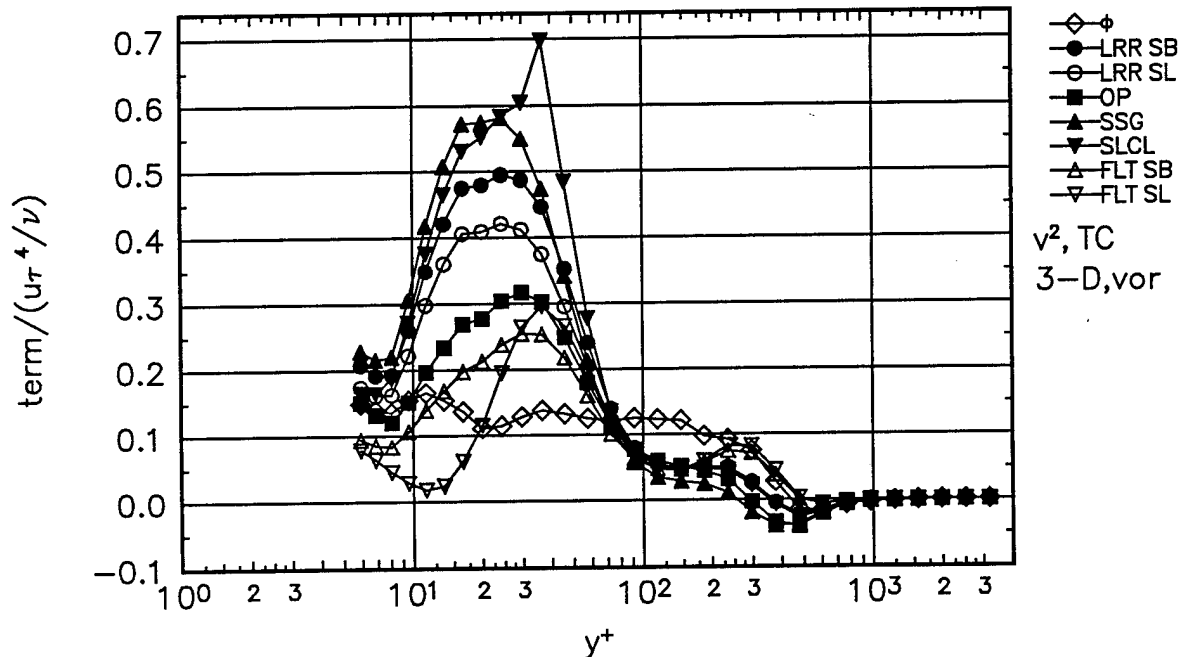
Figure 57. Comparison of $\overline{u^2}$ normal stress transport experimental pressure-strain term ◊, to theoretical pressure-strain terms for the 2-D station. Gibson-Launder, ●; Launder-Reece-Rodi (LRR), O; Oberlack-Peters (OP), ■; Speziale-Sarkar-Gatski (SSG), ▲; Shih-Lumley/Choi-Lumley (SLCL), ▼; Fu-Launder-Tselepidakis 1 (FLT1), △; Fu-Launder-Tselepidakis 2 (FLT2), ▽. No near-wall corrections, dissipation is assumed isotropic.
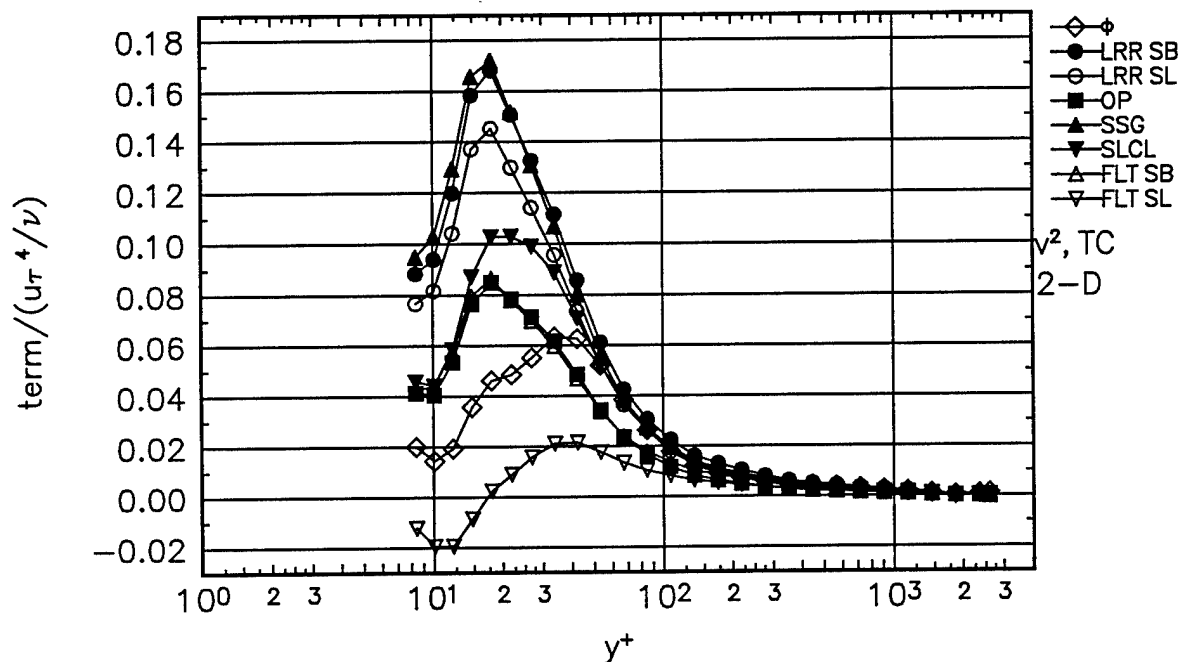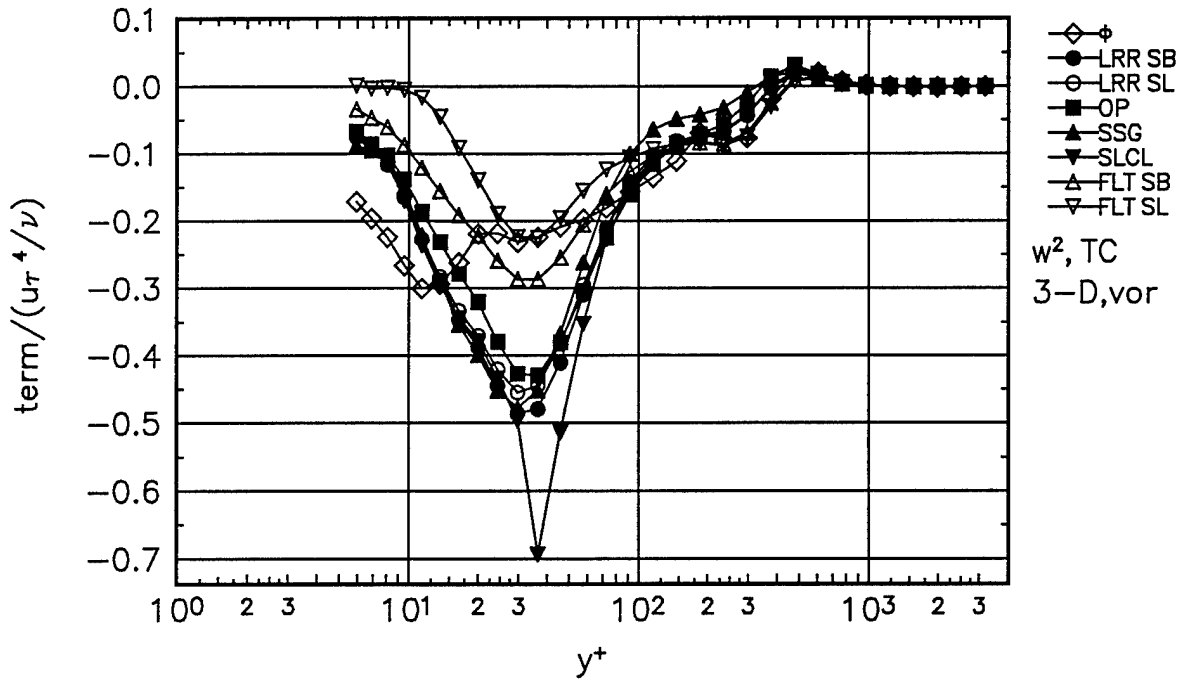

Figure 58. Comparison of $\overline{v^2}$ normal stress transport experimental pressure-strain term ◊, to theoretical pressure-strain terms for the 2-D station. Gibson-Launder, ●; Launder-Reece-Rodi (LRR), O; Oberlack-Peters (OP), ■; Speziale-Sarkar-Gatski (SSG), ▲; Shih-Lumley/Choi-Lumley (SLCL), ▼; Fu-Launder-Tselepidakis 1 (FLT1), △; Fu-Launder-Tselepidakis 2 (FLT2), ▽. No near-wall corrections, dissipation is assumed isotropic.
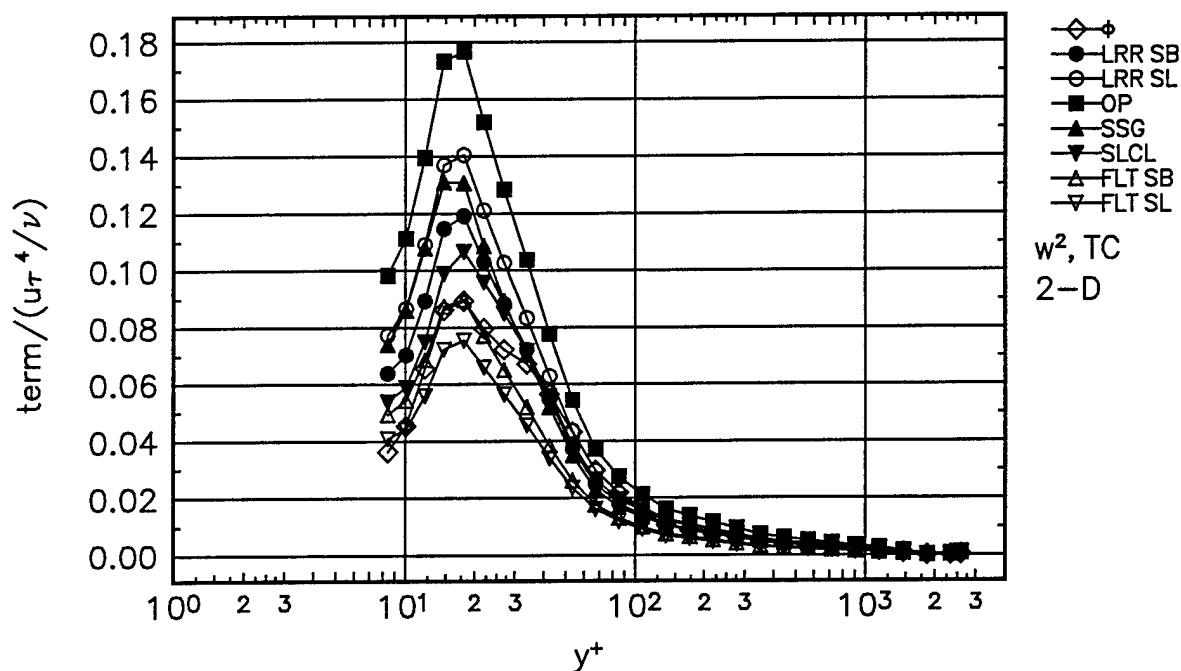
Figures

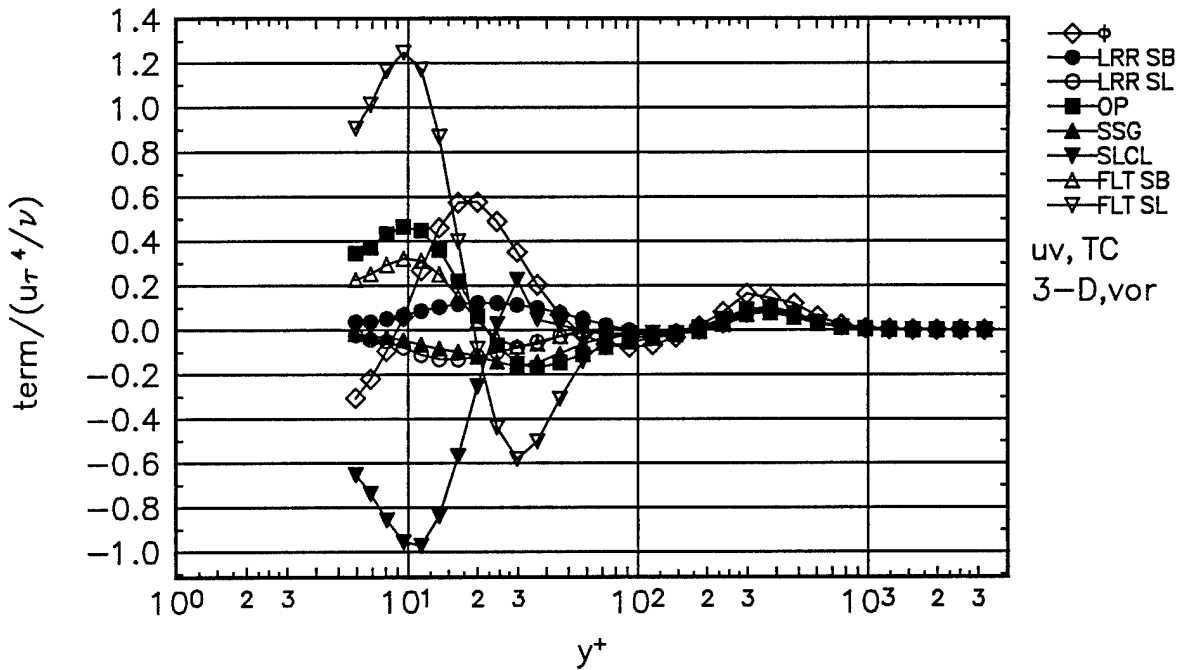Figure 59. Comparison of $\overline{w^2}$ normal stress transport experimental pressure-strain term ◊, to theoretical pressure-strain terms for the 2-D station. Gibson-Launder, ●; Launder-Reece-Rodi (LRR), O; Oberlack-Peters (OP), ■; Speziale-Sarkar-Gatski (SSG), ▲; Shih-Lumley/Choi-Lumley (SLCL), ▼; Fu-Launder-Tselepidakis 1 (FLT1), ▵; Fu-Launder-Tselepidakis 2 (FLT2), ▽. No near-wall corrections, dissipation is assumed isotropic.
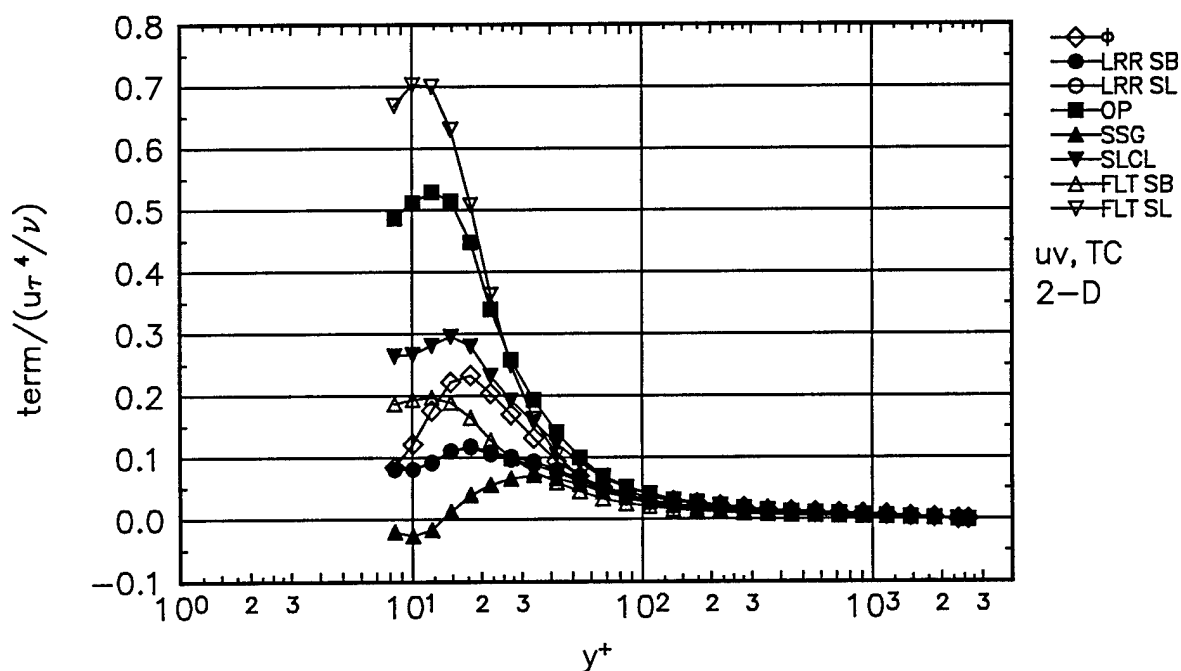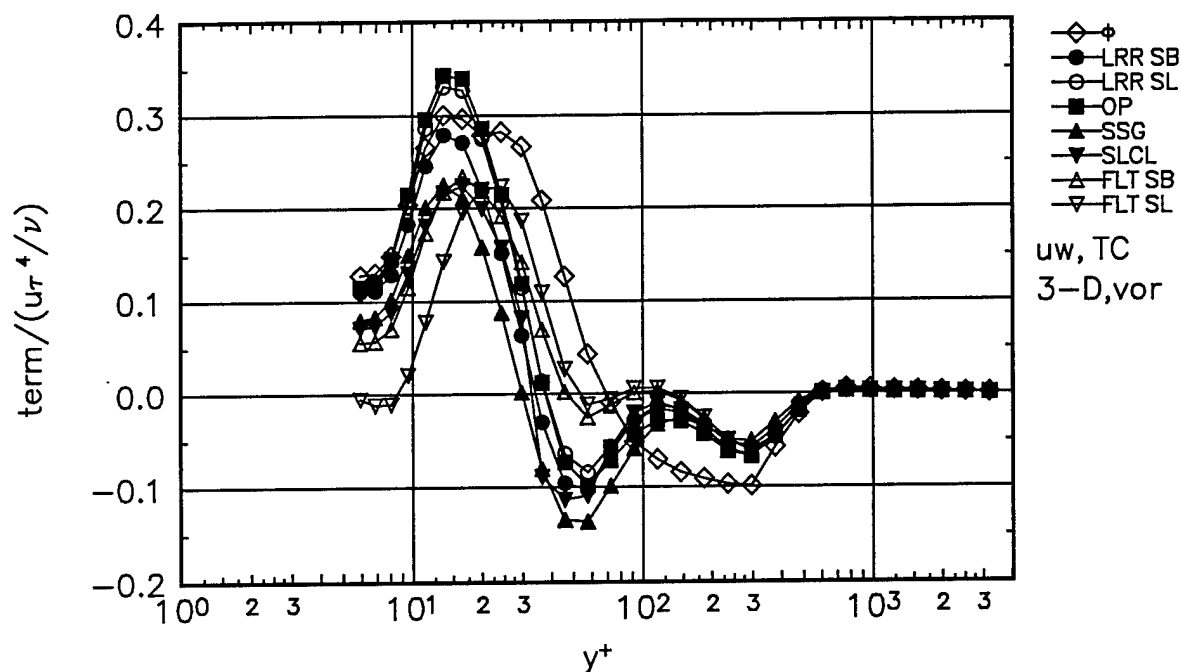

Figure 60. Comparison of $\overline{uv}$ shear stress transport experimental pressure-strain term ◊, to theoretical pressure-strain terms for the 2-D station. Gibson-Launder, ●; Launder-Reece-Rodi (LRR), O; Oberlack-Peters (OP), ■; Speziale-Sarkar-Gatski (SSG), ▲; Shih-Lumley/Choi-Lumley (SLCL), ▼; Fu-Launder-Tselepidakis 1 (FLT1), ▵; Fu-Launder-Tselepidakis 2 (FLT2), ▽. No near-wall corrections, dissipation is assumed zero.
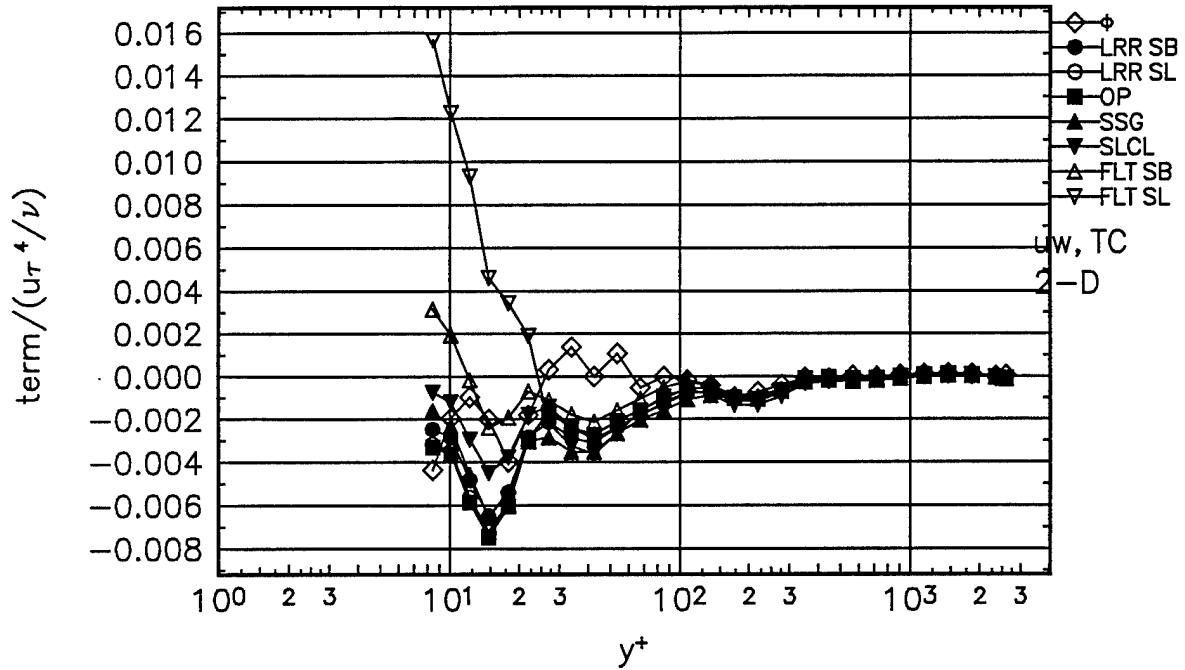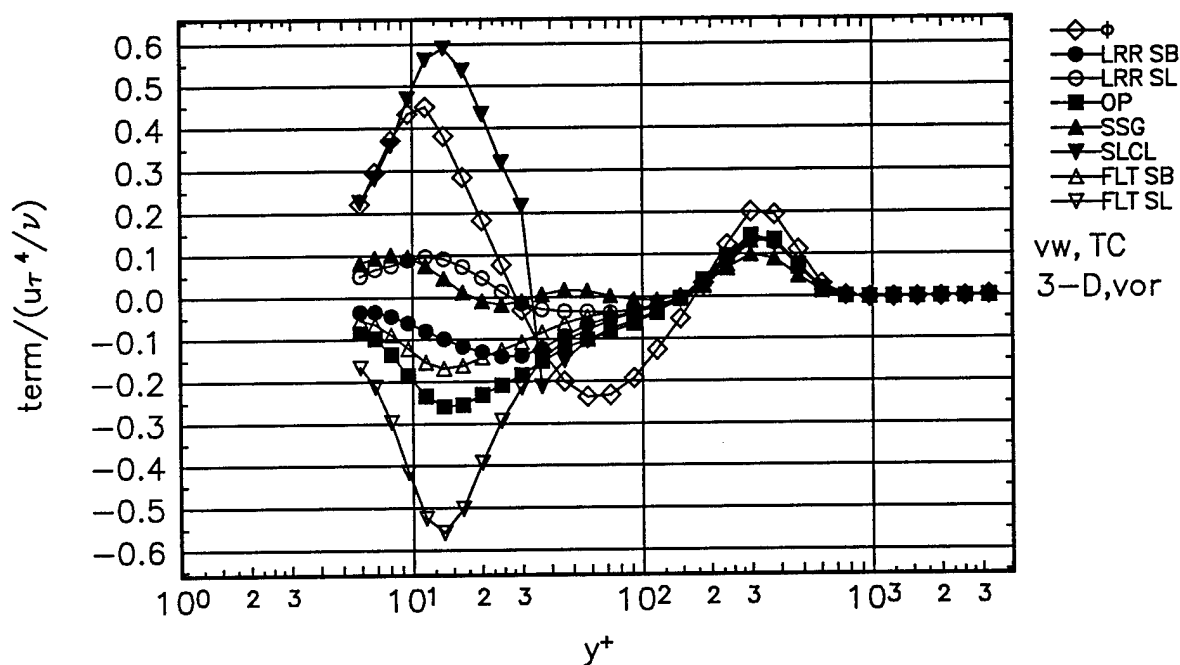
Figure 61. Comparison of $\overline{uw}$ shear stress transport experimental pressure-strain term ◊, to theoretical pressure-strain terms for the 2-D station. Gibson-Launder, ●; Launder-Reece-Rodi (LRR), O; Oberlack-Peters (OP), ■; Speziale-Sarkar-Gatski (SSG), ▲; Shih-Lumley/Choi-Lumley (SLCL), ▼; Fu-Launder-Tselepidakis 1 (FLT1), ▵; Fu-Launder-Tselepidakis 2 (FLT2), ▽. No near-wall corrections, dissipation is assumed zero.
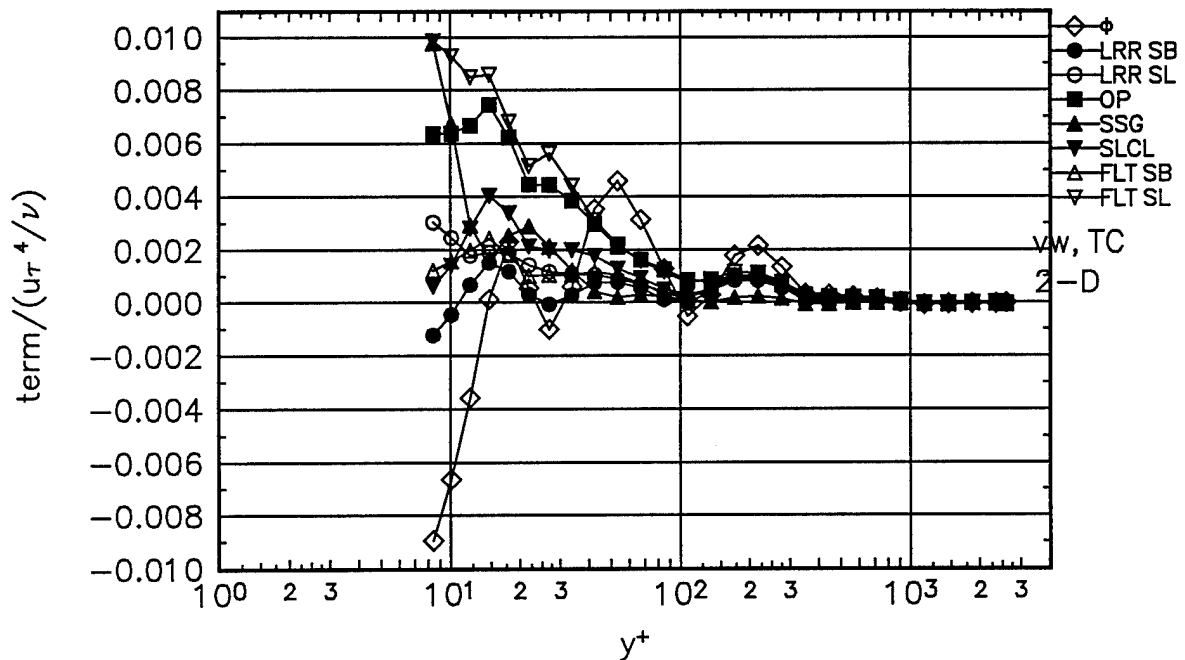
Figure 62. Comparison of $\overline{vw}$ shear stress transport experimental pressure-strain term ◊, to theoretical pressure-strain terms for the 2-D station. Gibson-Launder, ●; Launder-Reece-Rodi (LRR), O; Oberlack-Peters (OP), ■; Speziale-Sarkar-Gatski (SSG), ▲; Shih-Lumley/Choi-Lumley (SLCL), ▼; Fu-Launder-Tselepidakis 1 (FLT1), ▵; Fu-Launder-Tselepidakis 2 (FLT2), ▽. No near-wall corrections, dissipation is assumed zero.

Figures

85
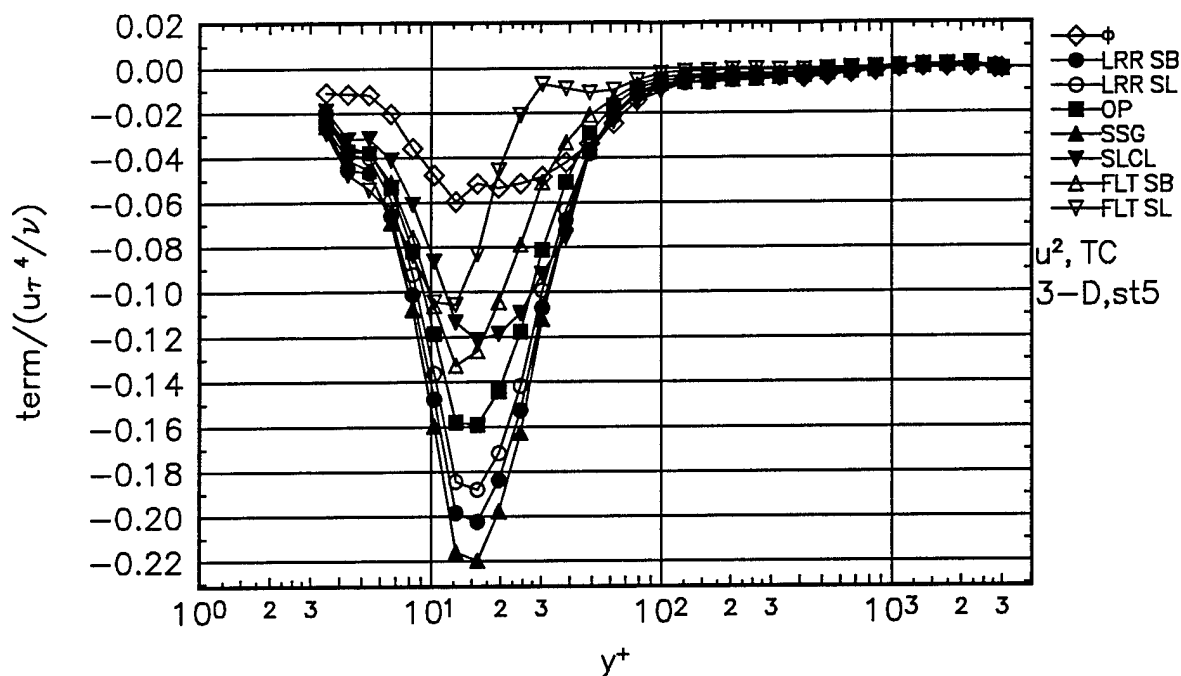
Figure 63. Comparison of $\overline{u^2}$ normal stress transport experimental pressure-strain term ◊, to theoretical pressure-strain terms for Station 5. Gibson-Launder, ●; Launder-Reece-Rodi (LRR), O; Oberlack-Peters (OP), ■; Speziale-Sarkar-Gatski (SSG), ▲; Shih-Lumley/Choi-Lumley (SLCL), ▼; Fu-Launder-Tselepidakis 1 (FLT1), ▲; Fu-Launder-Tselepidakis 2 (FLT2), ▽. No near-wall corrections, dissipation is assumed isotropic.
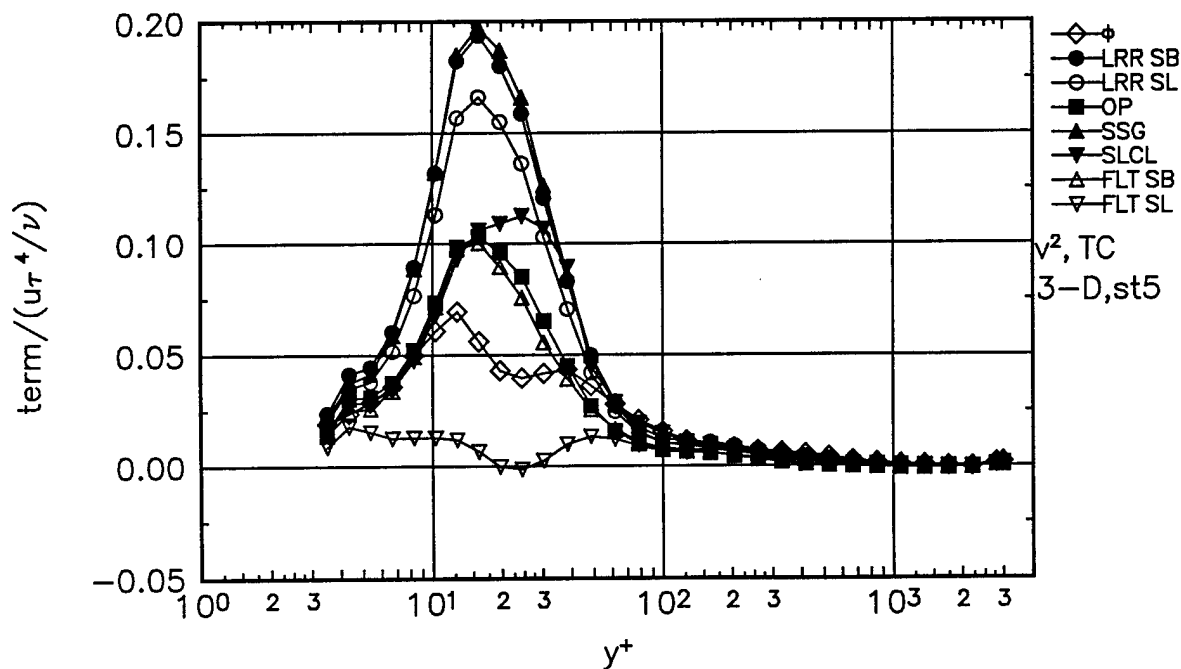
Figure 64. Comparison of $\overline{v^2}$ normal stress transport experimental pressure-strain term ◊, to theoretical pressure-strain terms for Station 5. Gibson-Launder, ●; Launder-Reece-Rodi (LRR), O; Oberlack-Peters (OP), ■; Speziale-Sarkar-Gatski (SSG), ▲; Shih-Lumley/Choi-Lumley (SLCL), ▼; Fu-Launder-Tselepidakis 1 (FLT1), ▲; Fu-Launder-Tselepidakis 2 (FLT2), ▽. No near-wall corrections, dissipation is assumed isotropic.
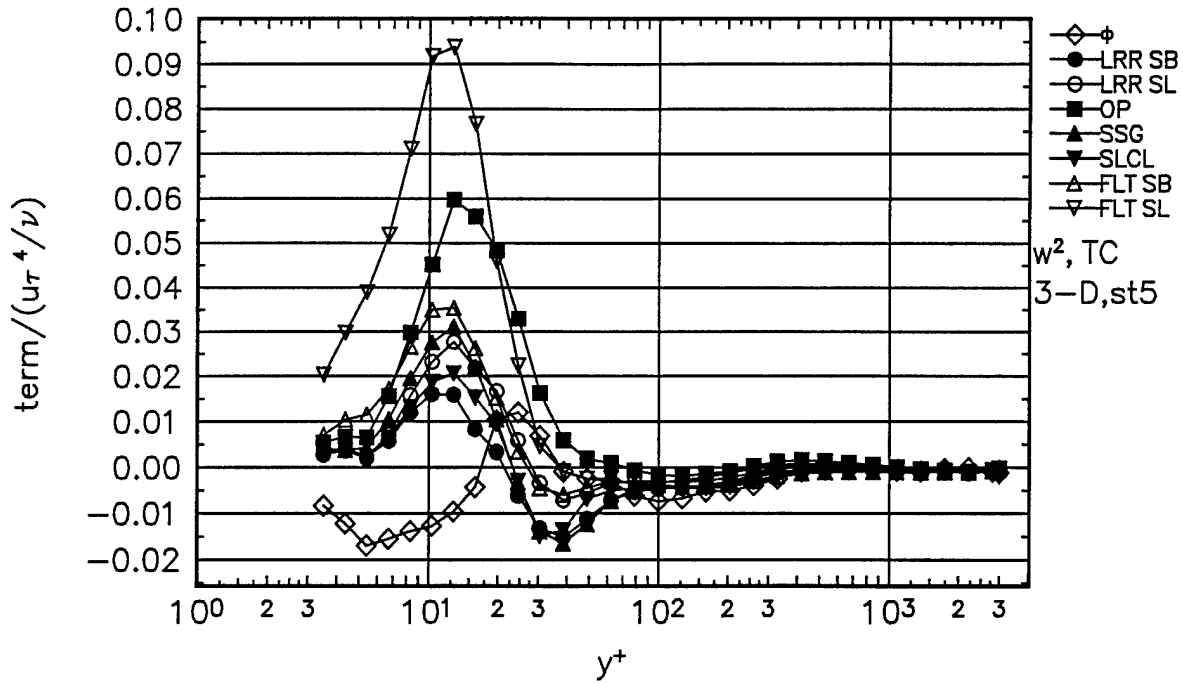
Figure 65. Comparison of $\overline{w^2}$ normal stress transport experimental pressure-strain term ◊, to theoretical pressure-strain terms for Station 5. Gibson-Launder, ●; Launder-Reece-Rodi (LRR), O; Oberlack-Peters (OP), ■; Speziale-Sarkar-Gatski (SSG), ▲; Shih-Lumley/Choi-Lumley (SLCL), ▼; Fu-Launder-Tselepidakis 1 (FLT1), ▵; Fu-Launder-Tselepidakis 2 (FLT2), ▽. No near-wall corrections, dissipation is assumed isotropic.
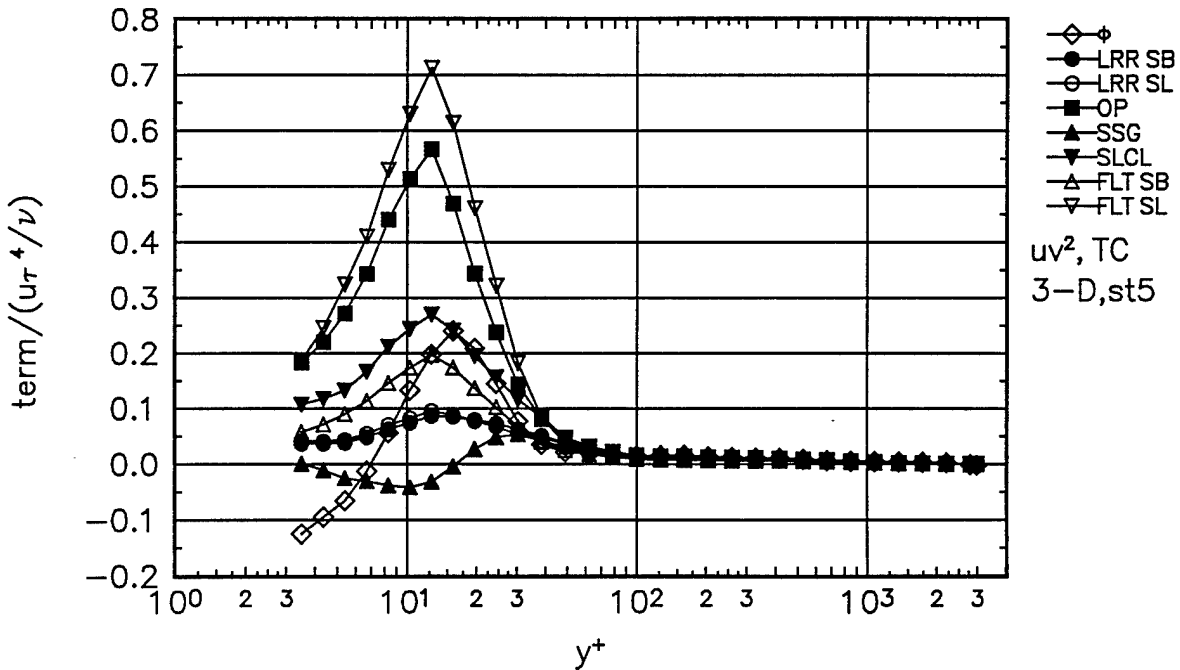
Figure 66. Comparison of $\overline{uv}$ shear stress transport experimental pressure-strain term ◊, to theoretical pressure-strain terms for Station 5. Gibson-Launder, ●; Launder-Reece-Rodi (LRR), O; Oberlack-Peters (OP), ■; Speziale-Sarkar-Gatski (SSG), ▲; Shih-Lumley/Choi-Lumley (SLCL), ▼; Fu-Launder-Tselepidakis 1 (FLT1), ▵; Fu-Launder-Tselepidakis 2 (FLT2), ▽. No near-wall corrections, dissipation is assumed zero.

Figures

87
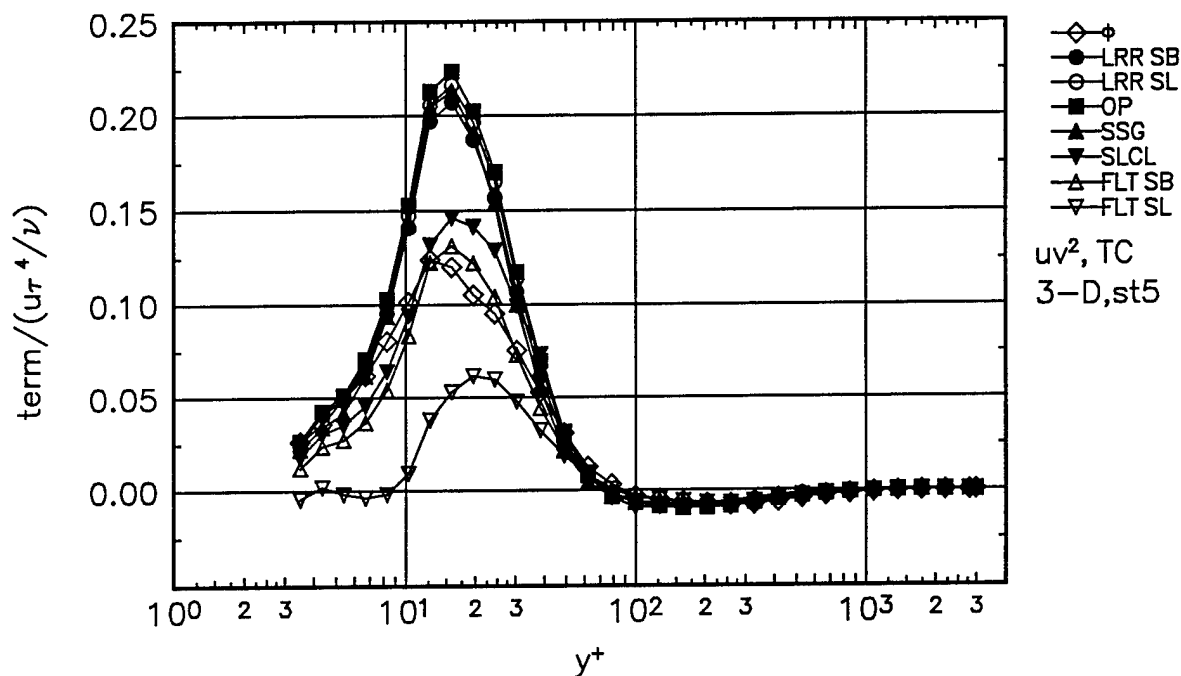
Figure 67. Comparison of $\overline{uw}$ shear stress transport experimental pressure-strain term ◊, to theoretical pressure-strain terms for Station 5. Gibson-Launder, ●; Launder-Reece-Rodi (LRR), O; Oberlack-Peters (OP), ■; Speziale-Sarkar-Gatski (SSG), ▲; Shih-Lumley/Choi-Lumley (SLCL), ▼; Fu-Launder-Tselepidakis 1 (FLT1), △; Fu-Launder-Tselepidakis 2 (FLT2), ▽. No near-wall corrections, dissipation is assumed zero.
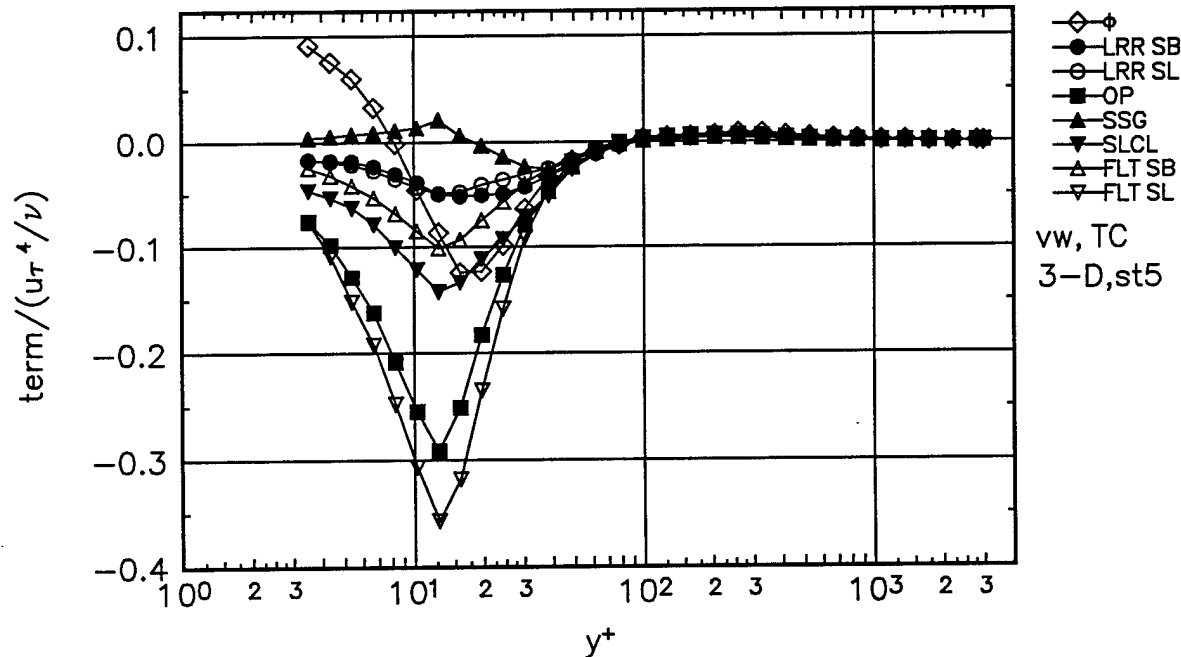
Figure 68. Comparison of $\overline{vw}$ shear stress transport experimental pressure-strain term ◊, to theoretical pressure-strain terms for Station 5. Gibson-Launder, ●; Launder-Reece-Rodi (LRR), O; Oberlack-Peters (OP), ■; Speziale-Sarkar-Gatski (SSG), ▲; Shih-Lumley/Choi-Lumley (SLCL), ▼; Fu-Launder-Tselepidakis 1 (FLT1), △; Fu-Launder-Tselepidakis 2 (FLT2), ▽. No near-wall corrections, dissipation is assumed zero.

Figures

88
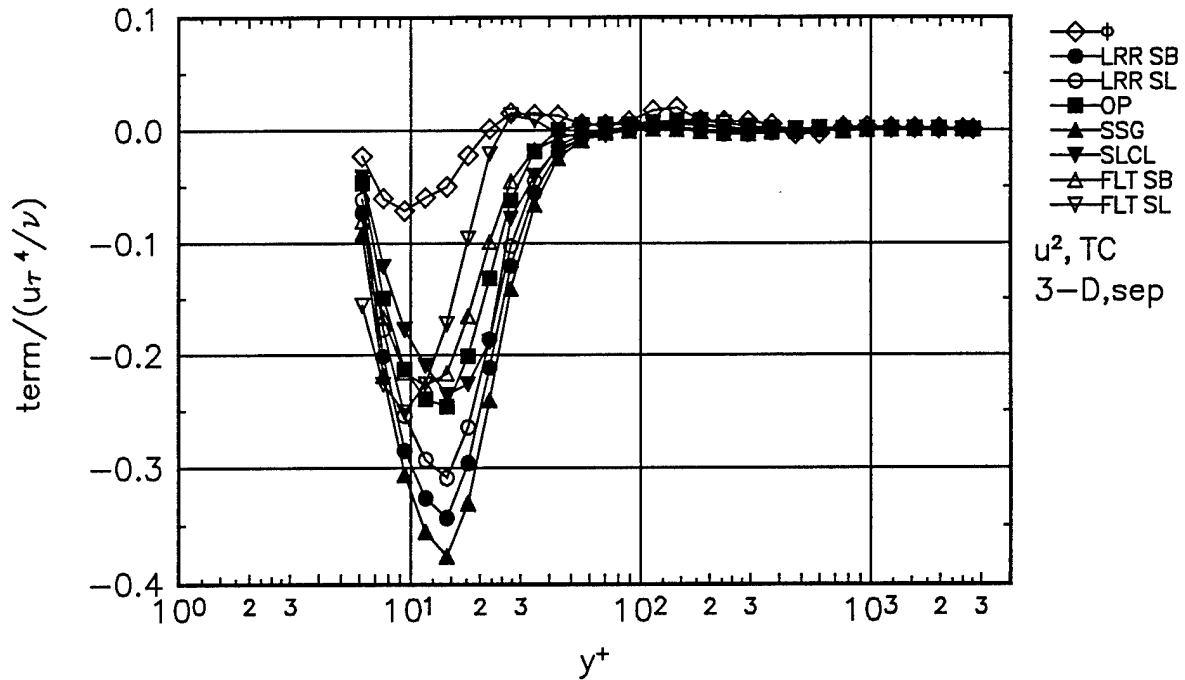
Figure 69. Comparison of $\overline{u^2}$ normal stress transport experimental pressure-strain term ◊, to theoretical pressure-strain terms for Separation station. Gibson-Launder, ●; Launder-Reece-Rodi (LRR), O; Oberlack-Peters (OP), ■; Speziale-Sarkar-Gatski (SSG), ▲; Shih-Lumley/Choi-Lumley (SLCL), ▼; Fu-Launder-Tselepidakis 1 (FLT1), △; Fu-Launder-Tselepidakis 2 (FLT2), ▽. No near-wall corrections, dissipation is assumed isotropic.
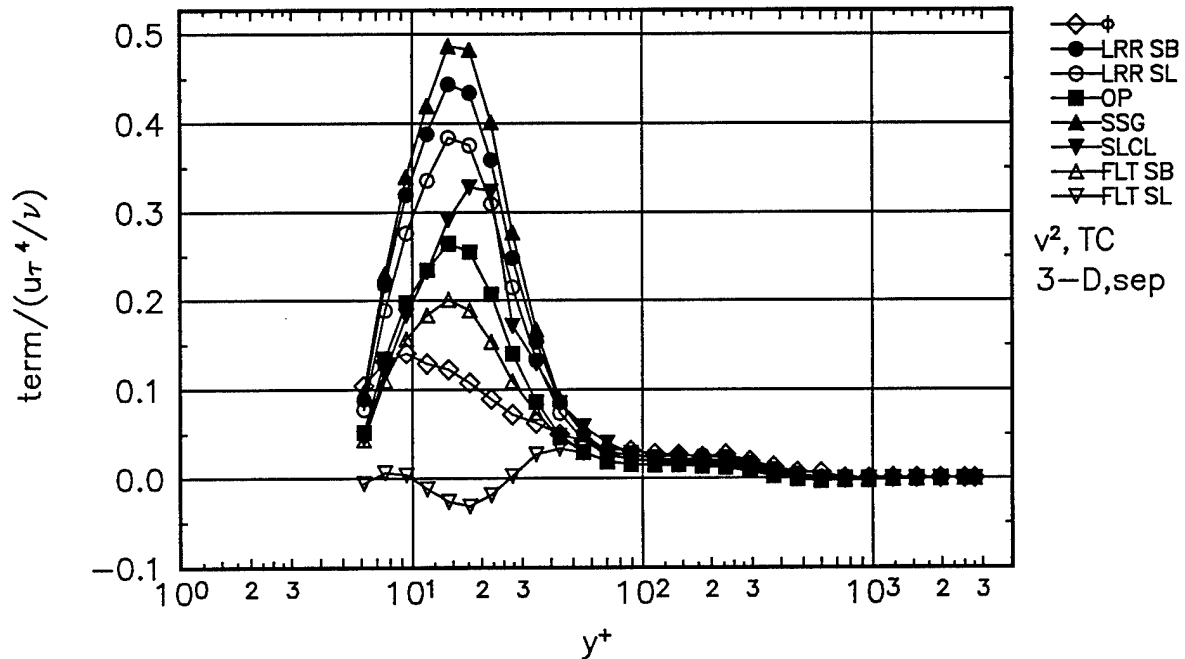
Figure 70. Comparison of $\overline{v^2}$ normal stress transport experimental pressure-strain term ◊, to theoretical pressure-strain terms for Separation station. Gibson-Launder, ●; Launder-Reece-Rodi (LRR), O; Oberlack-Peters (OP), ■; Speziale-Sarkar-Gatski (SSG), ▲; Shih-Lumley/Choi-Lumley (SLCL), ▼; Fu-Launder-Tselepidakis 1 (FLT1), △; Fu-Launder-Tselepidakis 2 (FLT2), ▽. No near-wall corrections, dissipation is assumed isotropic.
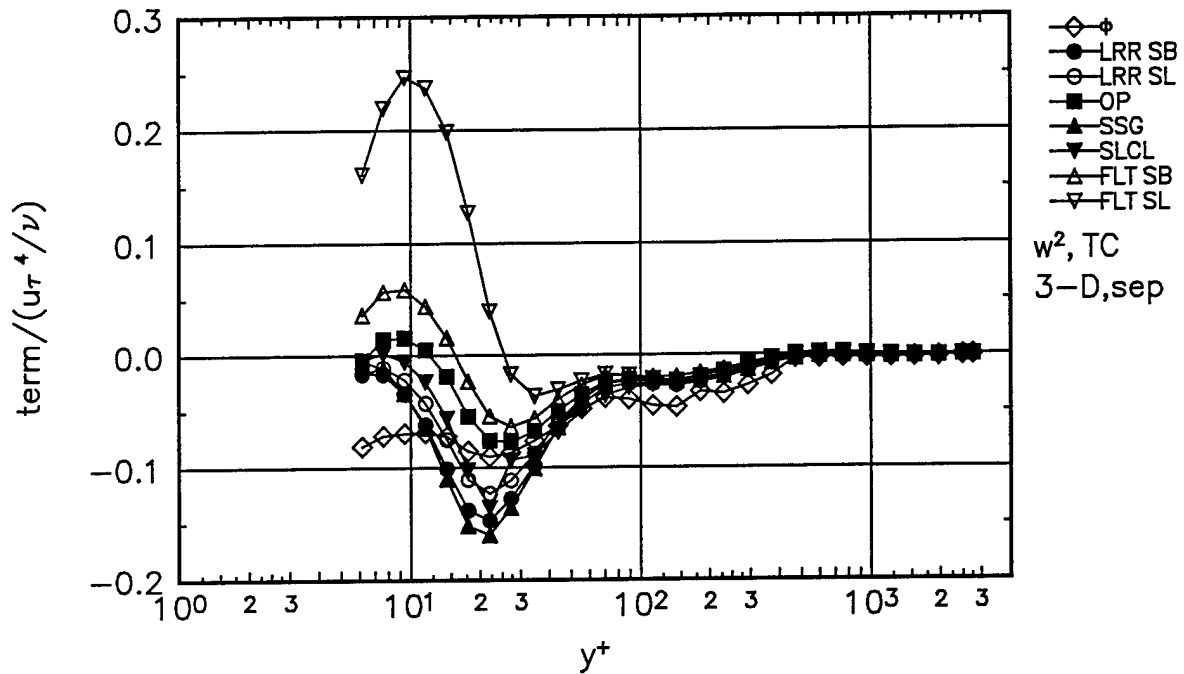
Figure 71. Comparison of $\overline{w^2}$ normal stress transport experimental pressure-strain term ◊, to theoretical pressure-strain terms for Separation station. Gibson-Launder, ●; Launder-Reece-Rodi (LRR), O; Oberlack-Peters (OP), ■; Speziale-Sarkar-Gatski (SSG), ▲; Shih-Lumley/Choi-Lumley (SLCL), ▼; Fu-Launder-Tselepidakis 1 (FLT1), △; Fu-Launder-Tselepidakis 2 (FLT2), ▽. No near-wall corrections, dissipation is assumed isotropic.
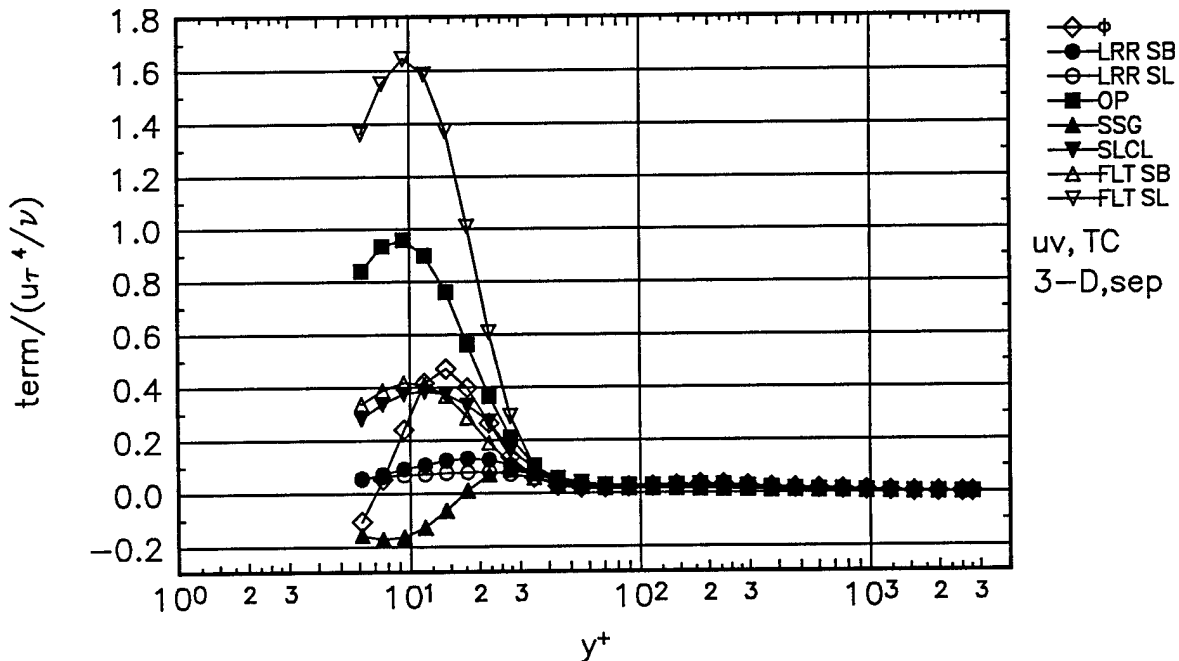
Figure 72. Comparison of $\overline{uv}$ shear stress transport experimental pressure-strain term ◊, to theoretical pressure-strain terms for Separation station. Gibson-Launder, ●; Launder-Reece-Rodi (LRR), O; Oberlack-Peters (OP), ■; Speziale-Sarkar-Gatski (SSG), ▲; Shih-Lumley/Choi-Lumley (SLCL), ▼; Fu-Launder-Tselepidakis 1 (FLT1), △; Fu-Launder-Tselepidakis 2 (FLT2), ▽. No near-wall corrections, dissipation is assumed zero.
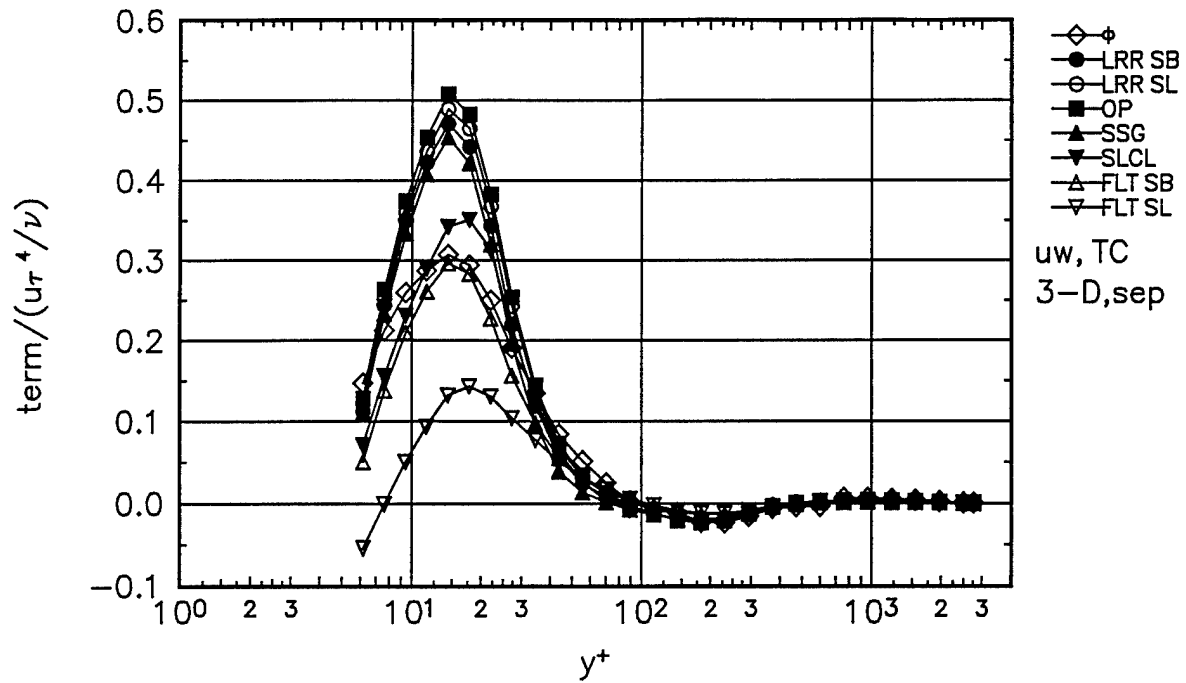
Figures   90

Figure 73. Comparison of $\overline{uw}$ shear stress transport experimental pressure-strain term ◊, to theoretical pressure-strain terms for Separation station. Gibson-Launder, ●; Launder-Reece-Rodi (LRR), O; Oberlack-Peters (OP), ■; Speziale-Sarkar-Gatski (SSG), ▲; Shih-Lumley/Choi-Lumley (SLCL), ▼; Fu-Launder-Tselepidakis 1 (FLT1), △; Fu-Launder-Tselepidakis 2 (FLT2), ▽. No near-wall corrections, dissipation is assumed zero.
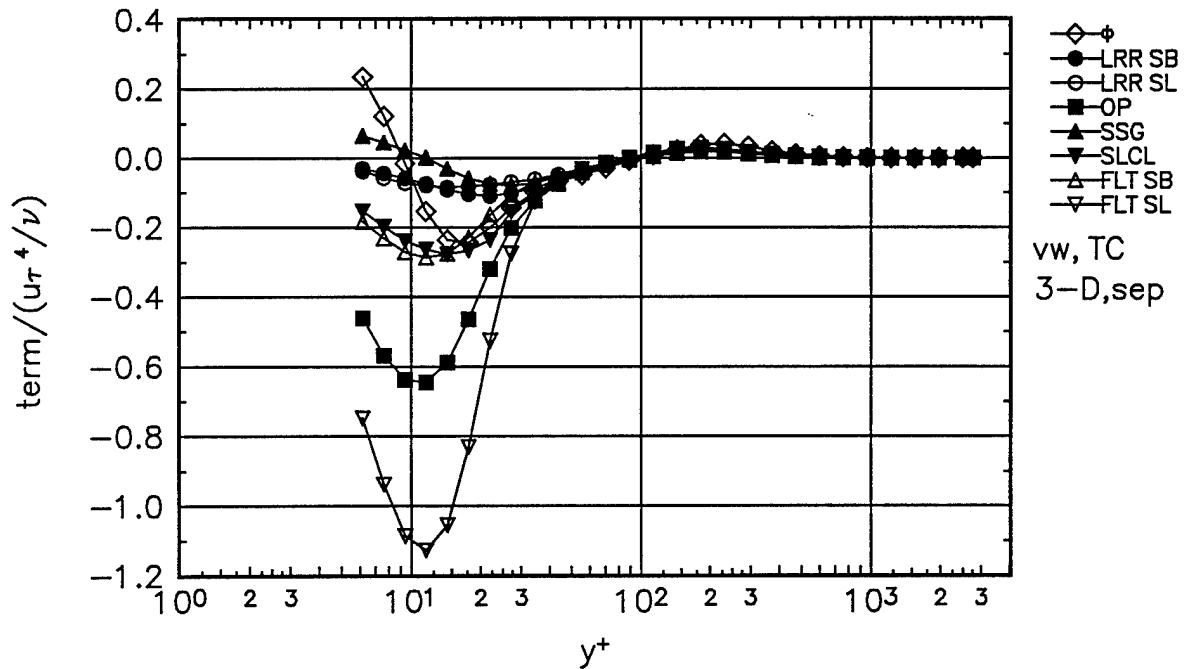
Figure 74. Comparison of $\overline{vw}$ shear stress transport experimental pressure-strain term ◊, to theoretical pressure-strain terms for Separation station. Gibson-Launder, ●; Launder-Reece-Rodi (LRR), O; Oberlack-Peters (OP), ■; Speziale-Sarkar-Gatski (SSG), ▲; Shih-Lumley/Choi-Lumley (SLCL), ▼; Fu-Launder-Tselepidakis 1 (FLT1), △; Fu-Launder-Tselepidakis 2 (FLT2), ▽. No near-wall corrections, dissipation is assumed zero.
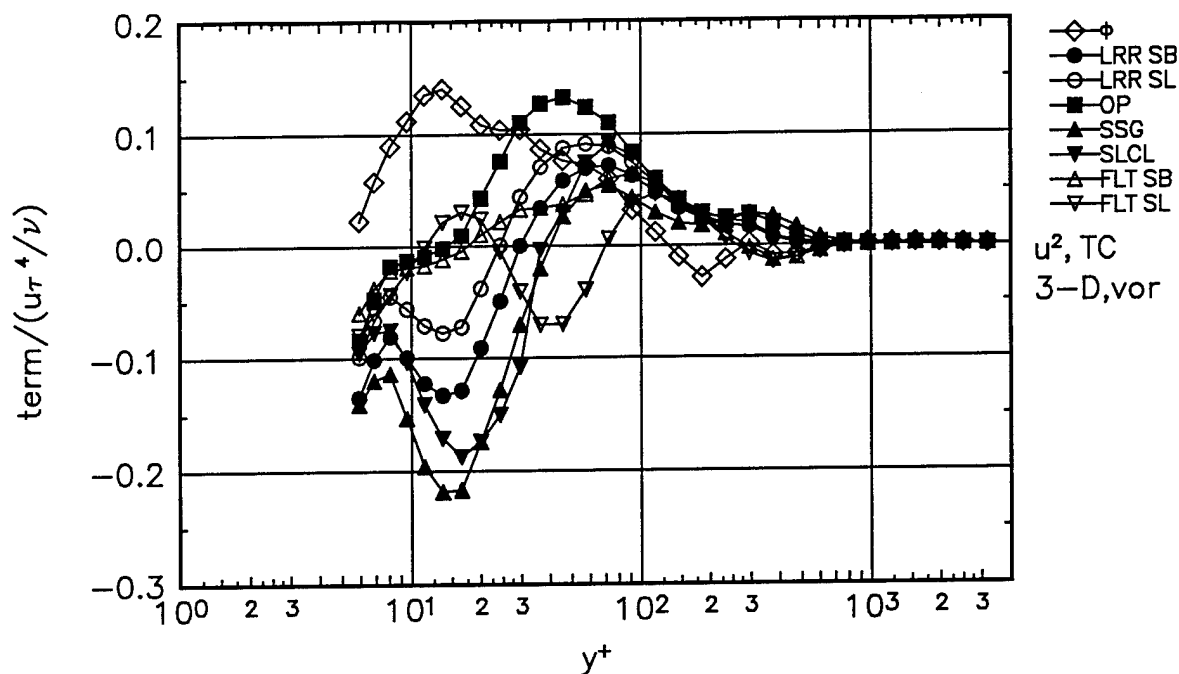
Figure 75. Comparison of $\overline{u^2}$ normal stress transport experimental pressure-strain term ◊, to theoretical pressure-strain terms for Vortex station. Gibson-Launder, ●; Launder-Reece-Rodi (LRR), O; Oberlack-Peters (OP), ■; Speziale-Sarkar-Gatski (SSG), ▲; Shih-Lumley/Choi-Lumley (SLCL), ▼; Fu-Launder-Tselepidakis 1 (FLT1), ▵; Fu-Launder-Tselepidakis 2 (FLT2), ▽. No near-wall corrections, dissipation is assumed isotropic.

Figure 76. Comparison of $\overline{v^2}$ normal stress transport experimental pressure-strain term ◊, to theoretical pressure-strain terms for Vortex station. Gibson-Launder, ●; Launder-Reece-Rodi (LRR), O; Oberlack-Peters (OP), ■; Speziale-Sarkar-Gatski (SSG), ▲; Shih-Lumley/Choi-Lumley (SLCL), ▼; Fu-Launder-Tselepidakis 1 (FLT1), ▵; Fu-Launder-Tselepidakis 2 (FLT2), ▽. No near-wall corrections, dissipation is assumed isotropic.

Figure 77. Comparison of $\overline{w^2}$ normal stress transport experimental pressure-strain term $\lozenge$, to theoretical pressure-strain terms for Vortex station. Gibson-Launder, ●; Launder-Reece-Rodi (LRR), O; Oberlack-Peters (OP), ■; Speziale-Sarkar-Gatski (SSG), ▲; Shih-Lumley/Choi-Lumley (SLCL), ▼; Fu-Launder-Tselepidakis 1 (FLT1), △; Fu-Launder-Tselepidakis 2 (FLT2), ▽. No near-wall corrections, dissipation is assumed isotropic.

Figure 78. Comparison of $\overline{uv}$ shear stress transport experimental pressure-strain term $\lozenge$, to theoretical pressure-strain terms for Vortex station. Gibson-Launder, ●; Launder-Reece-Rodi (LRR), O; Oberlack-Peters (OP), ■; Speziale-Sarkar-Gatski (SSG), ▲; Shih-Lumley/Choi-Lumley (SLCL), ▼; Fu-Launder-Tselepidakis 1 (FLT1), △; Fu-Launder-Tselepidakis 2 (FLT2), ▽. No near-wall corrections, dissipation is assumed zero.

Figures 93

Figure 79. Comparison of $\overline{uw}$ shear stress transport experimental pressure-strain term ◊, to theoretical pressure-strain terms for Vortex station. Gibson-Launder, ●; Launder-Reece-Rodi (LRR), O; Oberlack-Peters (OP), ■; Speziale-Sarkar-Gatski (SSG), ▲; Shih-Lumley/Choi-Lumley (SLCL), ▼; Fu-Launder-Tselepidakis 1 (FLT1), ▵; Fu-Launder-Tselepidakis 2 (FLT2), ▽. No near-wall corrections, dissipation is assumed zero.

Figure 80. Comparison of $\overline{vw}$ shear stress transport experimental pressure-strain term ◊, to theoretical pressure-strain terms for Vortex station. Gibson-Launder, ●; Launder-Reece-Rodi (LRR), O; Oberlack-Peters (OP), ■; Speziale-Sarkar-Gatski (SSG), ▲; Shih-Lumley/Choi-Lumley (SLCL), ▼; Fu-Launder-Tselepidakis 1 (FLT1), ▵; Fu-Launder-Tselepidakis 2 (FLT2), ▽. No near-wall corrections, dissipation is assumed zero.

Anisotropic dissipation tensor of Hallback, Groth, and Johansson, without the near wall corrections of Launder-Reece-Rodi. The balance figures change since the dissipation and pressure-strain terms are effected from these anisotropies.

anisotropic dissipation terms for 2—D by Hallback et al.
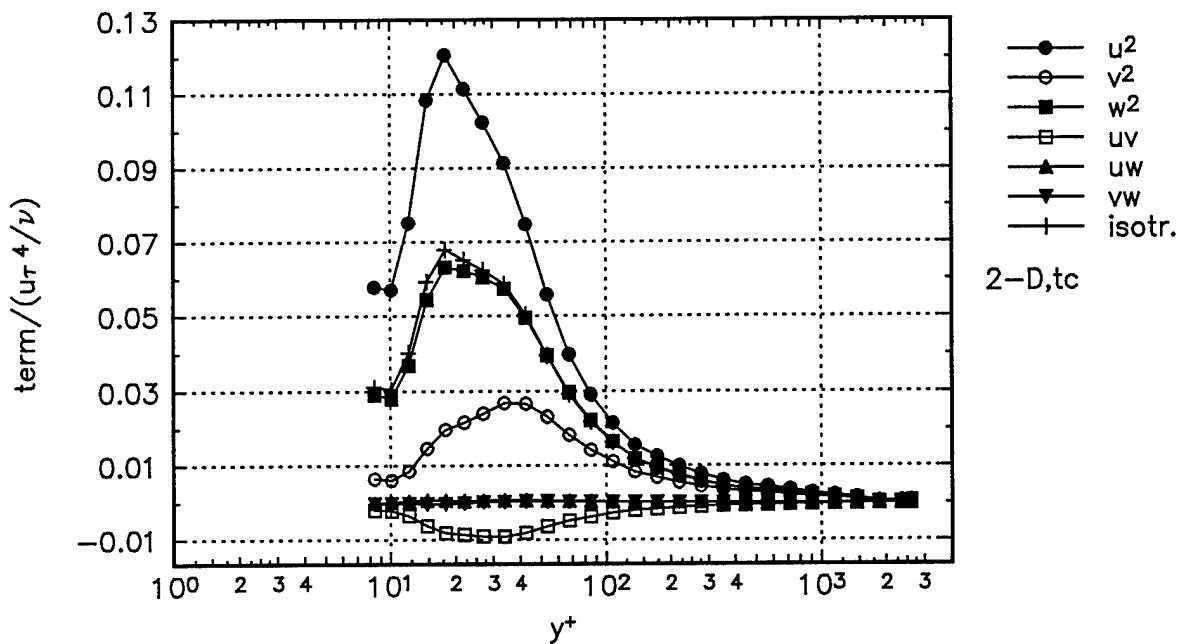
Figure 81. Anisotropic dissipation rate distribution calculated using Hallbäck et al. (1990) model for the 2-D station in tunnel coordinates. $\overline{u^2}$, ●; $\overline{v^2}$, O; $\overline{w^2}$, ■; $\overline{uv}$, □; $\overline{uw}$, ▲; $\overline{vw}$, ▼; isotropic distribution, +.

anisotropic dissipation terms for 3—D,st5 by Hallback et al.
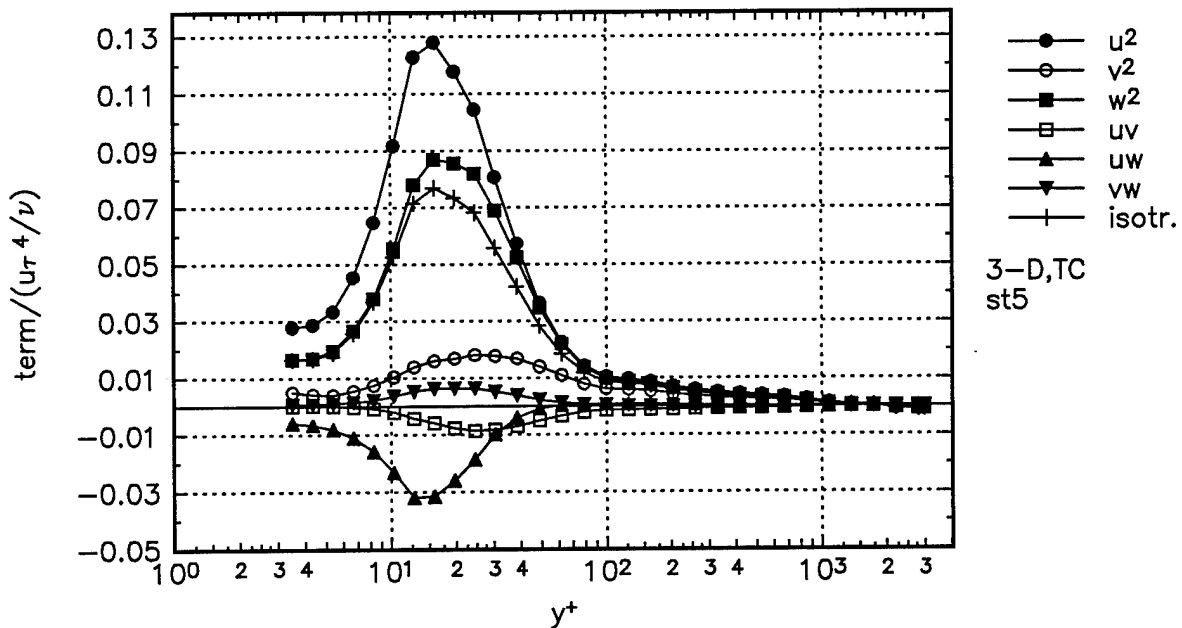
Figure 82. Anisotropic dissipation rate distribution calculated using Hallbäck et al. (1990) model for Station 5 in tunnel coordinates. $\overline{u^2}$, ●; $\overline{v^2}$, O; $\overline{w^2}$, ■; $\overline{uv}$, □; $\overline{uw}$, ▲; $\overline{vw}$, ▼; isotropic distribution, +.

anisotropic dissipation terms for 3–D,sep by Hallback et al.
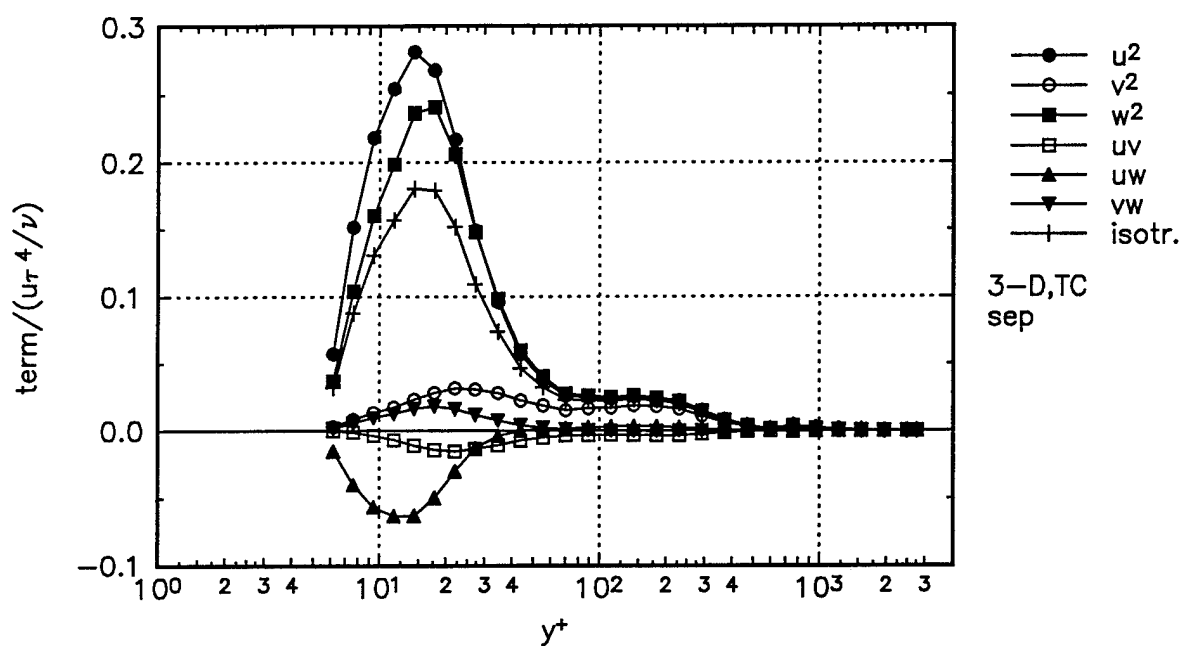
Figure 83. Anisotropic dissipation rate distribution calculated using Hallbäck et al. (1990) model for Separation station in tunnel coordinates. $\overline{u^2}$, ●; $\overline{v^2}$, O; $\overline{w^2}$, ■; $\overline{uv}$, □; $\overline{uw}$, ▲; $\overline{vw}$, ▼; isotropic distribution, +.

anisotropic dissipation terms for 3–D,sep by Hallback et al.
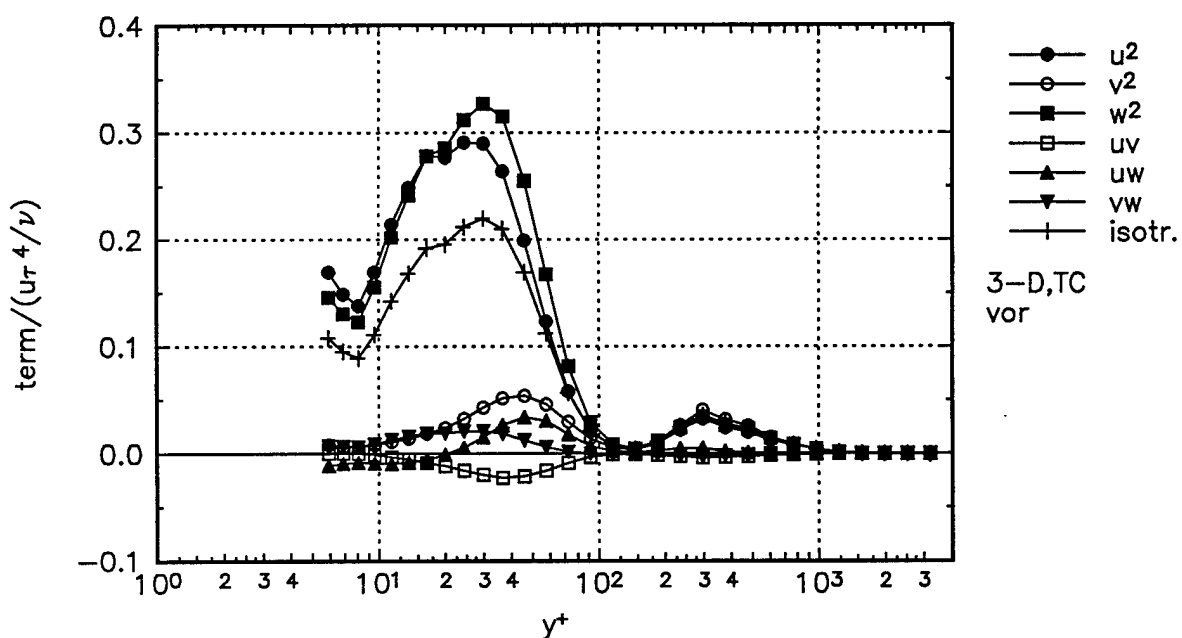
Figure 84. Anisotropic dissipation rate distribution calculated using Hallbäck et al. (1990) model for Vortex station in tunnel coordinates. $\overline{u^2}$, ●; $\overline{v^2}$, O; $\overline{w^2}$, ■; $\overline{uv}$, □; $\overline{uw}$, ▲; $\overline{vw}$, ▼; isotropic distribution, +.
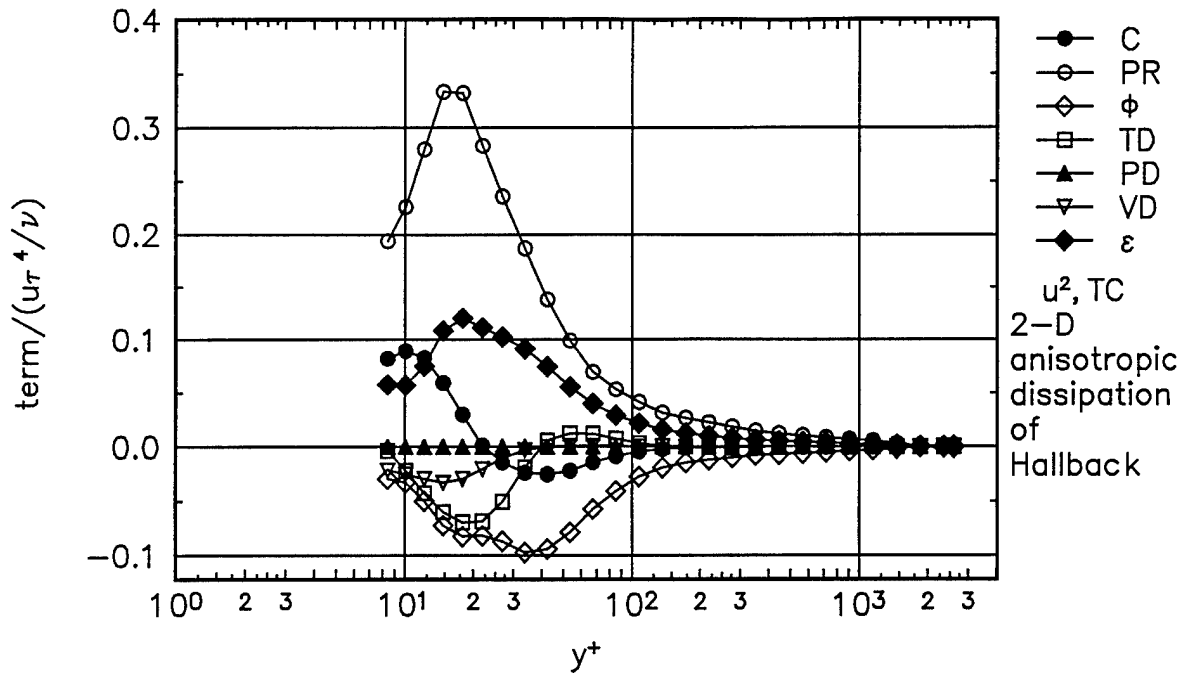
Figure 85. $\overline{u^2}$ normal stress transport budget with anisotropic dissipation model of Hallbäck et al (1990) at 2-D station in tunnel coordinates. ●, convection (C); ○, production (PR); ◊, pressure-strain (φ); □, turbulent diffusion (TD); ▲, pressure diffusion (PD); ▽, viscous diffusion (VD); ♦, dissipation (ε).
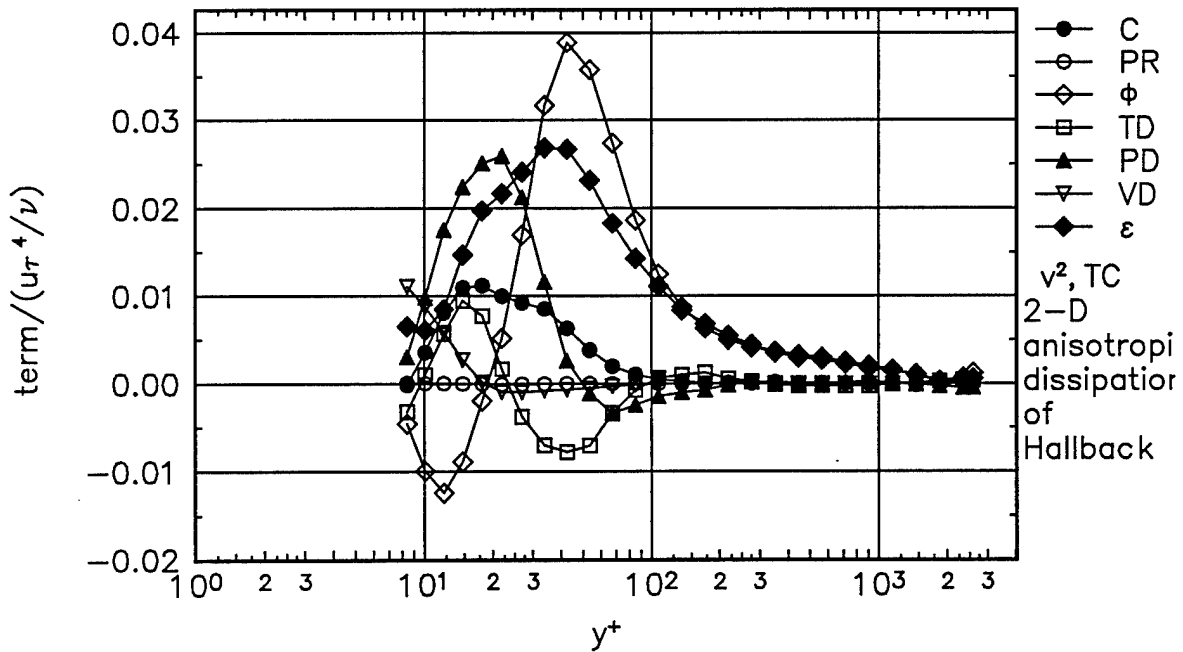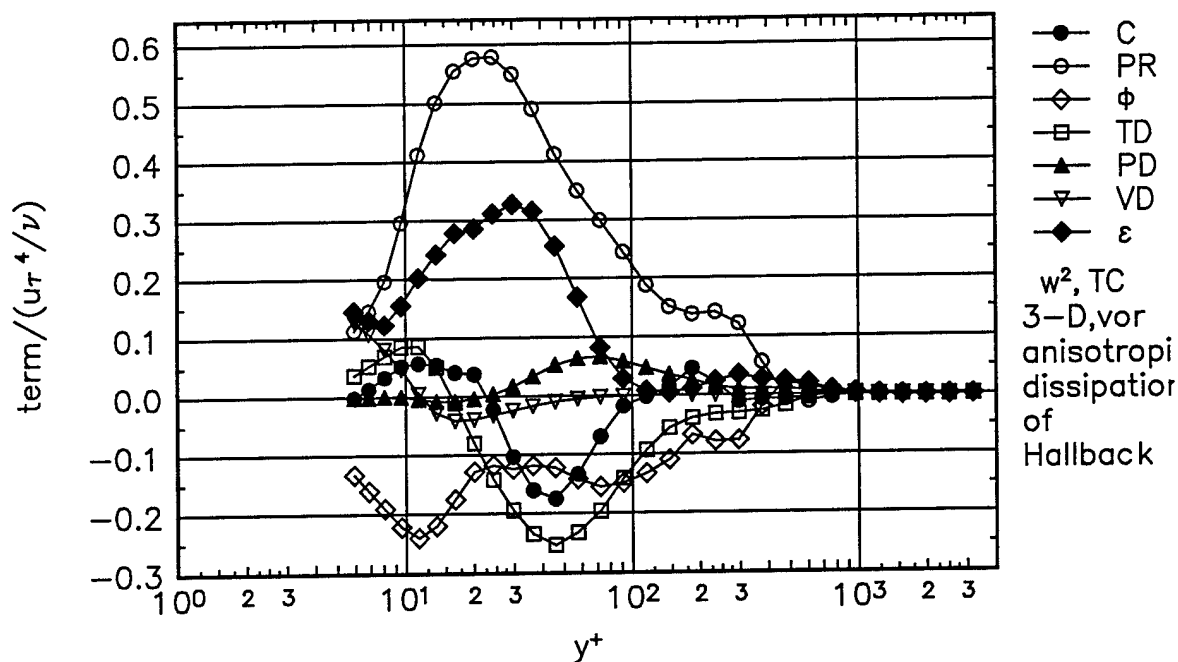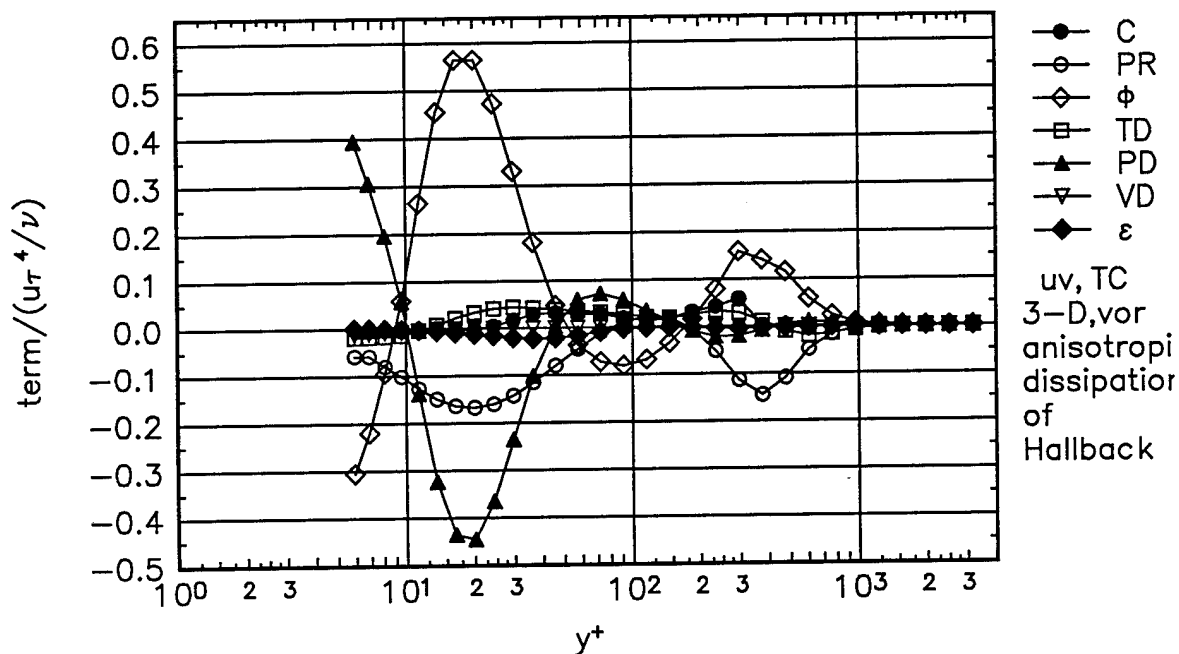

Figure 86. $\overline{v^2}$ normal stress transport budget with anisotropic dissipation model of Hallbäck et al (1990) at 2-D station in tunnel coordinates. ●, convection (C); ○, production (PR); ◊, pressure-strain (φ); □, turbulent diffusion (TD); ▲, pressure diffusion (PD); ▽, viscous diffusion (VD); ♦, dissipation (ε).
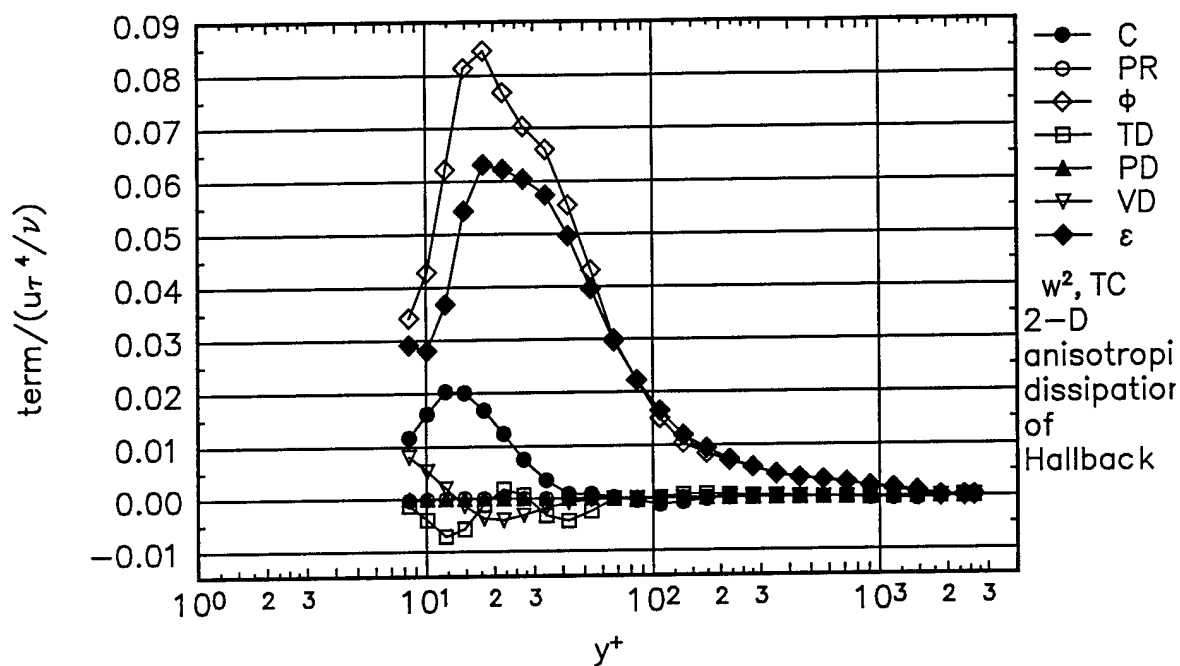
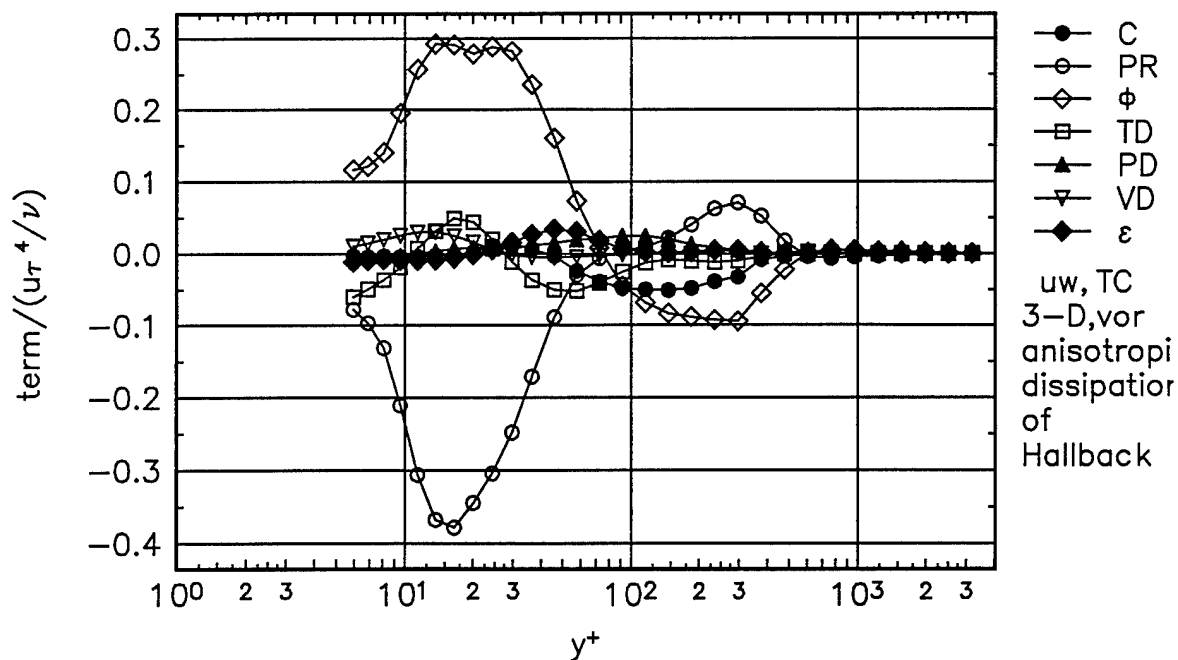Figures   97

Figure 87. $\overline{w^2}$ normal stress transport budget with anisotropic dissipation model of Hallbäck et al (1990) at 2-D station in tunnel coordinates. ●, convection (C); O, production (PR); ◊, pressure-strain (φ); □, turbulent diffusion (TD); ▲, pressure diffusion (PD); ▽, viscous diffusion (VD); ◆, dissipation (ε).
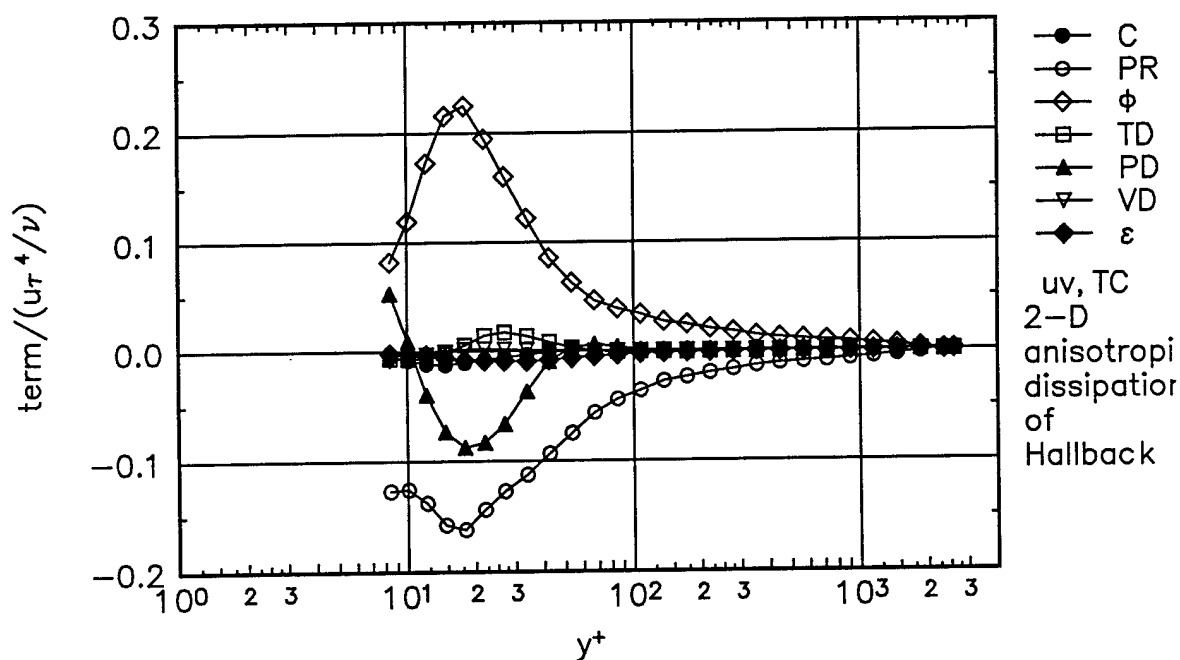
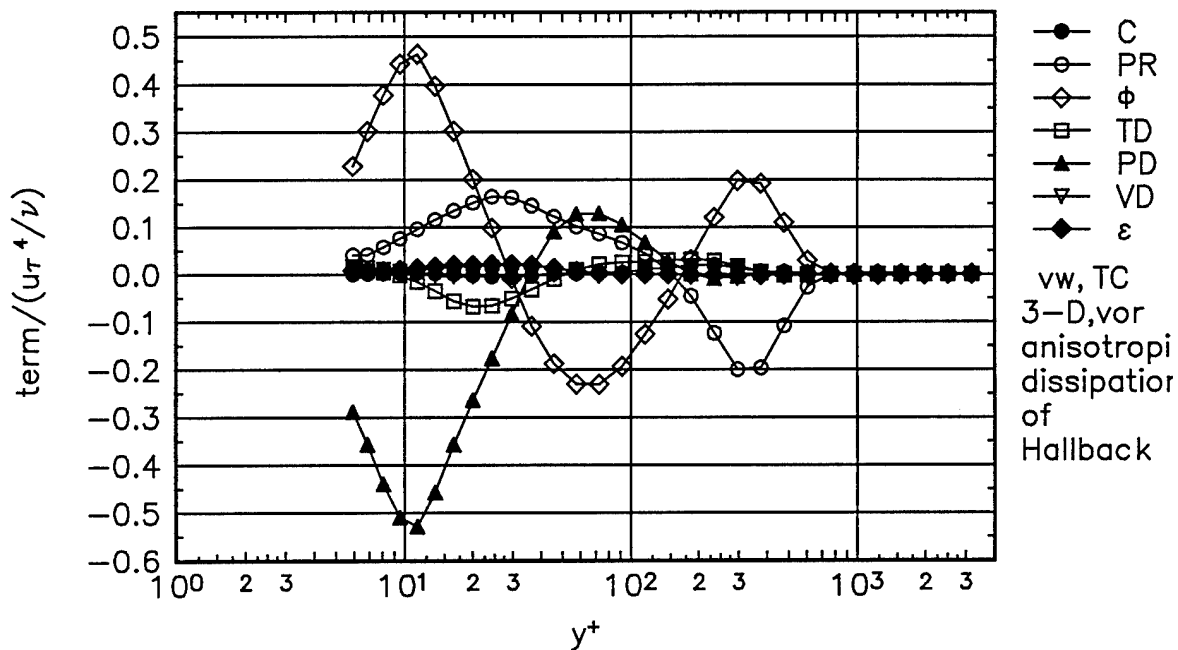Figure 88. $\overline{uv}$ shear stress transport budget with anisotropic dissipation model of Hallbäck et al (1990) at 2-D station in tunnel coordinates. ●, convection (C); O, production (PR); ◊, pressure-strain (φ); □, turbulent diffusion (TD); ▲, pressure diffusion (PD); ▽, viscous diffusion (VD); ◆, dissipation (ε).
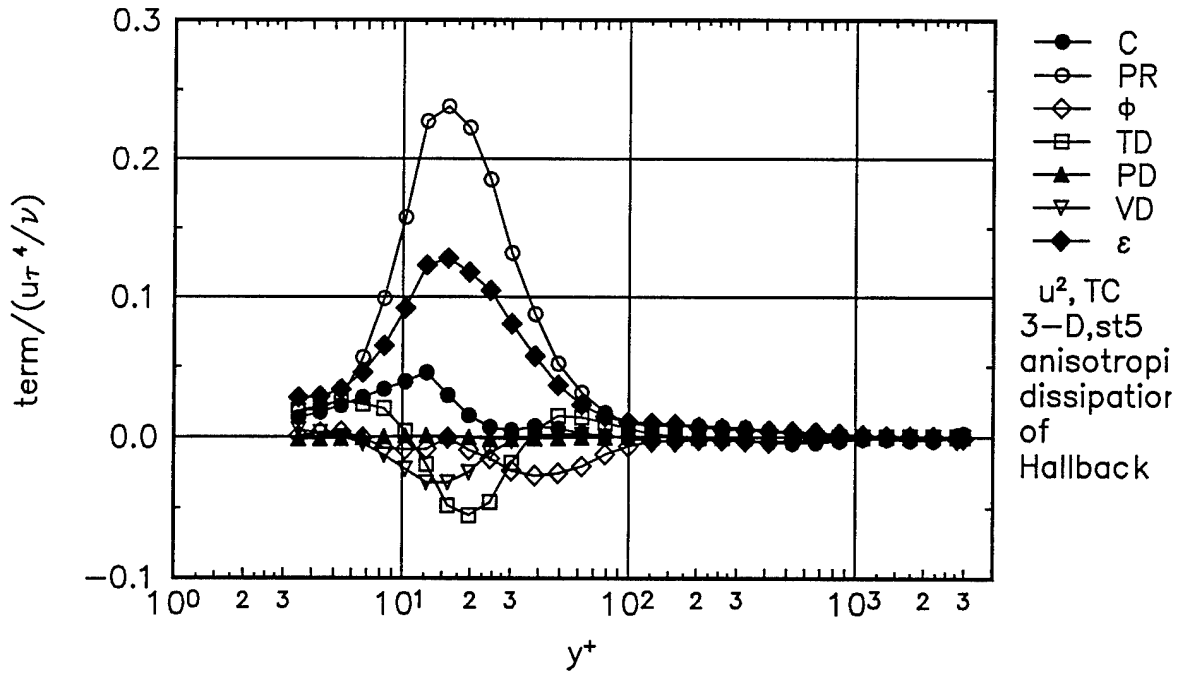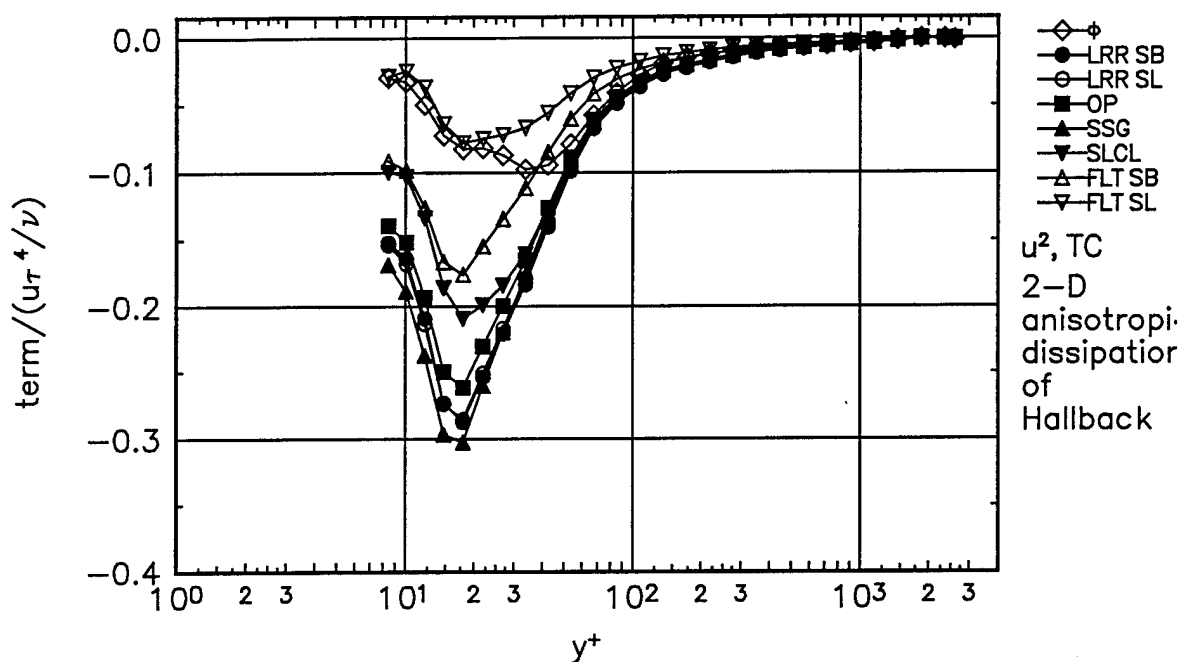
Figure 89. $\overline{u^2}$ normal stress transport budget with anisotropic dissipation model of Hallbäck et al (1990) at Station 5 in tunnel coordinates. ●, convection (C); O, production (PR); ◊, pressure-strain (φ); □, turbulent diffusion (TD); ▲, pressure diffusion (PD); ▽, viscous diffusion (VD); ♦, dissipation (ε).
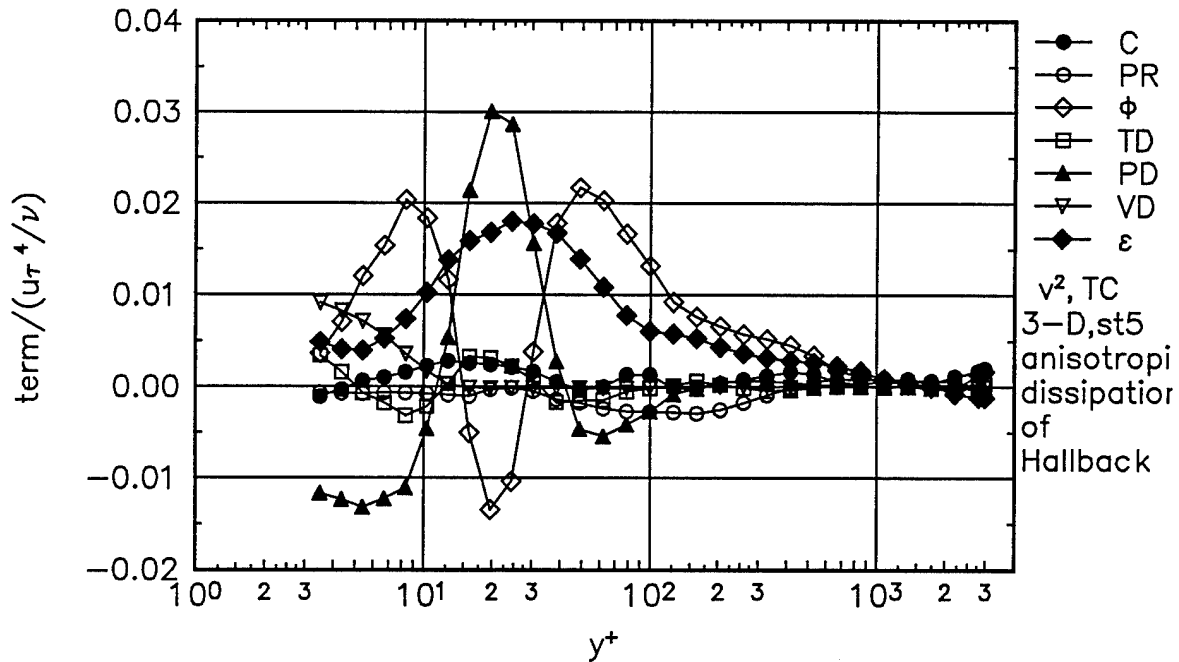
Figure 90. $\overline{v^2}$ normal stress transport budget with anisotropic dissipation model of Hallbäck et al (1990) at Station 5 in tunnel coordinates. ●, convection (C); O, production (PR); ◊, pressure-strain (φ); □, turbulent diffusion (TD); ▲, pressure diffusion (PD); ▽, viscous diffusion (VD); ♦, dissipation (ε).
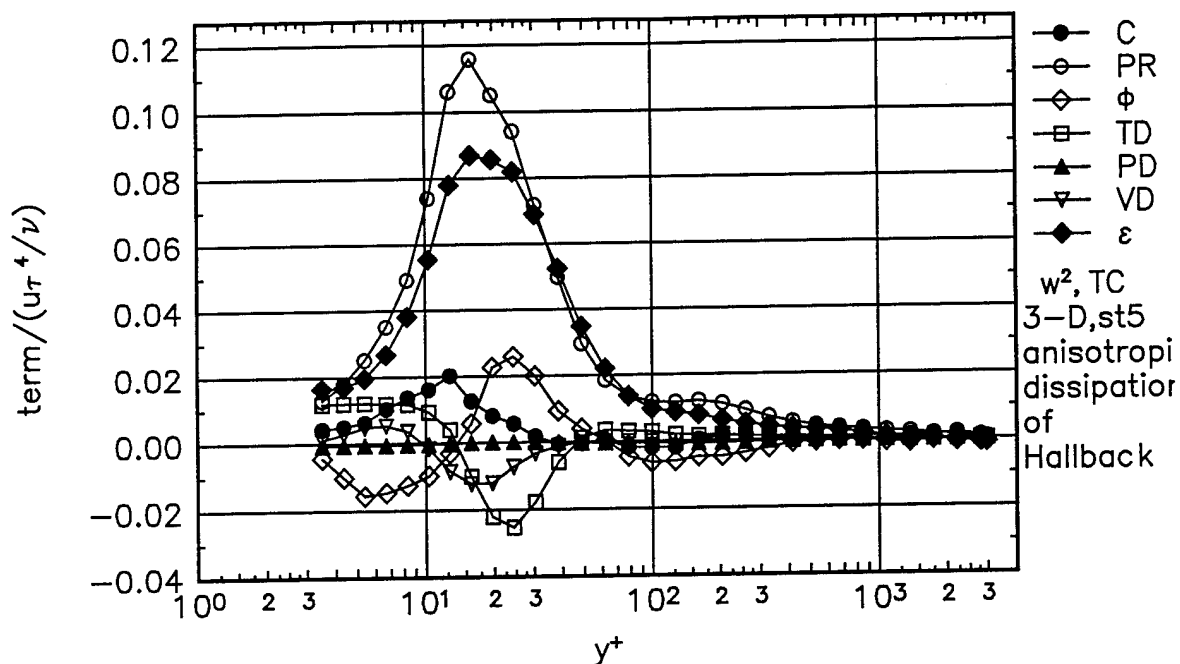
Figure 91. $\overline{w^2}$ normal stress transport budget with anisotropic dissipation model of Hallbäck et al (1990) at Station 5 in tunnel coordinates. ●, convection (C); O, production (PR); ◊, pressure-strain (φ); □, turbulent diffusion (TD); ▲, pressure diffusion (PD); ▽, viscous diffusion (VD); ◆, dissipation (ε).
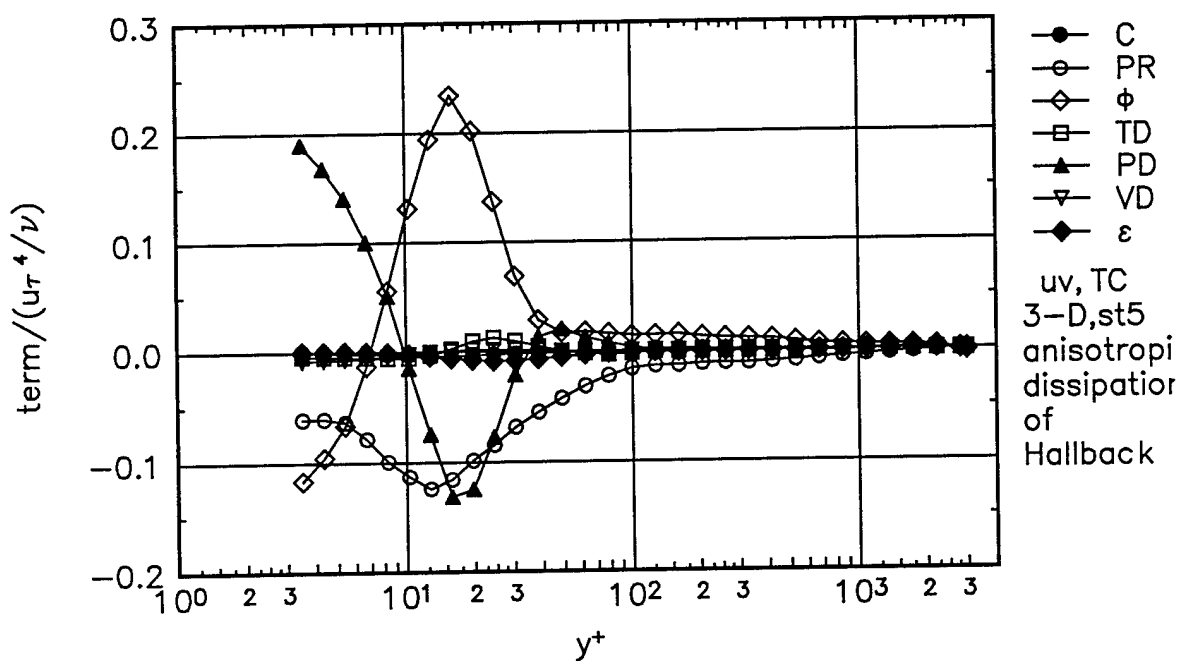
Figure 92. $\overline{uv}$ shear stress transport budget with anisotropic dissipation model of Hallbäck et al (1990) at Station 5 in tunnel coordinates. ●, convection (C); O, production (PR); ◊, pressure-strain (φ); □, turbulent diffusion (TD); ▲, pressure diffusion (PD); ▽, viscous diffusion (VD); ◆, dissipation (ε).
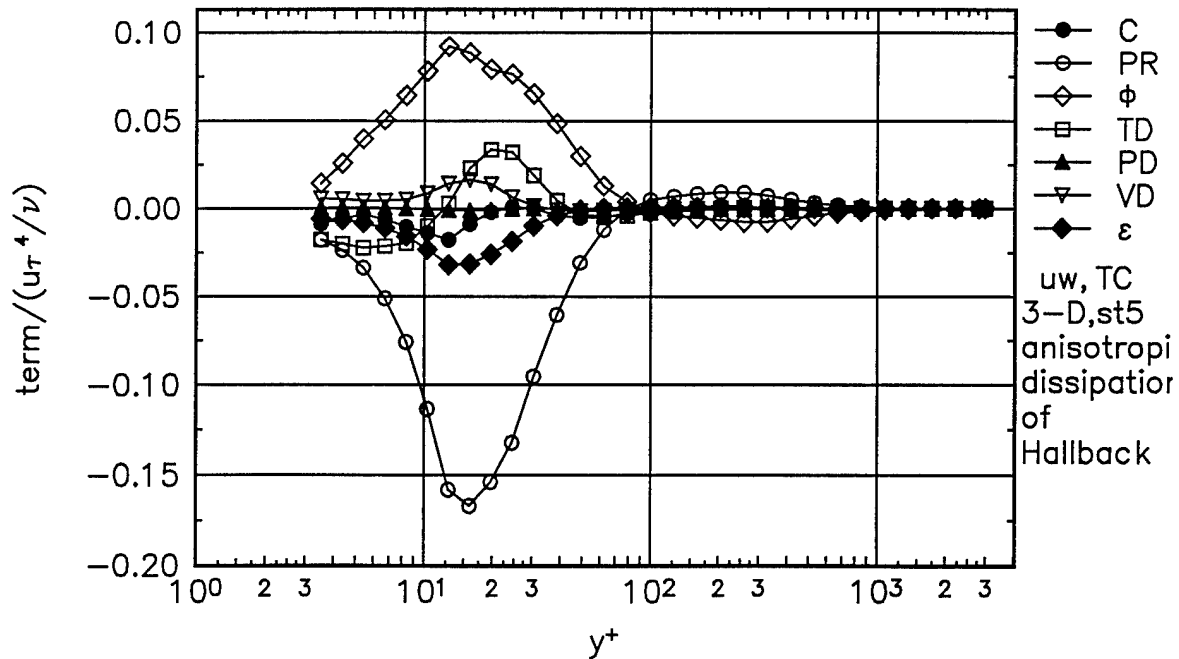
Figures

Figure 93. $\overline{uw}$ shear stress transport budget with anisotropic dissipation model of Hallbäck et al (1990) at Station 5 in tunnel coordinates. ●, convection (C); ○, production (PR); ◊, pressure-strain (φ); □, turbulent diffusion (TD); ▲, pressure diffusion (PD); ▽, viscous diffusion (VD); ◆, dissipation (ε).
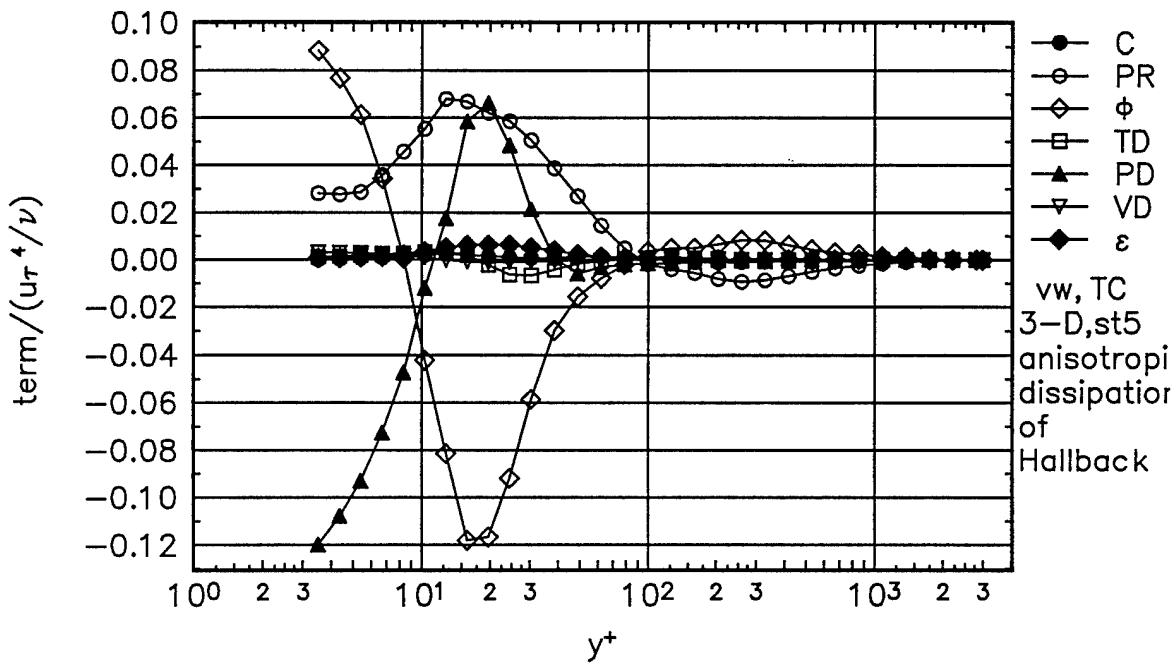
Figure 94. $\overline{vw}$ shear stress transport budget with anisotropic dissipation model of Hallbäck et al (1990) at Station 5 in tunnel coordinates. ●, convection (C); ○, production (PR); ◊, pressure-strain (φ); □, turbulent diffusion (TD); ▲, pressure diffusion (PD); ▽, viscous diffusion (VD); ◆, dissipation (ε).

Figures   101
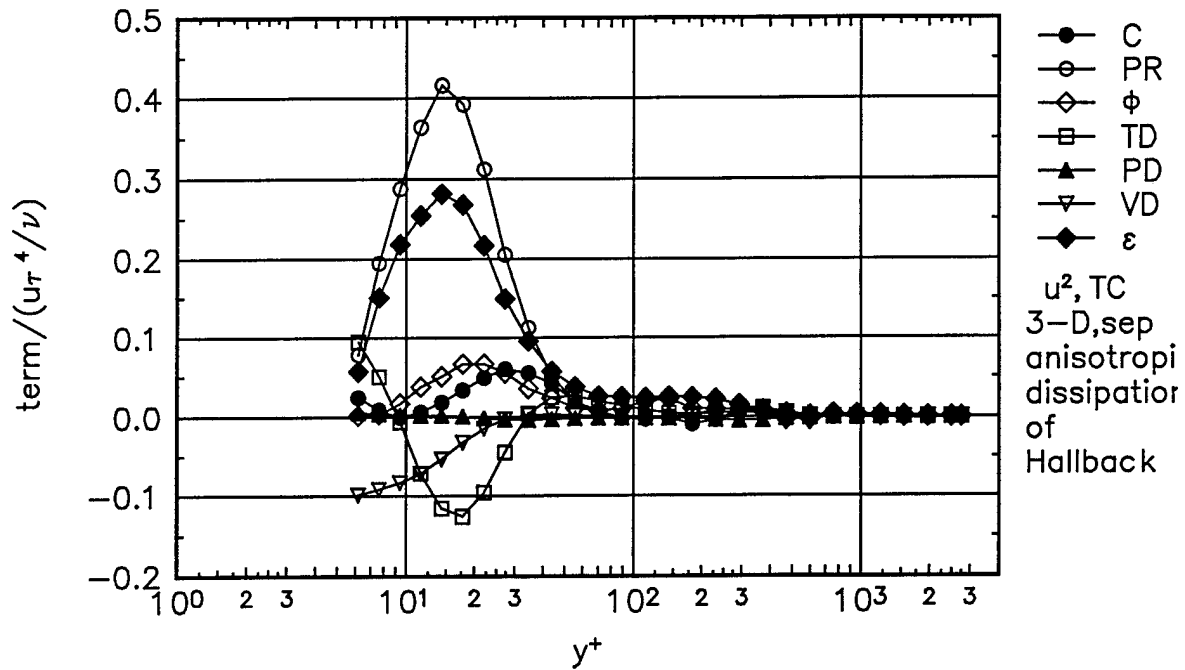
Figure 95. $\overline{u^2}$ normal stress transport budget with anisotropic dissipation model of Hallbäck et al (1990) at Separation station in tunnel coordinates. ●, convection (C); O, production (PR); ◊, pressure-strain (φ); □, turbulent diffusion (TD); ▲, pressure diffusion (PD); ▽, viscous diffusion (VD); ◆, dissipation (ε).
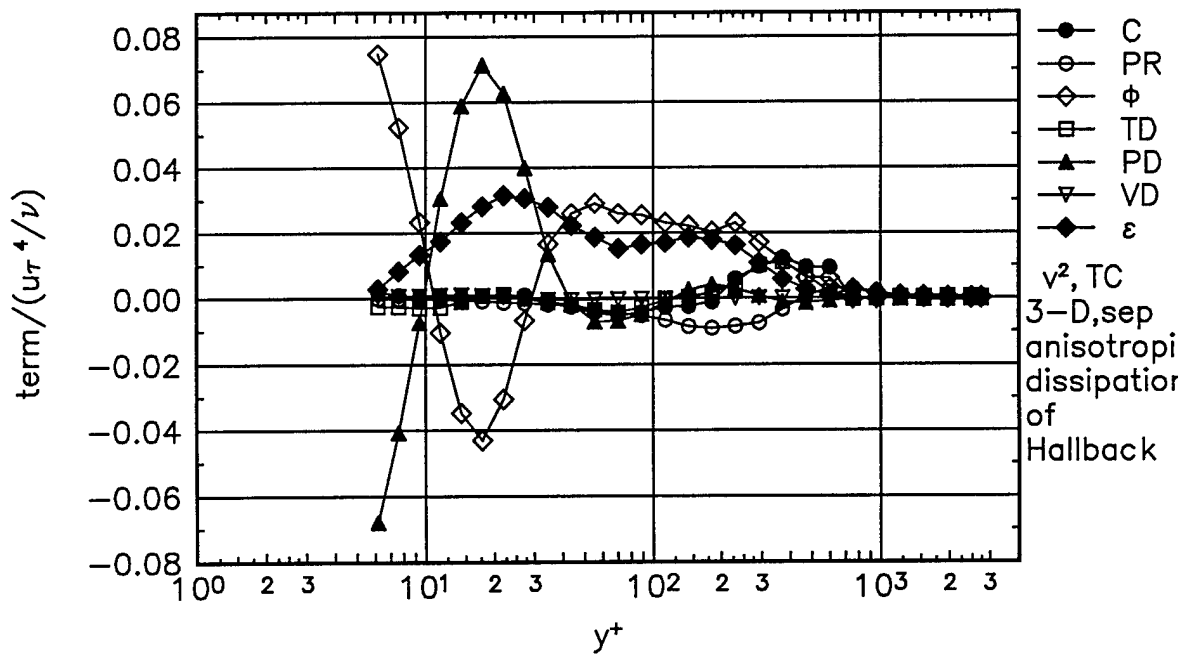
Figure 96. $\overline{v^2}$ normal stress transport budget with anisotropic dissipation model of Hallbäck et al (1990) at Separation station in tunnel coordinates. ●, convection (C); O, production (PR); ◊, pressure-strain (φ); □, turbulent diffusion (TD); ▲, pressure diffusion (PD); ▽, viscous diffusion (VD); ◆, dissipation (ε).

Figure 97. $\overline{w^2}$ normal stress transport budget with anisotropic dissipation model of Hallbäck et al (1990) at Separation station in tunnel coordinates. ●, convection (C); O, production (PR); ◊, pressure-strain (φ); □, turbulent diffusion (TD); ▲, pressure diffusion (PD); ▽, viscous diffusion (VD); ♦, dissipation (ε).

Figure 98. $\overline{uv}$ shear stress transport budget with anisotropic dissipation model of Hallbäck et al (1990) at Separation station in tunnel coordinates. ●, convection (C); O, production (PR); ◊, pressure-strain (φ); □, turbulent diffusion (TD); ▲, pressure diffusion (PD); ▽, viscous diffusion (VD); ♦, dissipation (ε).

Figures   103

Figure 99. $\overline{uw}$ shear stress transport budget with anisotropic dissipation model of Hallbäck et al (1990) at Separation station in tunnel coordinates. ●, convection (C); O, production (PR); ◊, pressure-strain (φ); □, turbulent diffusion (TD); ▲, pressure diffusion (PD); ▽, viscous diffusion (VD); ◆, dissipation (ε).
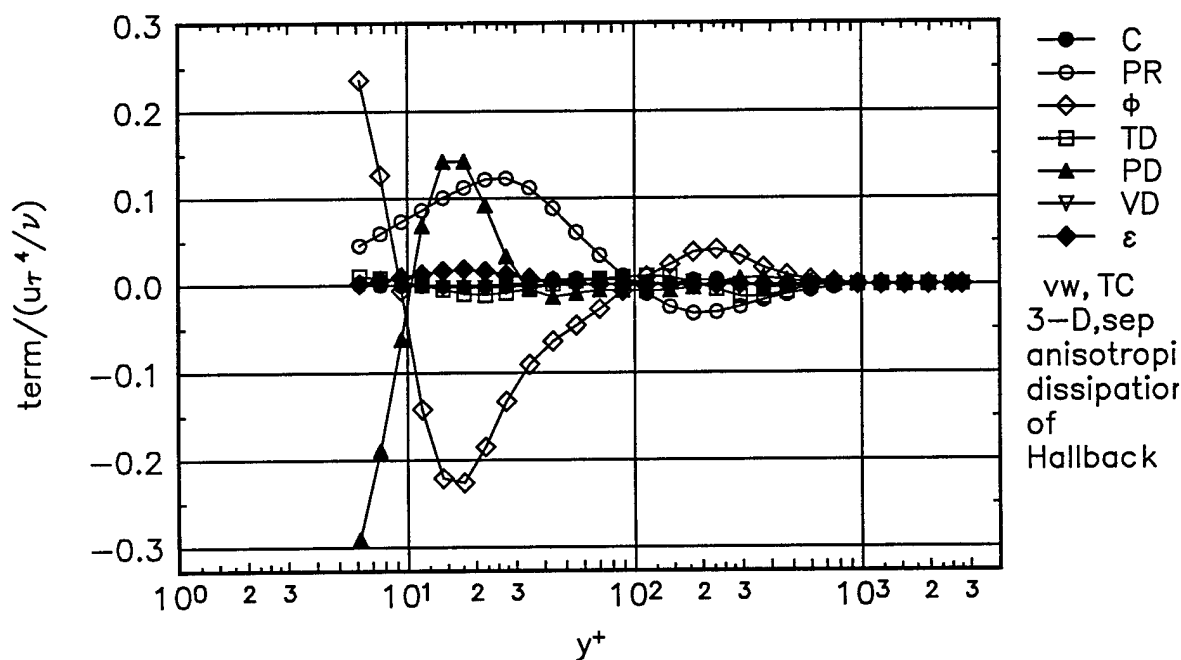
Figure 100. $\overline{vw}$ shear stress transport budget with anisotropic dissipation model of Hallbäck et al (1990) at Separation station in tunnel coordinates. ●, convection (C); O, production (PR); ◊, pressure-strain (φ); □, turbulent diffusion (TD); ▲, pressure diffusion (PD); ▽, viscous diffusion (VD); ◆, dissipation (ε).
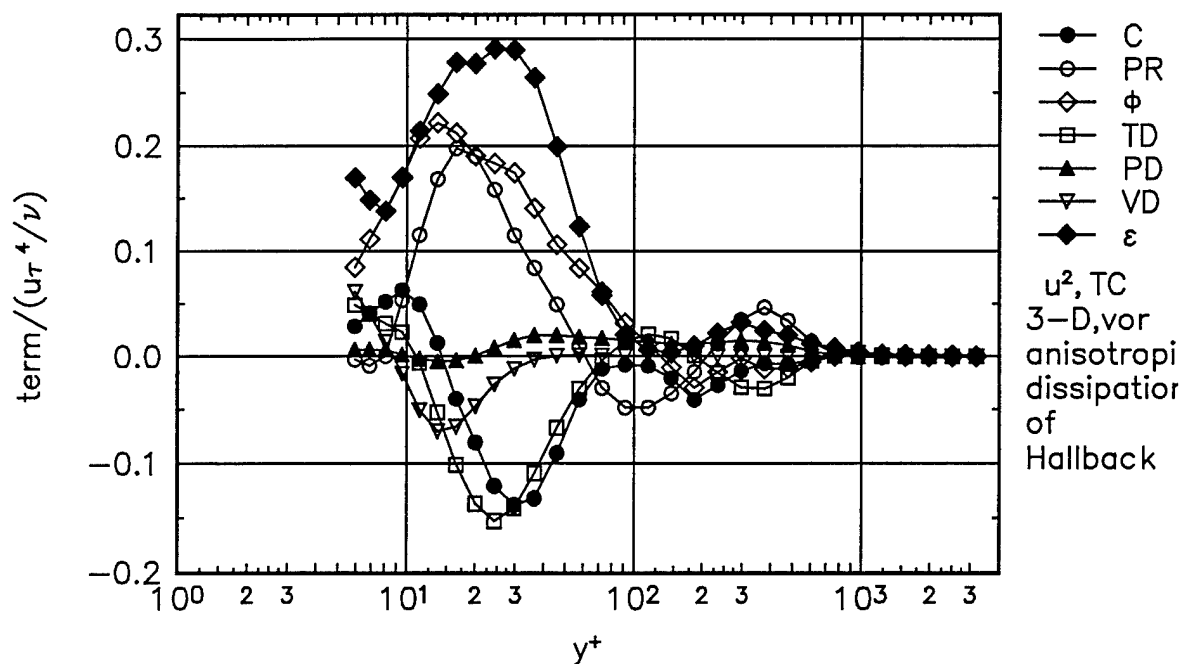
Figure 101. $\overline{u^2}$ normal stress transport budget with anisotropic dissipation model of Hallbäck et al (1990) at Vortex station in tunnel coordinates. ●, convection (C); ○, production (PR); ◊, pressure-strain (φ); □, turbulent diffusion (TD); ▲, pressure diffusion (PD); ▽, viscous diffusion (VD); ♦, dissipation (ε).
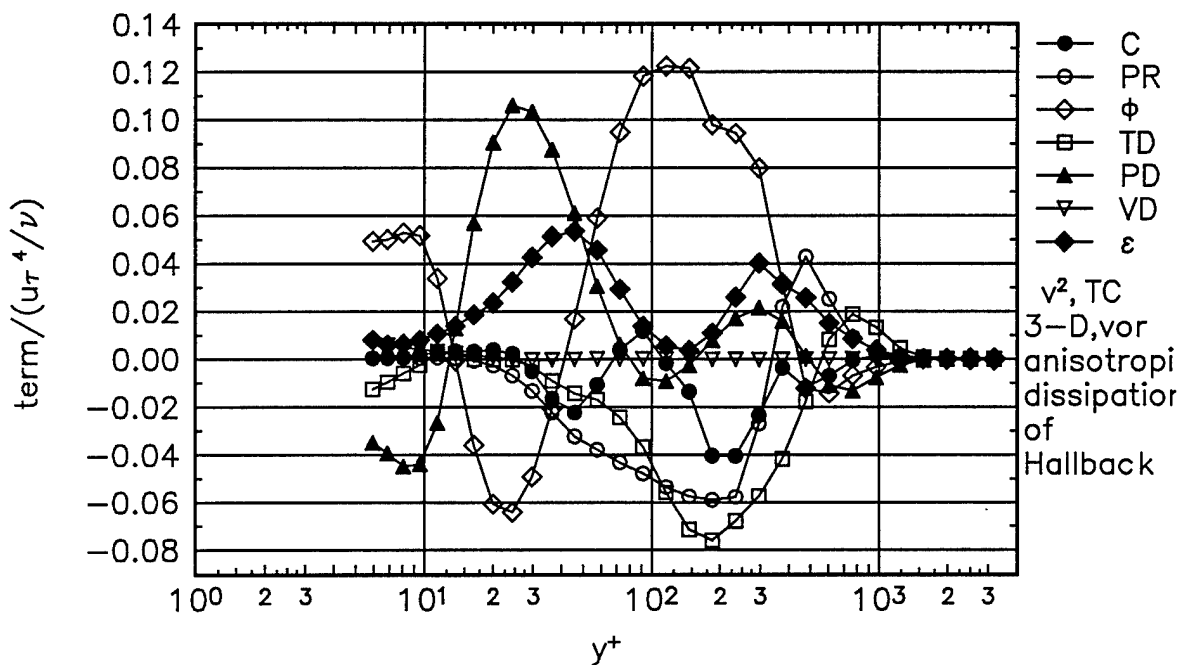
Figure 102. $\overline{v^2}$ normal stress transport budget with anisotropic dissipation model of Hallbäck et al (1990) at Vortex station in tunnel coordinates. ●, convection (C); ○, production (PR); ◊, pressure-strain (φ); □, turbulent diffusion (TD); ▲, pressure diffusion (PD); ▽, viscous diffusion (VD); ♦, dissipation (ε).

Figure 103. $\overline{w^2}$ normal stress transport budget with anisotropic dissipation model of Hallbäck et al (1990) at Vortex station in tunnel coordinates. ●, convection (C); O, production (PR); ◊, pressure-strain (φ); □, turbulent diffusion (TD); ▲, pressure diffusion (PD); ▽, viscous diffusion (VD); ♦, dissipation (ε).

Figure 104. $\overline{uv}$ shear stress transport budget with anisotropic dissipation model of Hallbäck et al (1990) at Vortex station in tunnel coordinates. ●, convection (C); O, production (PR); ◊, pressure-strain (φ); □, turbulent diffusion (TD); ▲, pressure diffusion (PD); ▽, viscous diffusion (VD); ♦, dissipation (ε).

Figures

Figure 105. $\overline{uw}$ shear stress transport budget with anisotropic dissipation model of Hallbäck et al (1990) at Vortex station in tunnel coordinates. ●, convection (C); O, production (PR); ◊, pressure-strain (φ); □, turbulent diffusion (TD); ▲, pressure diffusion (PD); ▽, viscous diffusion (VD); ♦, dissipation (ε).

Figure 106. $\overline{vw}$ shear stress transport budget with anisotropic dissipation model of Hallbäck et al (1990) at Vortex station in tunnel coordinates. ●, convection (C); O, production (PR); ◊, pressure-strain (φ); □, turbulent diffusion (TD); ▲, pressure diffusion (PD); ▽, viscous diffusion (VD); ♦, dissipation (ε).
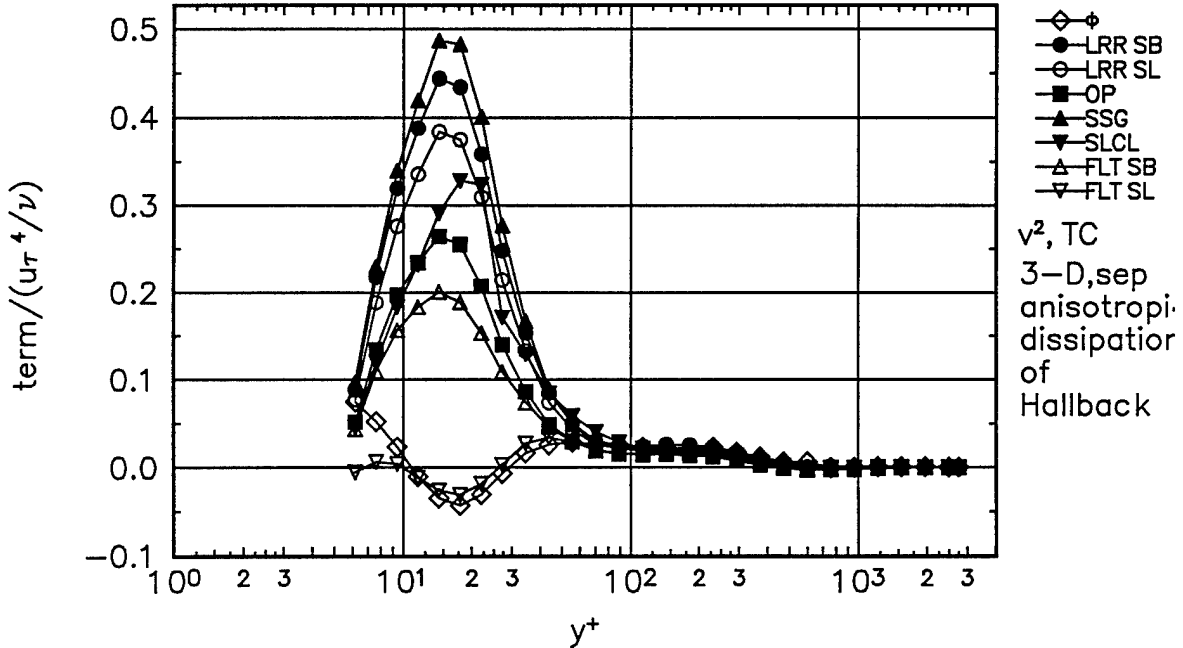
Figure 107. Comparison of $\overline{u^z}$ normal stress transport experimental pressure-strain term ◊, to theoretical pressure-strain terms for the 2-D station. Gibson-Launder, ●; Launder-Reece-Rodi (LRR), O; Oberlack-Peters (OP), ■; Speziale-Sarkar-Gatski (SSG), ▲; Shih-Lumley/Choi-Lumley (SLCL), ▼; Fu-Launder-Tselepidakis 1 (FLT1), △; Fu-Launder-Tselepidakis 2 (FLT2), ▽. No near-wall corrections, anisotropic dissipation of Hallbäck.

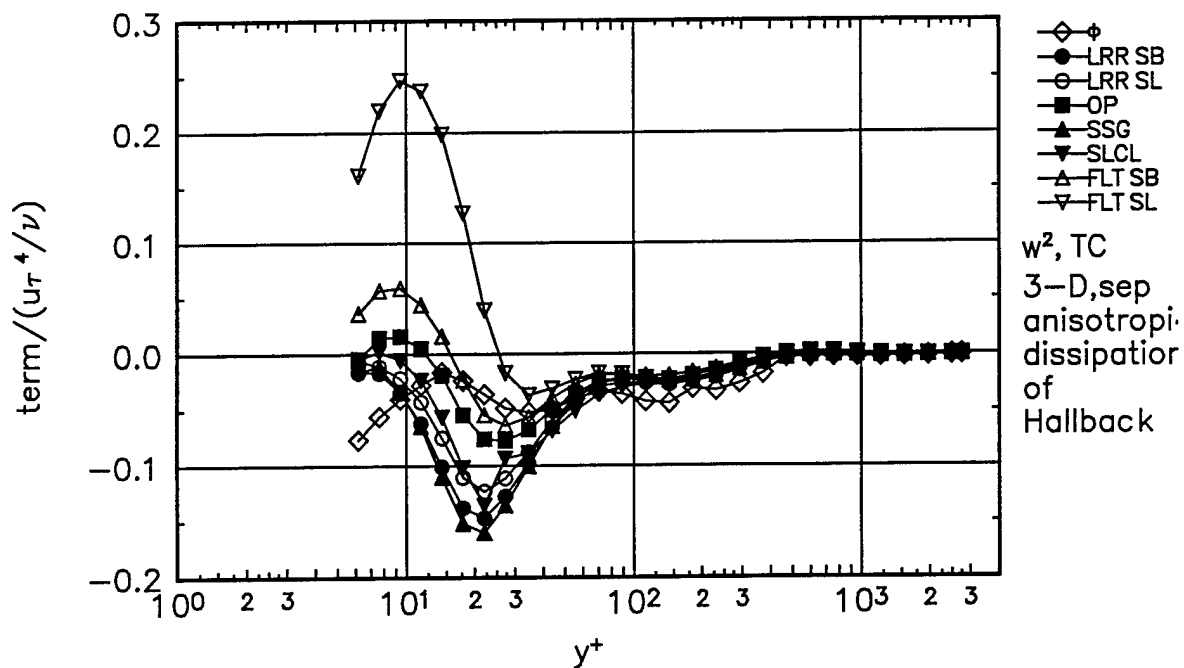

Figure 108. Comparison of $\overline{v^z}$ normal stress transport experimental pressure-strain term ◊, to theoretical pressure-strain terms for the 2-D station. Gibson-Launder, ●; Launder-Reece-Rodi (LRR), O; Oberlack-Peters (OP), ■; Speziale-Sarkar-Gatski (SSG), ▲; Shih-Lumley/Choi-Lumley (SLCL), ▼; Fu-Launder-Tselepidakis 1 (FLT1), △; Fu-Launder-Tselepidakis 2 (FLT2), ▽. No near-wall corrections, anisotropic dissipation of Hallbäck.
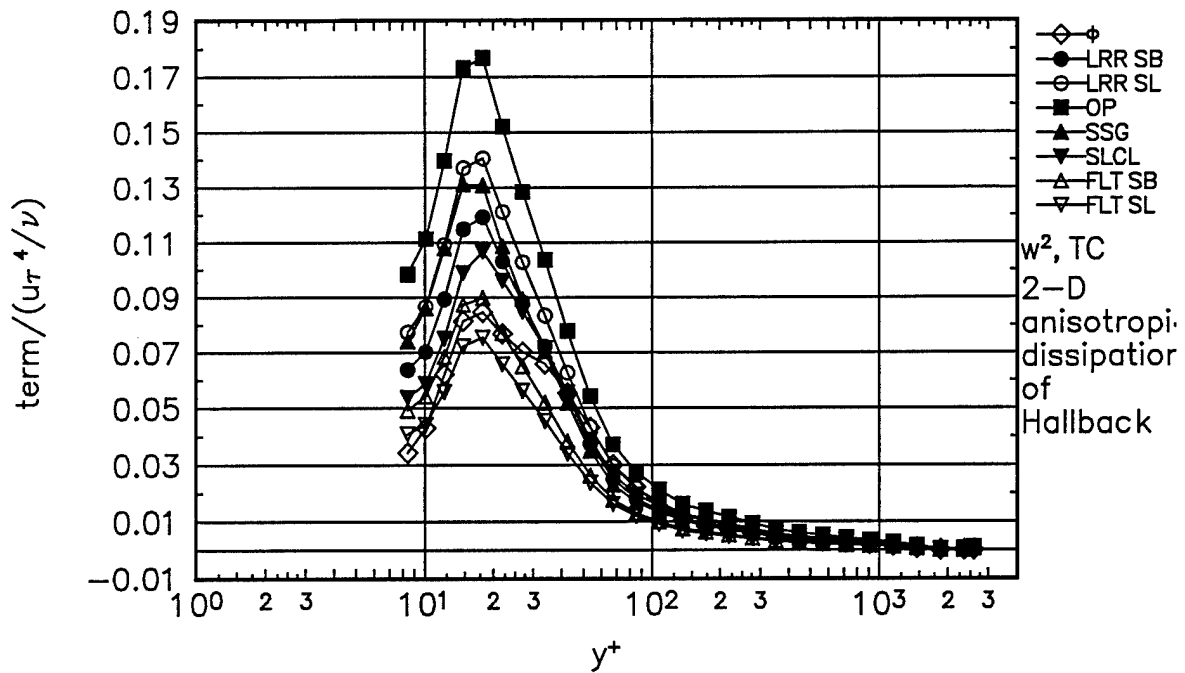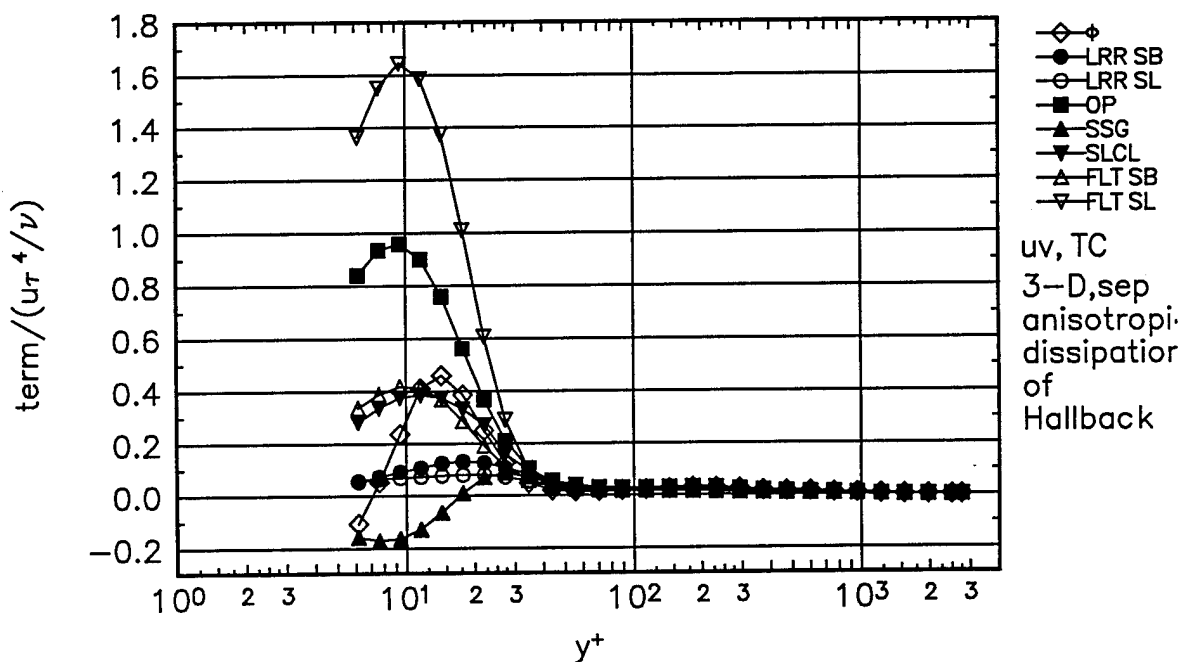
Figure 109. Comparison of $\overline{w^2}$ normal stress transport experimental pressure-strain term ◊, to theoretical pressure-strain terms for the 2-D station. Gibson-Launder, ●; Launder-Reece-Rodi (LRR), O; Oberlack-Peters (OP), ■; Speziale-Sarkar-Gatski (SSG), ▲; Shih-Lumley/Choi-Lumley (SLCL), ▼; Fu-Launder-Tselepidakis 1 (FLT1), △; Fu-Launder-Tselepidakis 2 (FLT2), ▽. No near-wall corrections, anisotropic dissipation of Hallbäck.
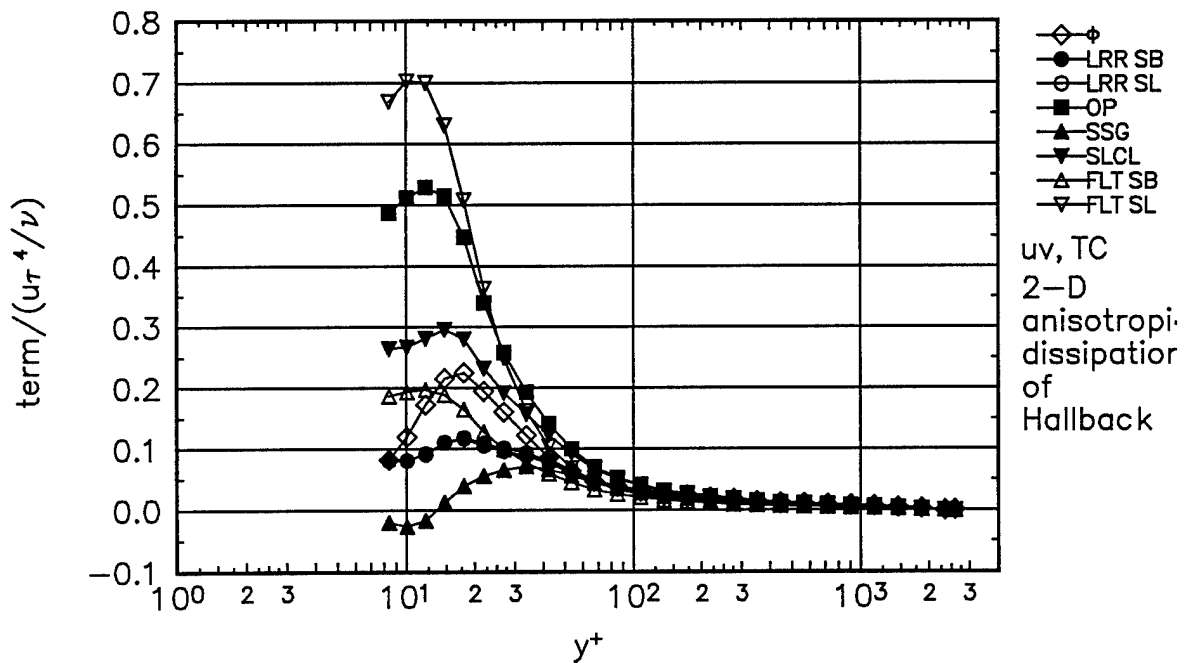
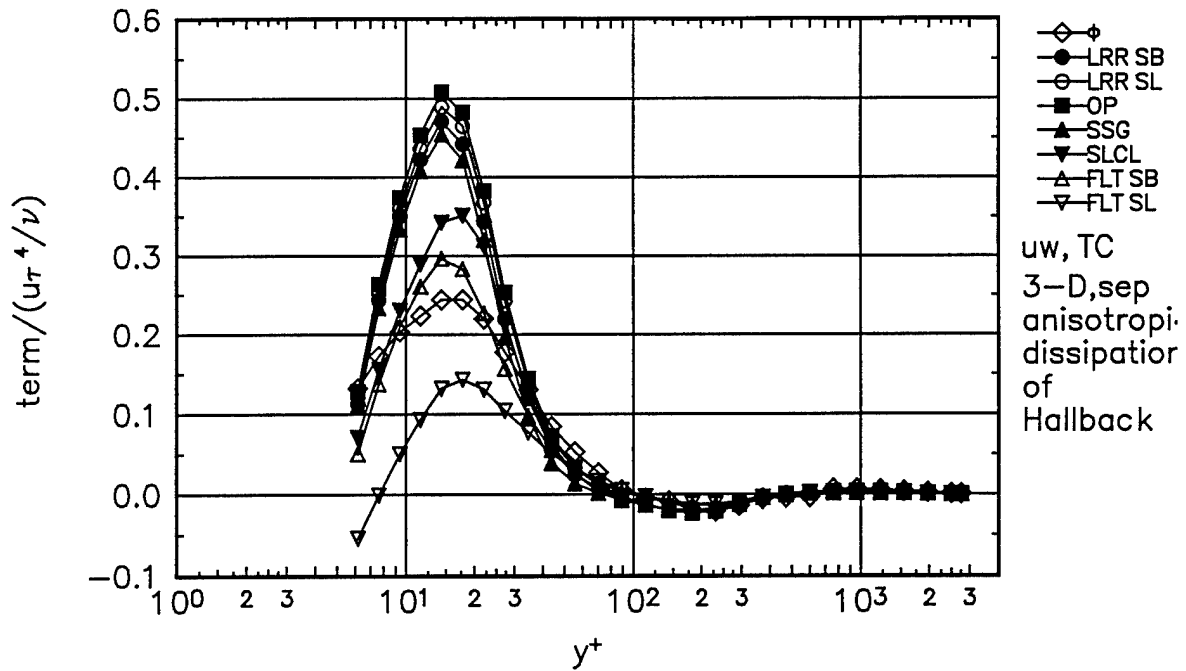

Figure 110. Comparison of $\overline{uv}$ shear stress transport experimental pressure-strain term ◊, to theoretical pressure-strain terms for the 2-D station. Gibson-Launder, ●; Launder-Reece-Rodi (LRR), O; Oberlack-Peters (OP), ■; Speziale-Sarkar-Gatski (SSG), ▲; Shih-Lumley/Choi-Lumley (SLCL), ▼; Fu-Launder-Tselepidakis 1 (FLT1), △; Fu-Launder-Tselepidakis 2 (FLT2), ▽. No near-wall corrections, anisotropic dissipation of Hallbäck.
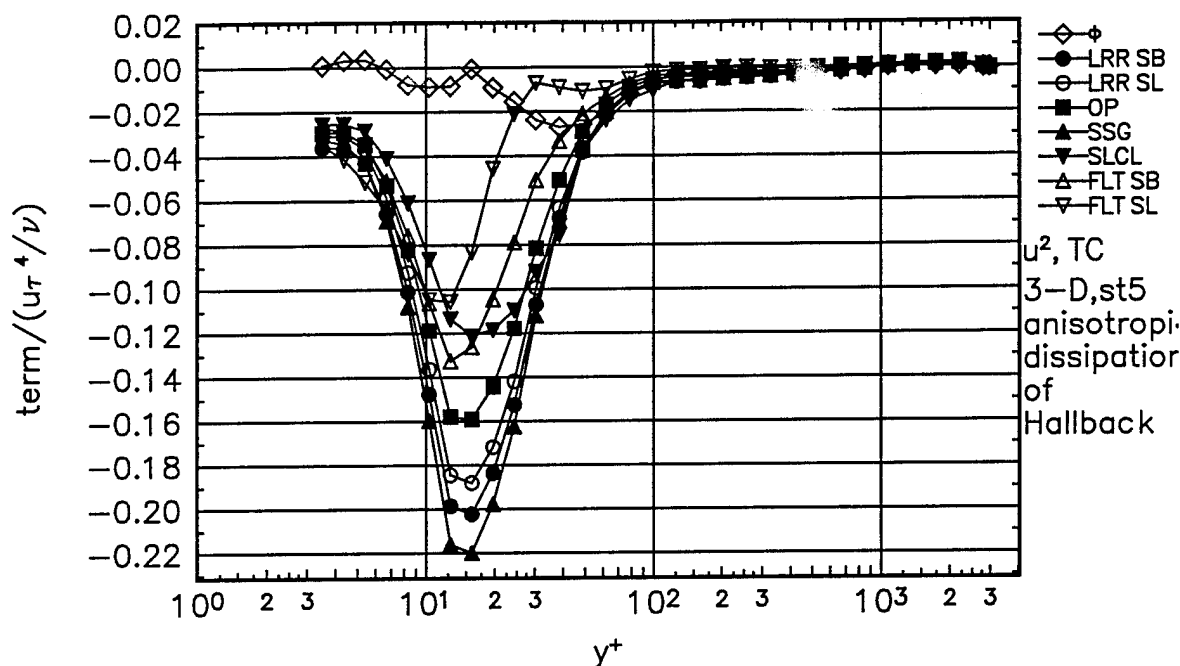
Figure 111. Comparison of $\overline{u^2}$ normal stress transport experimental pressure-strain term ◊, to theoretical pressure-strain terms for Station 5. Gibson-Launder, ●; Launder-Reece-Rodi (LRR), O; Oberlack-Peters (OP), ■; Speziale-Sarkar-Gatski (SSG), ▲; Shih-Lumley/Choi-Lumley (SLCL), ▼; Fu-Launder-Tselepidakis 1 (FLT1), △; Fu-Launder-Tselepidakis 2 (FLT2), ▽. No near-wall corrections, anisotropic dissipation of Hallbäck.
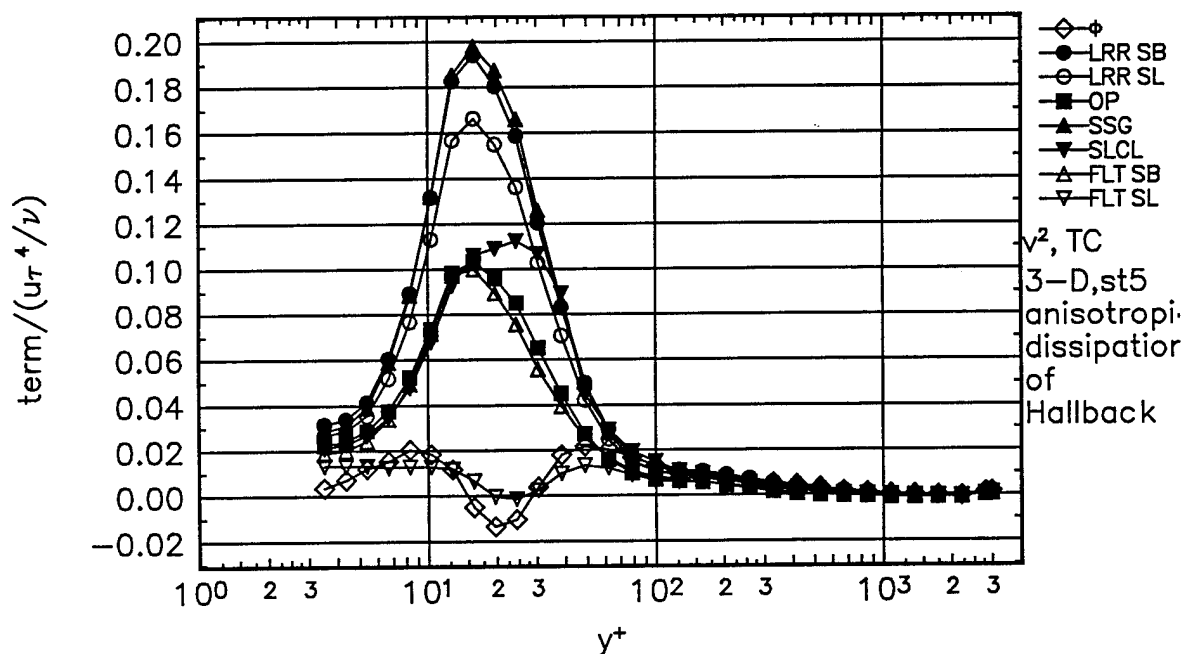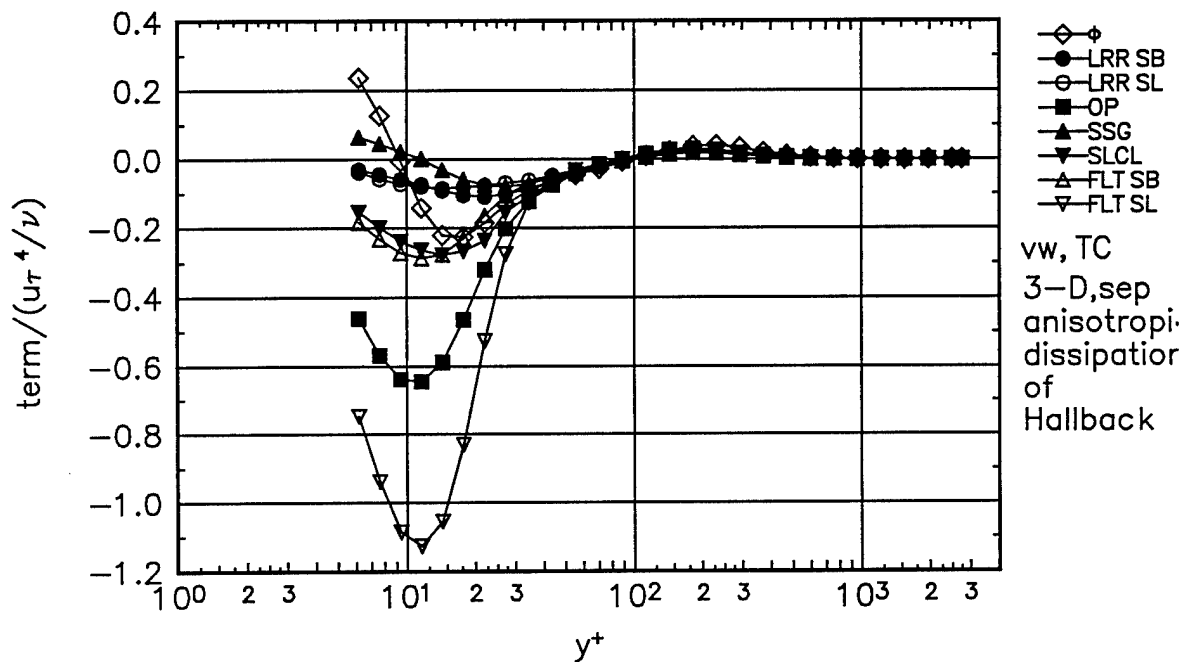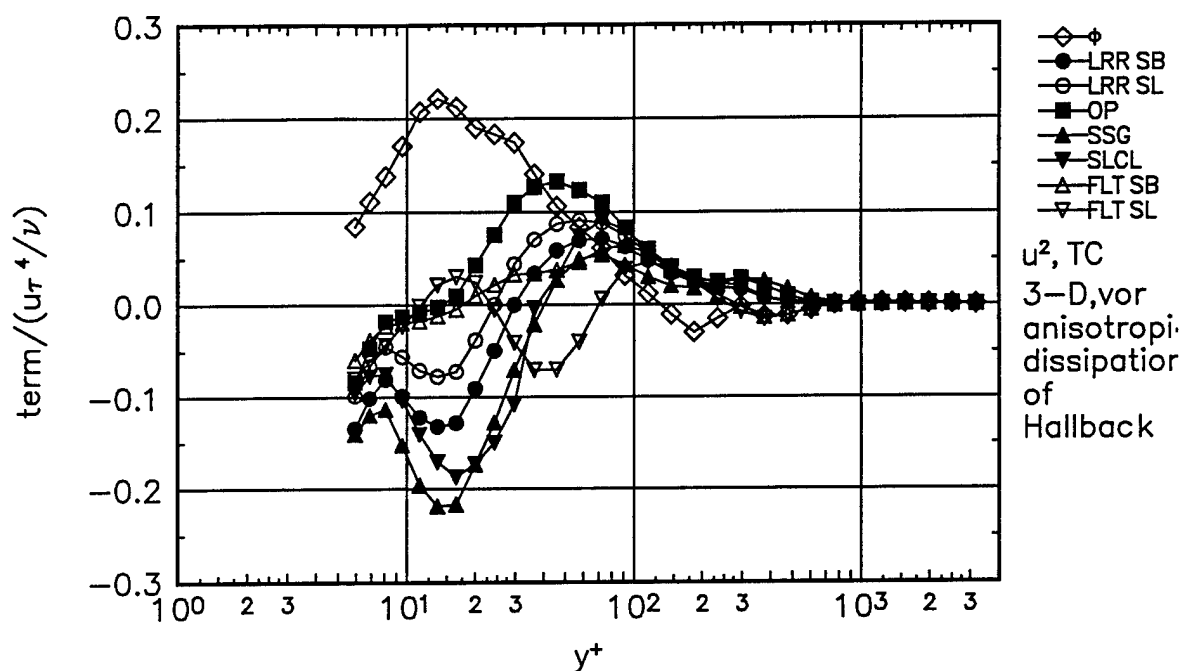

Figure 112. Comparison of $\overline{v^2}$ normal stress transport experimental pressure-strain term ◊, to theoretical pressure-strain terms for Station 5. Gibson-Launder, ●; Launder-Reece-Rodi (LRR), O; Oberlack-Peters (OP), ■; Speziale-Sarkar-Gatski (SSG), ▲; Shih-Lumley/Choi-Lumley (SLCL), ▼; Fu-Launder-Tselepidakis 1 (FLT1), △; Fu-Launder-Tselepidakis 2 (FLT2), ▽. No near-wall corrections, anisotropic dissipation of Hallbäck.

Figures

110
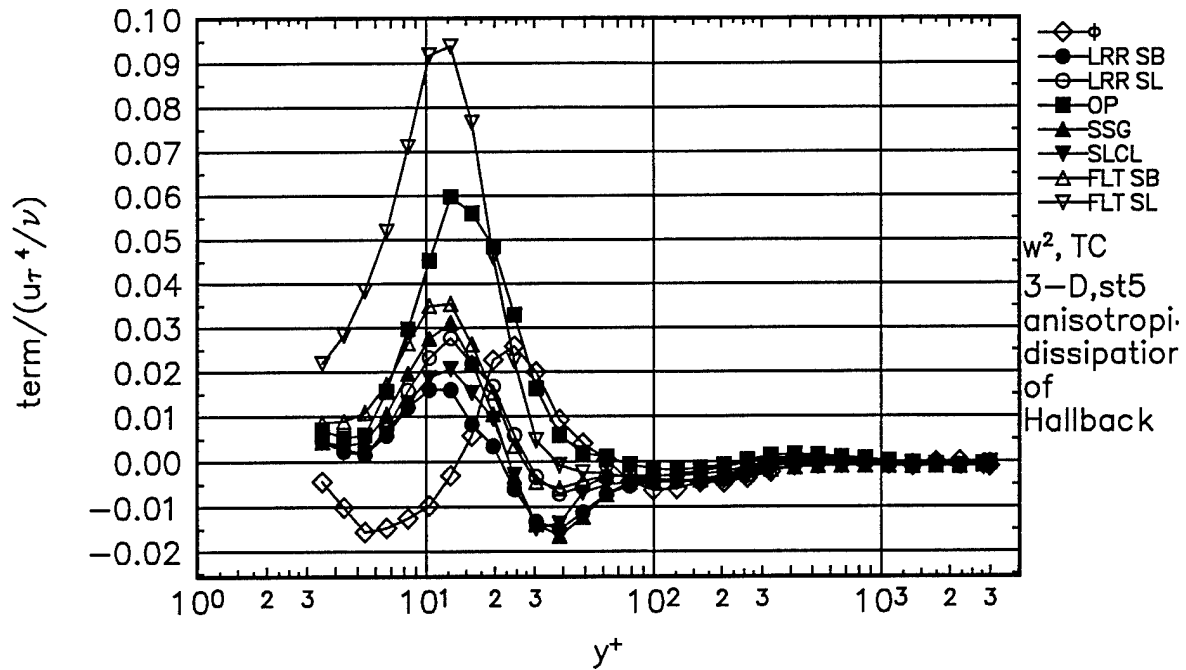
Figure 113. Comparison of $\overline{w^2}$ normal stress transport experimental pressure-strain term ◊, to theoretical pressure-strain terms for Station 5. Gibson-Launder, ●; Launder-Reece-Rodi (LRR), O; Oberlack-Peters (OP), ■; Speziale-Sarkar-Gatski (SSG), ▲; Shih-Lumley/Choi-Lumley (SLCL), ▼; Fu-Launder-Tselepidakis 1 (FLT1), △; Fu-Launder-Tselepidakis 2 (FLT2), ▽. No near-wall corrections, anisotropic dissipation of Hallbäck.
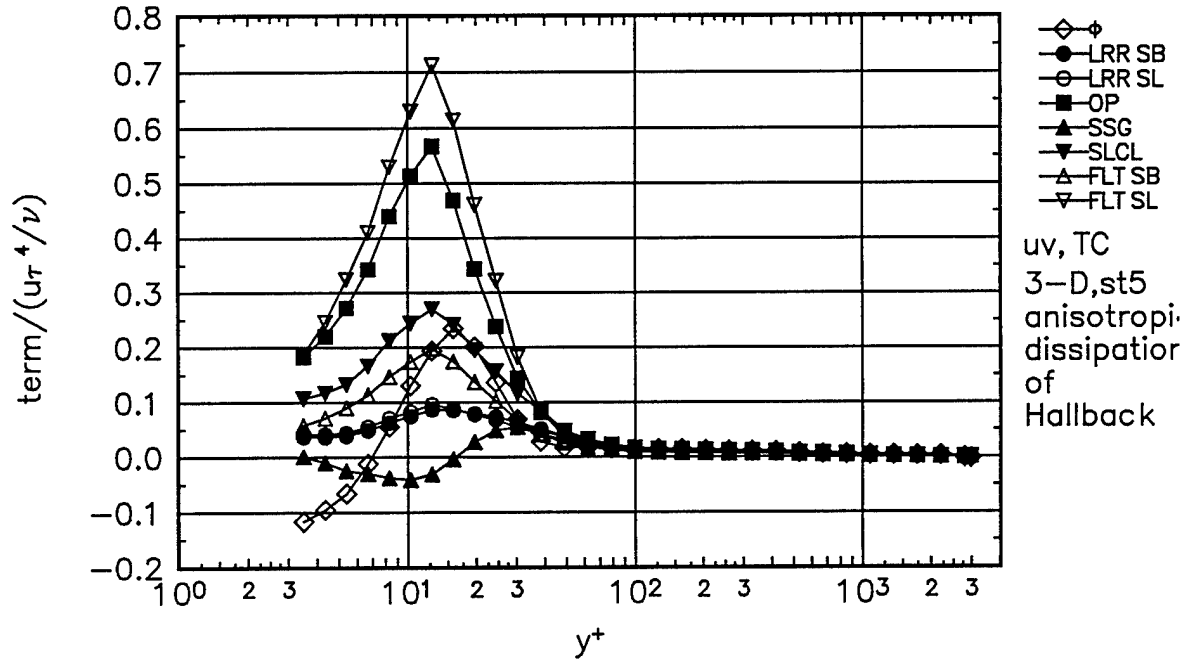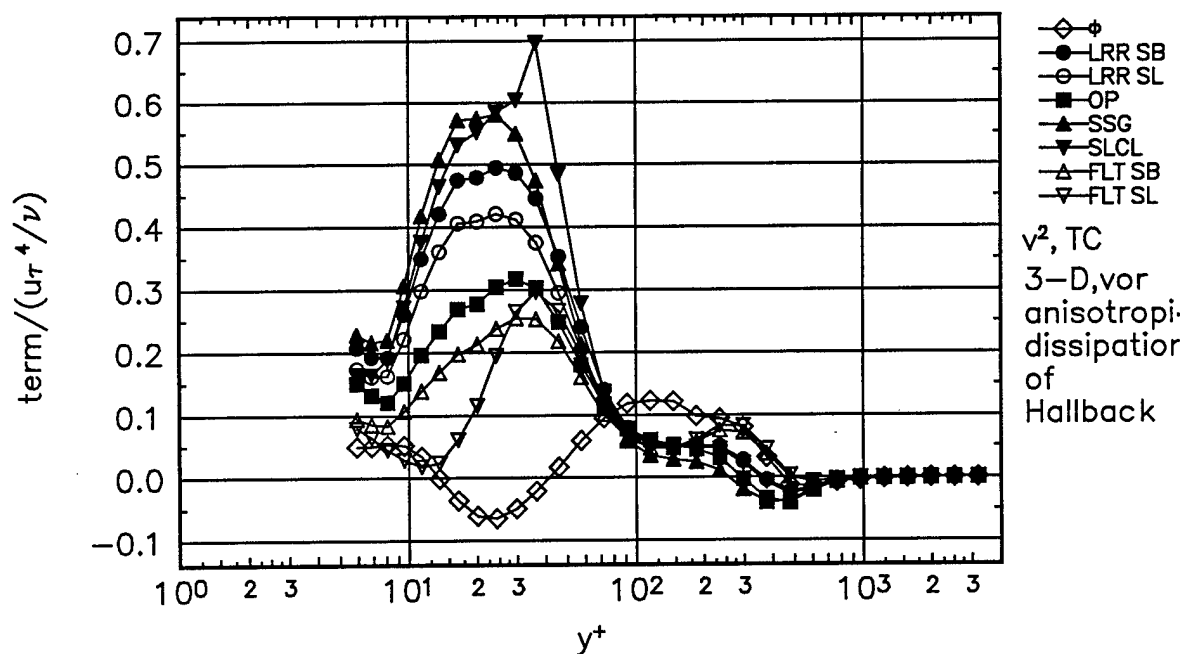

Figure 114. Comparison of $\overline{uv}$ shear stress transport experimental pressure-strain term ◊, to theoretical pressure-strain terms for Station 5. Gibson-Launder, ●; Launder-Reece-Rodi (LRR), O; Oberlack-Peters (OP), ■; Speziale-Sarkar-Gatski (SSG), ▲; Shih-Lumley/Choi-Lumley (SLCL), ▼; Fu-Launder-Tselepidakis 1 (FLT1), △; Fu-Launder-Tselepidakis 2 (FLT2), ▽. No near-wall corrections, anisotropic dissipation of Hallbäck.
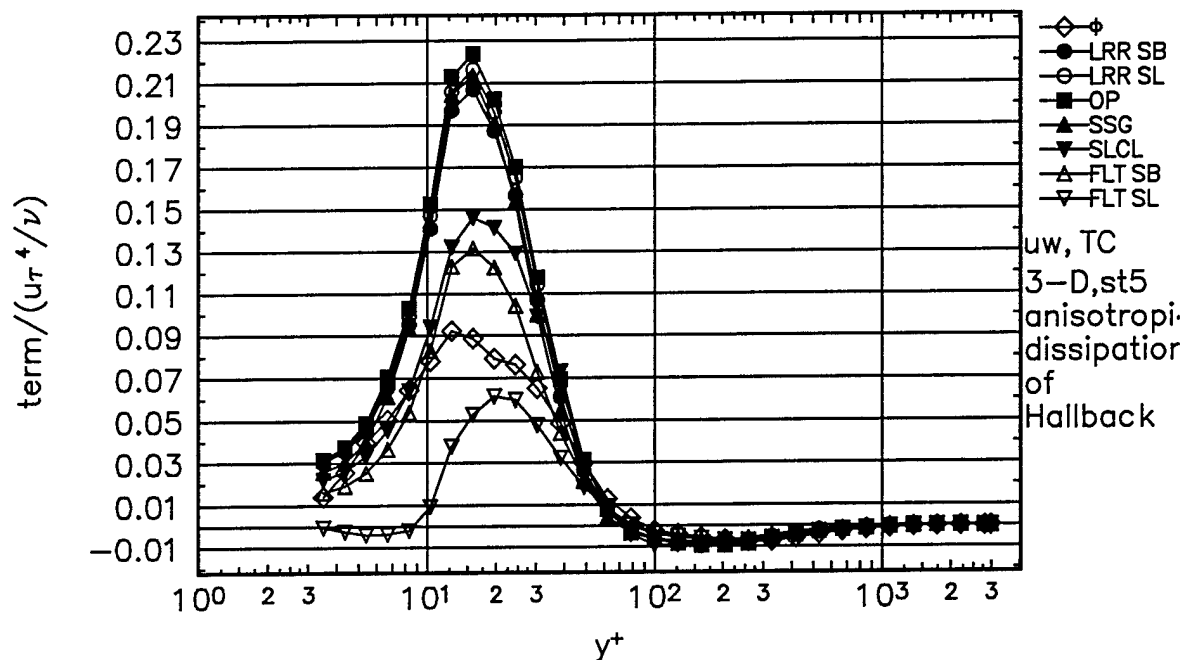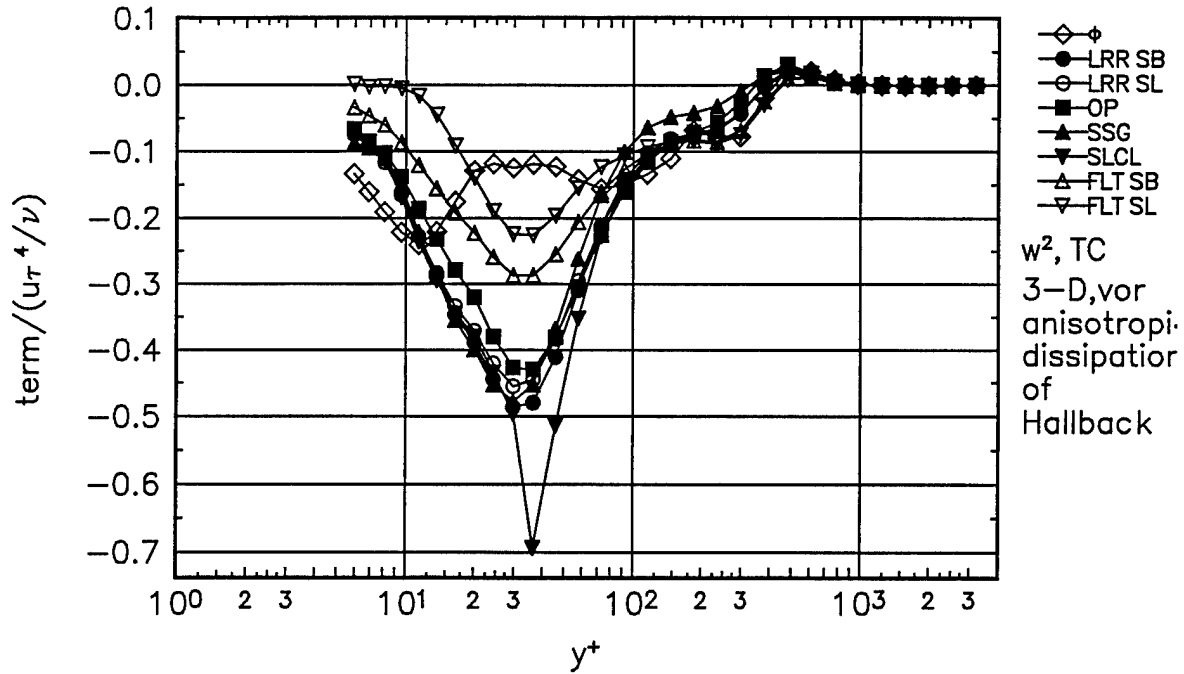
Figure 115. Comparison of $\overline{uw}$ shear stress transport experimental pressure-strain term ◊, to theoretical pressure-strain terms for Station 5. Gibson-Launder, ●; Launder-Reece-Rodi (LRR), O; Oberlack-Peters (OP), ■; Speziale-Sarkar-Gatski (SSG), ▲; Shih-Lumley/Choi-Lumley (SLCL), ▼; Fu-Launder-Tselepidakis 1 (FLT1), △; Fu-Launder-Tselepidakis 2 (FLT2), ▽. No near-wall corrections, anisotropic dissipation of Hallbäck.
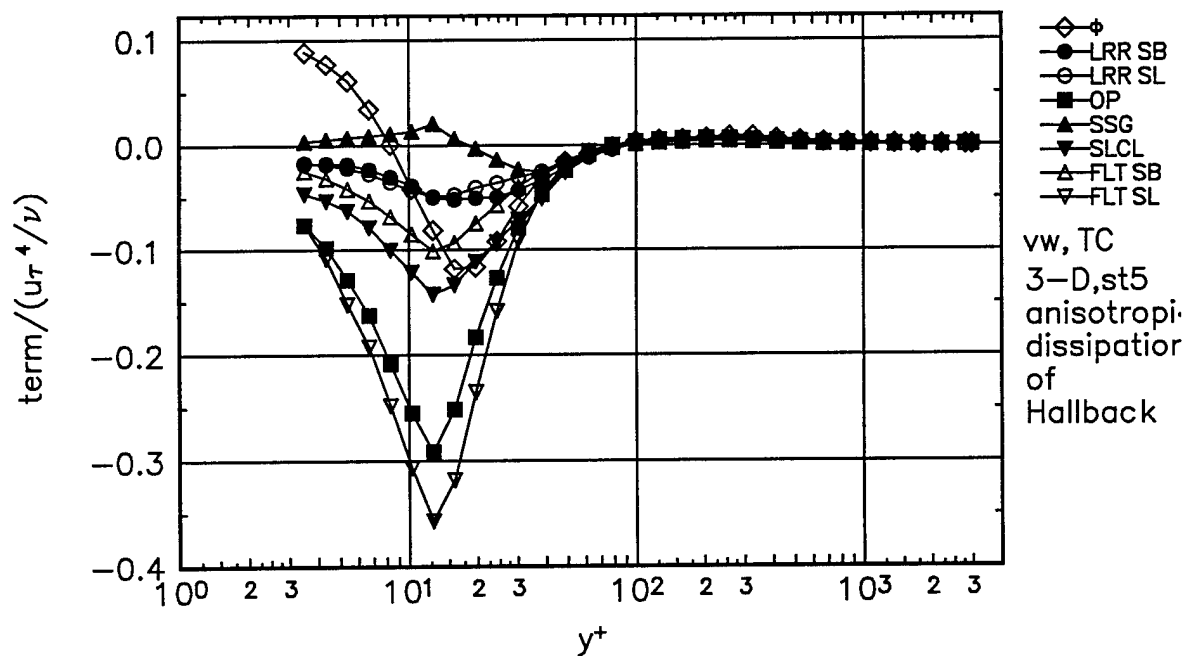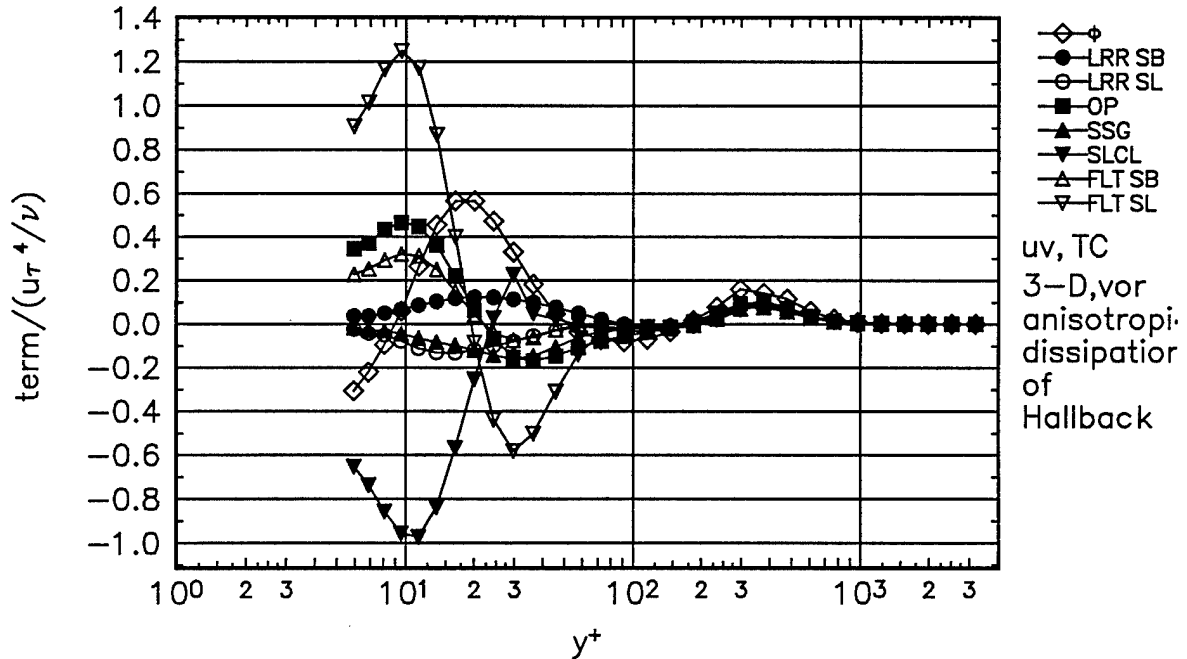

Figure 116. Comparison of $\overline{vw}$ shear stress transport experimental pressure-strain term ◊, to theoretical pressure-strain terms for Station 5. Gibson-Launder, ●; Launder-Reece-Rodi (LRR), O; Oberlack-Peters (OP), ■; Speziale-Sarkar-Gatski (SSG), ▲; Shih-Lumley/Choi-Lumley (SLCL), ▼; Fu-Launder-Tselepidakis 1 (FLT1), △; Fu-Launder-Tselepidakis 2 (FLT2), ▽. No near-wall corrections, anisotropic dissipation of Hallbäck.
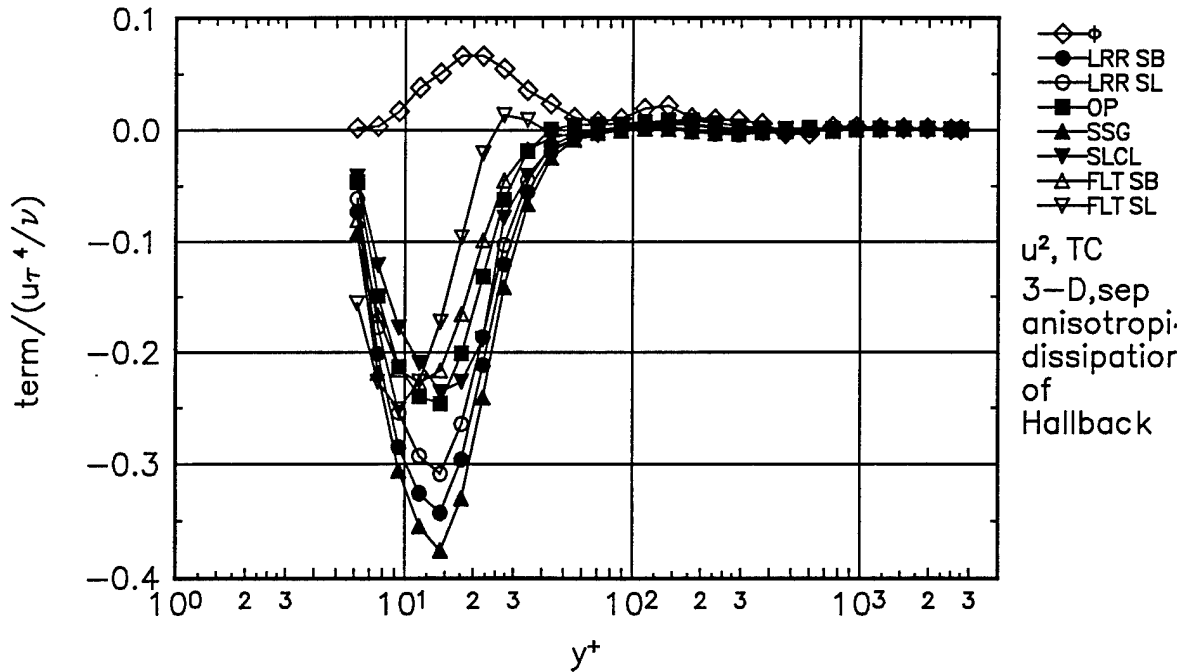
Figures

Figure 117. Comparison of $\overline{u^2}$ normal stress transport experimental pressure-strain term ◊, to theoretical pressure-strain terms for Separation station. Gibson-Launder, ●; Launder-Reece-Rodi (LRR), O; Oberlack-Peters (OP), ■; Speziale-Sarkar-Gatski (SSG), ▲; Shih-Lumley/Choi-Lumley (SLCL), ▼; Fu-Launder-Tselepidakis 1 (FLT1), △; Fu-Launder-Tselepidakis 2 (FLT2), ▽. No near-wall corrections, anisotropic dissipation of Hallbäck.
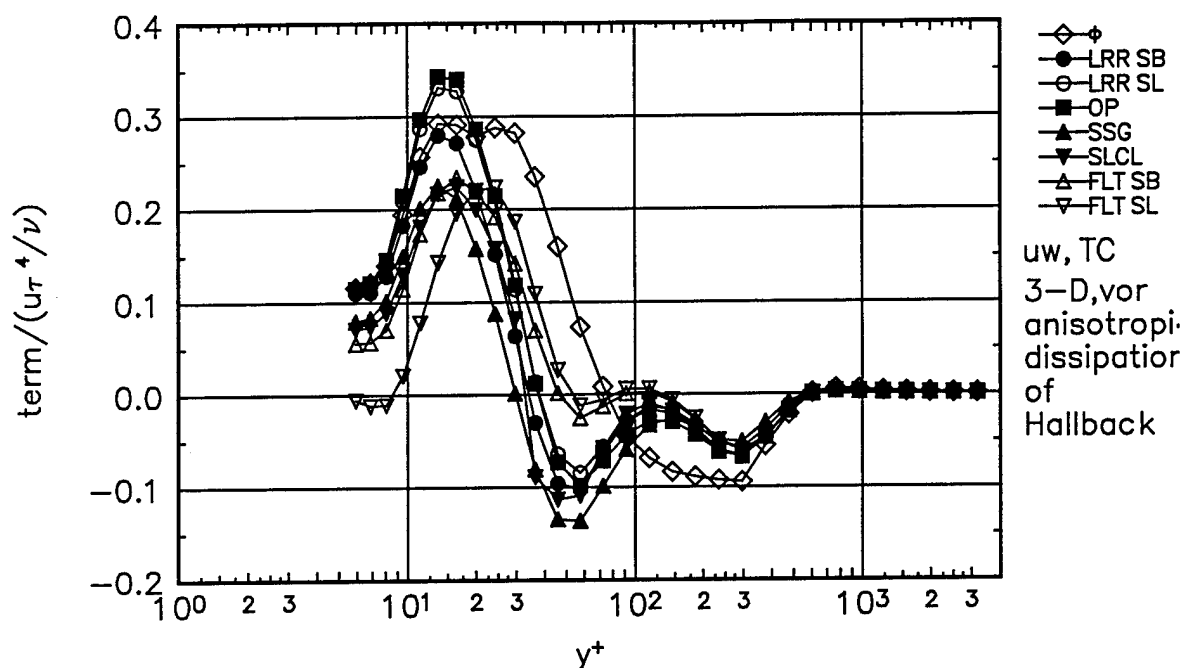

Figure 118. Comparison of $\overline{v^2}$ normal stress transport experimental pressure-strain term ◊, to theoretical pressure-strain terms for Separation station. Gibson-Launder, ●; Launder-Reece-Rodi (LRR), O; Oberlack-Peters (OP), ■; Speziale-Sarkar-Gatski (SSG), ▲; Shih-Lumley/Choi-Lumley (SLCL), ▼; Fu-Launder-Tselepidakis 1 (FLT1), △; Fu-Launder-Tselepidakis 2 (FLT2), ▽. No near-wall corrections, anisotropic dissipation of Hallbäck.
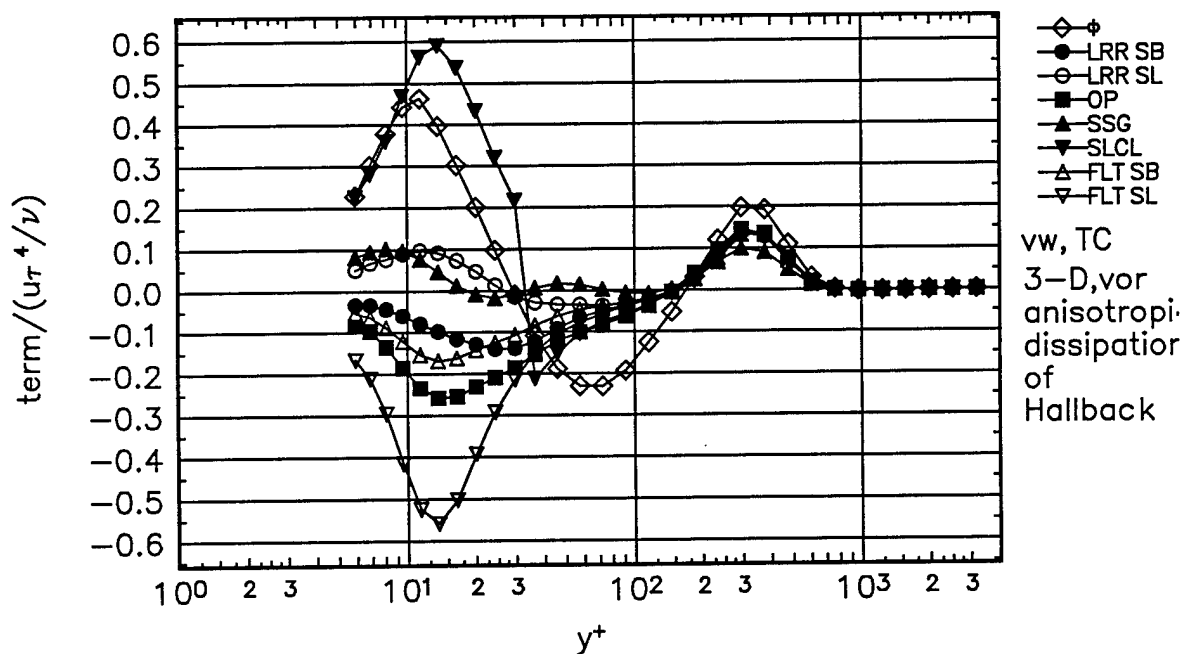
Figures   113

Figure 119. Comparison of $\overline{w^2}$ normal stress transport experimental pressure-strain term ◊, to theoretical pressure-strain terms for Separation station. Gibson-Launder, ●; Launder-Reece-Rodi (LRR), O; Oberlack-Peters (OP), ■; Speziale-Sarkar-Gatski (SSG), ▲; Shih-Lumley/Choi-Lumley (SLCL), ▼; Fu-Launder-Tselepidakis 1 (FLT1), △; Fu-Launder-Tselepidakis 2 (FLT2), ▽. No near-wall corrections, anisotropic dissipation of Hallbäck.


Figure 120. Comparison of $\overline{uv}$ shear stress transport experimental pressure-strain term ◊, to theoretical pressure-strain terms for Separation station. Gibson-Launder, ●; Launder-Reece-Rodi (LRR), O; Oberlack-Peters (OP), ■; Speziale-Sarkar-Gatski (SSG), ▲; Shih-Lumley/Choi-Lumley (SLCL), ▼; Fu-Launder-Tselepidakis 1 (FLT1), △; Fu-Launder-Tselepidakis 2 (FLT2), ▽. No near-wall corrections, anisotropic dissipation of Hallbäck.

0.6

0.5

0.4

0.3

0.2

0.1

0.0

-0.1

term/(u_τ^4/ν)

10^0 2 3 10^1 2 3 10^2 2 3 10^3 2 3

y^+

◇—φ
●—LRR SB
◉—LRR SL
■—OP
▲—SSG
▼—SLCL
△—FLT SB
▽—FLT SL

uw, TC
3−D,sep
anisotropi·
dissipatior
of
Hallbac k

Figure 121. Comparison of $\overline{uw}$ shear stress transport experimental pressure-strain term ◊, to theoretical pressure-strain terms for Separation station. Gibson-Launder, ●; Launder-Reece-Rodi (LRR), O; Oberlack-Peters (OP), ■; Speziale-Sarkar-Gatski (SSG), ▲; Shih-Lumley/Choi-Lumley (SLCL), ▼; Fu-Launder-Tselepidakis 1 (FLT1), △; Fu-Launder-Tselepidakis 2 (FLT2), ▽. No near-wall corrections, anisotropic dissipation of Hallbäck.

0.4

0.2

0.0

-0.2

-0.4

-0.6

-0.8

-1.0

-1.2

term/(u_τ^4/ν)

10^0 2 3 10^1 2 3 10^2 2 3 10^3 2 3

y^+

◇—φ
●—LRR SB
◉—LRR SL
■—OP
▲—SSG
▼—SLCL
△—FLT SB
▽—FLT SL

vw, TC
3−D,sep
anisotropi·
dissipatior
of
Hallbac k

Figure 122. Comparison of $\overline{vw}$ shear stress transport experimental pressure-strain term ◊, to theoretical pressure-strain terms for Separation station. Gibson-Launder, ●; Launder-Reece-Rodi (LRR), O; Oberlack-Peters (OP), ■; Speziale-Sarkar-Gatski (SSG), ▲; Shih-Lumley/Choi-Lumley (SLCL), ▼; Fu-Launder-Tselepidakis 1 (FLT1), △; Fu-Launder-Tselepidakis 2 (FLT2), ▽. No near-wall corrections, anisotropic dissipation of Hallbäck.
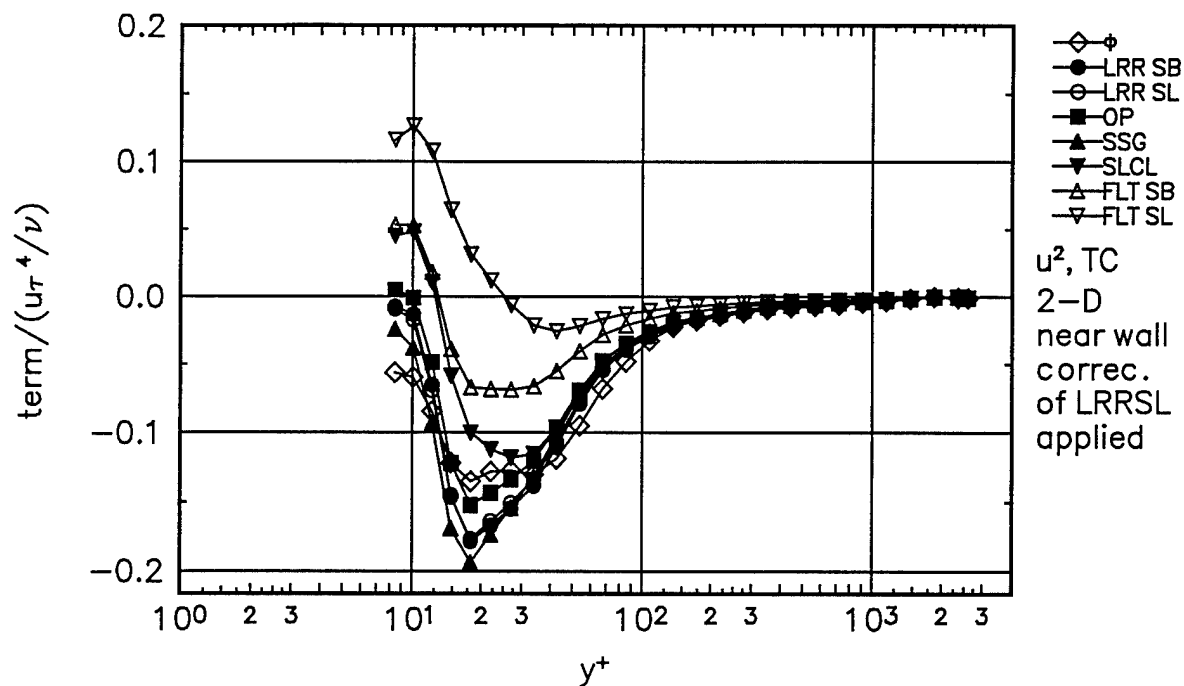
Figures

Figure 123. Comparison of $\overline{u^2}$ normal stress transport experimental pressure-strain term ◊, to theoretical pressure-strain terms for Vortex station. Gibson-Launder, ●; Launder-Reece-Rodi (LRR), O; Oberlack-Peters (OP), ■; Speziale-Sarkar-Gatski (SSG), ▲; Shih-Lumley/Choi-Lumley (SLCL), ▼; Fu-Launder-Tselepidakis 1 (FLT1), ▵; Fu-Launder-Tselepidakis 2 (FLT2), ▽. No near-wall corrections, anisotropic dissipation of Hallbäck.

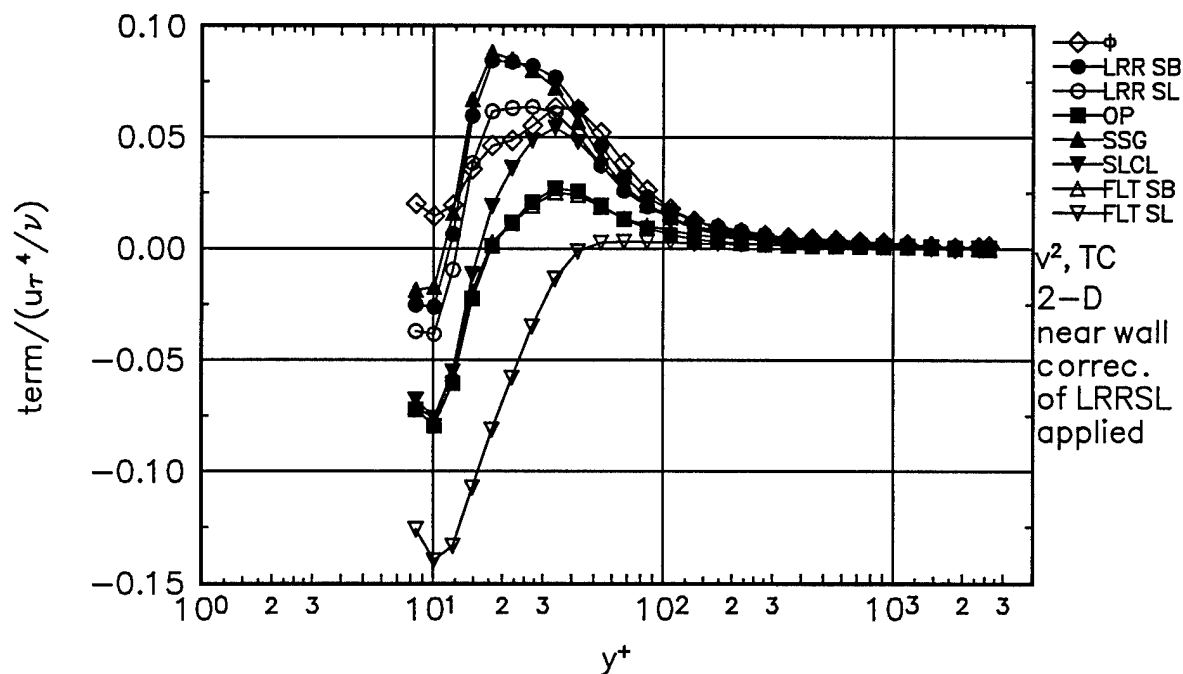
Figure 124. Comparison of $\overline{v^2}$ normal stress transport experimental pressure-strain term ◊, to theoretical pressure-strain terms for Vortex station. Gibson-Launder, ●; Launder-Reece-Rodi (LRR), O; Oberlack-Peters (OP), ■; Speziale-Sarkar-Gatski (SSG), ▲; Shih-Lumley/Choi-Lumley (SLCL), ▼; Fu-Launder-Tselepidakis 1 (FLT1), ▵; Fu-Launder-Tselepidakis 2 (FLT2), ▽. No near-wall corrections, anisotropic dissipation of Hallbäck.
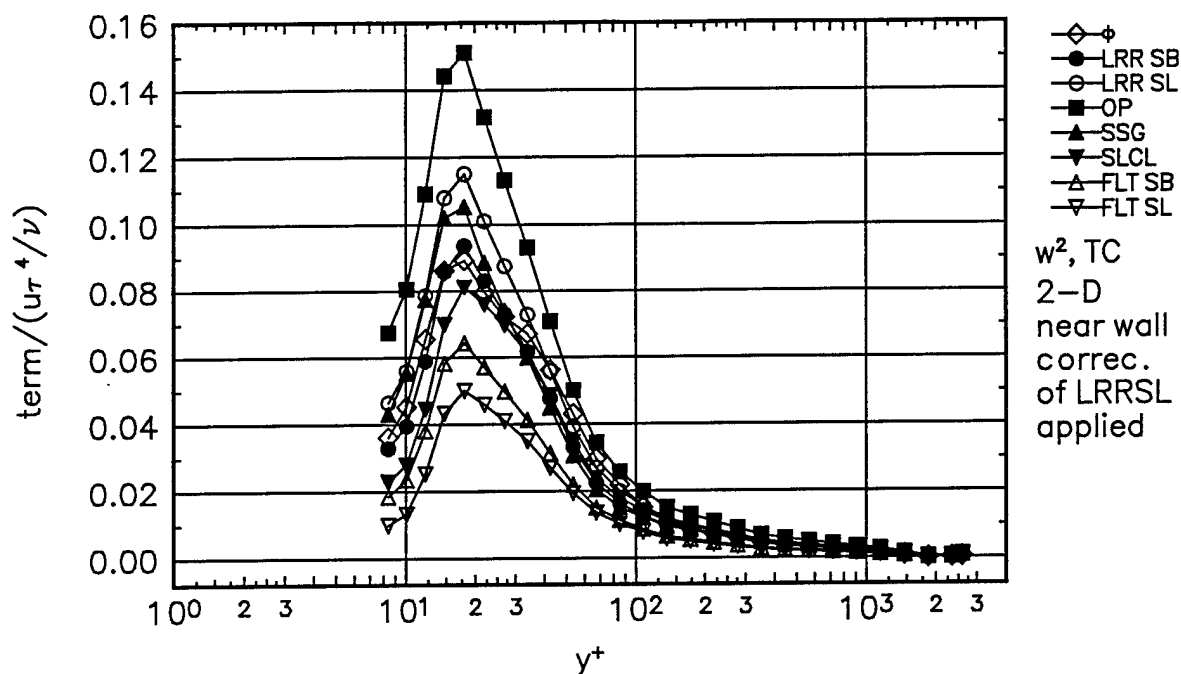
Figures

Figure 125. Comparison of $\overline{w^2}$ normal stress transport experimental pressure-strain term ◊, to theoretical pressure-strain terms for Vortex station. Gibson-Launder, ●; Launder-Reece-Rodi (LRR), O; Oberlack-Peters (OP), ■; Speziale-Sarkar-Gatski (SSG), ▲; Shih-Lumley/Choi-Lumley (SLCL), ▼; Fu-Launder-Tselepidakis 1 (FLT1), △; Fu-Launder-Tselepidakis 2 (FLT2), ▽. No near-wall corrections, anisotropic dissipation of Hallbäck.

Figure 126. Comparison of $\overline{uv}$ shear stress transport experimental pressure-strain term ◊, to theoretical pressure-strain terms for Vortex station. Gibson-Launder, ●; Launder-Reece-Rodi (LRR), O; Oberlack-Peters (OP), ■; Speziale-Sarkar-Gatski (SSG), ▲; Shih-Lumley/Choi-Lumley (SLCL), ▼; Fu-Launder-Tselepidakis 1 (FLT1), △; Fu-Launder-Tselepidakis 2 (FLT2), ▽. No near-wall corrections, anisotropic dissipation of Hallbäck.
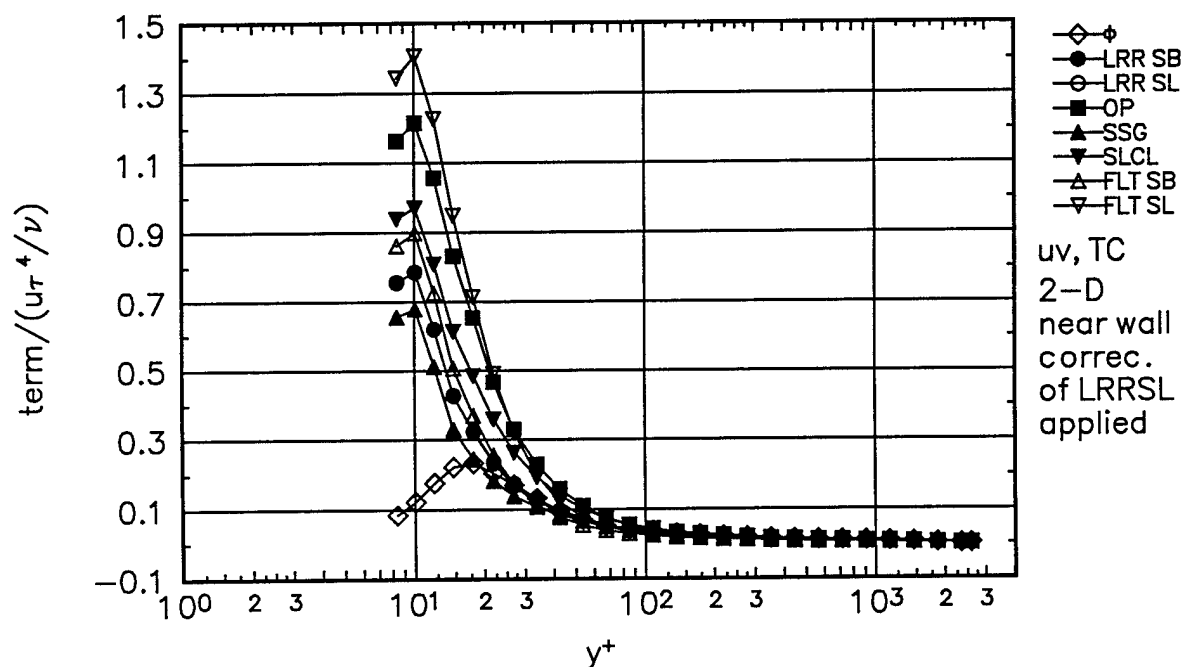
Figure 127. Comparison of $\overline{uw}$ shear stress transport experimental pressure-strain term ◊, to theoretical pressure-strain terms for Vortex station. Gibson-Launder, ●; Launder-Reece-Rodi (LRR), O; Oberlack-Peters (OP), ■; Speziale-Sarkar-Gatski (SSG), ▲; Shih-Lumley/Choi-Lumley (SLCL), ▼; Fu-Launder-Tselepidakis 1 (FLT1), ▵; Fu-Launder-Tselepidakis 2 (FLT2), ▽. No near-wall corrections, anisotropic dissipation of Hallbäck.

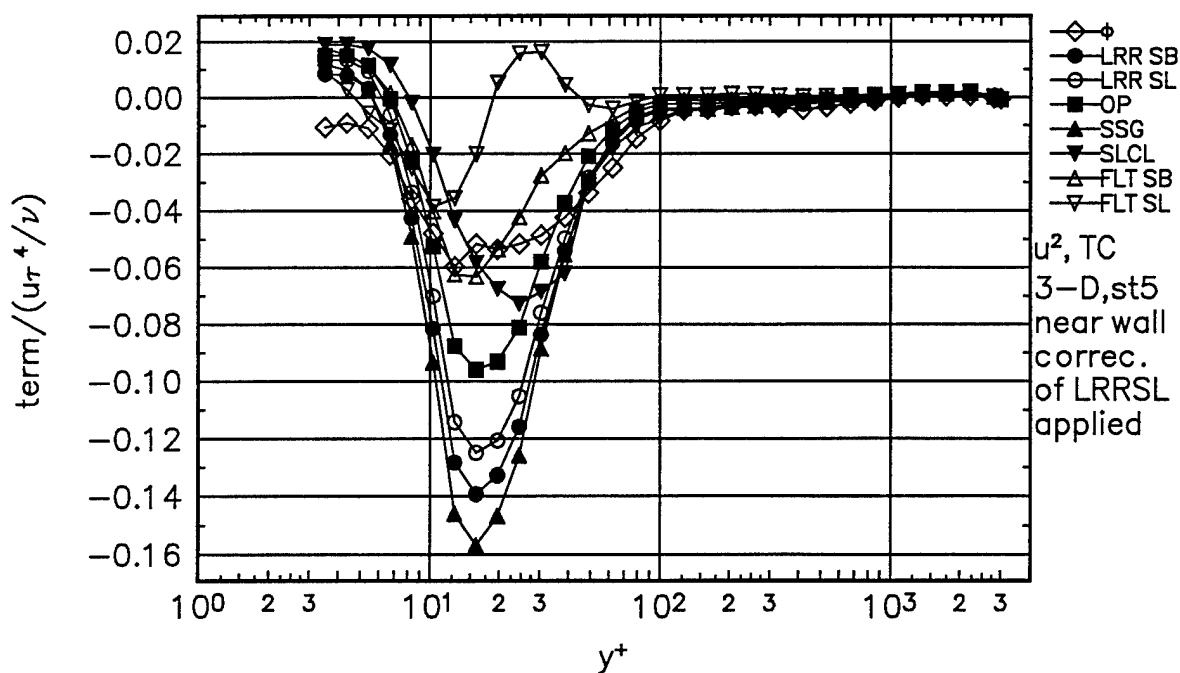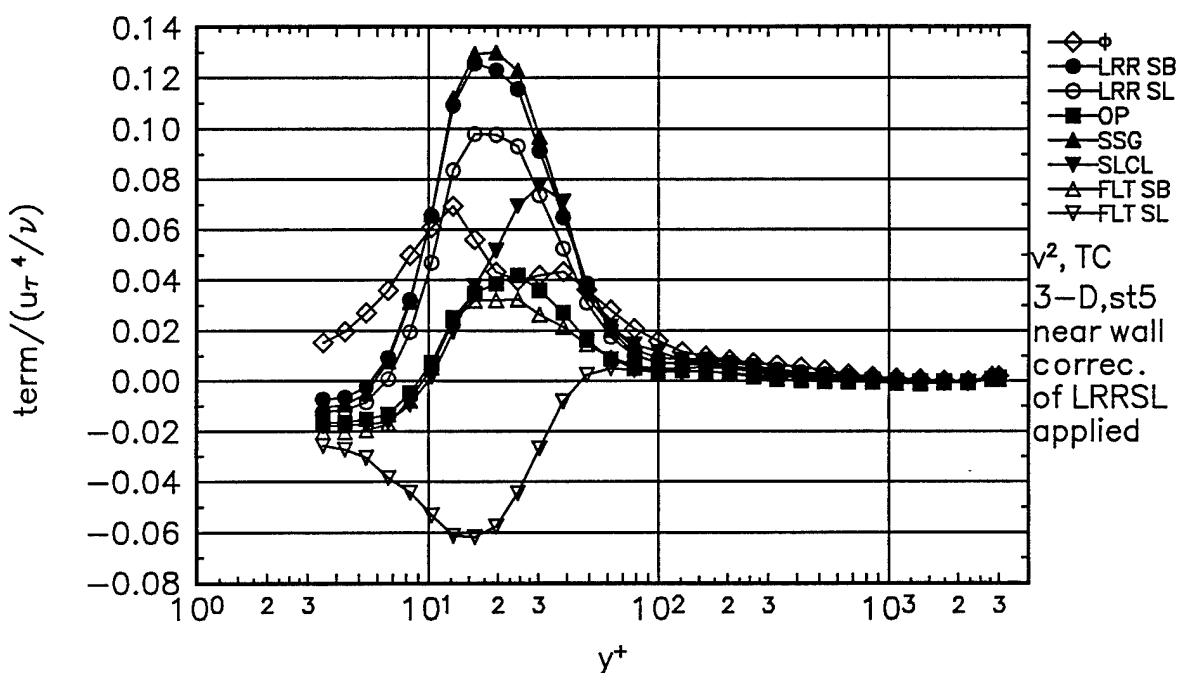Figure 128. Comparison of $\overline{vw}$ shear stress transport experimental pressure-strain term ◊, to theoretical pressure-strain terms for Vortex station. Gibson-Launder, ●; Launder-Reece-Rodi (LRR), O; Oberlack-Peters (OP), ■; Speziale-Sarkar-Gatski (SSG), ▲; Shih-Lumley/Choi-Lumley (SLCL), ▼; Fu-Launder-Tselepidakis 1 (FLT1), ▵; Fu-Launder-Tselepidakis 2 (FLT2), ▽. No near-wall corrections, anisotropic dissipation of Hallbäck.

Figures   118

pressure—strain near wall correction terms for 2—D by LRRSL
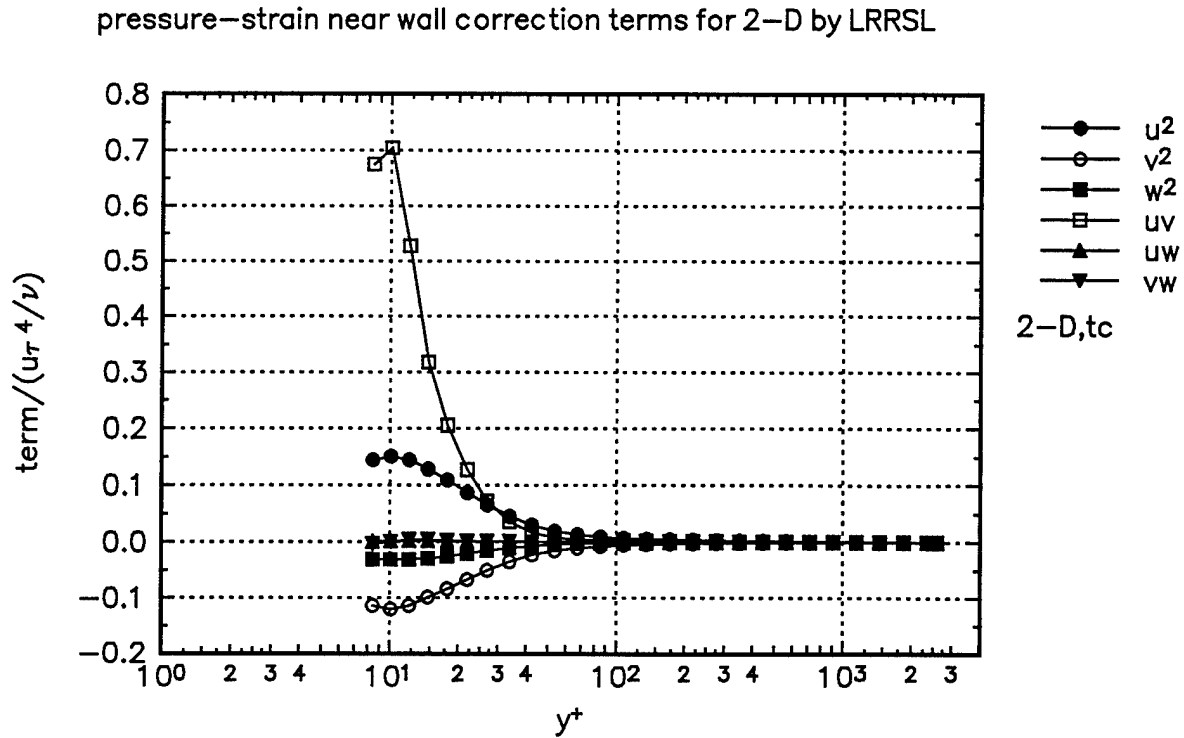
Figure 129. Near-wall correction to the pressure-strain rate distribution calculated using Launder-Reece-Rodi (1975) model for the 2-D station in tunnel coordinates. $\overline{u^2}$, ●; $\overline{v^2}$, O; $\overline{w^2}$, ■; $\overline{uv}$, □; $\overline{uw}$, ▲; $\overline{vw}$, ▼.

pressure—strain near wall correction terms for 3D—st5 by LRRSL
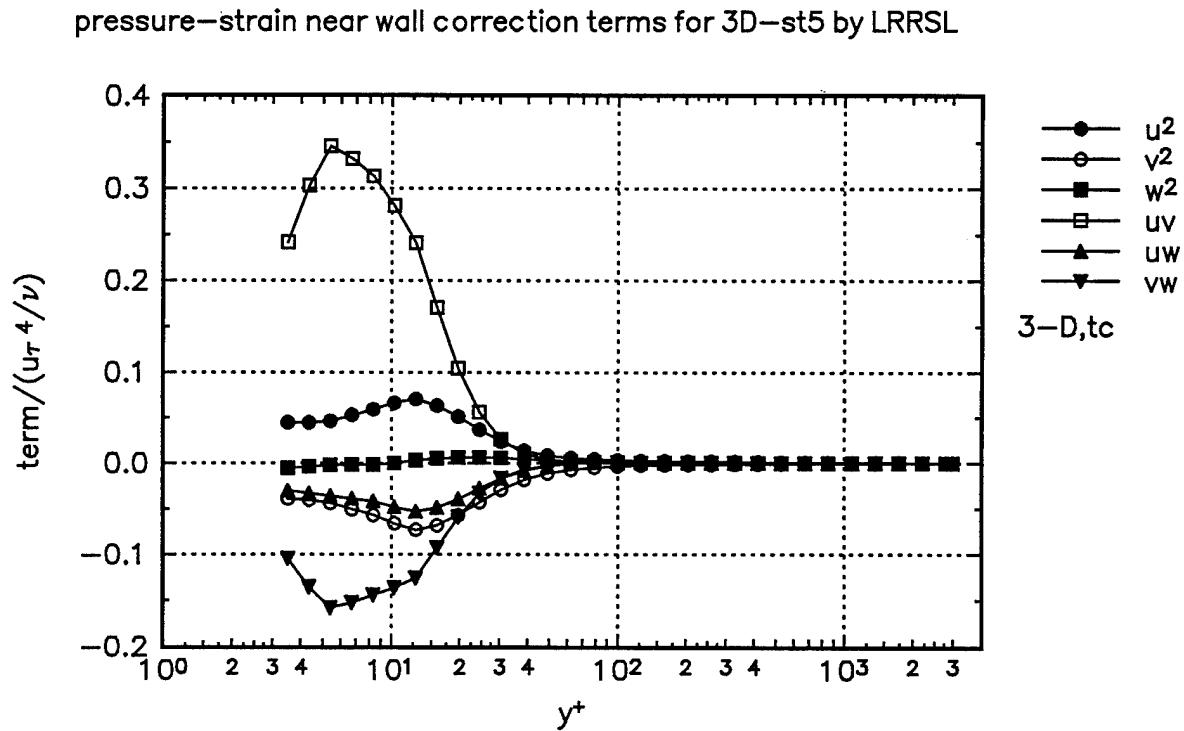
Figure 130. Near-wall correction to the pressure-strain rate distribution calculated using Launder-Reece-Rodi (1975) model at Station 5 in tunnel coordinates. $\overline{u^2}$, ●; $\overline{v^2}$, O; $\overline{w^2}$, ■; $\overline{uv}$, □; $\overline{uw}$, ▲; $\overline{vw}$, ▼.

pressure—strain near wall correction terms for 3D—sep by LRRSL
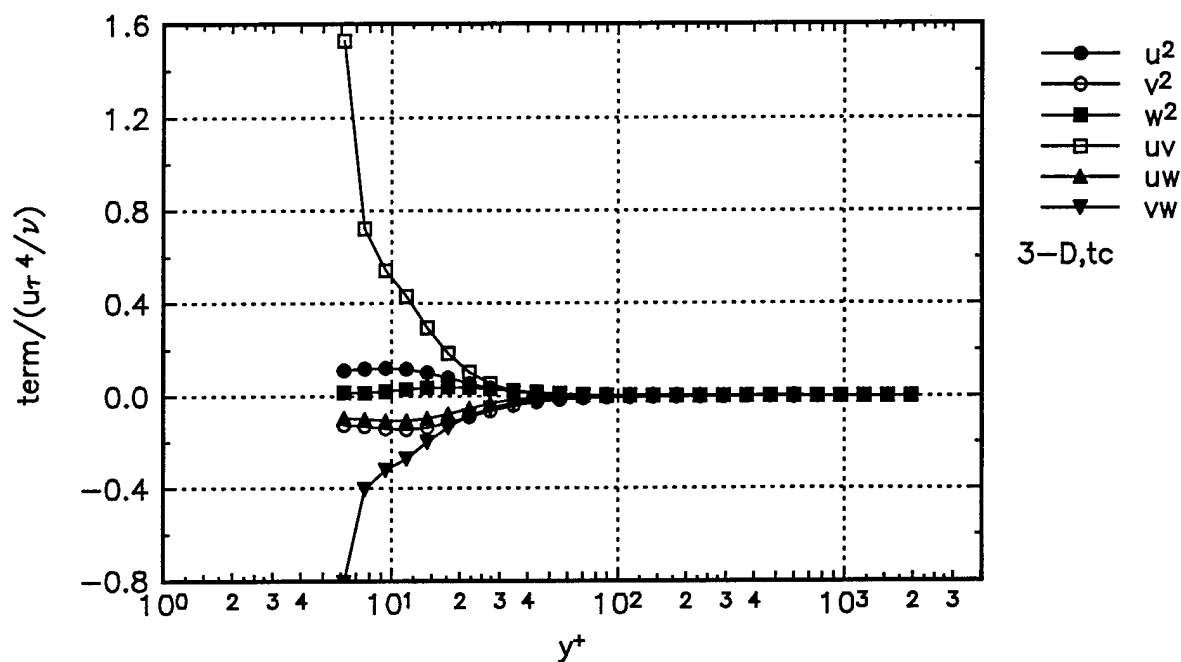
Figure 131. Near-wall correction to the pressure-strain rate distribution calculated using Launder-Reece-Rodi (1975) model for Separation station in tunnel coordinates. $\overline{u^2}$, ●; $\overline{v^2}$, O; $\overline{w^2}$, ■; $\overline{uv}$, □; $\overline{uw}$, ▲; $\overline{vw}$, ▼.

pressure—strain near wall correction terms for 3D—vor by LRRSL
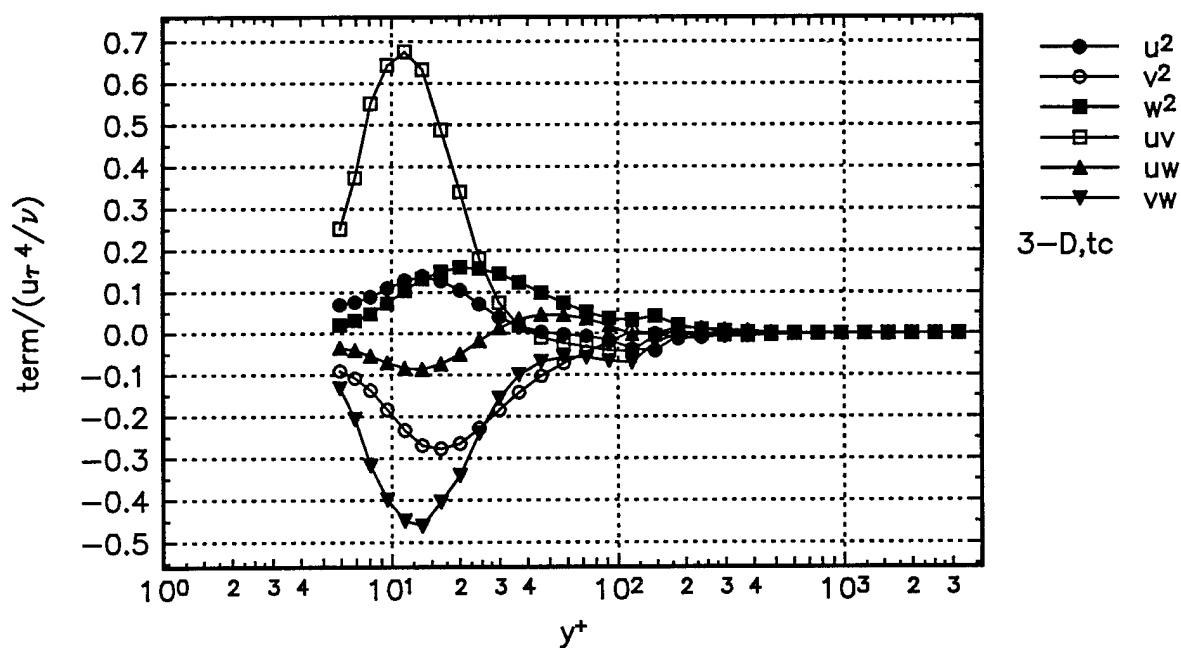
Figure 132. Near-wall correction to the pressure-strain rate distribution calculated using Launder-Reece-Rodi (1975) model for Vortex station in tunnel coordinates. $\overline{u^2}$, ●; $\overline{v^2}$, O; $\overline{w^2}$, ■; $\overline{uv}$, □; $\overline{uw}$, ▲; $\overline{vw}$, ▼.

Figures

Near wall correction of Launder-Reece-Rodi Shih-Lumley paper applied for all the models
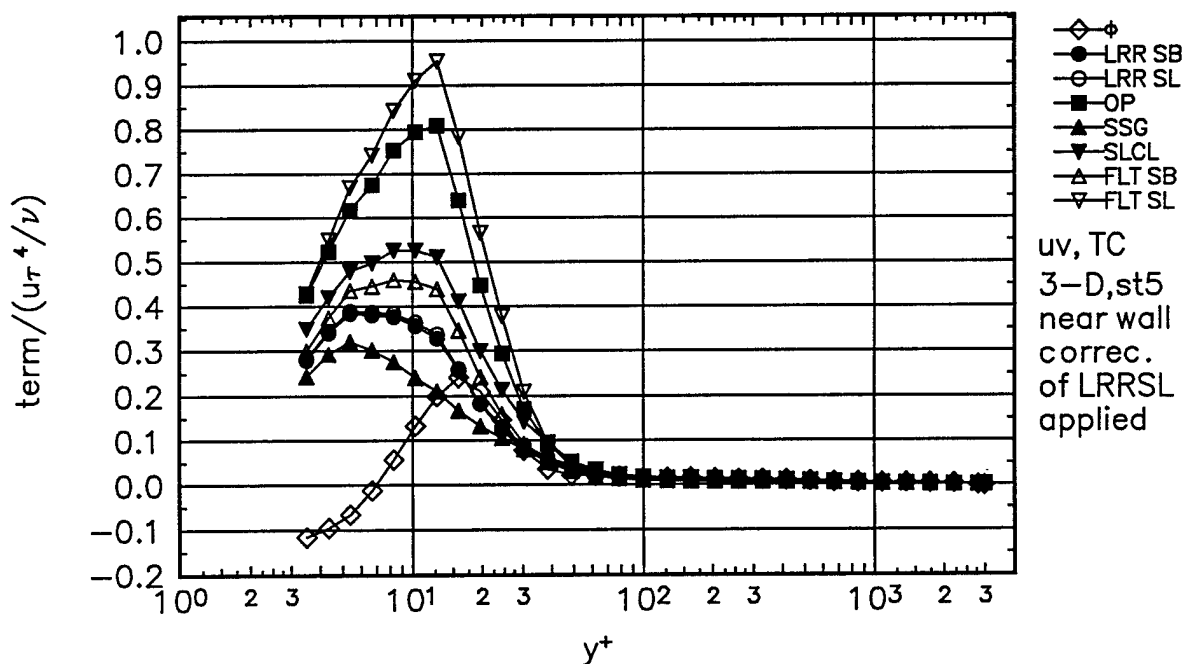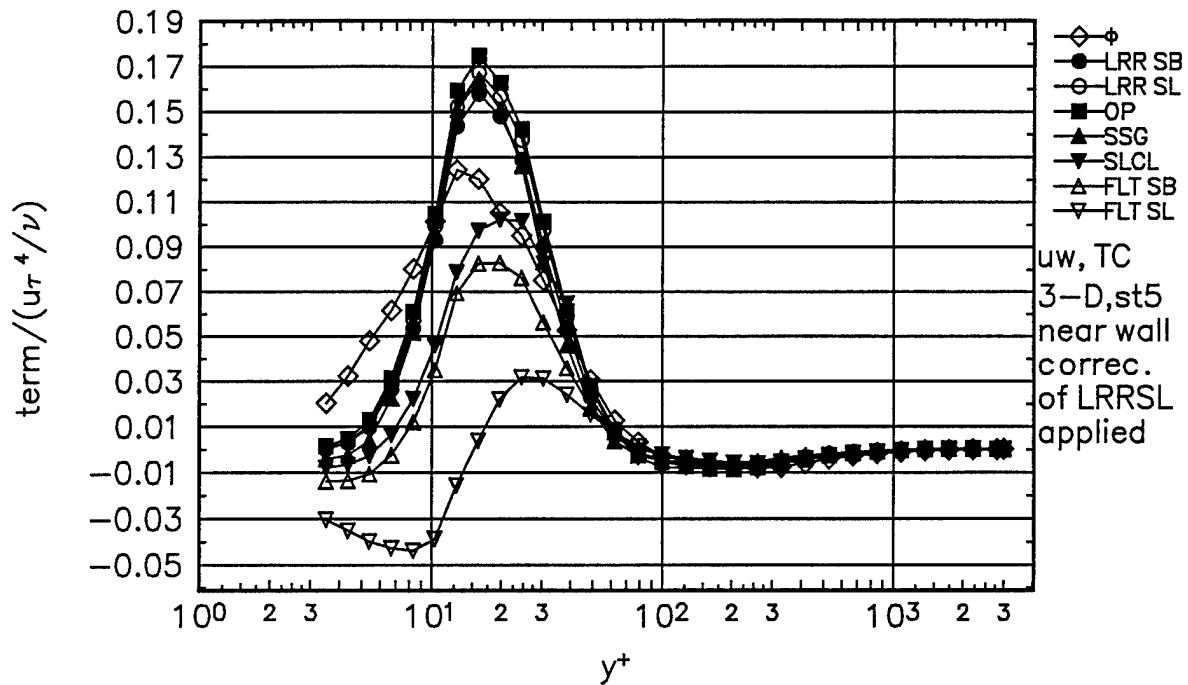

Figure 133. Comparison of $\overline{u^2}$ normal stress transport experimental pressure-strain term ◊, to theoretical pressure-strain terms for the 2-D station. Gibson-Launder, ●; Launder-Reece-Rodi (LRR), O; Oberlack-Peters (OP), ■; Speziale-Sarkar-Gatski (SSG), ▲; Shih-Lumley/Choi-Lumley (SLCL), ▼; Fu-Launder-Tselepidakis 1 (FLT1), △; Fu-Launder-Tselepidakis 2 (FLT2), ▽. Near-wall corrections of Launder-Reece-Rodi (1975), dissipation is assumed isotropic.
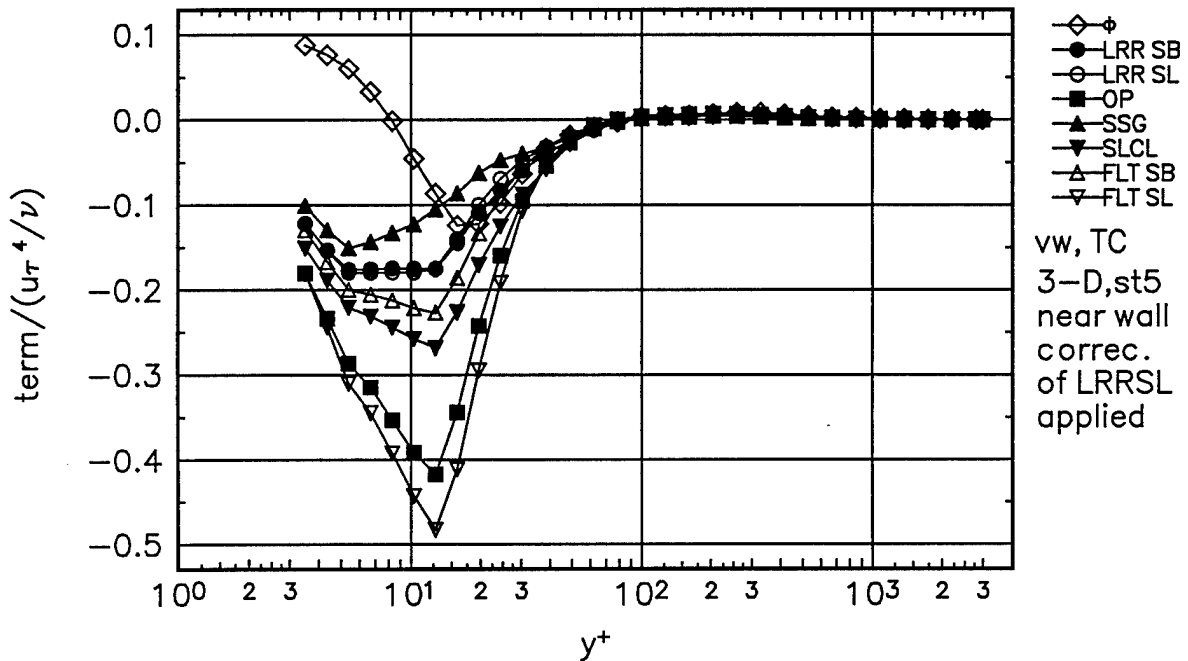

Figure 134. Comparison of $\overline{v^2}$ normal stress transport experimental pressure-strain term ◊, to theoretical pressure-strain terms for the 2-D station. Gibson-Launder, ●; Launder-Reece-Rodi (LRR), O; Oberlack-Peters (OP), ■; Speziale-Sarkar-Gatski (SSG), ▲; Shih-Lumley/Choi-Lumley (SLCL), ▼; Fu-Launder-Tselepidakis 1 (FLT1), △; Fu-Launder-Tselepidakis 2 (FLT2), ▽. Near-wall corrections of Launder-Reece-Rodi (1975), dissipation is assumed isotropic.
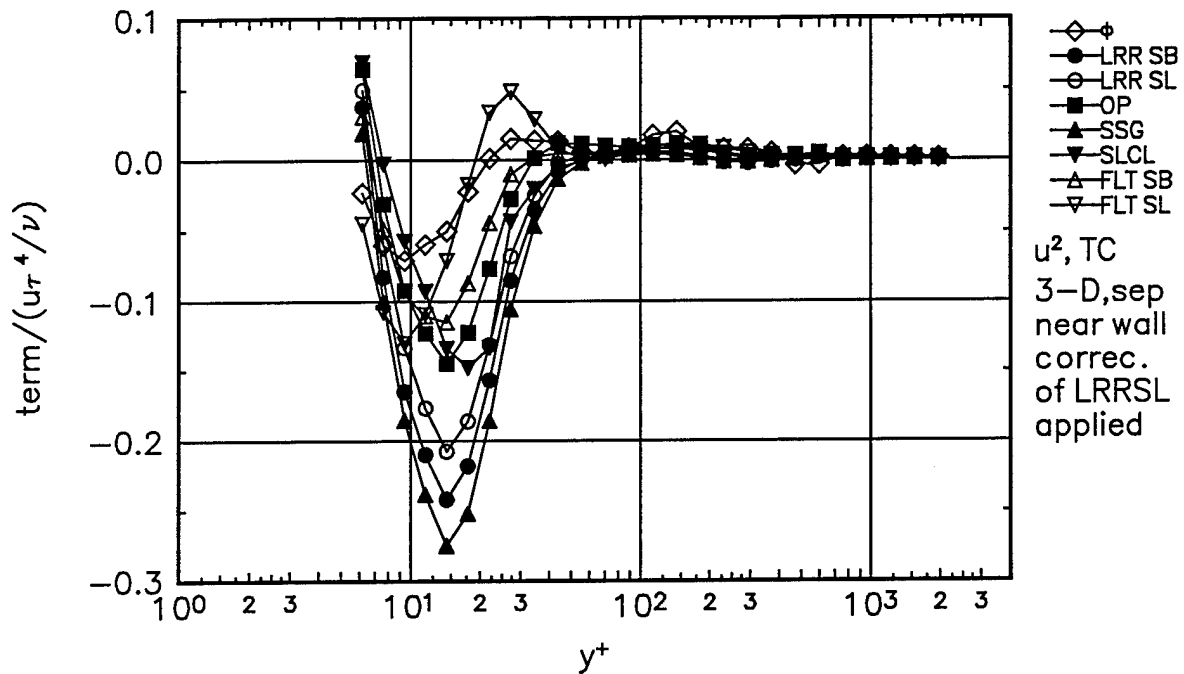
Figure 135. Comparison of $\overline{w^2}$ normal stress transport experimental pressure-strain term ◊, to theoretical pressure-strain terms for the 2-D station. Gibson-Launder, ●; Launder-Reece-Rodi (LRR), O; Oberlack-Peters (OP), ■; Speziale-Sarkar-Gatski (SSG), ▲; Shih-Lumley/Choi-Lumley (SLCL), ▼; Fu-Launder-Tselepidakis 1 (FLT1), △; Fu-Launder-Tselepidakis 2 (FLT2), ▽. Near-wall corrections of Launder-Reece-Rodi (1975), dissipation is assumed isotropic.

Figure 136. Comparison of $\overline{uv}$ shear stress transport experimental pressure-strain term ◊, to theoretical pressure-strain terms for the 2-D station. Gibson-Launder, ●; Launder-Reece-Rodi (LRR), O; Oberlack-Peters (OP), ■; Speziale-Sarkar-Gatski (SSG), ▲; Shih-Lumley/Choi-Lumley (SLCL), ▼; Fu-Launder-Tselepidakis 1 (FLT1), △; Fu-Launder-Tselepidakis 2 (FLT2), ▽. Near-wall corrections of Launder-Reece-Rodi (1975), dissipation is assumed zero.
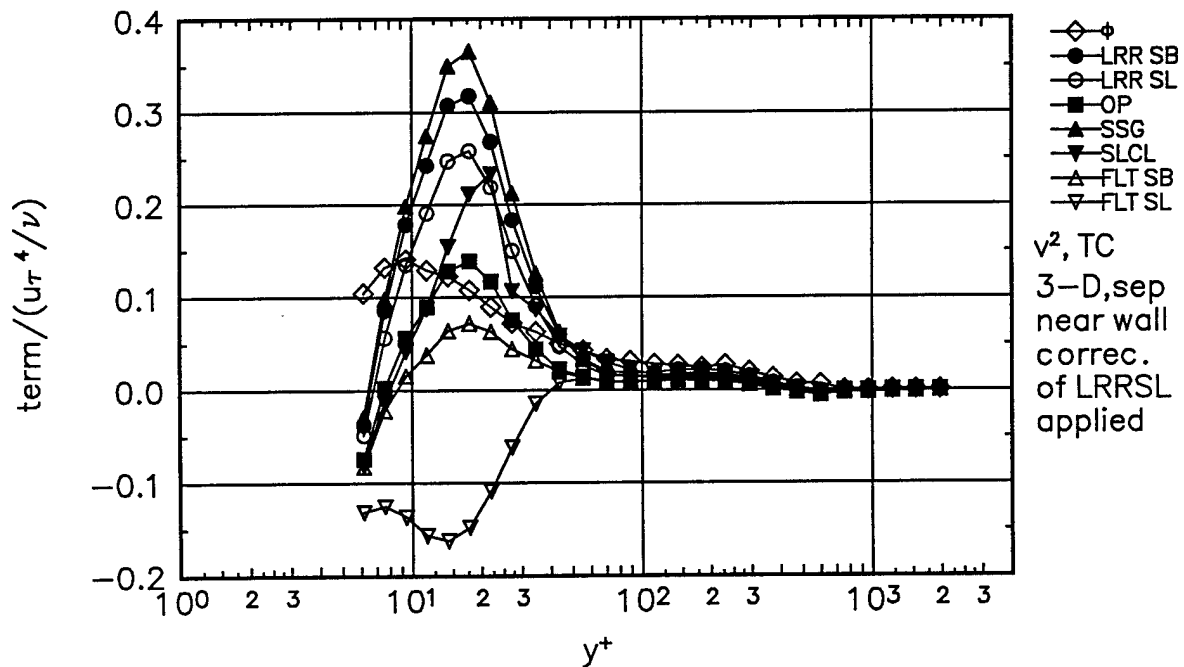
Figure 137. Comparison of $\overline{u^z}$ normal stress transport experimental pressure-strain term ◊, to theoretical pressure-strain terms for Station 5. Gibson-Launder, ●; Launder-Reece-Rodi (LRR), O; Oberlack-Peters (OP), ■; Speziale-Sarkar-Gatski (SSG), ▲; Shih-Lumley/Choi-Lumley (SLCL), ▼; Fu-Launder-Tselepidakis 1 (FLT1), △; Fu-Launder-Tselepidakis 2 (FLT2), ▽. Near-wall corrections of Launder-Reece-Rodi (1975), dissipation is assumed isotropic.
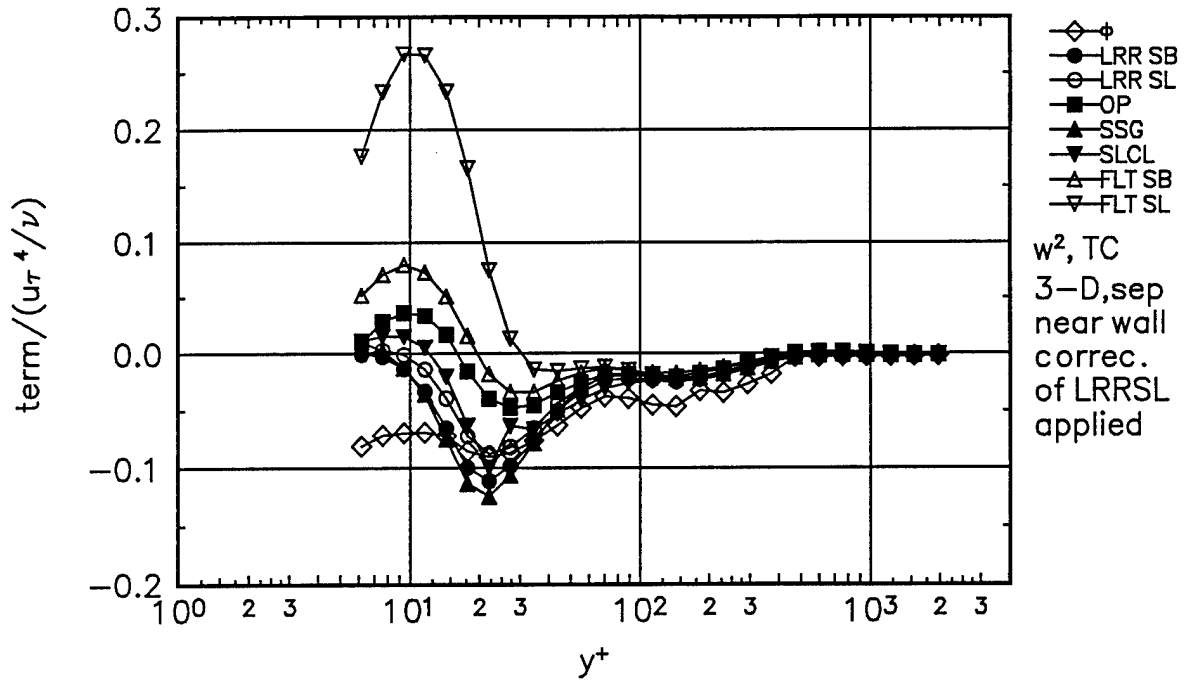

Figure 138. Comparison of $\overline{v^z}$ normal stress transport experimental pressure-strain term ◊, to theoretical pressure-strain terms for Station 5. Gibson-Launder, ●; Launder-Reece-Rodi (LRR), O; Oberlack-Peters (OP), ■; Speziale-Sarkar-Gatski (SSG), ▲; Shih-Lumley/Choi-Lumley (SLCL), ▼; Fu-Launder-Tselepidakis 1 (FLT1), △; Fu-Launder-Tselepidakis 2 (FLT2), ▽. Near-wall corrections of Launder-Reece-Rodi (1975), dissipation is assumed isotropic.
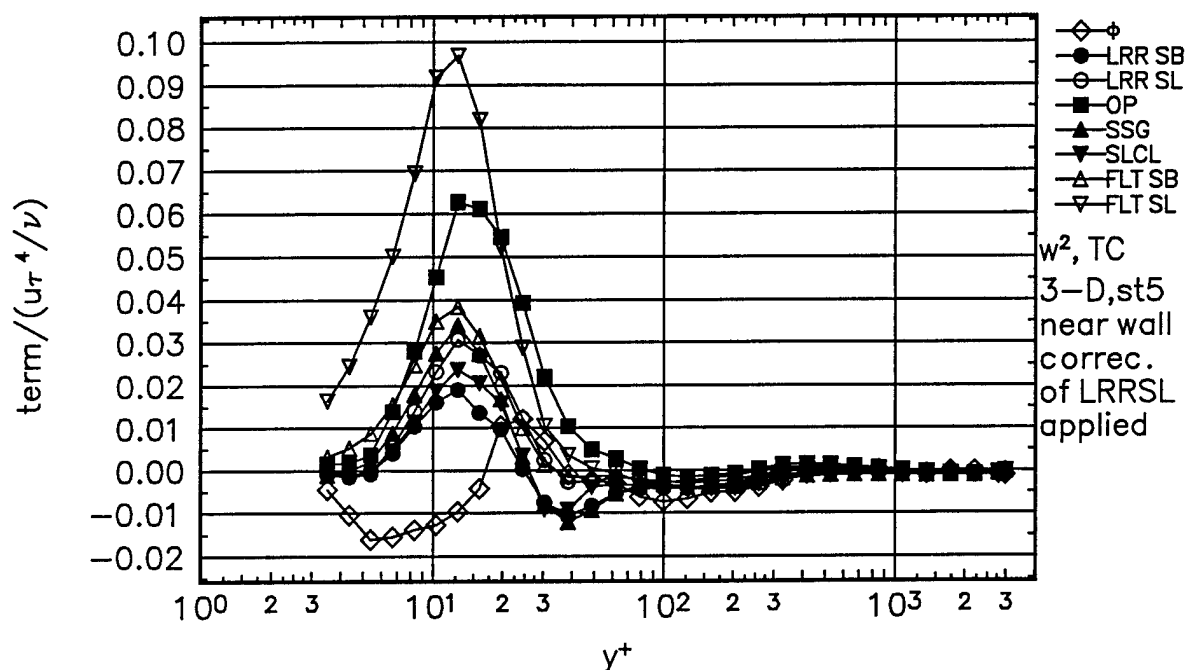
Figure 139. Comparison of $\overline{w^2}$ normal stress transport experimental pressure-strain term ◊, to theoretical pressure-strain terms for Station 5. Gibson-Launder, ●; Launder-Reece-Rodi (LRR), O; Oberlack-Peters (OP), ■; Speziale-Sarkar-Gatski (SSG), ▲; Shih-Lumley/Choi-Lumley (SLCL), ▼; Fu-Launder-Tselepidakis 1 (FLT1), ▵; Fu-Launder-Tselepidakis 2 (FLT2), ▽. Near-wall corrections of Launder-Reece-Rodi (1975), dissipation is assumed isotropic.
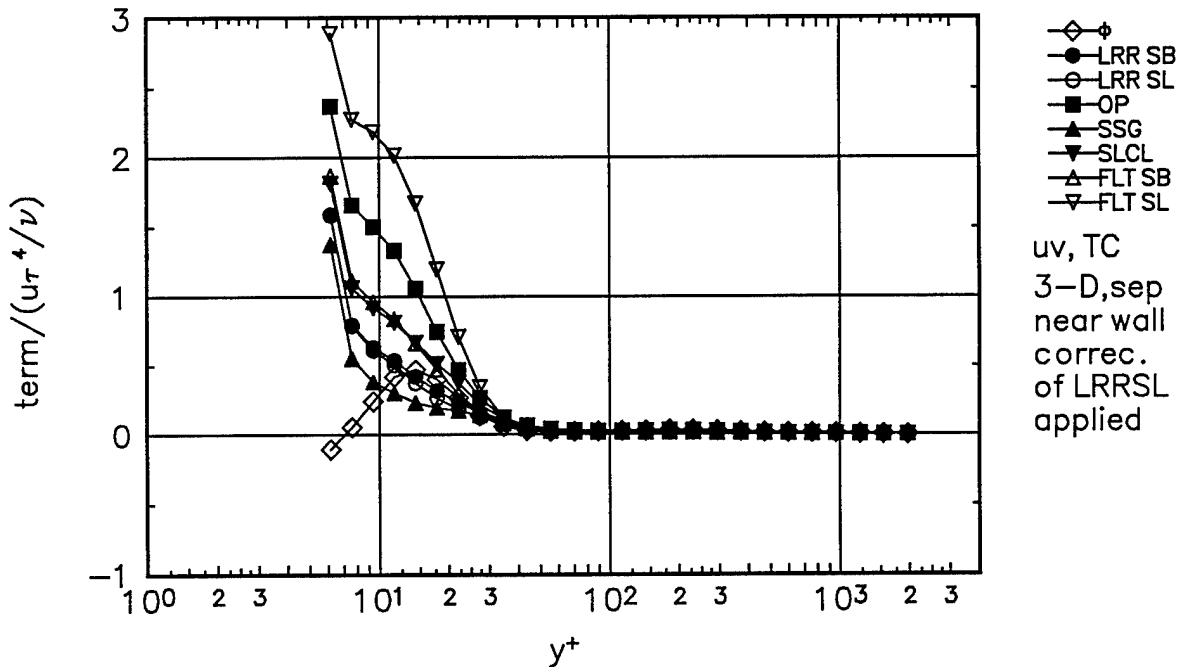
Figure 140. Comparison of $\overline{uv}$ shear stress transport experimental pressure-strain term ◊, to theoretical pressure-strain terms for Station 5. Gibson-Launder, ●; Launder-Reece-Rodi (LRR), O; Oberlack-Peters (OP), ■; Speziale-Sarkar-Gatski (SSG), ▲; Shih-Lumley/Choi-Lumley (SLCL), ▼; Fu-Launder-Tselepidakis 1 (FLT1), ▵; Fu-Launder-Tselepidakis 2 (FLT2), ▽. Near-wall corrections of Launder-Reece-Rodi (1975), dissipation is assumed zero.
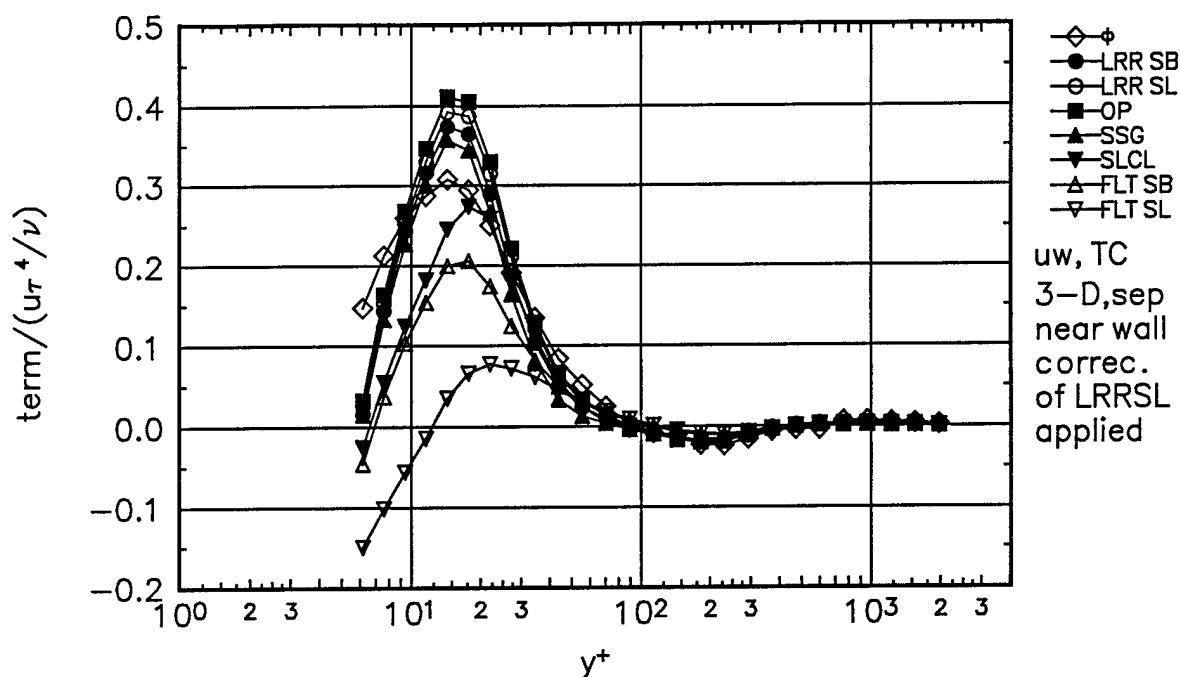
Figure 141. Comparison of $\overline{uw}$ shear stress transport experimental pressure-strain term ◊, to theoretical pressure-strain terms for Station 5. Gibson-Launder, ●; Launder-Reece-Rodi (LRR), ○; Oberlack-Peters (OP), ■; Speziale-Sarkar-Gatski (SSG), ▲; Shih-Lumley/Choi-Lumley (SLCL), ▼; Fu-Launder-Tselepidakis 1 (FLT1), △; Fu-Launder-Tselepidakis 2 (FLT2), ▽. Near-wall corrections of Launder-Reece-Rodi (1975), dissipation is assumed zero.
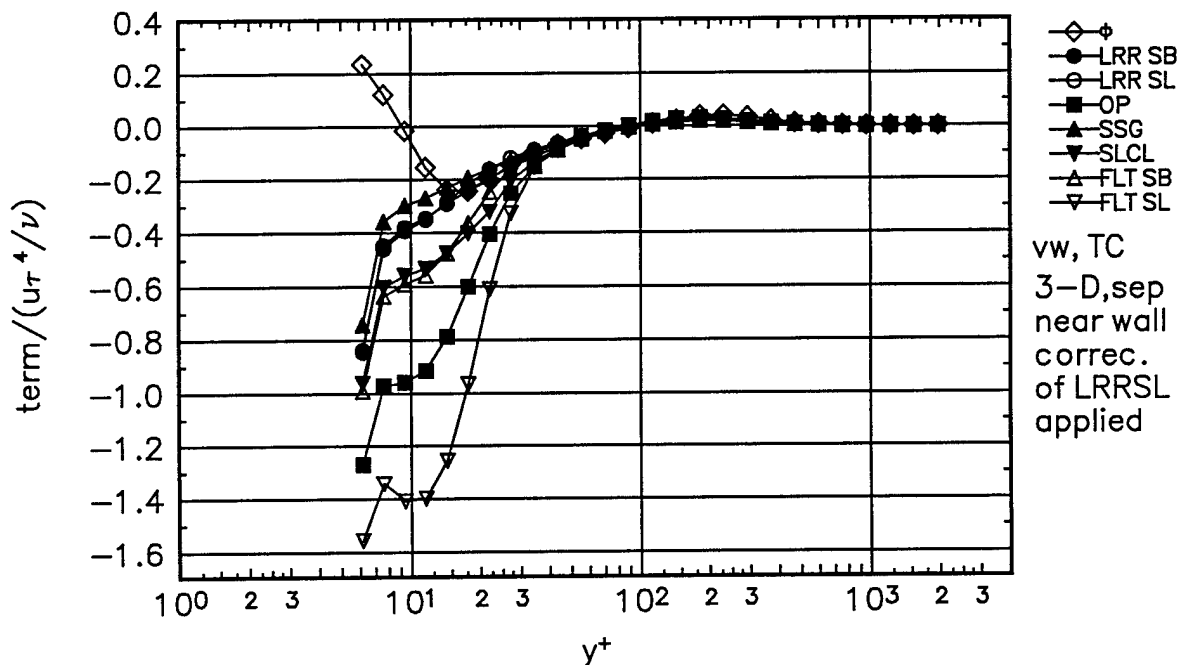

Figure 142. Comparison of $\overline{vw}$ shear stress transport experimental pressure-strain term ◊, to theoretical pressure-strain terms for Station 5. Gibson-Launder, ●; Launder-Reece-Rodi (LRR), ○; Oberlack-Peters (OP), ■; Speziale-Sarkar-Gatski (SSG), ▲; Shih-Lumley/Choi-Lumley (SLCL), ▼; Fu-Launder-Tselepidakis 1 (FLT1), △; Fu-Launder-Tselepidakis 2 (FLT2), ▽. Near-wall corrections of Launder-Reece-Rodi (1975), dissipation is assumed zero.
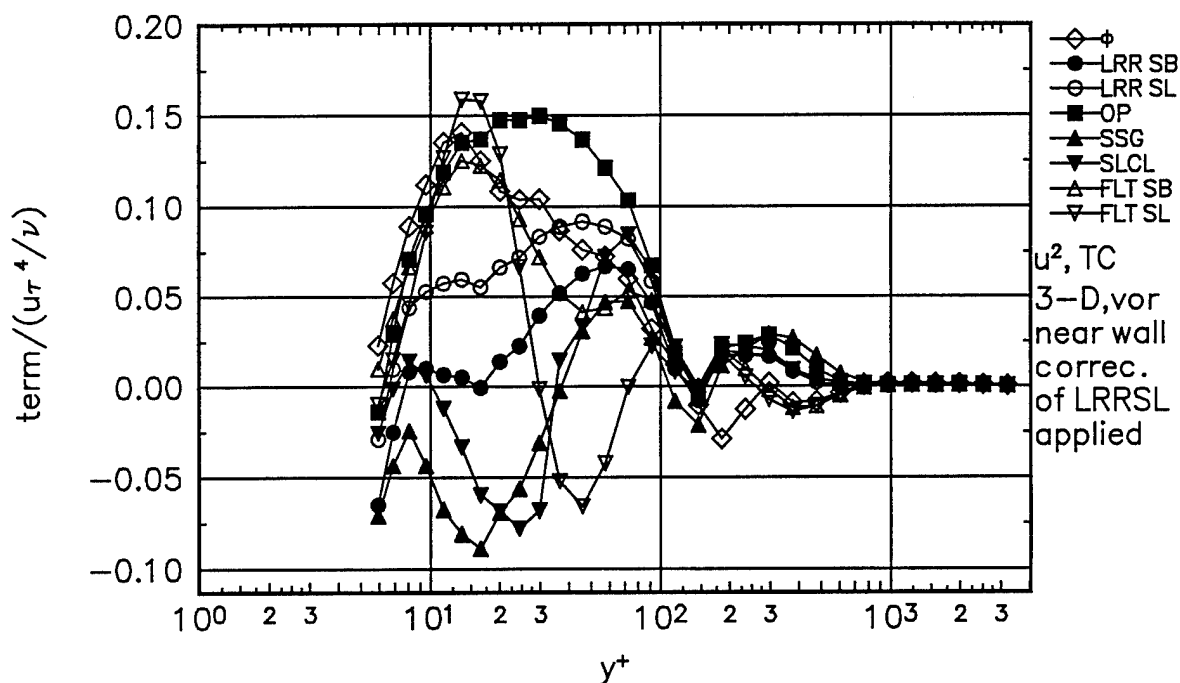
Figure 143. Comparison of $\overline{u^2}$ normal stress transport experimental pressure-strain term ◊, to theoretical pressure-strain terms for Separation station. Gibson-Launder, ●; Launder-Reece-Rodi (LRR), O; Oberlack-Peters (OP), ■; Speziale-Sarkar-Gatski (SSG), ▲; Shih-Lumley/Choi-Lumley (SLCL), ▼; Fu-Launder-Tselepidakis 1 (FLT1), △; Fu-Launder-Tselepidakis 2 (FLT2), ▽. Near-wall corrections of Launder-Reece-Rodi (1975), dissipation is assumed isotropic.
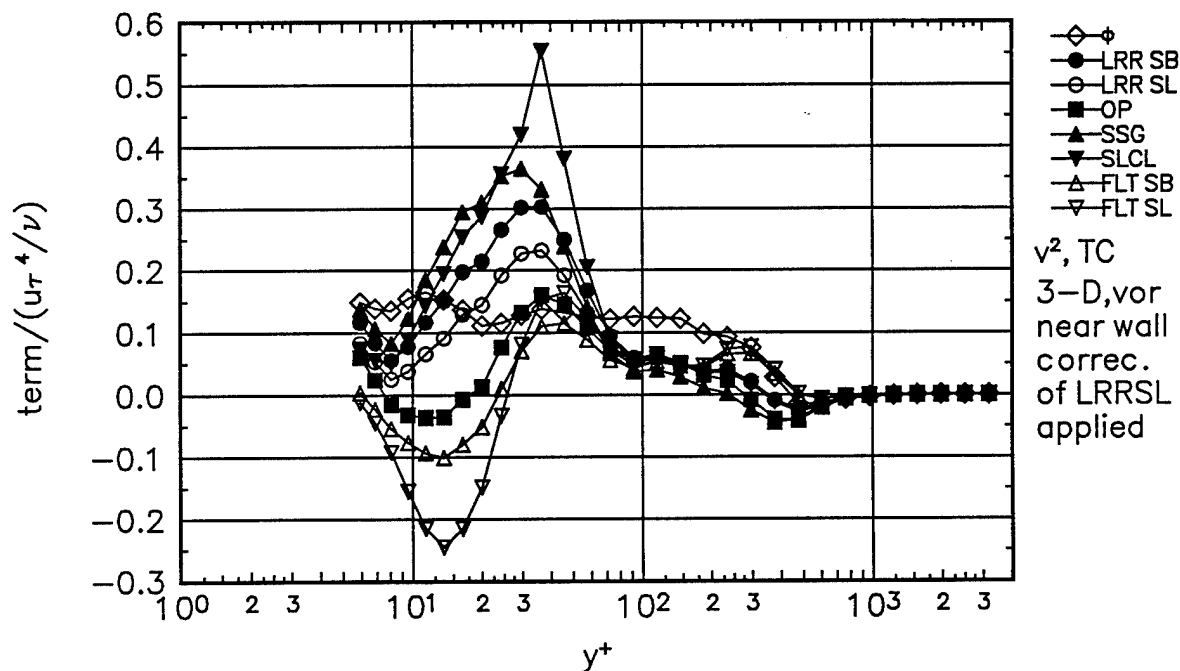

Figure 144. Comparison of $\overline{v^2}$ normal stress transport experimental pressure-strain term ◊, to theoretical pressure-strain terms for Separation station. Gibson-Launder, ●; Launder-Reece-Rodi (LRR), O; Oberlack-Peters (OP), ■; Speziale-Sarkar-Gatski (SSG), ▲; Shih-Lumley/Choi-Lumley (SLCL), ▼; Fu-Launder-Tselepidakis 1 (FLT1), △; Fu-Launder-Tselepidakis 2 (FLT2), ▽. Near-wall corrections of Launder-Reece-Rodi (1975), dissipation is assumed isotropic.
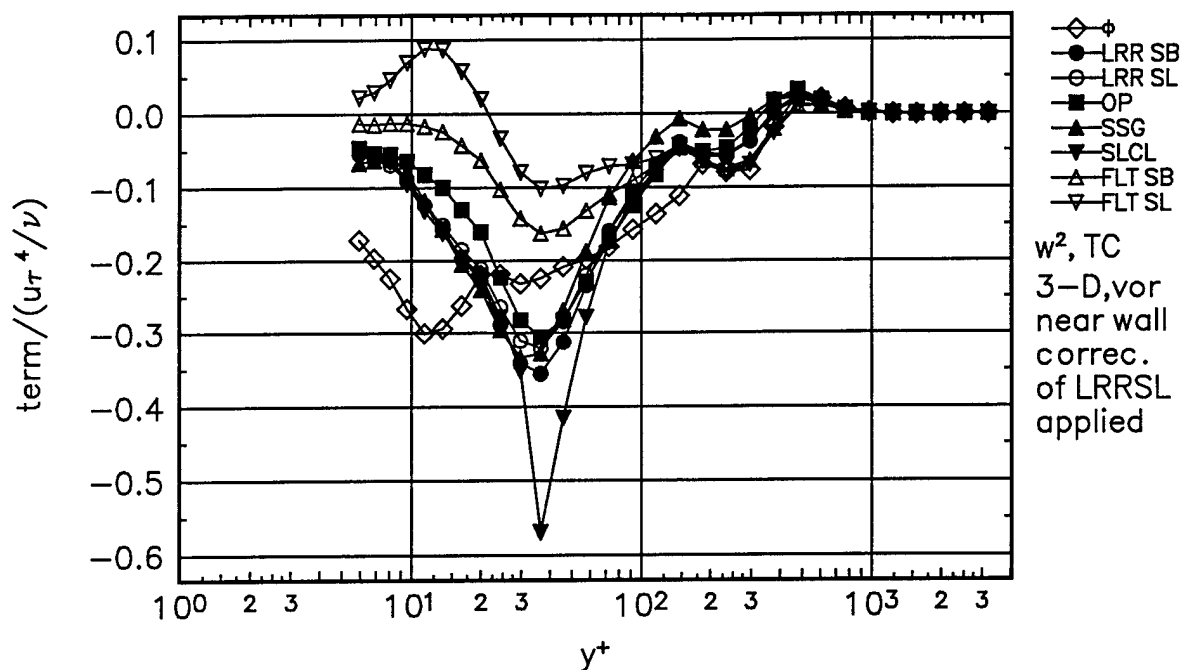
Figure 145. Comparison of $\overline{w^2}$ normal stress transport experimental pressure-strain term ◊, to theoretical pressure-strain terms for Separation station. Gibson-Launder, ●; Launder-Reece-Rodi (LRR), O; Oberlack-Peters (OP), ■; Speziale-Sarkar-Gatski (SSG), ▲; Shih-Lumley/Choi-Lumley (SLCL), ▼; Fu-Launder-Tselepidakis 1 (FLT1), △; Fu-Launder-Tselepidakis 2 (FLT2), ▽. Near-wall corrections of Launder-Reece-Rodi (1975), dissipation is assumed isotropic.

Figure 146. Comparison of $\overline{uv}$ shear stress transport experimental pressure-strain term ◊, to theoretical pressure-strain terms for Separation station. Gibson-Launder, ●; Launder-Reece-Rodi (LRR), O; Oberlack-Peters (OP), ■; Speziale-Sarkar-Gatski (SSG), ▲; Shih-Lumley/Choi-Lumley (SLCL), ▼; Fu-Launder-Tselepidakis 1 (FLT1), △; Fu-Launder-Tselepidakis 2 (FLT2), ▽. Near-wall corrections of Launder-Reece-Rodi (1975), dissipation is assumed zero.
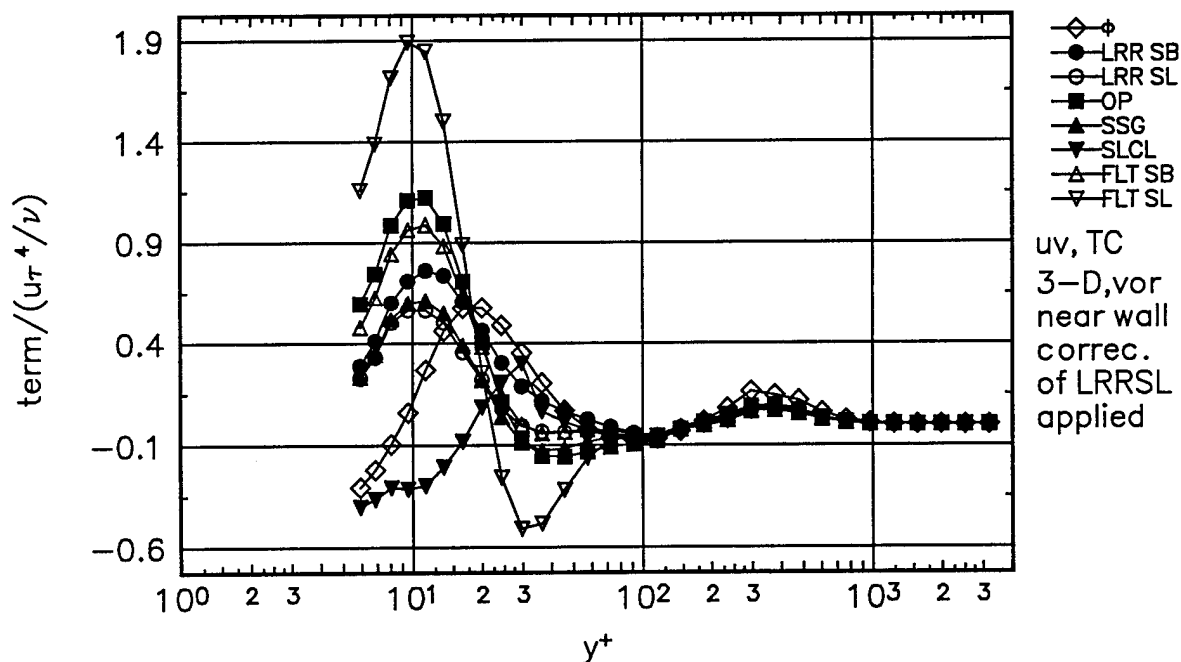
Figures

Figure 147. Comparison of $\overline{uw}$ shear stress transport experimental pressure-strain term ◊, to theoretical pressure-strain terms for Separation station. Gibson-Launder, ●; Launder-Reece-Rodi (LRR), O; Oberlack-Peters (OP), ■; Speziale-Sarkar-Gatski (SSG), ▲; Shih-Lumley/Choi-Lumley (SLCL), ▼; Fu-Launder-Tselepidakis 1 (FLT1), △; Fu-Launder-Tselepidakis 2 (FLT2), ▽. Near-wall corrections of Launder-Reece-Rodi (1975), dissipation is assumed zero.
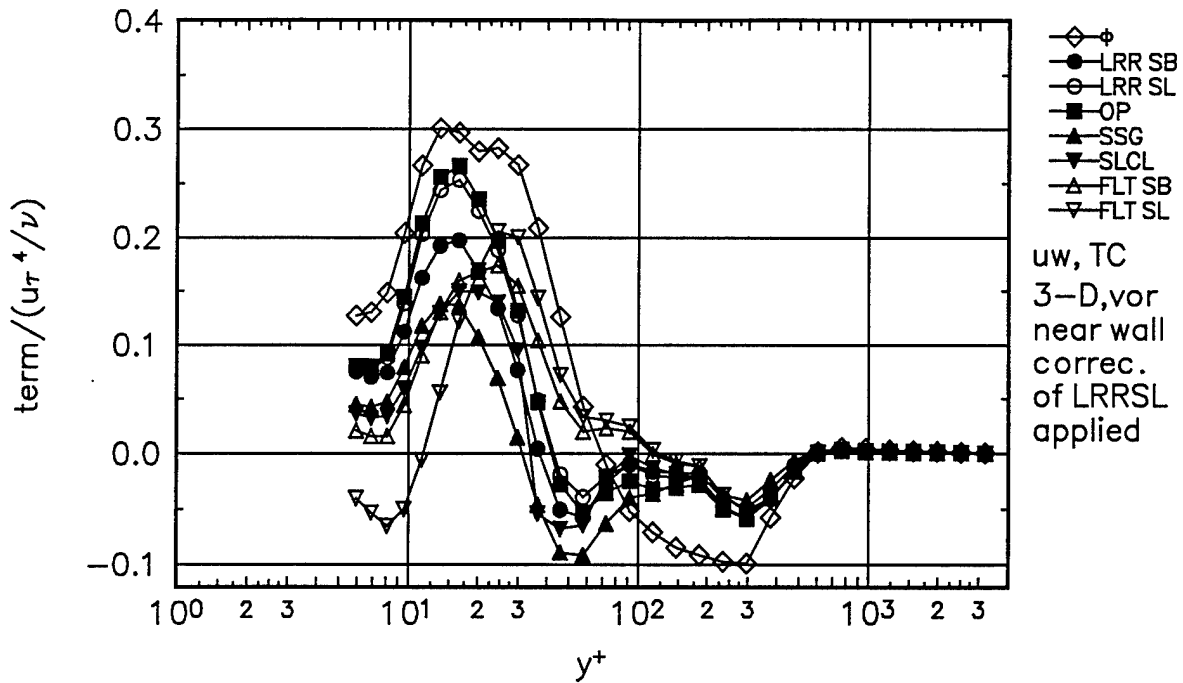

Figure 148. Comparison of $\overline{vw}$ shear stress transport experimental pressure-strain term ◊, to theoretical pressure-strain terms for Separation station. Gibson-Launder, ●; Launder-Reece-Rodi (LRR), O; Oberlack-Peters (OP), ■; Speziale-Sarkar-Gatski (SSG), ▲; Shih-Lumley/Choi-Lumley (SLCL), ▼; Fu-Launder-Tselepidakis 1 (FLT1), △; Fu-Launder-Tselepidakis 2 (FLT2), ▽. Near-wall corrections of Launder-Reece-Rodi (1975), dissipation is assumed zero.
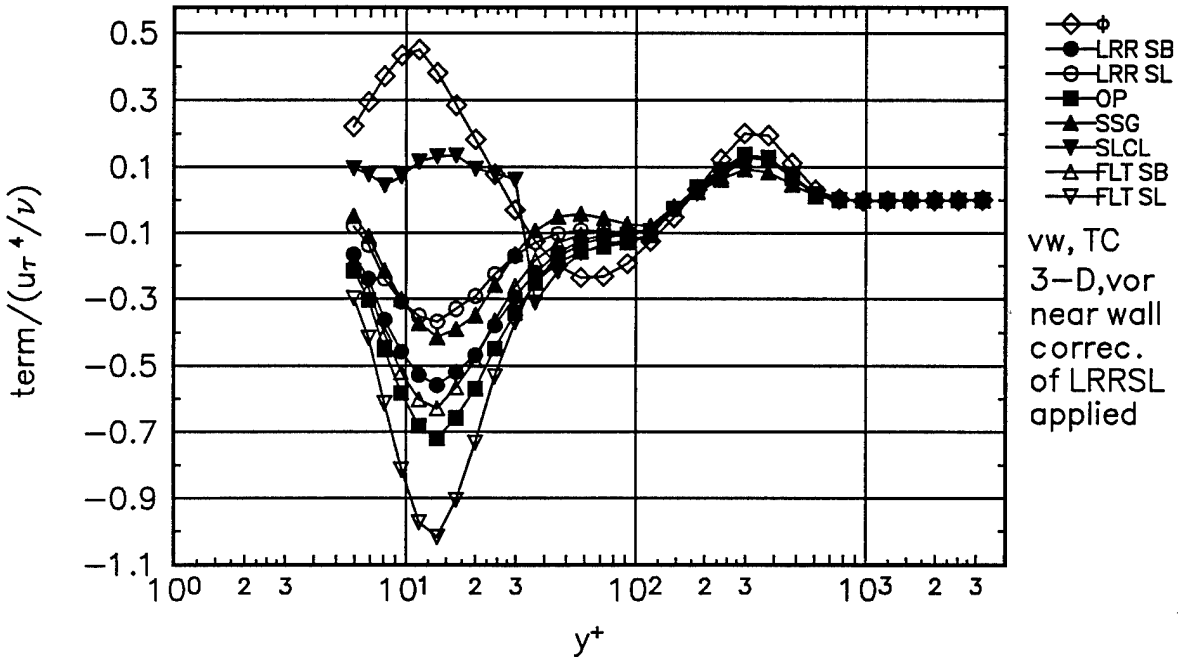
Figure 149. Comparison of $\overline{u^2}$ normal stress transport experimental pressure-strain term ◊, to theoretical pressure-strain terms for Vortex station. Gibson-Launder, ●; Launder-Reece-Rodi (LRR), O; Oberlack-Peters (OP), ■; Speziale-Sarkar-Gatski (SSG), ▲; Shih-Lumley/Choi-Lumley (SLCL), ▼; Fu-Launder-Tselepidakis 1 (FLT1), ▵; Fu-Launder-Tselepidakis 2 (FLT2), ▽. Near-wall corrections of Launder-Reece-Rodi (1975), dissipation is assumed isotropic.

Figure 150. Comparison of $\overline{v^2}$ normal stress transport experimental pressure-strain term ◊, to theoretical pressure-strain terms for Vortex station. Gibson-Launder, ●; Launder-Reece-Rodi (LRR), O; Oberlack-Peters (OP), ■; Speziale-Sarkar-Gatski (SSG), ▲; Shih-Lumley/Choi-Lumley (SLCL), ▼; Fu-Launder-Tselepidakis 1 (FLT1), ▵; Fu-Launder-Tselepidakis 2 (FLT2), ▽. Near-wall corrections of Launder-Reece-Rodi (1975), dissipation is assumed isotropic.
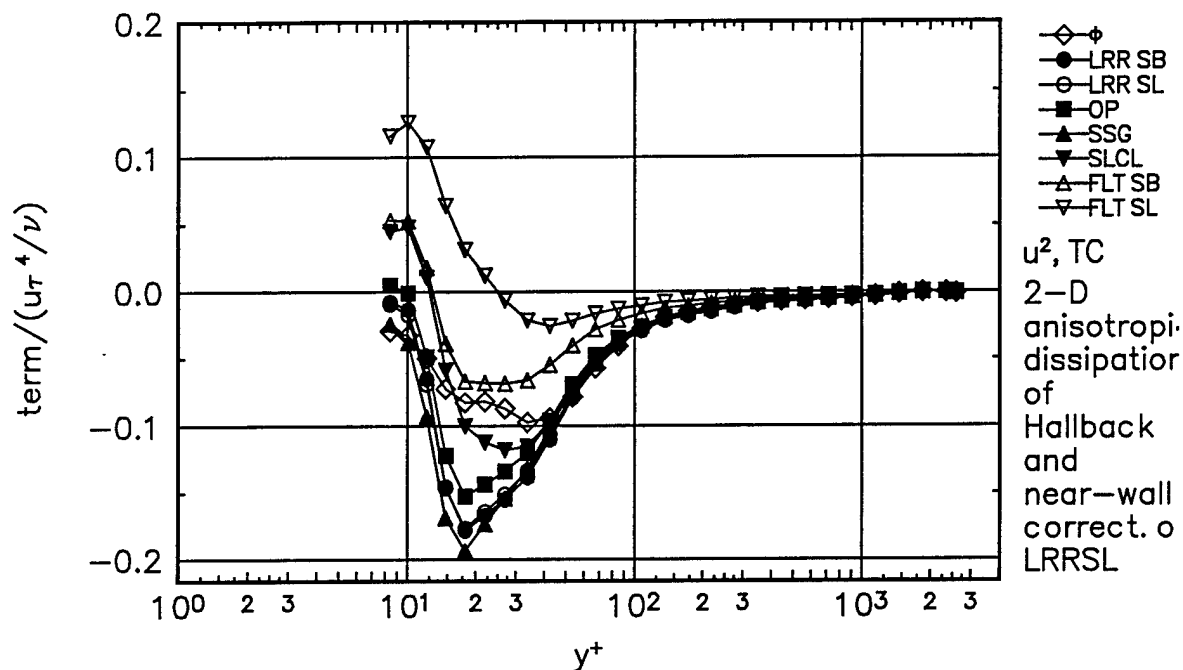
Figure 151. Comparison of $\overline{w^2}$ normal stress transport experimental pressure-strain term ◊, to theoretical pressure-strain terms for Vortex station. Gibson-Launder, ●; Launder-Reece-Rodi (LRR), O; Oberlack-Peters (OP), ■; Speziale-Sarkar-Gatski (SSG), ▲; Shih-Lumley/Choi-Lumley (SLCL), ▼; Fu-Launder-Tselepidakis 1 (FLT1), ▵; Fu-Launder-Tselepidakis 2 (FLT2), ▽. Near-wall corrections of Launder-Reece-Rodi (1975), dissipation is assumed isotropic.
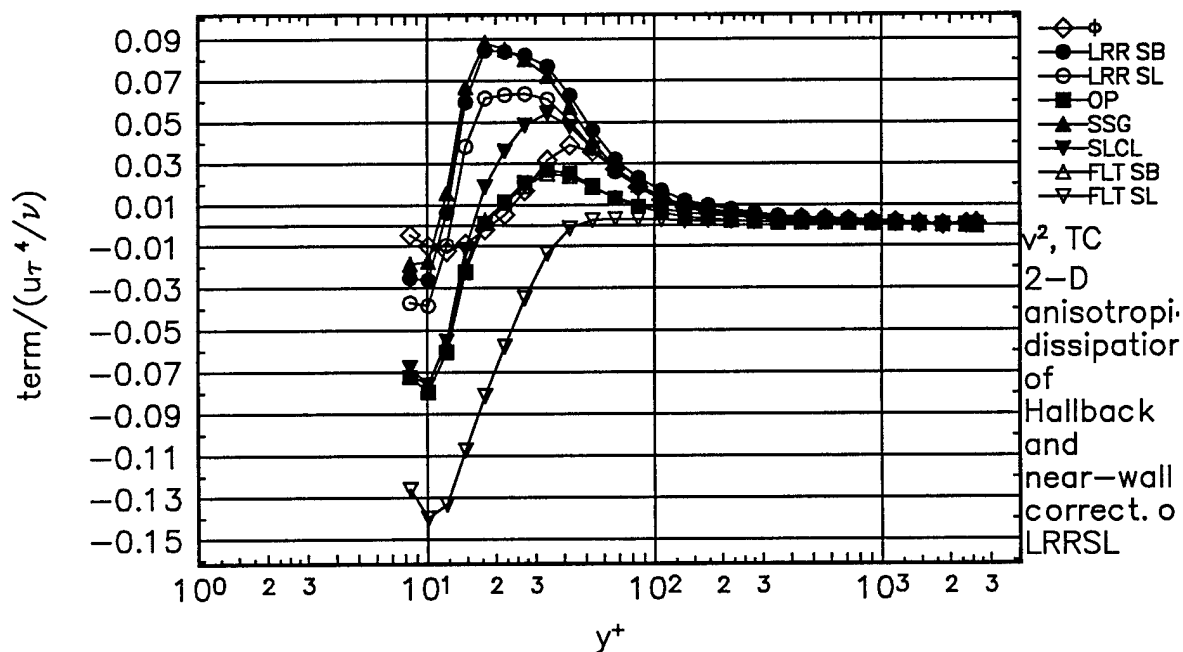

Figure 152. Comparison of $\overline{uv}$ shear stress transport experimental pressure-strain term ◊, to theoretical pressure-strain terms for Vortex station. Gibson-Launder, ●; Launder-Reece-Rodi (LRR), O; Oberlack-Peters (OP), ■; Speziale-Sarkar-Gatski (SSG), ▲; Shih-Lumley/Choi-Lumley (SLCL), ▼; Fu-Launder-Tselepidakis 1 (FLT1), ▵; Fu-Launder-Tselepidakis 2 (FLT2), ▽. Near-wall corrections of Launder-Reece-Rodi (1975), dissipation is assumed zero.
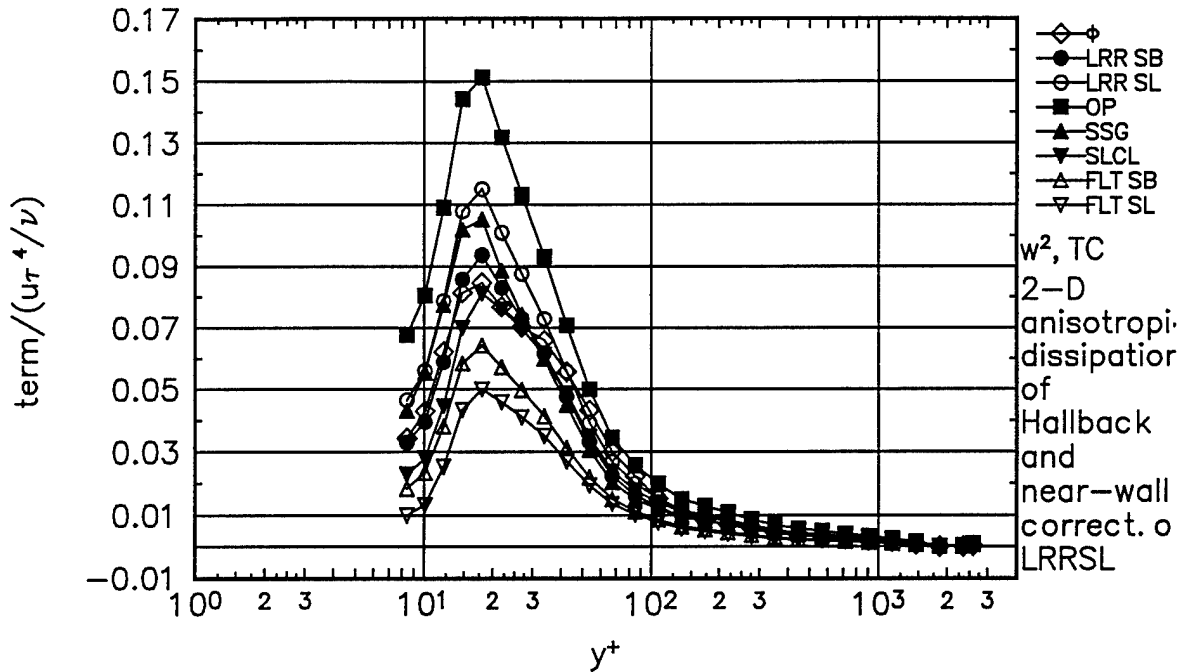
Figure 153. Comparison of $\overline{uw}$ shear stress transport experimental pressure-strain term ◊, to theoretical pressure-strain terms for Vortex station. Gibson-Launder, ●; Launder-Reece-Rodi (LRR), O; Oberlack-Peters (OP), ■; Speziale-Sarkar-Gatski (SSG), ▲; Shih-Lumley/Choi-Lumley (SLCL), ▼; Fu-Launder-Tselepidakis 1 (FLT1), ▵; Fu-Launder-Tselepidakis 2 (FLT2), ▽. Near-wall corrections of Launder-Reece-Rodi (1975), dissipation is assumed zero.
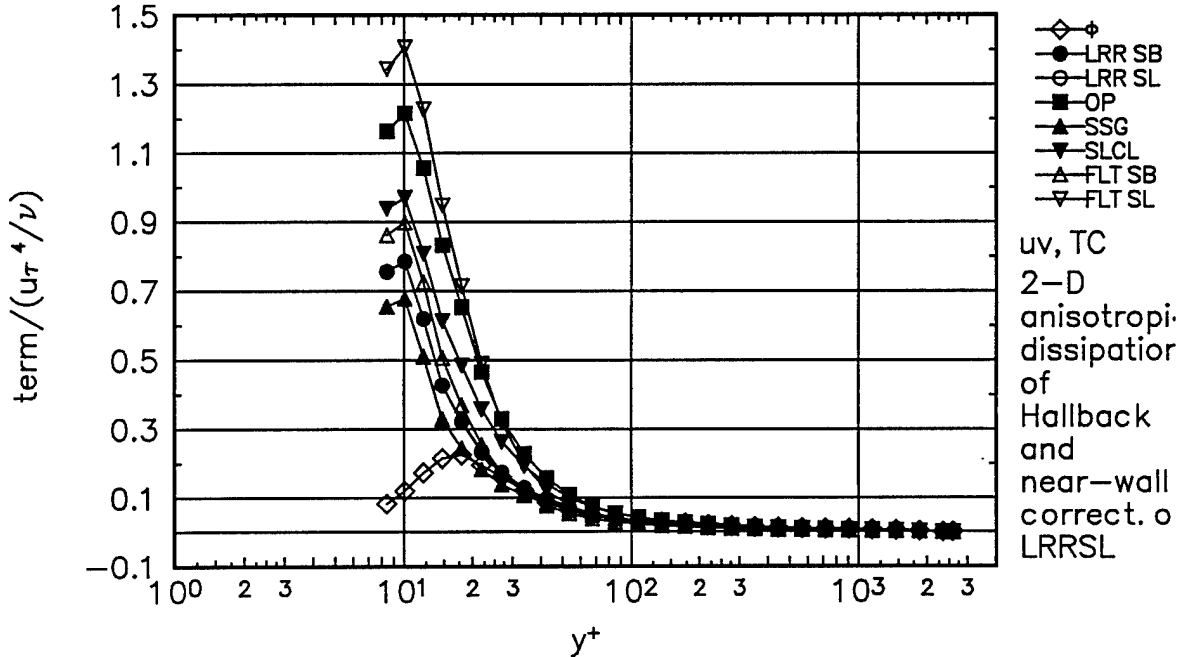

Figure 154. Comparison of $\overline{vw}$ shear stress transport experimental pressure-strain term ◊, to theoretical pressure-strain terms for Vortex station. Gibson-Launder, ●; Launder-Reece-Rodi (LRR), O; Oberlack-Peters (OP), ■; Speziale-Sarkar-Gatski (SSG), ▲; Shih-Lumley/Choi-Lumley (SLCL), ▼; Fu-Launder-Tselepidakis 1 (FLT1), ▵; Fu-Launder-Tselepidakis 2 (FLT2), ▽. Near-wall corrections of Launder-Reece-Rodi (1975), dissipation is assumed zero.

Both near wall correction of LRR and anisotropic dissipation rate of Hallback are applied.

Figure 155. Comparison of $\overline{u^2}$ normal stress transport experimental pressure-strain term ◊, to theoretical pressure-strain terms for the 2-D station. Gibson-Launder, ●; Launder-Reece-Rodi (LRR), O; Oberlack-Peters (OP), ■; Speziale-Sarkar-Gatski (SSG), ▲; Shih-Lumley/Choi-Lumley (SLCL), ▼; Fu-Launder-Tselepidakis 1 (FLT1), △; Fu-Launder-Tselepidakis 2 (FLT2), ▽. Near-wall corrections of Launder-Reece-Rodi (1975), anisotropic dissipation of Hallbäck (1990).
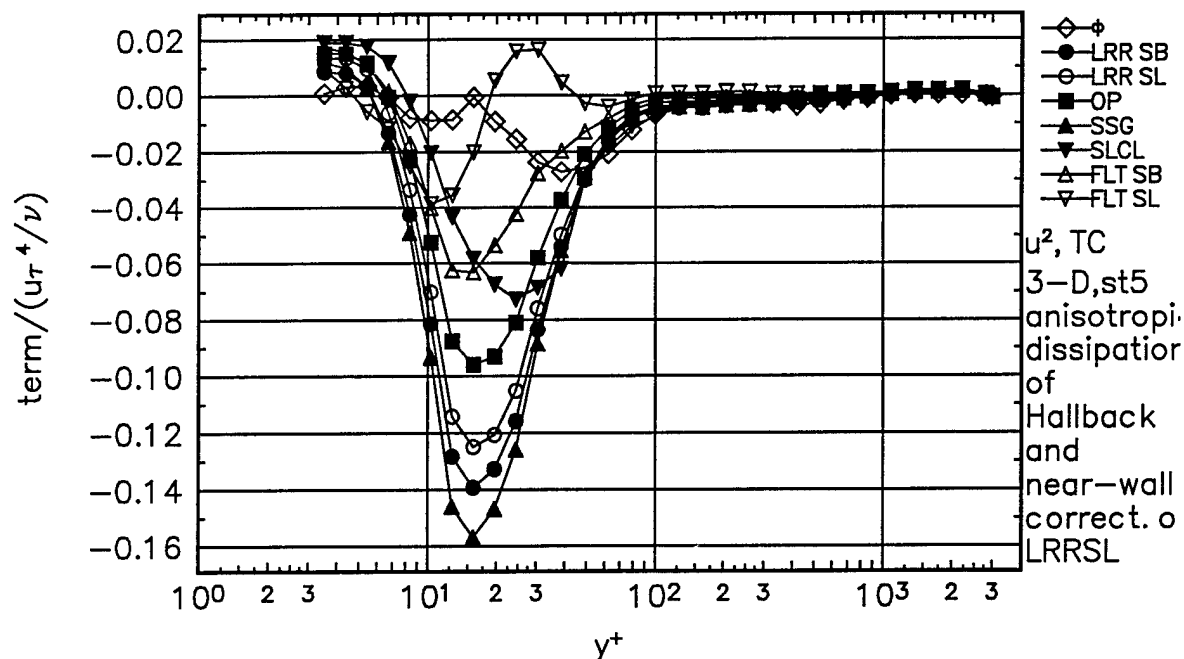

Figure 156. Comparison of $\overline{v^2}$ normal stress transport experimental pressure-strain term ◊, to theoretical pressure-strain terms for the 2-D station. Gibson-Launder, ●; Launder-Reece-Rodi (LRR), O; Oberlack-Peters (OP), ■; Speziale-Sarkar-Gatski (SSG), ▲; Shih-Lumley/Choi-Lumley (SLCL), ▼; Fu-Launder-Tselepidakis 1 (FLT1), △; Fu-Launder-Tselepidakis 2 (FLT2), ▽. Near-wall corrections of Launder-Reece-Rodi (1975), anisotropic dissipation of Hallbäck (1990).
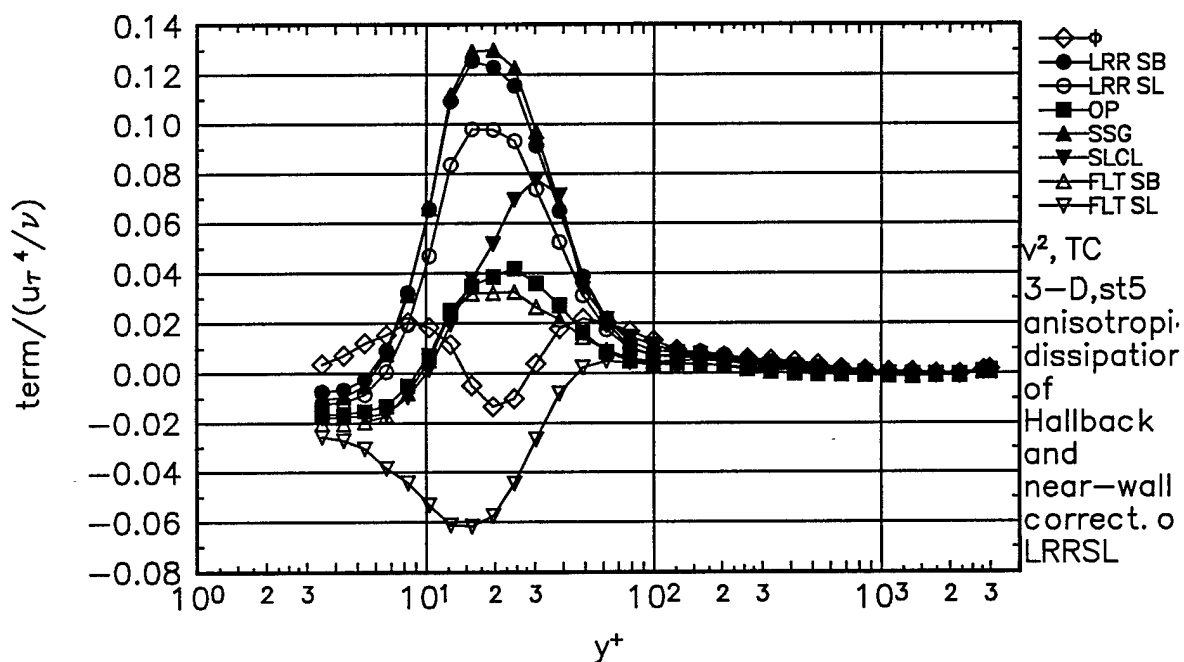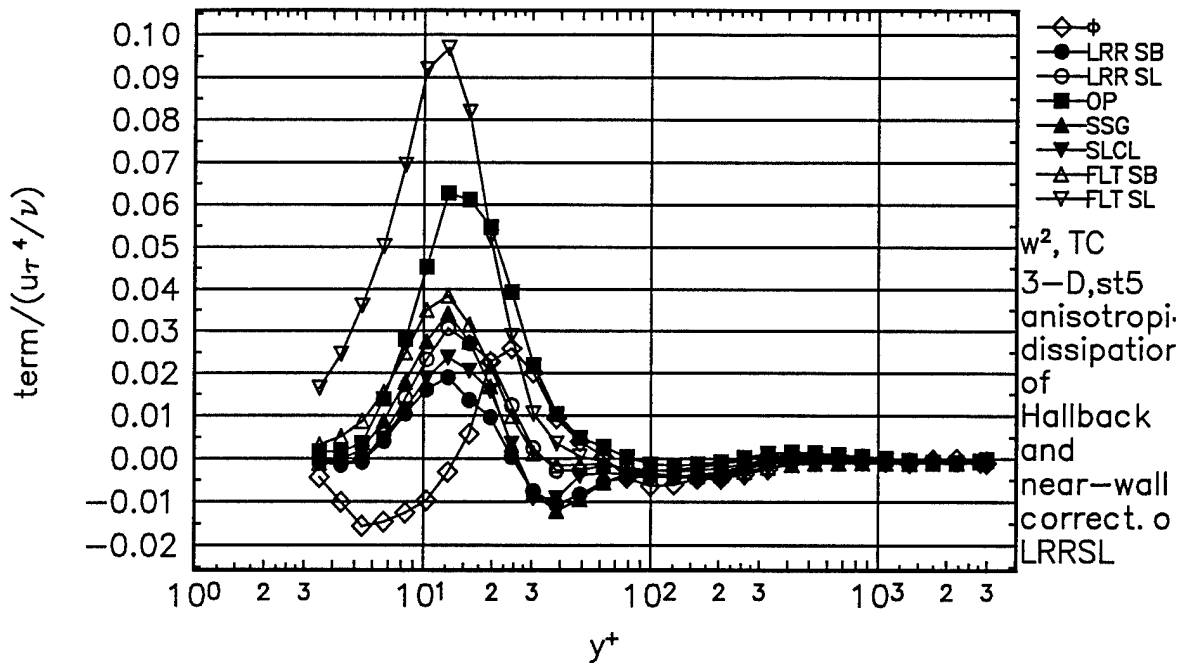
Figure 157. Comparison of $\overline{w^2}$ normal stress transport experimental pressure-strain term ◊, to theoretical pressure-strain terms for the 2-D station. Gibson-Launder, ●; Launder-Reece-Rodi (LRR), O; Oberlack-Peters (OP), ■; Speziale-Sarkar-Gatski (SSG), ▲; Shih-Lumley/Choi-Lumley (SLCL), ▼; Fu-Launder-Tselepidakis 1 (FLT1), ▵; Fu-Launder-Tselepidakis 2 (FLT2), ▽. Near-wall corrections of Launder-Reece-Rodi (1975), anisotropic dissipation of Hallbäck (1990).

Figure 158. Comparison of $\overline{uv}$ shear stress transport experimental pressure-strain term ◊, to theoretical pressure-strain terms for the 2-D station. Gibson-Launder, ●; Launder-Reece-Rodi (LRR), O; Oberlack-Peters (OP), ■; Speziale-Sarkar-Gatski (SSG), ▲; Shih-Lumley/Choi-Lumley (SLCL), ▼; Fu-Launder-Tselepidakis 1 (FLT1), ▵; Fu-Launder-Tselepidakis 2 (FLT2), ▽. Near-wall corrections of Launder-Reece-Rodi (1975), anisotropic dissipation of Hallbäck (1990).
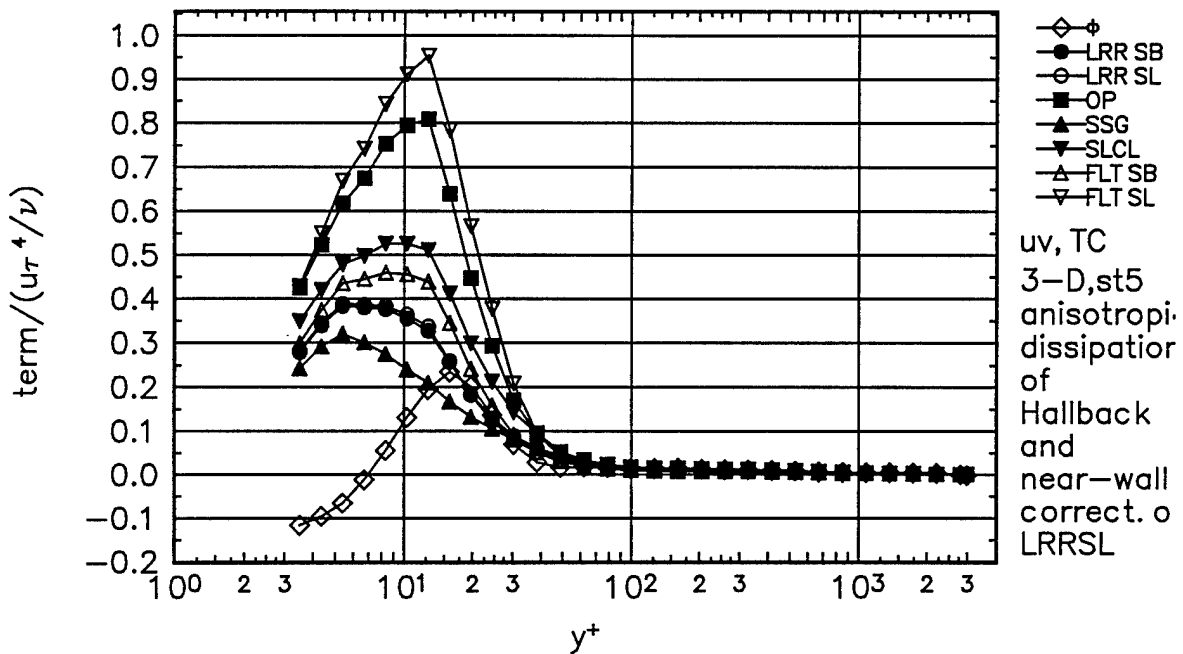
Figures

Figure 159. Comparison of $\overline{u^2}$ normal stress transport experimental pressure-strain term ◊, to theoretical pressure-strain terms for Station 5. Gibson-Launder, ●; Launder-Reece-Rodi (LRR), O; Oberlack-Peters (OP), ■; Speziale-Sarkar-Gatski (SSG), ▲; Shih-Lumley/Choi-Lumley (SLCL), ▼; Fu-Launder-Tselepidakis 1 (FLT1), ▵; Fu-Launder-Tselepidakis 2 (FLT2), ▽. Near-wall corrections of Launder-Reece-Rodi (1975), anisotropic dissipation of Hallbäck (1990).

Figure 160. Comparison of $\overline{v^2}$ normal stress transport experimental pressure-strain term ◊, to theoretical pressure-strain terms for Station 5. Gibson-Launder, ●; Launder-Reece-Rodi (LRR), O; Oberlack-Peters (OP), ■; Speziale-Sarkar-Gatski (SSG), ▲; Shih-Lumley/Choi-Lumley (SLCL), ▼; Fu-Launder-Tselepidakis 1 (FLT1), ▵; Fu-Launder-Tselepidakis 2 (FLT2), ▽. Near-wall corrections of Launder-Reece-Rodi (1975), anisotropic dissipation of Hallbäck (1990).

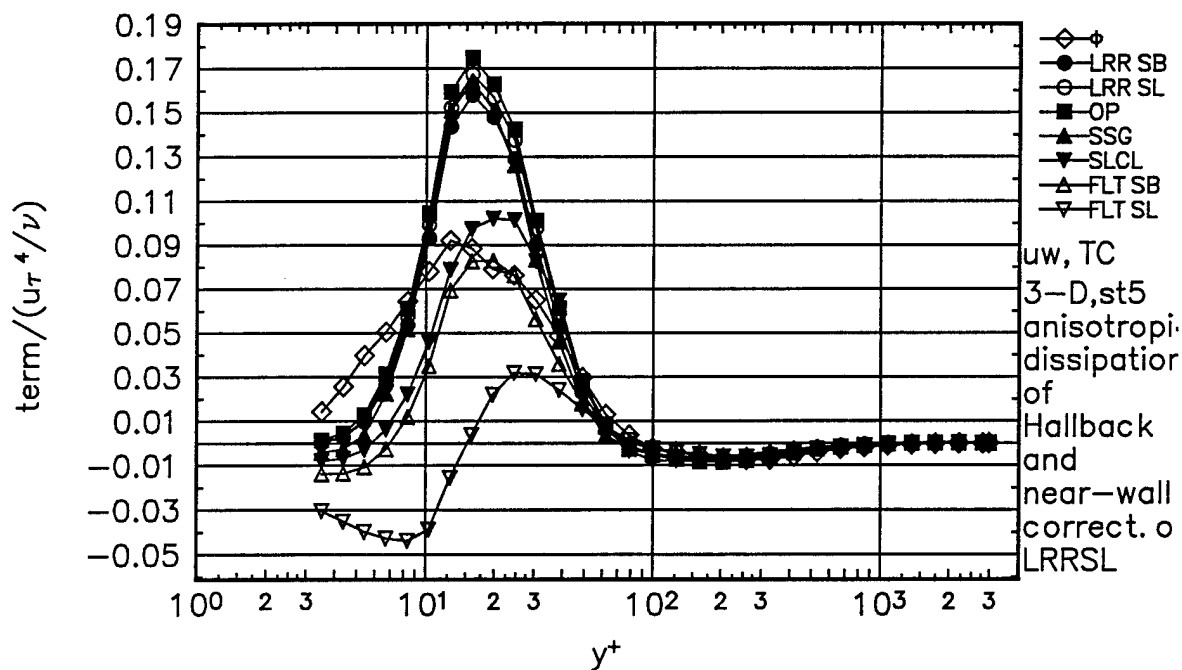Figure 161. Comparison of $\overline{w^2}$ normal stress transport experimental pressure-strain term ◊, to theoretical pressure-strain terms for Station 5. Gibson-Launder, ●; Launder-Reece-Rodi (LRR), O; Oberlack-Peters (OP), ■; Speziale-Sarkar-Gatski (SSG), ▲; Shih-Lumley/Choi-Lumley (SLCL), ▼; Fu-Launder-Tselepidakis 1 (FLT1), ∆; Fu-Launder-Tselepidakis 2 (FLT2), ▽. Near-wall corrections of Launder-Reece-Rodi (1975), anisotropic dissipation of Hallbäck (1990).

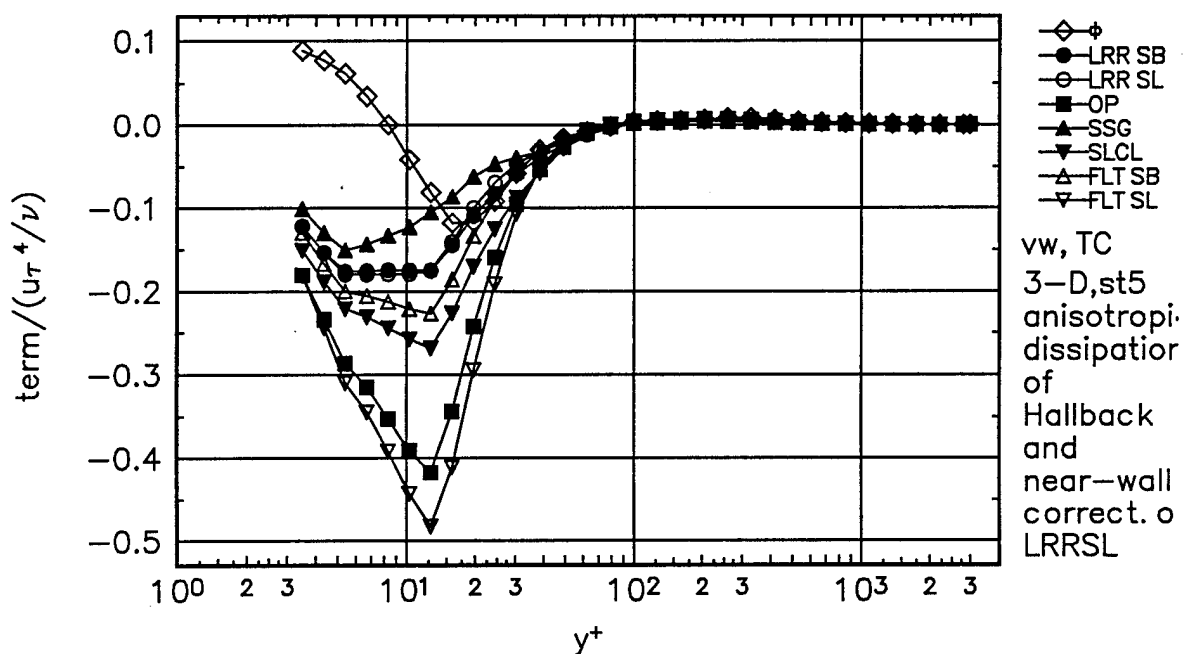Figure 162. Comparison of $\overline{uv}$ shear stress transport experimental pressure-strain term ◊, to theoretical pressure-strain terms for Station 5. Gibson-Launder, ●; Launder-Reece-Rodi (LRR), O; Oberlack-Peters (OP), ■; Speziale-Sarkar-Gatski (SSG), ▲; Shih-Lumley/Choi-Lumley (SLCL), ▼; Fu-Launder-Tselepidakis 1 (FLT1), ∆; Fu-Launder-Tselepidakis 2 (FLT2), ▽. Near-wall corrections of Launder-Reece-Rodi (1975), anisotropic dissipation of Hallbäck (1990).

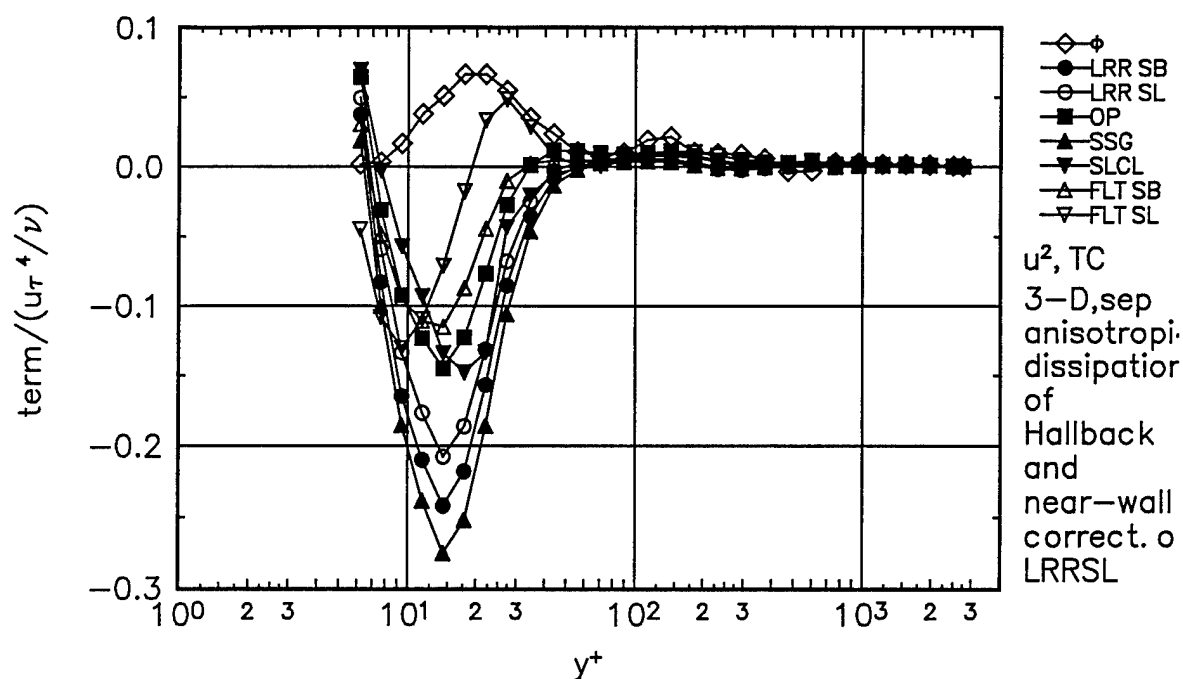Figure 163. Comparison of $\overline{uw}$ shear stress transport experimental pressure-strain term ◊, to theoretical pressure-strain terms for Station 5. Gibson-Launder, ●; Launder-Reece-Rodi (LRR), O; Oberlack-Peters (OP), ■; Speziale-Sarkar-Gatski (SSG), ▲; Shih-Lumley/Choi-Lumley (SLCL), ▼; Fu-Launder-Tselepidakis 1 (FLT1), △; Fu-Launder-Tselepidakis 2 (FLT2), ▽. Near-wall corrections of Launder-Reece-Rodi (1975), anisotropic dissipation of Hallbäck (1990).
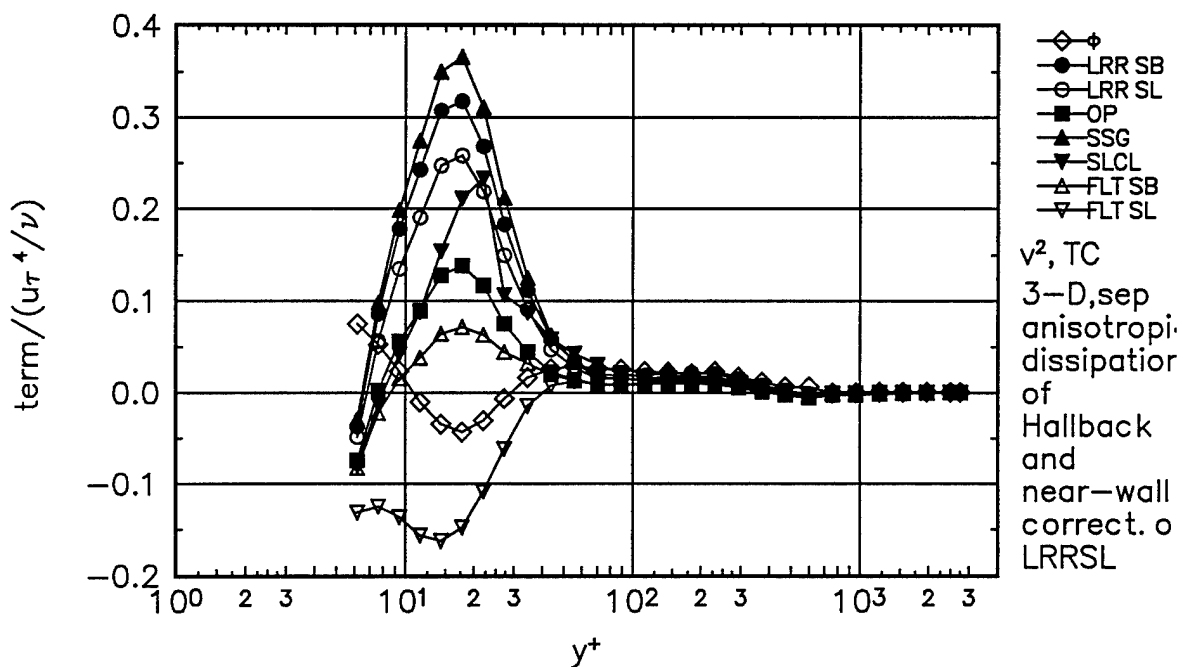

Figure 164. Comparison of $\overline{vw}$ shear stress transport experimental pressure-strain term ◊, to theoretical pressure-strain terms for Station 5. Gibson-Launder, ●; Launder-Reece-Rodi (LRR), O; Oberlack-Peters (OP), ■; Speziale-Sarkar-Gatski (SSG), ▲; Shih-Lumley/Choi-Lumley (SLCL), ▼; Fu-Launder-Tselepidakis 1 (FLT1), △; Fu-Launder-Tselepidakis 2 (FLT2), ▽. Near-wall corrections of Launder-Reece-Rodi (1975), anisotropic dissipation of Hallbäck (1990).

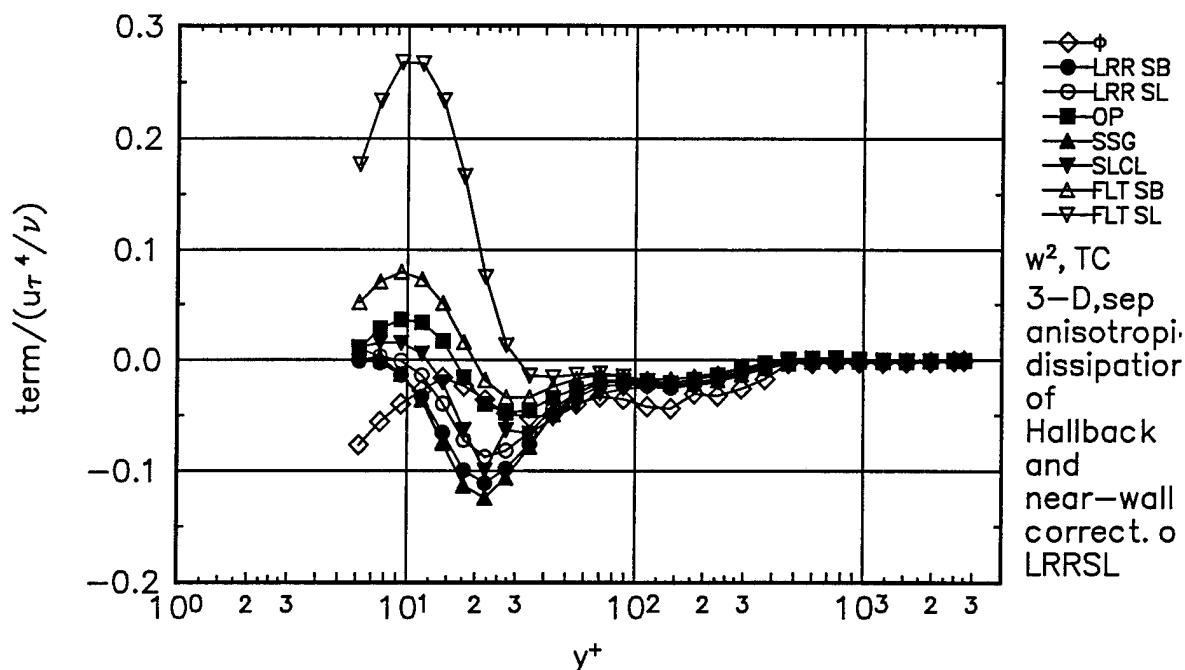Figures   136

Figure 165. Comparison of $\overline{u^2}$ normal stress transport experimental pressure-strain term ◊, to theoretical pressure-strain terms for Separation station. Gibson-Launder, ●; Launder-Reece-Rodi (LRR), O; Oberlack-Peters (OP), ■; Speziale-Sarkar-Gatski (SSG), ▲; Shih-Lumley/Choi-Lumley (SLCL), ▼; Fu-Launder-Tselepidakis 1 (FLT1), △; Fu-Launder-Tselepidakis 2 (FLT2), ▽. Near-wall corrections of Launder-Reece-Rodi (1975), anisotropic dissipation of Hallbäck (1990).

Figure 166. Comparison of $\overline{v^2}$ normal stress transport experimental pressure-strain term ◊, to theoretical pressure-strain terms for Separation station. Gibson-Launder, ●; Launder-Reece-Rodi (LRR), O; Oberlack-Peters (OP), ■; Speziale-Sarkar-Gatski (SSG), ▲; Shih-Lumley/Choi-Lumley (SLCL), ▼; Fu-Launder-Tselepidakis 1 (FLT1), △; Fu-Launder-Tselepidakis 2 (FLT2), ▽. Near-wall corrections of Launder-Reece-Rodi (1975), anisotropic dissipation of Hallbäck (1990).
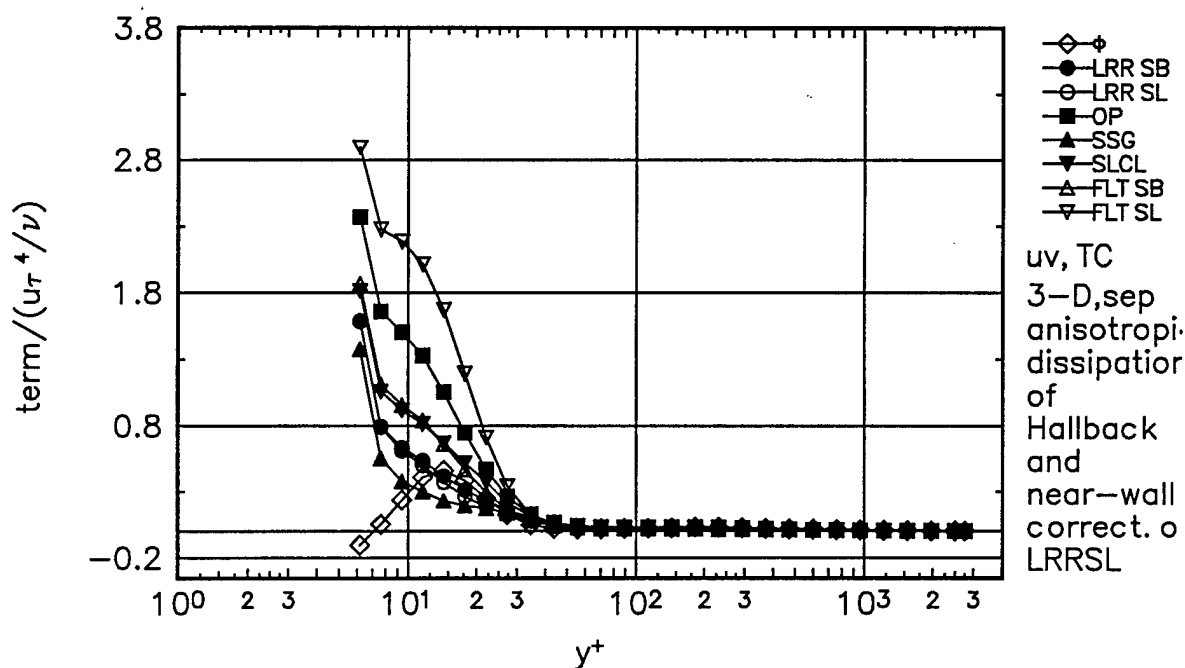
Figures

137

Figure 167. Comparison of $\overline{w^2}$ normal stress transport experimental pressure-strain term ◊, to theoretical pressure-strain terms for Separation station. Gibson-Launder, ●; Launder-Reece-Rodi (LRR), O; Oberlack-Peters (OP), ■; Speziale-Sarkar-Gatski (SSG), ▲; Shih-Lumley/Choi-Lumley (SLCL), ▼; Fu-Launder-Tselepidakis 1 (FLT1), ▵; Fu-Launder-Tselepidakis 2 (FLT2), ▽. Near-wall corrections of Launder-Reece-Rodi (1975), anisotropic dissipation of Hallbäck (1990).
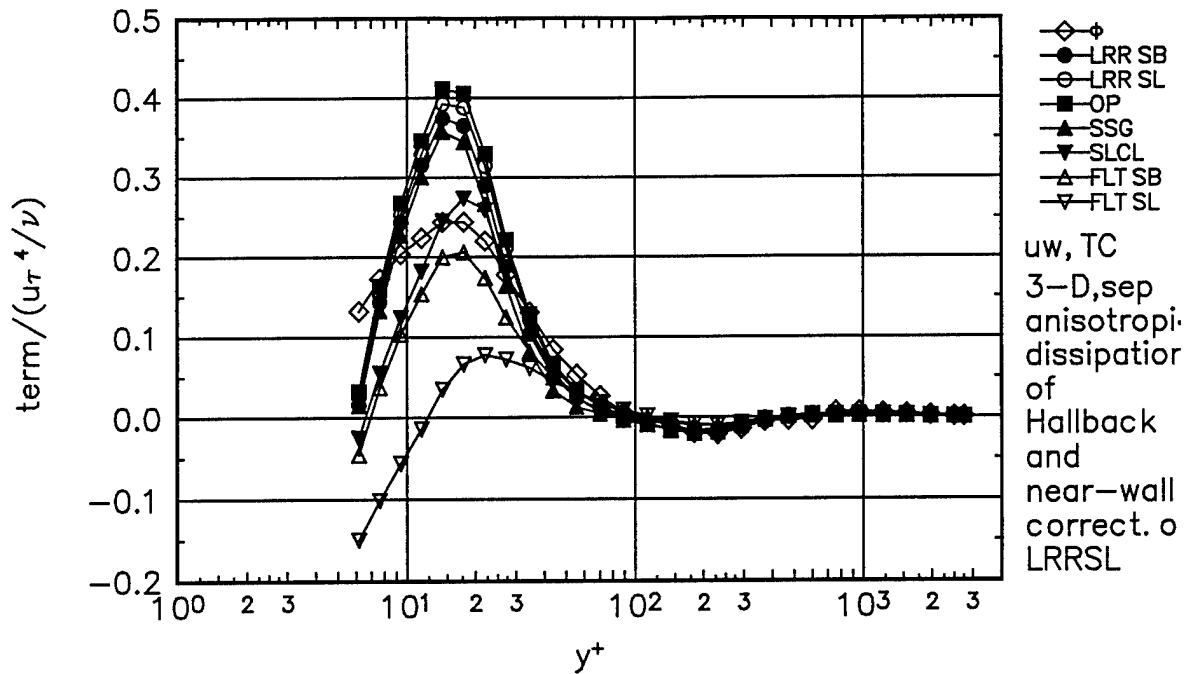

Figure 168. Comparison of $\overline{uv}$ shear stress transport experimental pressure-strain term ◊, to theoretical pressure-strain terms for Separation station. Gibson-Launder, ●; Launder-Reece-Rodi (LRR), O; Oberlack-Peters (OP), ■; Speziale-Sarkar-Gatski (SSG), ▲; Shih-Lumley/Choi-Lumley (SLCL), ▼; Fu-Launder-Tselepidakis 1 (FLT1), ▵; Fu-Launder-Tselepidakis 2 (FLT2), ▽. Near-wall corrections of Launder-Reece-Rodi (1975), anisotropic dissipation of Hallbäck (1990).
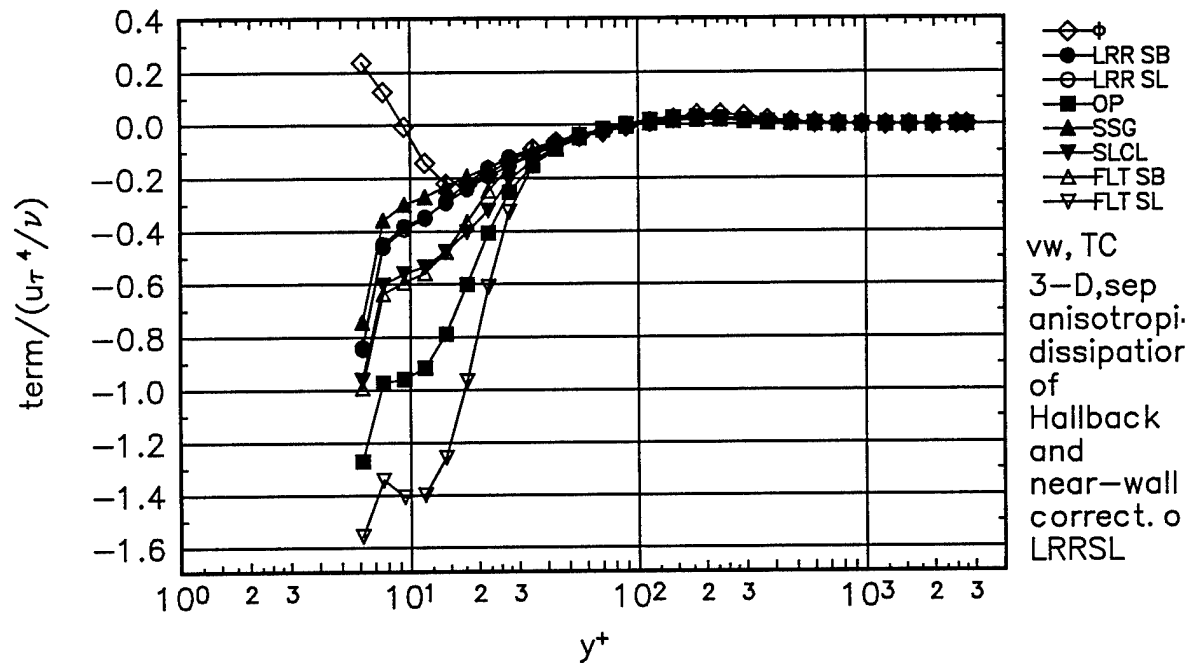
Figure 169. Comparison of $\overline{uw}$ shear stress transport experimental pressure-strain term ◊, to theoretical pressure-strain terms for Separation station. Gibson-Launder, ●; Launder-Reece-Rodi (LRR), O; Oberlack-Peters (OP), ■; Speziale-Sarkar-Gatski (SSG), ▲; Shih-Lumley/Choi-Lumley (SLCL), ▼; Fu-Launder-Tselepidakis 1 (FLT1), △; Fu-Launder-Tselepidakis 2 (FLT2), ▽. Near-wall corrections of Launder-Reece-Rodi (1975), anisotropic dissipation of Hallbäck (1990).
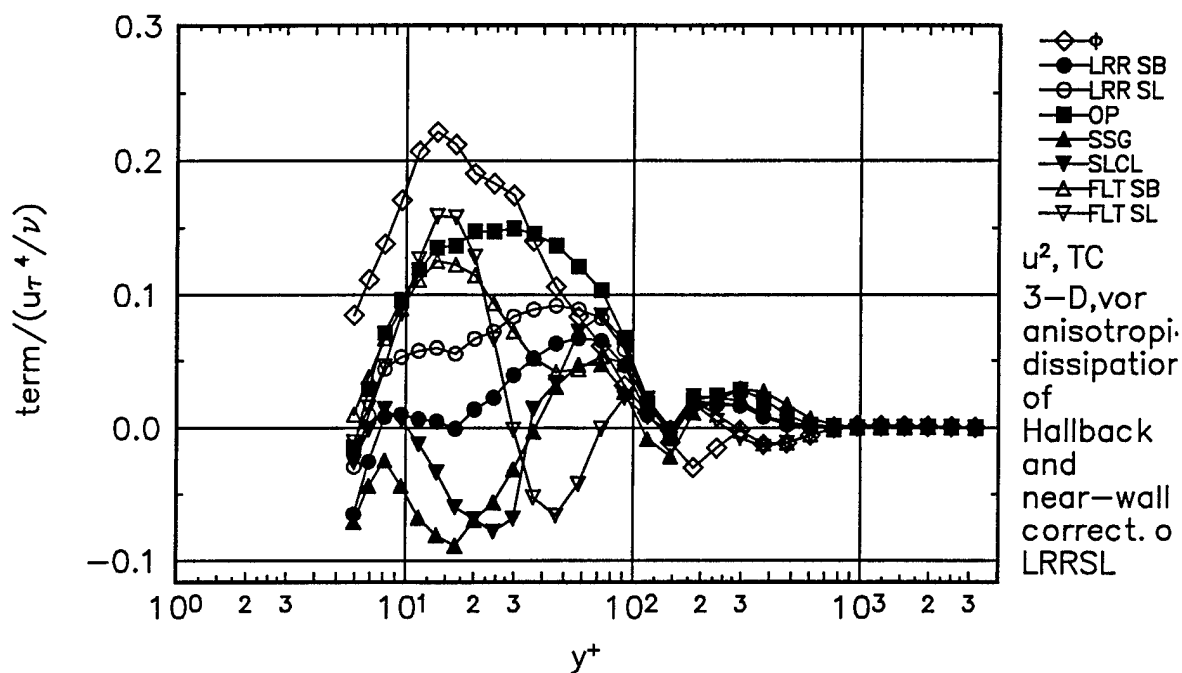

Figure 170. Comparison of $\overline{vw}$ shear stress transport experimental pressure-strain term ◊, to theoretical pressure-strain terms for Separation station. Gibson-Launder, ●; Launder-Reece-Rodi (LRR), O; Oberlack-Peters (OP), ■; Speziale-Sarkar-Gatski (SSG), ▲; Shih-Lumley/Choi-Lumley (SLCL), ▼; Fu-Launder-Tselepidakis 1 (FLT1), △; Fu-Launder-Tselepidakis 2 (FLT2), ▽. Near-wall corrections of Launder-Reece-Rodi (1975), anisotropic dissipation of Hallbäck (1990).
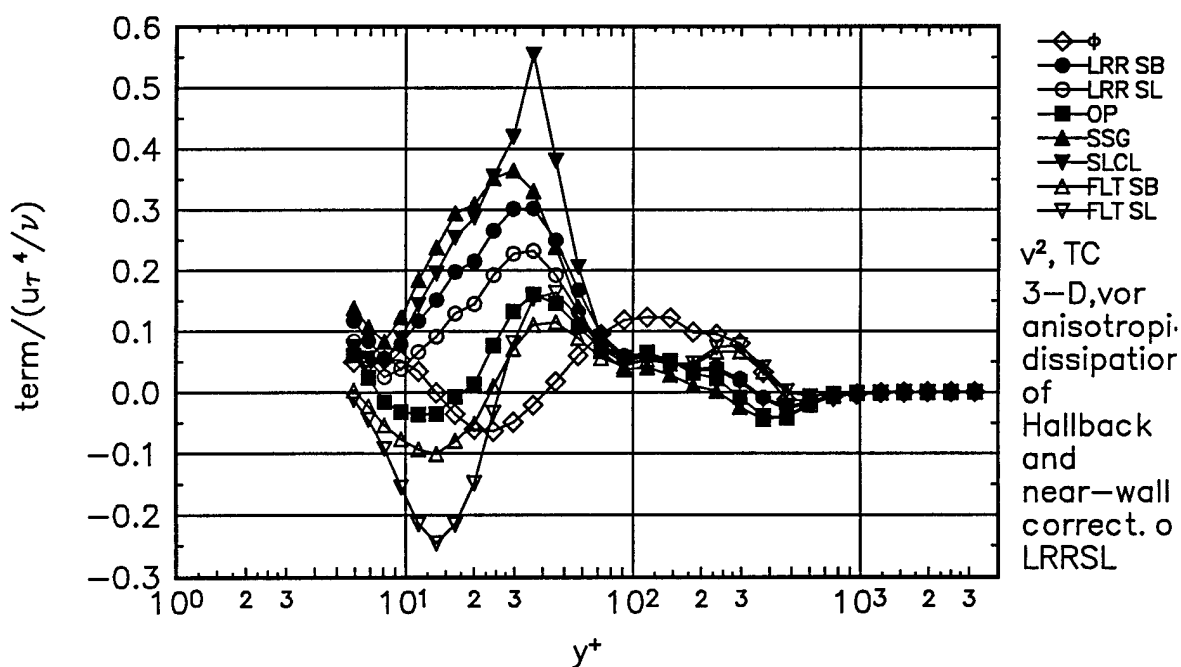
Figures

139

Figure 171. Comparison of $\overline{u^2}$ normal stress transport experimental pressure-strain term ◊, to theoretical pressure-strain terms for Vortex station. Gibson-Launder, ●; Launder-Reece-Rodi (LRR), O; Oberlack-Peters (OP), ■; Speziale-Sarkar-Gatski (SSG), ▲; Shih-Lumley/Choi-Lumley (SLCL), ▼; Fu-Launder-Tselepidakis 1 (FLT1), ▵; Fu-Launder-Tselepidakis 2 (FLT2), ▽. Near-wall corrections of Launder-Reece-Rodi (1975), anisotropic dissipation of Hallbäck (1990).
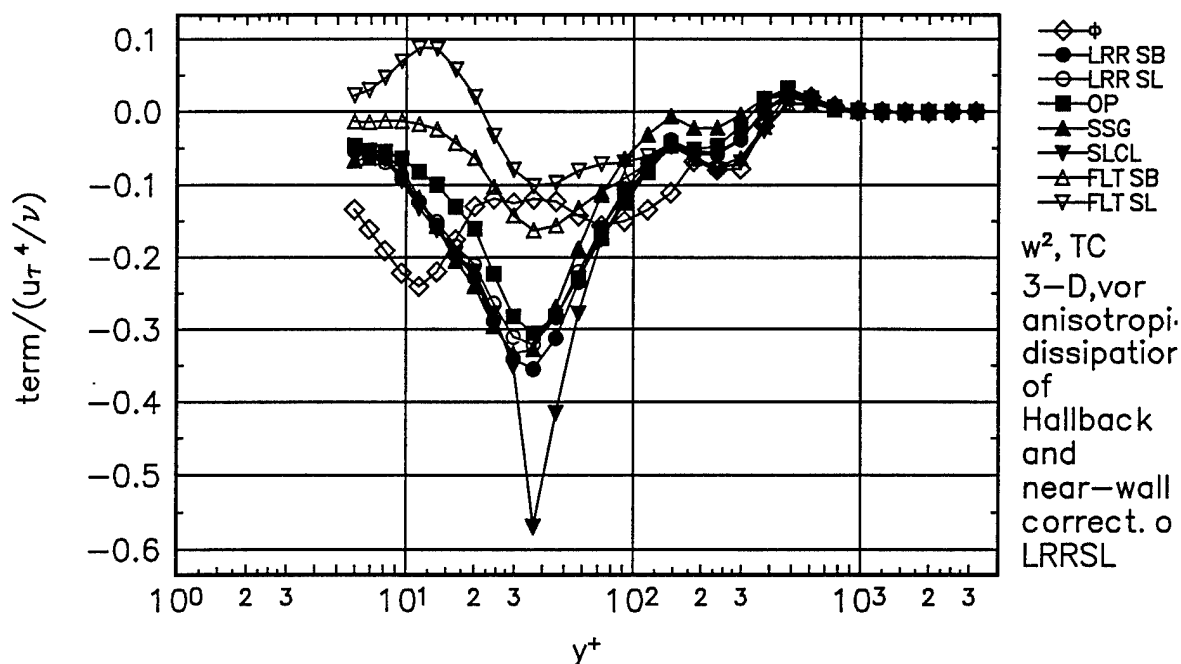

Figure 172. Comparison of $\overline{v^2}$ normal stress transport experimental pressure-strain term ◊, to theoretical pressure-strain terms for Vortex station. Gibson-Launder, ●; Launder-Reece-Rodi (LRR), O; Oberlack-Peters (OP), ■; Speziale-Sarkar-Gatski (SSG), ▲; Shih-Lumley/Choi-Lumley (SLCL), ▼; Fu-Launder-Tselepidakis 1 (FLT1), ▵; Fu-Launder-Tselepidakis 2 (FLT2), ▽. Near-wall corrections of Launder-Reece-Rodi (1975), anisotropic dissipation of Hallbäck (1990).

Figure 173. Comparison of $\overline{w^2}$ normal stress transport experimental pressure-strain term ◊, to theoretical pressure-strain terms for Vortex station. Gibson-Launder, ●; Launder-Reece-Rodi (LRR), O; Oberlack-Peters (OP), ■; Speziale-Sarkar-Gatski (SSG), ▲; Shih-Lumley/Choi-Lumley (SLCL), ▼; Fu-Launder-Tselepidakis 1 (FLT1), △; Fu-Launder-Tselepidakis 2 (FLT2), ▽. Near-wall corrections of Launder-Reece-Rodi (1975), anisotropic dissipation of Hallbäck (1990).
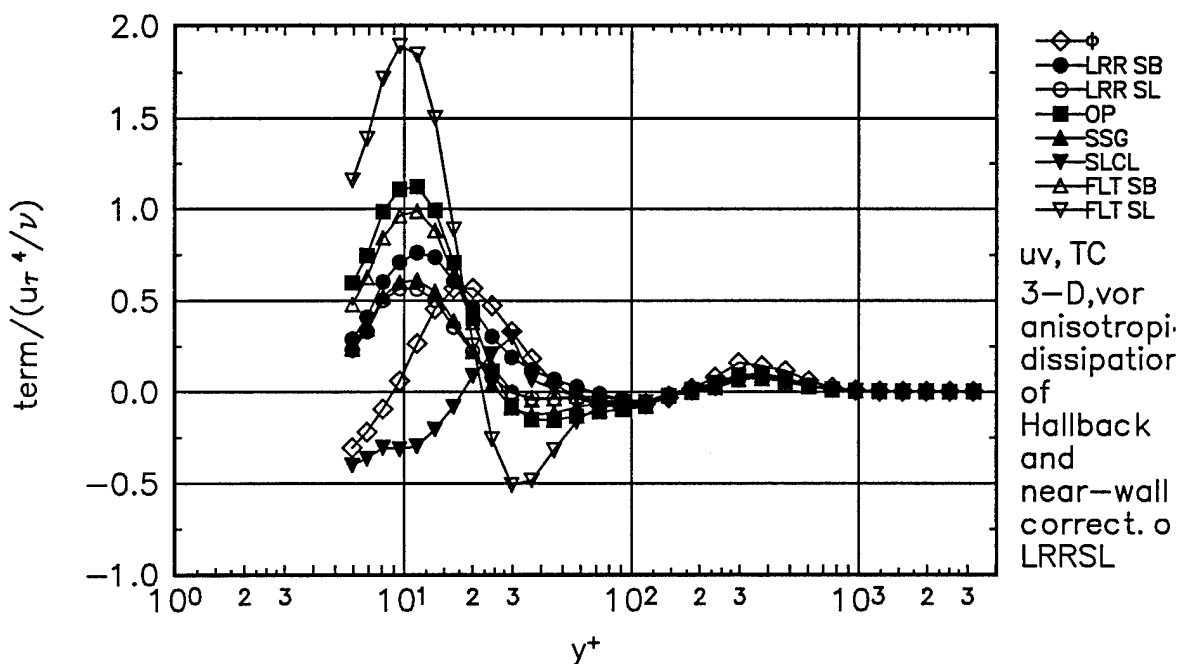

Figure 174. Comparison of $\overline{uv}$ shear stress transport experimental pressure-strain term ◊, to theoretical pressure-strain terms for Vortex station. Gibson-Launder, ●; Launder-Reece-Rodi (LRR), O; Oberlack-Peters (OP), ■; Speziale-Sarkar-Gatski (SSG), ▲; Shih-Lumley/Choi-Lumley (SLCL), ▼; Fu-Launder-Tselepidakis 1 (FLT1), △; Fu-Launder-Tselepidakis 2 (FLT2), ▽. Near-wall corrections of Launder-Reece-Rodi (1975), anisotropic dissipation of Hallbäck (1990).
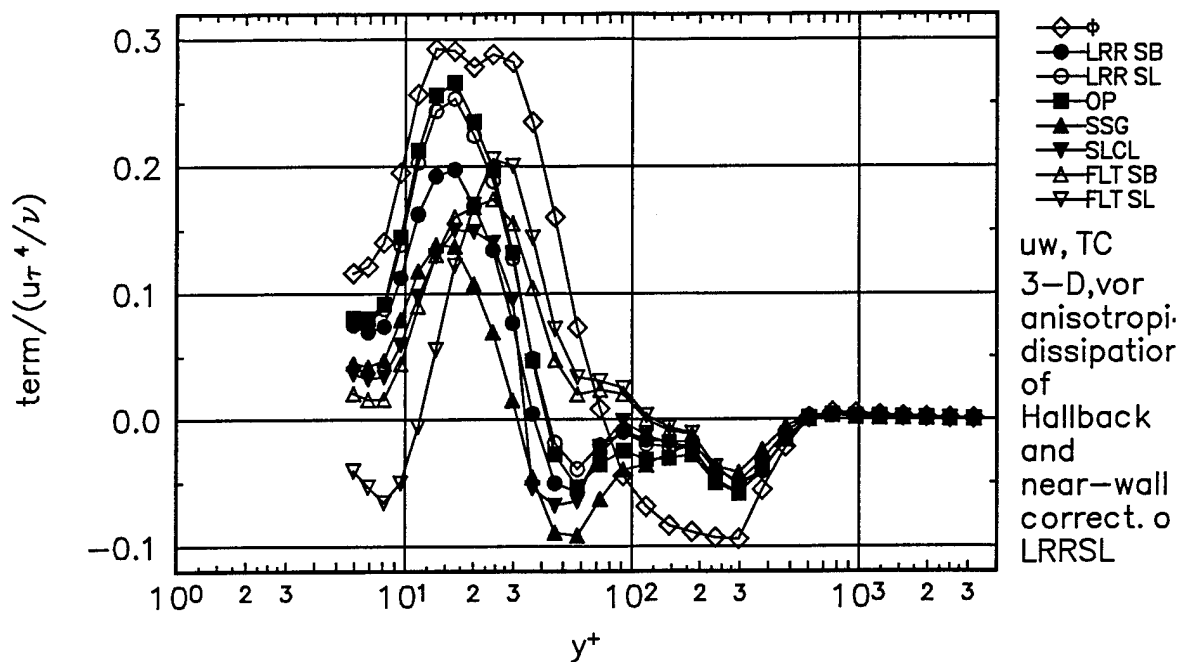
Figure 175. Comparison of $\overline{uw}$ shear stress transport experimental pressure-strain term ◊, to theoretical pressure-strain terms for Vortex station. Gibson-Launder, ●; Launder-Reece-Rodi (LRR), O; Oberlack-Peters (OP), ■; Speziale-Sarkar-Gatski (SSG), ▲; Shih-Lumley/Choi-Lumley (SLCL), ▼; Fu-Launder-Tselepidakis 1 (FLT1), △; Fu-Launder-Tselepidakis 2 (FLT2), ▽. Near-wall corrections of Launder-Reece-Rodi (1975), anisotropic dissipation of Hallbäck (1990).

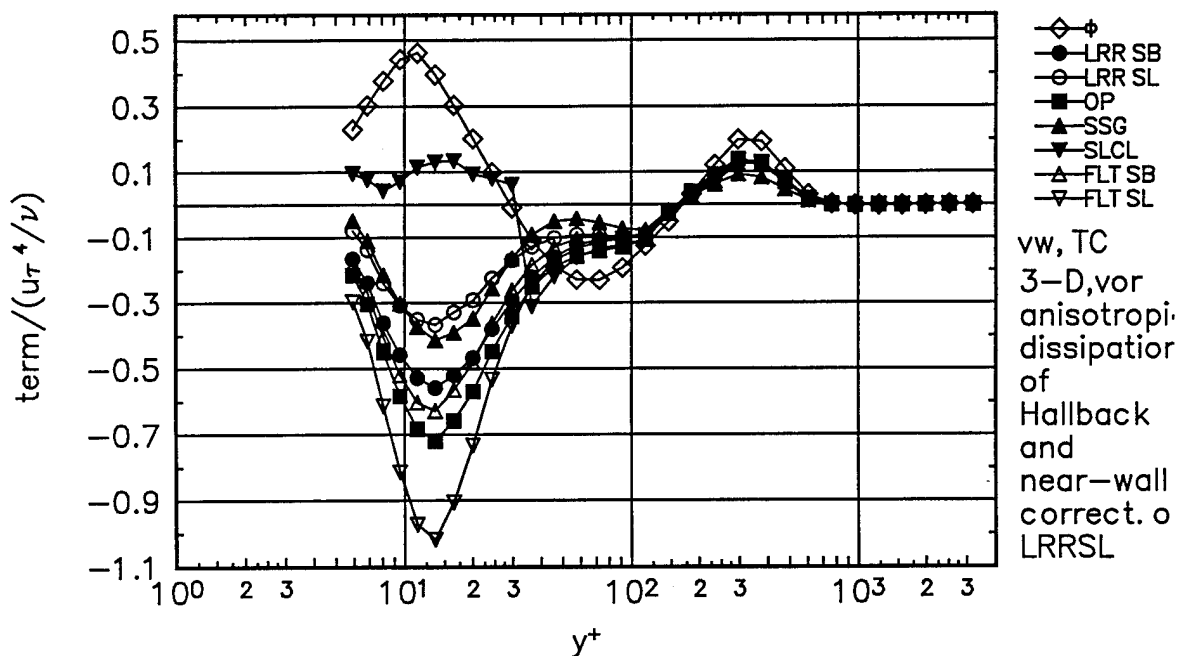

Figure 176. Comparison of $\overline{vw}$ shear stress transport experimental pressure-strain term ◊, to theoretical pressure-strain terms for Vortex station. Gibson-Launder, ●; Launder-Reece-Rodi (LRR), O; Oberlack-Peters (OP), ■; Speziale-Sarkar-Gatski (SSG), ▲; Shih-Lumley/Choi-Lumley (SLCL), ▼; Fu-Launder-Tselepidakis 1 (FLT1), △; Fu-Launder-Tselepidakis 2 (FLT2), ▽. Near-wall corrections of Launder-Reece-Rodi (1975), anisotropic dissipation of Hallbäck (1990).